NOVEL APPROACHES FOR IMAGE ANALYSIS OF IN VITRO EPITHELIAL CULTURES WITH APPLICATION TO SILVER NANOPARTICLE TOXICITY

by

RACHEL CATHARINE FLIGHT

A thesis submitted to the University of Birmingham for the degree of

DOCTOR OF PHILOSOPHY

PSIBS Doctoral Training Centre

College of Engineering and Physical Sciences

University of Birmingham

August 2016

Abstract

A novel imaging approach was developed for the purpose of counting cells from phase contrast microscopy images of laboratory grown (*in vitro*) cultures of epithelial cells. Validation through comparison with standard laboratory cell counting techniques showed this approach provided consistent and comparable results, whilst overcoming limitations of these existing techniques, such as operator variability and sample destruction.

The imaging approach was subsequently applied to investigate the effects of silver nanoparticles (AgNP) on H400 oral keratinocytes. Concurrent investigations into antimicrobial effects of AgNP were performed on *Escherichia coli, Staphylococcus aureus* and *Streptococcus mutans* to provide models for Gram-positive and Gram-negative infection, and to compare with the literature and oral keratinocyte toxicity. It was found that AgNP elicit size-, dose- and time-dependent growth inhibition in both human cells and bacteria, although bacterial inhibition was not achieved without significant cytotoxicity at the same concentrations.

DEDICATED TO MY FAMILY

Acknowledgements

I would firstly like to thank my supervisors, Professor Paul Cooper, Professor Gabriel Landini, Dr Iain Styles, Dr Mike Milward and Dr Dick Shelton for the opportunity to undertake this PhD project and for their support and guidance throughout.

As a relative novice in biology and chemistry laboratory work at the beginning of this project I owe a great debt of gratitude to the people who helped me learn these skills. Thank you to Dr Phillipa White and Khawla Doudin for their assistance in microbiology and Dr Rachel Sammons for the use of her lab, Chris Stepanek and Professor Zoe Pikramenou for their advice and patient training in nanoparticle synthesis and characterisation and the Hannon group for the use of their lab, and the technical team at the School of Dentistry for their ongoing support in all cell culture matters, particularly Gay Smith and Michelle Holder. I'm also grateful for technical assistance and sample preparation from Theresa Morris and Paul Stanley at the University of Birmingham Centre for Electron Microscopy, and Eimear Orgill at School of Geography, Earth and Environmental Sciences.

Thank you to the past and present members of the University of Birmingham and Birmingham City korfball clubs for providing me with an incredible antidote to the stresses of PhD life. Particular thanks to Sam Bailey, who has been my rock in the last couple of years.

I'm also grateful to the support of my fellow PhD students in the School of Dentistry: they say blood, sweat and tears go into doing a PhD but I never realised it would be so literal until I encountered the 7th floor postgraduate sauna and my hypodermic needle-wielding colleagues. I will really miss seeing them all every day, despite all the leeching.

I also thank the past and present members of the PSIBS DTC for making it an interesting and enjoyable group to be a part of. Special thanks go to my friends in the 2011 cohort, with whom I've shared this "unique" journey every step of the way.

Most of all, I thank my family. Anything I have achieved has been thanks to their unwavering love and support, and words are insufficient to express how grateful I am for everything they've done for me (even when it was just acting as a "cardboard cut-out").

Project outcomes

Peer-reviewed conference proceedings:

- R. Flight, G. Landini, I. Styles, R. Shelton, M. Milward, and P. Cooper, "Semi-automated cell counting in phase contrast images of epithelial monolayers," in *Proceedings of the 18th Conference on Medical Image Understanding and Analysis*, City University London, 2014, pp. 241–246.
- R. Flight, G. Landini, I. Styles, R. Shelton, M. Milward, and P. Cooper, "Automated optimisation of cell segmentation parameters in phase contrast using discrete mereotopology," in *Proceedings of the 19th Conference on Medical Image Understanding and Analysis*, University of Lincoln, 2015, pp. 126–131.

Conference presentations:

- R. Flight, G. Landini, I. Styles, R. Shelton, M. Milward, and P. Cooper, "Semi-automated cell counting in phase contrast images of epithelial monolayers". (Poster presentation.) Microscience Microscopy Congress. Manchester, UK. July 2014.
- R. Flight, G. Landini, I. Styles, R. Shelton, M. Milward, and P. Cooper, "Image analysis of phase contrast images for cell counting in epithelial monolayers". (Oral and poster presentation.) 5th Annual BEAR Conference. Birmingham, UK. December, 2014.
- R. Flight, G. Landini, I. Styles, R. Shelton, M. Milward, and P. Cooper, "Optimisation of cell segmentation in phase contrast microscopy images of epithelial monolayers using discrete mereotopology". (Poster presentation.) International Symposium on Biomedical Imaging. Brooklyn, NY, USA. April 2015
- R. Flight, G. Landini, I. Styles, R. Shelton, M. Milward, and P. Cooper "Investigation into silver nanoparticle toxicity using phase contrast microscopy". (Poster presentation.) Id^{2}bham 2015. Birmingham, UK. June 2015.

Awards:

- Best poster presentation, MIUA 2015.

Table of Contents

List of figures

List of tables

List of abbreviations

AgNP	Silver nanoparticles
ANOVA	Analysis of variance
ATCC	American Type Culture Collection
ATP	Adenosine triphosphate
BHI	Brain heart infusion
BPA	Bovine pituitary extract
CCD	Charge coupled device
CFU	Colony forming unit
CPF	Cumulative probability function
DAPI	4',6-diamidino-2-phenylindole
DLS	Dynamic light scattering
DM	Discrete mereotopology
DMEM	Dulbeccos Modified Eagle Medium
DMSO	Dimethyl sulfoxide
DNA	Deoxyribonucleic acid
EDS	Energy dispersive spectroscopy
EDTA	Ethylenediaminetetraacetic acid
EGF	Epidermal growth factor
FCS	Foetal calf serum
FN	False negative
FP	False positive
FWHM	Full width at half maximum
hTERT	Human telomerase reverse transcriptase
ICP-OES	Inductively coupled plasma optical emission spectroscopy
LDA	Linear discriminant analysis
MBC	Minimum bactericidal concentration
MIC	Minimum inhibitory concentration

MTT	3-(4,5-Dimethylthiazol-2-Yl)-2,5-Diphenyltetrazolium Bromide
OD	Optical density
PBS	Phosphate buffered saline
PC	Phase contrast
PCA	Principal component analysis
PFA	Paraformaldehyde
ppb	Parts per billion
PVP	Polyvinylpyrrolidone
RCC(D)	(Discrete) region connected calculus
RO water	Water purified by reverse osmosis
ROS	Reactive Oxygen species
rpm	Rotations per minute
RPMI	Roswell Park Memorial Institute (cell media)
SCC	Squamous cell carcinoma
SPR	Surface plasmon resonance
SVM	Support vector machine
TEM	Transmission electron microscopy
TN	True negative
TP	True positive
UV-vis	Ultraviolet to visible wavelengths of light

1 INTRODUCTION

1.1 Overview

The oral epithelium provides one of the first lines of defence for protecting the underlying structures of the oral cavity, thus research into the effects of potential therapeutic drugs or toxicants to which oral epithelium is exposed is important. Experimental analysis of tissues cultured in the laboratory, known as "*in vitro*" cultures, provides a convenient approach to study the response of cells and tissues to injury, disease or external stimuli at a cellular level under controlled conditions, and is of significant interest in drug development and toxicological studies which will ultimately benefit human health. In such investigations, cell numbers are often evaluated to determine cell viability, growth and proliferation rates compared with controls. However, many of the laboratory techniques used to monitor cell numbers in culture have significant disadvantages, such as destruction of cell cultures as part of the analytical process and high rates of operator error, thus developing novel non-invasive and non-destructive approaches is desirable. Analysis of phase contrast microscopy images was identified as a potential source for the development of a method for counting cells in culture to address the limitations of current methodologies. As a result, this thesis describes the development and validation of such a technique, and subsequently its application for the investigation of silver nanoparticles effects on *in vitro* cultures of oral epithelial cells.

The introduction to this thesis (section 1.1) firstly provides background information on the structure and biology of the oral cavity since this environment was the biological focus of this work, and an oral epithelial cell line was used in the development and application stages of the image analysis method. Sections 1.3 - 1.4 detail the use of *in vitro* cell cultures and assays for the study of cell responses, focussing specifically on current methods for

evaluating cell growth and their limitations. Subsequently, a number of microscopy techniques and image analysis methods for the purpose of cell counting are reviewed in sections 1.5 - 1.6. Finally, in section 1.7, silver nanoparticles are introduced and previous studies regarding their toxicity to human and bacterial cells is discussed, with particular focus on the oral environment.

1.2 The oral cavity

The oral cavity is a portal of entry to the respiratory and gastrointestinal systems and plays an important role in the essential processes of eating, drinking, breathing and, in humans, speaking. The main structural features of the oral cavity are the palate, gingiva, tongue and teeth; all but the latter are lined by oral mucosal tissue (Figure 1.1). The oral mucosa provides an initial line of defence for protecting the other underlying tissues of the oral cavity from infection and physical trauma [1].

1.2.1 Structure and function of the oral mucosa

The oral mucosa is a mucous membrane consisting of a stratified squamous epithelium – layers of flattened epithelial cells – supported by underlying connective tissue which is termed the “lamina propria” (Figure 1.2) [2]. The oral mucosa is divided into three types, which have different properties according to their location and function. These are: i) the masticatory mucosa, ii) the lining mucosa and iii) the specialised mucosa, and their locations are shown in Figure 1.1 [1]. The epithelium of masticatory mucosa is characterised by the presence the structural protein keratin, known as “keratinisation”, in the superficial layers (Figure 1.2). Keratin is a filamentous structural cytoskeletal protein that provides the tissue with its structural integrity. Epithelial cells in keratinised mucosa, or keratinocytes,

differentially express specific keratins as they develop and migrate suprabasally through the layers of the epithelium (Figure 1.2). Eventually keratinocytes develop into non-living corneocytes in the keratinised layer which are ultimately sloughed away and replaced [3]. Aided by tight connections of the oral epithelium with the underlying lamina propria via the basement membrane, the masticatory mucosa is able to withstand mechanical stress and therefore is located in regions associated with chewing, such as the hard palate and gingiva. Conversely, the lining mucosa consists of non-keratinised epithelium which is attached to the lamina propria by a flexible connective tissue. The increased elasticity of the lining mucosa permits the range of movement required for chewing, speaking and swallowing, thus this tissue is located on the internal surfaces of the cheeks and lips, and floor of the mouth [2]. Finally, specialised mucosa is found at locations in the oral cavity where specific functions are required, for example, the upper surface of the tongue contains both keratinised and non-keratinised papillae (tiny protrusions in the epithelium) which aid with mastication and taste perception [4].

In all of the types of oral mucosa described, the main function of the oral epithelium is to provide protection for the underlying structures. When the continuity of epithelial tissue is broken (described in section 1.2.2), epithelial cells respond by increasing proliferation and migrate and differentiate from the basal population surrounding the lesion to close the wound [5].

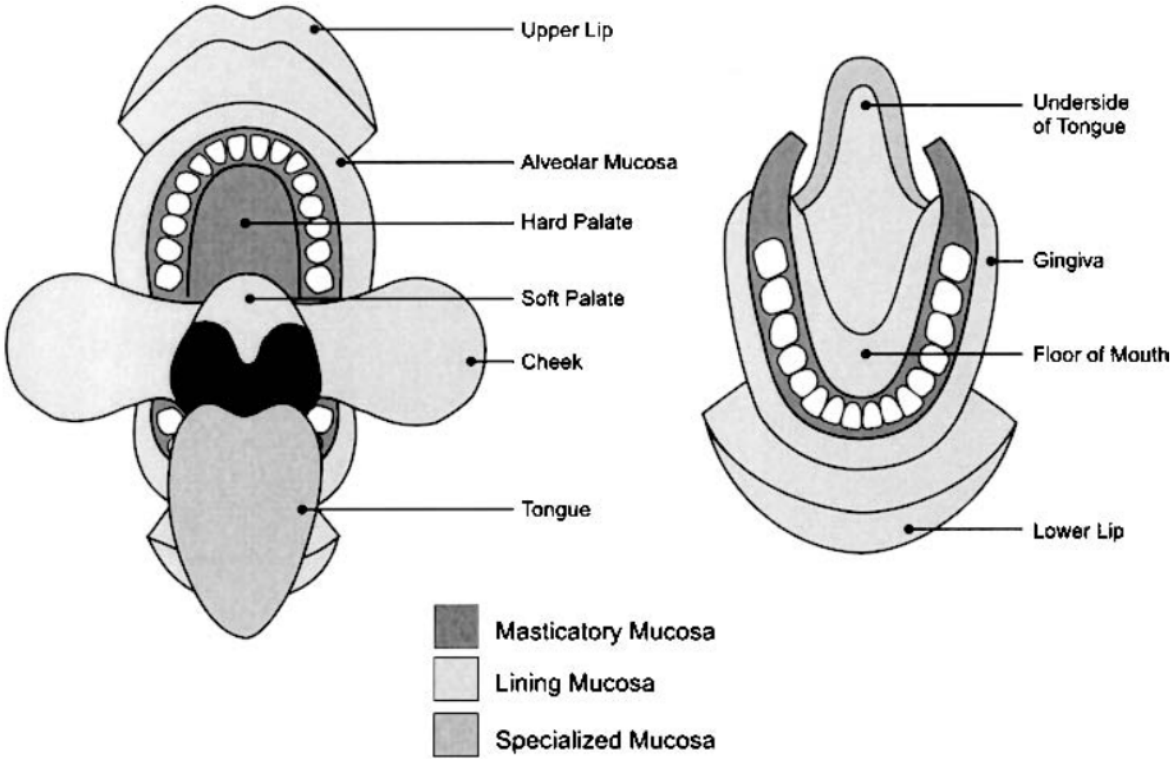

Figure 1.1 – Schematic diagram indicating the locations of the different types of oral mucosa tissue. *Keratinised oral epithelium is located on the hard palate and gingiva, and non-keratinised epithelium is present on the soft palate, insides of cheeks, underside of the tongue and floor of the mouth. Specialised structures, such as taste buds and tonsils, are covered by the specialised mucosa of the tongue. Figure taken from [1].*

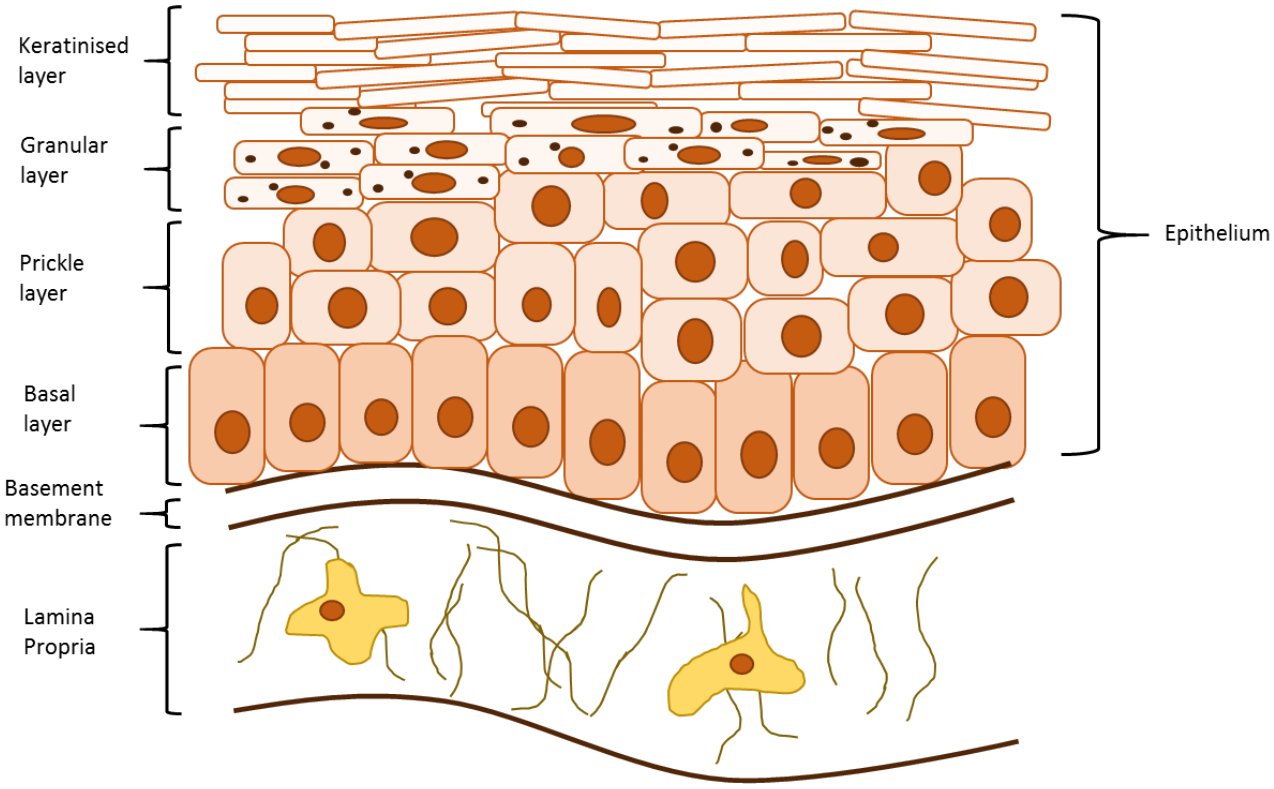

Figure 1.2 – Schematic diagram of the composition of the oral masticatory mucosa. *This tissue consists of the surface stratified squamous epithelium and the supporting lamina propria (locations as indicated in figure), consisting of connective tissues and cells such as collagen-producing fibroblasts and immune cells. The cells in each layer of the oral epithelium differentially express the protein keratin as cells differentiate and migrate suprabasally. Cells develop granules of protein structure keratohyalin (indicated by black dots in figure) in the granular layer which promote cross-linking of keratin fibres to reinforce the tissue, and ultimately become non-living corneocytes in the keratinised layer before desquamation (shedding). In the lining mucosa the equivalent top two layers of oral epithelium are termed the intermediate and superficial layers, and cells do not express keratin (not shown).*

1.2.2 Trauma and disease affecting the oral epithelium

Disturbances in the integrity of the oral epithelium results in the underlying tissues becoming susceptible to physical damage, dehydration and infection. Mechanical or thermal damage from food consumption is a source of minor trauma; more extensive disturbances can occur from irritation due to poorly fitting dentures or dental surgery, such as following tooth extraction. Non-traumatic oral epithelium lesions such as ulcers can be symptomatic of other local causes or systemic conditions, including infections, genetic diseases,

immunological disorders, neoplastic disease and nutritional deficiencies [6]. Additionally, a number of medications are known to cause ulcerations to the oral mucosa, such as cytotoxic chemotherapeutic and non-steroidal anti-inflammatory drug use [7].

Oral inflammatory conditions, such as stomatitis, gingivitis and periodontitis are extremely common and it is estimated that 95% of the adult population experiences gingivitis within their lifetime [8]. Gingivitis manifests as swelling of the gingival crevices, the narrow space between the tooth and gingival epithelium (the location of the gingiva is indicated in Figure 1.1). This swelling leads to ulceration of the gingival epithelium and subsequent pain and bleeding, particularly when tooth brushing. Gingivitis is generally caused by a build-up of bacterial biofilms, commonly known as plaque, and is reversible when this is regularly removed. However, in extreme cases and/or in the presence of certain aetiological bacterial species (discussed in section 1.2.3), gingivitis may progress into periodontitis. The disease is characterised by gingival recession, lesions of the oral epithelium and exposure of underlying tissues, progressive loss of bone tissue causing loosening and ultimately loss of teeth (Figure 1.3) [8].

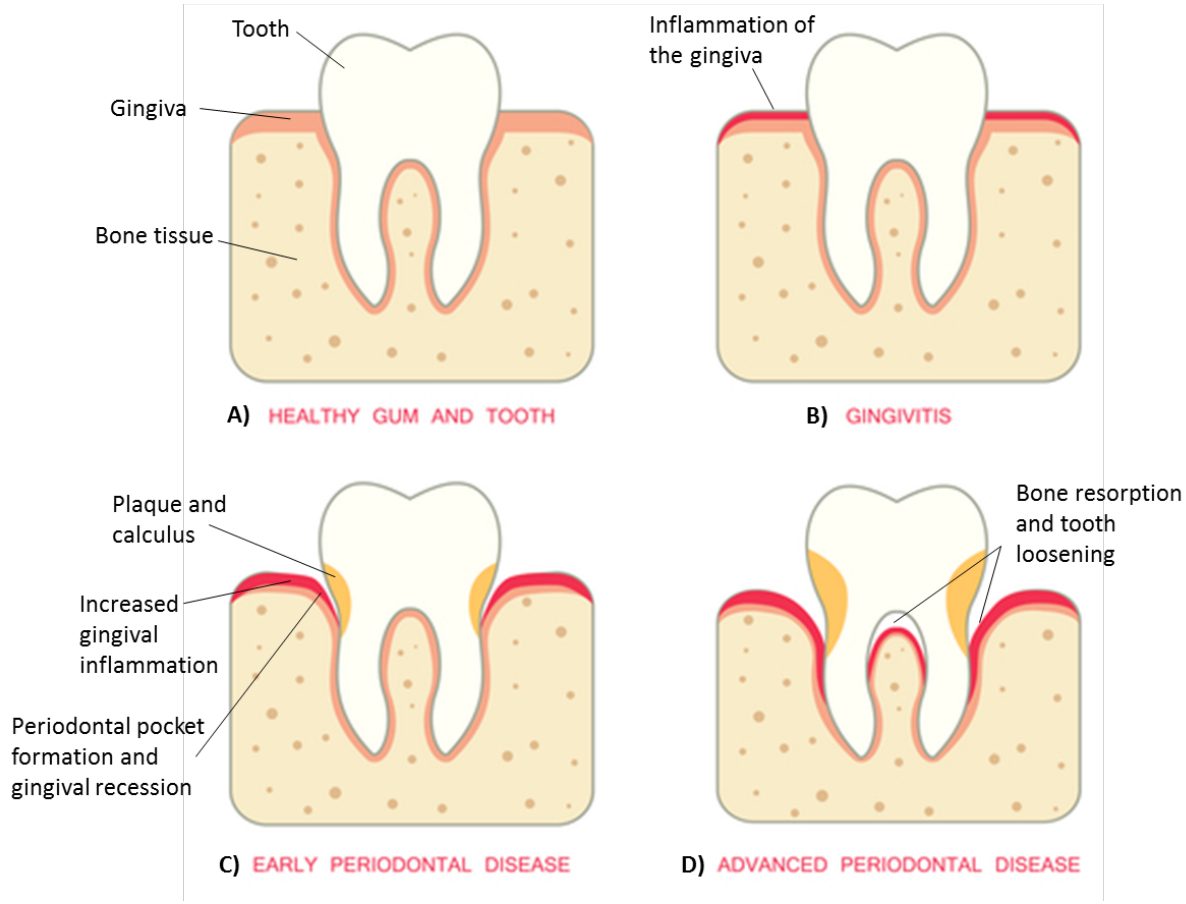

Figure 1.3 – Diagram showing the progression of periodontal disease. *A) A healthy oral cavity. B) Oral cavity with gingivitis, characterised by inflammation of the gingiva, leading to bleeding and ulceration. C) As gingivitis progress into early periodontitis, inflammation of the gingiva increases and unremoved bacterial biofilms (plaque) harden to become dental calculus. The gums begin to recede from the tooth forming a periodontal pocket. D) As periodontal disease advances, gingival recession worsens and bone tissue is resorbed, leading to tooth loosening and, eventually, tooth loss. Adapted from* [9].

The predominant cancer of the oral cavity also affects the oral epithelium. Oral squamous cell carcinoma (SCC) accounts for 90% of oral cancers [10] and is characterised by a red or white speckled, potentially ulcerated, tumour located on the oral mucosa, often located on the ventral or lateral surfaces of the tongue [10]. Regular alcohol [11], tobacco [12] and betel quid chewing [13] are significant risk factors for the development of oral SCC, thus preventative measures constitute a large part of the effort to reduce the incidence of this cancer. Oral SCC accounts for 2-4% of all cancers worldwide [13], although prevalence is

higher in south Asia in areas where betel quid chewing is prevalent, i.e. oral SCC accounts for up to 45% of cancers in India [13]. Treatment of oral SCC usually consists of surgery to remove the tumours, followed by radiotherapy and in some cases chemotherapy. Survival rates are however generally poor, with a five year survival rate of only 50% [10], thus research into alternative treatments is ongoing [14].

Exposure to such extraneous agents, such as chemicals or micro- / nano-scale particles consumed in food and drink [11], tobacco [12] or oral hygiene products [15] may also effect cytotoxicity in the oral mucosa. Cytotoxicity can occur through a number of mechanisms. For example, covalent bonding of toxic chemicals to proteins, enzymes or DNA may lead to altered cell function and cause, for example, inhibition of respiration or activation of cell death pathways [16]. The specific three-dimensional shape of molecules may also bind to receptors and inhibit enzyme function [17]. Cellular damage may also be caused indirectly if toxic agents contribute to the production of reactive oxygen species (ROS) [18]. Whilst ROS are produced and neutralised by the cell as part of normal cell function, they can become cytotoxic if they are produced at a higher rate than that at which they are neutralised.

Other factors affecting cytotoxicity include size [19] and charge [20] of the exposed molecules or particles, since these features affect the ability of toxic agents to penetrate the cell membrane into the cytoplasm of the cell. For example, large molecules may be too large to pass through channels in the cell membrane and consequently are unable to effect damage to cellular contents. Dose is also a critical parameter [21]: at low enough concentrations cells may be able to metabolise toxins and repair cellular damage, whereas at higher concentrations the same molecule or particle causes cell death.

1.2.3 Oral microbiota

The presence of bacteria drives several diseases in the oral cavity as the relatively warm, humid environment with a regular supply of nutrients provides ideal conditions for bacteria to flourish. Additionally, the variety of environmental niches, i.e. different pH and oxygenation levels, supports colonisation for a wide range of bacterial species. Over 700 bacterial species have been detected in the oral cavity, which exist in interacting communities as biofilms on the surfaces of the teeth and oral mucosa [22]. Under normal conditions most oral bacteria are reportedly commensal or even beneficial, contributing to such processes as digestion and regulation of metabolism, and the prevention or suppression of harmful microbial colonisation [23]. However host-related changes such as immunosuppression or dietary changes may trigger dysbiosis wherein normally commensal bacteria become pathogenic and/or populations of pathogenic species increase to harmful levels [24]. For example *Porphyromonas gingivalis*, can exist commensally inside healthy oral epithelial cells, but is also strongly linked to the development of periodontal disease when its levels in subgingival plaque accumulate to relatively high levels. Subsequently the host mounts an inflammatory response and the consequent increased flow of appropriate nutrients, such as iron, to the infected site and local pH changes result in further increases in *P. gingivalis* to pathogenic levels [23], [25]. Another example of harmful microbial colonisation is provided by *Streptococcus mutans*, which is one of the leading aetiological agents for dental caries, otherwise known as tooth decay. *S. mutans* adheres strongly to the tooth surfaces, and is one of the first colonising species necessary for the formation of plaque biofilm where it produces acid as a by-product of anaerobic fermentation of dietary sugars, subsequently dissolving the tooth's mineralised tissues. Furthermore, the plaque

established by *S. mutans* is colonised by further cariogenic/ pathogenic bacterial species, and causes environmental changes leading to the proliferation of other bacterial pathogens such as *P. gingivalis* as discussed previously [26]. Advanced caries can lead to significant hard tissue loss and pulpitis (inflammation of the central soft pulp tissue). Progression of this disease can result in significant pain, difficulties in eating and, if left untreated, can result in necrosis of the dental pulp, apical abscesses, and resorption of the underlying supporting tooth tissues leading to tooth loss (Figure 1.4). Treatment of advanced dental caries/pulp infection involves root filling or in more extreme cases tooth extraction [27]. A number of approaches for treatment or removal of *S. mutans* have therefore been proposed, and these range from mechanical debridement of plaque biofilm and reduction in the volume and frequency of dietary sugar intake, to the use of antimicrobial agents such as nanoparticles and antimicrobial peptides [28], [29]. Whilst tooth-associated biofilms may not exert direct pathogenic effects on the oral mucosa, any treatment applied to remove, kill or disrupt these bacteria will have potential effects on the adjacent oral epithelial barrier. It is therefore essential to evaluate the cytotoxicity of any treatments frequently used within the oral cavity to ensure they do not exert any detrimental effects on supporting surrounding and associated tissues.

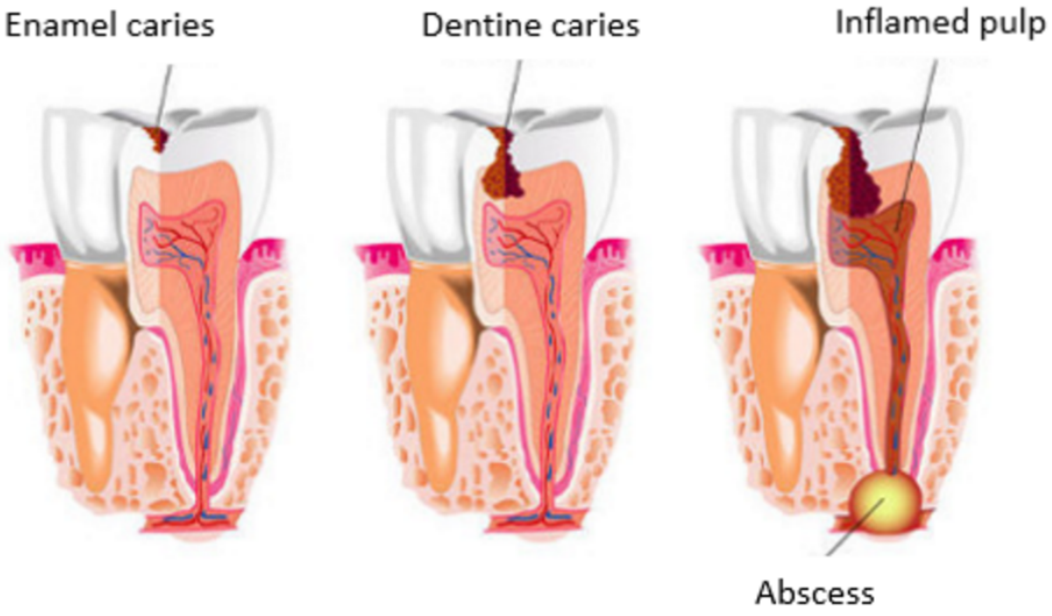

Figure 1.4 – Progression of dental caries. *Caries initially form in the hard outer enamel layer of the tooth, before progressing to the dentine layer and finally to the dental pulp, where nerves and blood vessels are located. This provides a source of significant pain and may lead to infection and abscess formation. Adapted from* [30]

1.3 *In vitro* epithelial cell cultures as model systems for health and disease

Studies utilising *in vitro* cell cultures are generally one of the first steps used in developing an understanding of disease pathogenesis and in toxicological or drug development studies as they provide a convenient, cost-effective and relevant approach for identifying the response to stimuli on a cellular level under controlled conditions [31]. The simplest form of *in vitro* cell culture analysis uses a single cell type cultivated in adherent 2D monolayers. The selection of the cell line for *in vitro* studies requires careful consideration and several factors are important in this process and relate to relative ease of culture/propagation and relevance to the *in vivo* (in the body) situation. One important factor is deciding between the use of primary and immortalised cell lines. Primary cells are isolated from tissue excised *in vivo* and replicated in culture until natural senescence (cessation of division). Conversely, immortalised cell lines are artificially transformed from primary cell cultures using viral

vectors to deliver genetic material or naturally transformed and derived from cancer tissue and can be cultured indefinitely [32].

Whilst primary cells are arguably more representative of the healthy oral epithelium than immortalised cell lines, the added steps of acquiring them under ethical approval and processing samples for the isolation of cells is a relatively time-consuming process. Primary cell lines often require co-culturing with “feeder layers” of different cell lines, typically fibroblasts for epithelial cells, which provide the necessary cytokines/growth factors for growth, however they can impede investigations on the primary cell line of interest, i.e. growth rate assays and imaging [33]. Furthermore, there will be variation between samples acquired from different individuals as wells as species, age, sex and disease status variations which will impact on the experimental outcome [32], [34].

Conversely, immortalised epithelial cell lines are more readily available and relatively easy to cultivate *in vitro* indefinitely since they do not enter natural senescence as primary cells do, and are not subject to the logistical and technical difficulties associated with primary cell isolation. Immortality may be induced in cells from healthy tissue through a number of mechanisms, including gamma irradiation to induce genetic mutation or retroviral induction of oncogenes associated with immortality in cancer, although these methods are often associated with altered phenotypes compared with the original cells [32], [35]. Similarly, it is worth noting that immortalised cancer cells can also exhibit an altered metabolism and phenotype compared with normal/healthy primary cells. Therefore immortalised cells may not give fully representative results in experiments aiming to model normal healthy epithelia, for example, in disease pathogenesis, toxicology or wound healing studies. One

example of an immortalised cell line frequently used to study oral epithelial responses is the H400 cell line, which was derived from an oral SCC [36]. Cultures of immortalised cell lines, such as H400 cells, have been used previously in oral epithelium model systems to investigate the response of oral epithelial cells to stimuli, such as potential cancer therapies and periodontal disease associated bacteria [37], [38].

A number of investigative techniques can be applied to *in vitro* epithelial cultures once established including analysis at the genetic, molecular and cellular levels, as well as analysis of entire cell populations [38], [39]. In particular, assays to monitor cell numbers and culture growth rates are of considerable importance in disease, toxicological or drug development studies to determine inhibitory or stimulatory responses.

1.4 Determination of cell number in *in vitro* cultures

One fundamental measure in the analysis of cell cultures *in vitro* is the determination of cell numbers. These measurements are important for determining culture growth rates and viability in response to exposures [40]. Several approaches may be taken to achieve cell enumeration:

i) Removal of cells from culture for counting cells in suspension [40]

ii) Indirect inference of cell numbers through changes in fluorescence or opacity due to chemical reactions that capitalise on cell-number dependent processes [41], [42]

iii) Counting cells from images of the culture [43], [44]

The sub-sections below describe the approaches i) and ii). Approach iii) will be discussed in section 1.6.2 in the context of microscopy and image analysis.

1.4.1 Approaches for counting of cells from suspension

1.4.1.1 Haemocytometer method

The improved Neubauer haemocytometer chamber is a glass slide with a 9 x 9 mm grid etched onto the surface [40]. A glass cover slip is affixed to the haemocytometer leaving a small gap into which a suspension of cells is pipetted. Cell density is determined by counting the numbers of cells in the defined 1 mm^2 grids. For haemocytometer counts to be reliable, cells must be homogeneously distributed in the suspension, and it is recommended that a minimum of 100 cells be counted, although this is often not achievable at low cell densities [45].

The haemocytometer method is a standardised and commonly used method for counting cells due to its simplicity and relatively low cost, and is utilised as the gold standard reference for evaluating other cell counting techniques [46]. However, it is manually intensive and relatively laborious, and as this technique requires adherent cultures to be disrupted by chemical/enzymatic dissolution to produce a cell suspension prior to cell counting it can only be used as an end-point assay, thus there is no ability to monitor cell growth longitudinally. Consequently, in the case of growth curve generation, this approach necessitates sets of replicate cultures to be established, treated and maintained for each time-point evaluated, which consumes time and resources. Furthermore, it has been reported that haemocytometer cell counts are associated with low precision and accuracy, and are subject to operator bias [45], [47]. Coefficients of variation between 9-20% have typically been reported [46], [48].

1.4.1.2 Automated cell counting approaches

There is a growing market for equipment which enables relatively rapid automated cell counting from light microscopy images of cell suspensions and such equipment effectively acts as automated haemocytometers. Current commercially available examples of this equipment include the Countess® Automated Cell Counter (Thermo Fisher Scientific), Cell Counter model R1 (Olympus) and the LUNA™ cell counter (Logos Biosystems).

Generally, adherent cell cultures are detached and resuspended before being pipetted into specialised slides and inserted into an imaging unit to be counted automatically using proprietary software. This automated approach has the advantage of reducing the time and operator bias associated with manual haemocytometer counting, although accuracy is dependent on subjective manual adjustment of image analysis parameters and image focus. However, this approach is substantially more expensive than counting using a haemocytometer due to the costs of the cell counting unit and the ongoing costs of specialised disposable slides. Furthermore, the image analysis software used to count cells is proprietary thus it is not possible to determine whether strange or anomalous results are valid or artefacts of the algorithm, and the meanings of analysis parameters set by the user such as “noise reduction” are ambiguous. Sample destruction, as previously highlighted for the haemocytometer method (section 1.4.1.1), also remains an issue.

1.4.2 Spectrophotometric and fluorometric assays for cell number determination

Cell number can be determined indirectly through spectrophotometric measurements of reactions that are proportionate to the number of cells present. Such approaches utilise metabolic reactions or enzymatic activity following incubation with a reagent which is

converted to an opaque product [49]. Perhaps the most well-known spectrophotometric assay for measuring cell number and viability is the 3-(4,5-dimethylthiazol-2-yl)-2,5-diphenyletetrazolium bromide (MTT) assay. It is a relatively simple and inexpensive assay that may be easily applied to large sample numbers, notably other tetrazolium compounds are now commercially available which operate similarly [49]. This assay involves adding MTT to a cell culture, which is subsequently reduced to formazan, a purple water-insoluble dye, by the dehydrogenase enzymes produced in living cells during respiration [41]. The amount of formazan dye produced is determined by measuring the absorption of light by formazan using a spectrophotometer, typically with wavelengths of 570 – 630 nm [49]. Although absorbance is technically a measure of cell respiration activity, it may be used to deduce relative numbers of cells, since more cells produce higher amounts of soluble formazan crystals due to the higher numbers of mitochondria present. A calibration curve is used to determine the relationship between cell number and absorbance change for each cell-type. However, absorbance alone is insufficient to distinguish a change in mitochondrial activity from a change in cell number or proliferation rate, i.e. the same number of cells may give different MTT readings if their metabolic rates are different. Tetrazolium compounds are generally cytotoxic chemicals, thus cell number may only be measured once using this type of assay, making them inappropriate for longitudinal studies. Non-toxic commercial tetrazolium derivatives such as the EZ4U assay do not kill cells but give non-linear responses when applied in medium to high density cultures, thus are unsuitable for generating growth curves [42].

Fluorometric methods for cell counting use a similar approach to that of the MTT assays, although the reaction product generated is a fluorophore and the fluorescent intensity is

used as a surrogate measure of cell number. Fluorometric approaches utilise reagents such as resazurin, which is reduced to fluorescent resorufin by viable cells, and glycylphenylalanyl-aminofluorocoumarin (GF-AFC), which becomes fluorescent aminofluorocoumarin (AFC) following protease digestion of the substrate [49]. Similarly, in fluorescently-stained or fluorophore-expressing cells, cell number may be deduced from relative differences in intensity without the requirement of a reagent (a more detailed explanation of fluorescence and a discussion of the advantages and disadvantages of fluorescent staining is provided in section 1.5.3).

A further downside of using methods which measure the product of a biochemical reaction is that some stimuli used to treat cells may react independently with the assay reagents leading to erroneous results [34].

1.5 Microscopy

Optical microscopy is a powerful tool in cell biology as it enables visualisation of cells, organelles and even molecules which are not visible or quantifiable using the naked eye. In its most basic form, a microscope is a series of lenses to magnify samples illuminated by light, although different microscopy techniques make use of different light sources, stains and optical components to enhance contrast or visualise specific cellular structures [50]. One use of microscopy is to acquire images of cell cultures from which to perform cell counts [43], [51]. This section describes three microscopy techniques which can be used to acquire images suitable for cell counting, and an overview of the image analysis approaches for cell counting for each technique is provided in section 1.6.

1.5.1 Brightfield optical microscopy

In brightfield optical microscopy contrast in samples is visualised according to the degree of light absorption: this is usually provided by tissue pigments or by histological dyes since the intrinsic transparency of cells results in poor contrast when observed using brightfield microscopy in unstained samples (Figure 1.5A). Strategies for enhancing contrast in brightfield images include the use of histological stains such as haematoxylin and eosin, or defocusing images by relatively small amounts to introduce contrast through interference from out-of-focus light [52], [53]. Notably these approaches have limitations as staining require samples to be fixed before analysis, thus this approach is unsuitable for analysis of live cultures. Furthermore the increase in contrast achieved by defocusing comes at the cost of loss of cellular detail.

1.5.2 Phase contrast microscopy

An alternative analytical method to brightfield microscopy is phase contrast (PC) microscopy, which uses a similar optical system to magnify specimens, however it requires additional components to exploit the phase changes of light passing through the sample to generate image contrast (Figure 1.5B) [54].

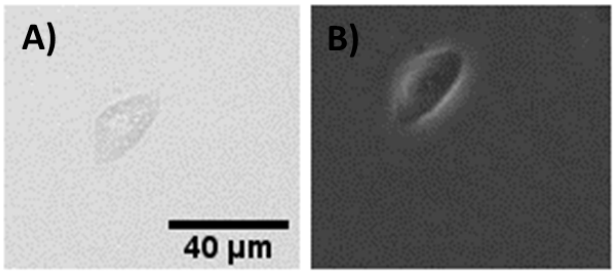

Figure 1.5 – Image of a H400 keratinocyte cell taken using A) brightfield microscopy and B) phase contrast microscopy. *Note the increased contrast observed in the phase contrast image, in particular at cell edges where the bright "halo" regions are observed. A scale bar for both images is shown in A).*

1.5.2.1 Principles of phase contrast image generation and microscope configuration

Semi-coherent light passing through an object with a different refractive index to the surrounding media experiences a small shift in phase, $\Delta\varphi$, compared with light that does not pass through the object, or "background" light. When background and object light are recombined there is destructive interference due to this phase shift resulting in a slight change in the amplitude (brightness) of light that has passed through the object relative to the background light (Figure 1.6A). However, the magnitude of this change in amplitude is insufficient to create contrast which can be visually detected. The principle of PC microscopy is that an in increase $\Delta\varphi$ creates interference which is substantial enough to generate contrast between the object and background in the resulting image [55].

In reality, this is achieved through addition of a condenser annulus and a phase plate to the basic microscopy configuration (Figure 1.7). Light first passes through the condenser annulus to create a hollow cone of light, which is then focused on the specimen. Light incident on the specimen plane either passes through undeviated (background light), or passes through the specimen and is diffracted and phase-shifted. The phase plate is aligned such that the cone of undiffracted background light passes through and is shifted in phase by 90°, whereas the diffracted light emerging from the specimen does not pass through. This results in a larger $\Delta\varphi$ such that when both light paths recombine in the image plane, the interference is sufficient to generate visible variation in contrast (Figure 1.6B). For relatively thin samples of near-constant refractive index such as cells, the intensity in the PC image is proportional to sample thickness, thus images can be easily interpreted to provide morphological information pertaining to the sample [55].

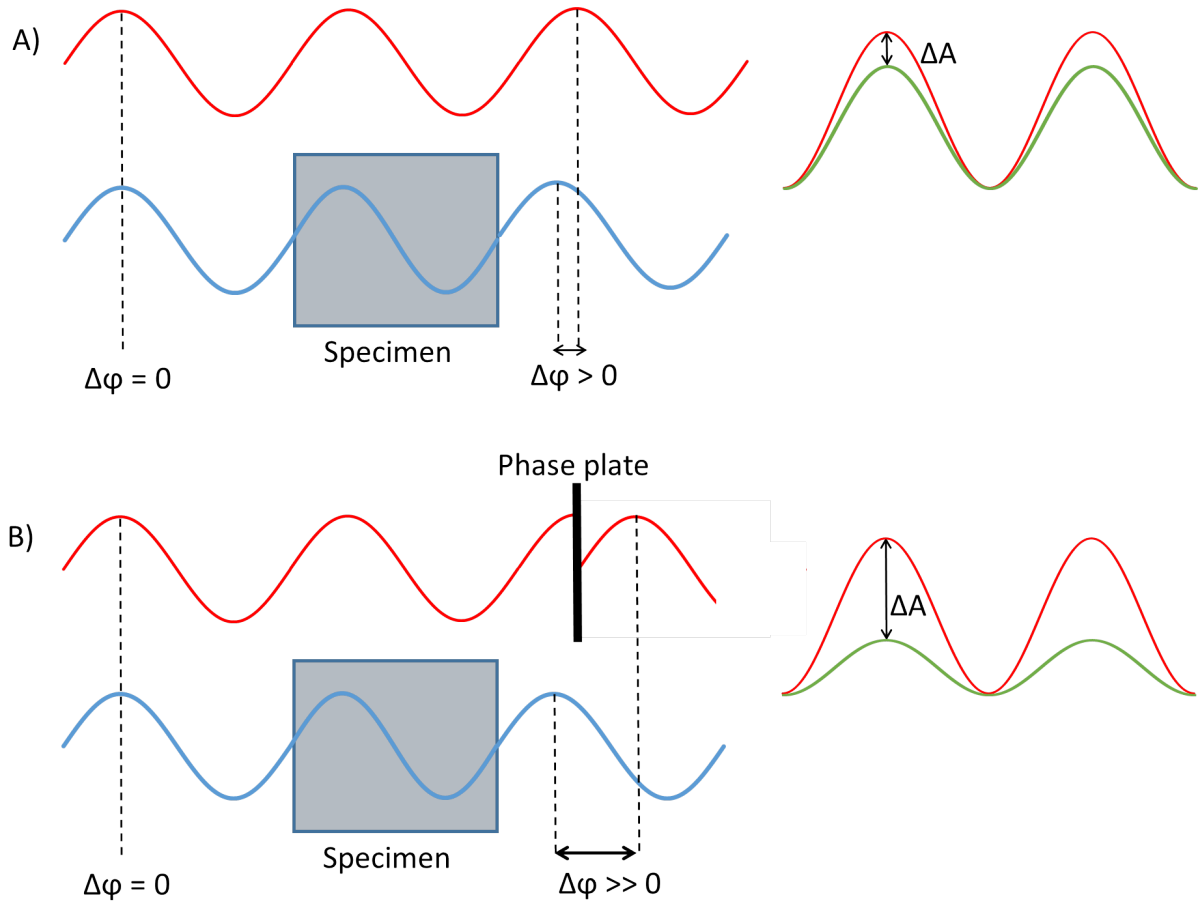

Figure 1.6 – Schematic diagram showing the principle of contrast generation in PC microscopy. *A) In brightfield microscopy the phase, **φ**, of a light wave passing through a specimen (blue wave) is shifted slightly with respect to the background light (red wave). When recombined the waves interfere destructively resulting in a wave with slightly reduced amplitude, **A**, (green) with respect to the background. However this small change in amplitude does not generate high contrast between specimen and background. B) When the phase of the background light is differentially advanced by 90° using a phase plate, the amplitude of the resultant wave is considerably reduced, creating improved contrast with the background.*

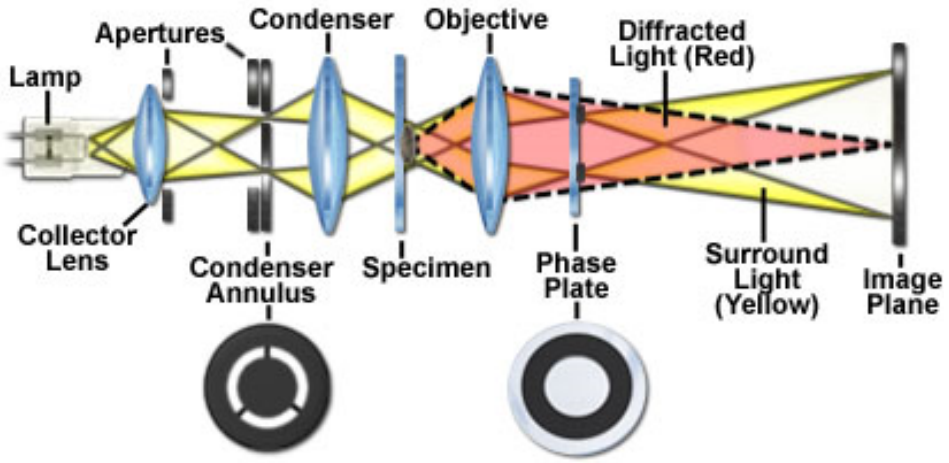

Figure 1.7 – Schematic diagram of phase contrast microscope configuration. *The optical system is similar to that of a brightfield microscopy except for the addition of condenser annulus and phase plate, usually contained within the objective lens. From* [56].

1.5.2.2 Image artefacts

To achieve perfect image formation in a phase contrast microscope, only the background light should pass through the phase plate however since the specimen diffracts light in all directions, a small amount of specimen light also passes through and is phase retarded. This phase shifted specimen wave interacts with the un-shifted specimen wave and results in the so-called “halo effect”, an image artefact which manifests as spurious bright regions which do not correspond to changes in refractive index or thickness in the specimen. The effect is particularly evident at the boundaries of objects, for example at rounded cell edges, since low spatial frequency object waves are disproportionately diffracted into the phase plate (Figure 1.5B) [57]. This presence of the halo effect is an unavoidable artefact of the method of PC image formation and presents a challenge for cell boundary segmentation in PC images.

Since PC images are formed through manipulation of small phase shifts, any disturbances to the direction, and thus the length, of light paths will also manifest strongly as a reduction in

image quality [58]. The radii of the condenser annulus and phase plate are matched in size and must be carefully aligned along the light path length and the radial axis (as shown in Figure 1.8) since misalignment of these two annuli results in a disruption to the light path lengths leading to a loss of contrast in PC images.

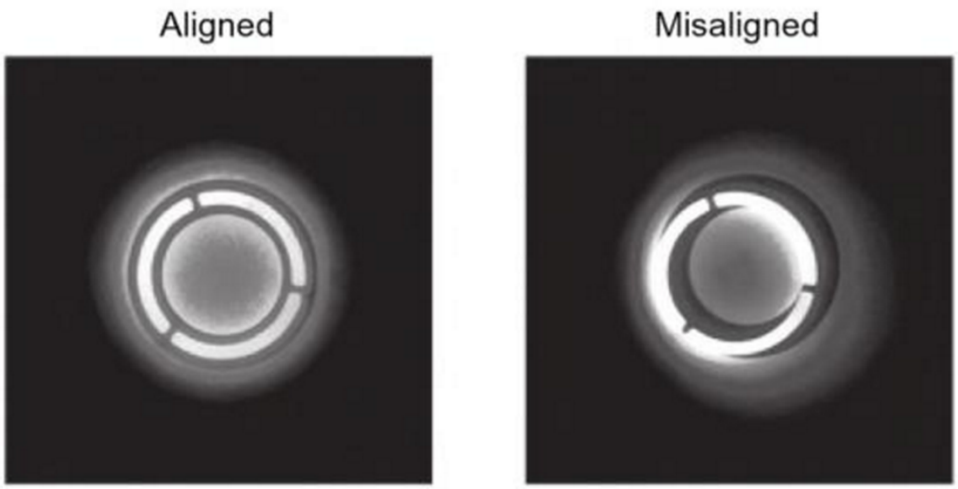

Figure 1.8 – Image showing condenser annulus (bright circle) alignment with phase plate (dark circle) in its correct alignment and out of alignment. *Misalignment of these two annuli cause a loss in PC image contrast. From* [55].

Another source of path length disruption is derived from the meniscus formed by culture media at the edges of the wells, which causes the surface of the media to form an angle with respect to the incident light. Small shifts may be corrected through re-alignment of the condenser annulus however large shifts close to the edges of the wells result in an irreversible loss of contrast. Specialised cultureware has been developed to remove the meniscus, however this is generally more expensive than regular cultureware and not routinely used [58].

1.5.3 Fluorescence microscopy

The phenomenon known as fluorescence occurs when molecules called fluorophores are irradiated with electromagnetic radiation of a specific wavelength, which is absorbed by its orbital electrons, causing them to become excited from the ground state to higher energy levels. After excitation, electrons quickly release the energy via heat dissipation and emission of electromagnetic radiation of a longer wavelength in the visible spectrum, to relax back to the ground state (Figure 1.9). The difference in wavelength between excitation and emission wavelengths is called Stokes' shift [59].

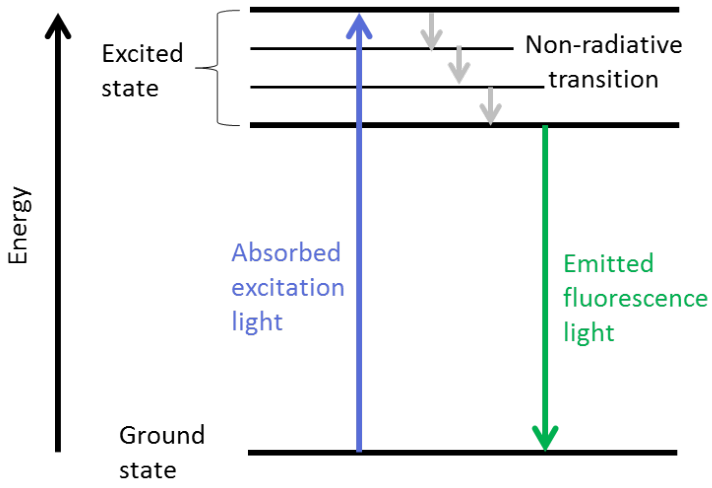

Figure 1.9 – Schematic Jablonski diagram showing the transition states of an electron in a fluorophore. *The electron first absorbs radiation to move to an excited state. A small amount of energy is lost in the form of vibrational / heat energy before the electron emits a photon to move back to the ground state.*

Rather than the absorption or phase information in specimens that create contrast in brightfield or PC microscopy, fluorescence microscopy uses the light emitted by fluorophores in the specimen when stimulated with appropriate radiation wavelengths to generate image contrast. Although some structures in cells are weakly autofluorescent, generally fluorophores are introduced into cells through labelling with chemical stains or

antibodies conjugated to fluorophores. However antibodies and many chemical stains are unable to permeate the live cell membrane so cell cultures must be fixed before imaging, resulting in this approach not being suitable for monitoring culture behaviour [60]. Furthermore, fluorescent stains have limited lifetimes due to photobleaching which is an irreversible, photochemical alteration of the fluorophore, which occurs over time such that it is no longer able to fluoresce [59]. Short-range interactions with other molecules in the environment of the fluorophore may also cause a reduction in fluorescent intensity, known as quenching [61], which limits the application of fluorescence microscopy in such environments.

The fluorescence microscope uses a similar optical system as the brightfield microscope to magnify specimens but uses a monochromatic light source rather than a broad spectrum source, usually a laser or light emitting diode (LED), the wavelength of which is specific to the excitation wavelength of the fluorophore being illuminated. Due to the relative low intensity of the Stokes-shifted emitted light compared with excitation light, additional filters or dichroic mirrors are incorporated in the setup to ensure only emission wavelengths are included in the image. Specimen preparation and observation must be performed under darkened conditions to avoid photobleaching and reduce background light [59].

1.5.3.1 Fluorescent labels and stains

Cells may be stained using cell permeant dyes such as CellTracker (ThermoFisher Scientific, UK), a live cell stain which permeates live cell membranes and reacts with the ubiquitous chemical glutathione to become impermeant (not to be confused with the image processing software also named Celltracker [62]). This has been used to monitor cell growth in live cells,

although fluorescence is limited to 72 hours due to dilution of signal after several generations of cell division [63]. Furthermore, cytoplasmic staining can cause individual cells to become indistinguishable at high density. Other stains can be used to highlight cellular features, allowing specific structures of the cell to be observed. Nuclear stains are frequently used for the purpose of cell counting as they enable cells which are in contact to be discriminately identified more efficiently than using a cytoplasmic stain. 4',6-diamidino- 2-phenylindole (DAPI) is a fluorescent nuclear stain that binds to the minor groove of the DNA double helix. Although DAPI can pass through the cell membrane to enable live cell staining, it is more efficient when used to stain fixed cells due to the increased permeability of their membranes [60]. Similarly to DAPI, Hoechst 33342 (referred to henceforth only as Hoechst) is a nuclear stain that binds to the minor groove of the DNA helix. However, the increased lipophilicity of the Hoechst stain compared with DAPI, enables it to better permeate the cell membrane and therefore stains nuclei in live cells more efficiently [64]. This, combined with its comparatively lower toxicity, makes Hoechst a better choice for staining live cells. Both DAPI and Hoechst intercalate DNA, and are excited by wavelengths in the UV wavelength range of the electromagnetic spectrum, thus samples must be irradiated with UV light. Both of these visualisation features have the potential to cause mutagenic effects thus neither dye is suited to the application of monitoring cells over relatively long incubation time-periods. Example images of cells stained with Hoechst and DAPI can be seen in Figure 4.4).

A further approach for introducing fluorophores into live cells is to use gene transfer techniques which can enable cells to stably express fluorescent proteins, e.g. green fluorescent protein. This approach has the advantage of generating a heritable fluorophore, however transfection is rarely undertaken for the purpose of cell enumeration since cells

may not be transfected with equal efficiency. Furthermore stable transfection is difficult to achieve consistently in some cell lines [65].

1.5.3.2 Cell fixation

Fixation describes the process of halting all cellular biochemical reactions and preserving cell/tissue structure so that further processing under toxic or abiotic conditions can be undertaken without decay or bacterial/fungal invasion. Importantly for the preparation of fluorescent microscopy samples, fixation allows the cell membrane to be permeabilised to stains. *In vitro* cultures are generally immersed in a fixative for a period of time prior to downstream processing. Formaldehyde is one of the most popular fixative chemicals used in fluorescent microscopy analysis, although other aldehydes, such as paraformaldehyde and glutaraldehyde, are also used. Aldehyde fixatives work by adding to the side chains of amino acids and causing crosslinks between proteins, halting their function and effectively 'gluing' them together [66]. A further alternative is fixation with alcohols such as methanol or ethanol, which work by displacing water in cells and precipitating large protein molecules. Distortion and shrinkage of cell morphology is associated with all types of fixative, and different fixatives can cause degradation or dissipation of different molecules of interest [67]. Since no fixative is able to preserve cells perfectly, a choice must be made based on the priorities of the experiment.

1.6 Approaches for analysis of microscopic images for cell segmentation and counting

Since microscopy enables visualisation of cells in culture, counts of cells may be achieved through analysis of microscopy images. Image processing approaches can therefore be

employed to enhance images to enable relevant information acquisition. For microscopy images of *in vitro* cultures, the desired information required is typically localisation or segmentation and subsequent analysis of cells or subcellular features. There are several approaches used to enhance and analyse images, however the most productive approach generally depends on the features available resulting from the image formation process [68]. The sections below begin with an overview of some techniques used for microscopy analysis before discussing approaches for cell segmentation and counting in each of the microscopy modalities presented in section 1.5.

1.6.1 Greyscale image processing principles

Greyscale digital images are represented as an array of pixels, each of which is assigned a number representing image intensity at that point. There are many approaches to enhance various image properties, identify regions of interest and gain information from images. Some operations are performed on the global intensity histogram (a histogram of all intensity values present in the image). For example, image contrast may be enhanced using intensity normalisation (Figure 1.10B) [69] or objects may be segmented using Otsu thresholding (Figure 1.10C) [70].

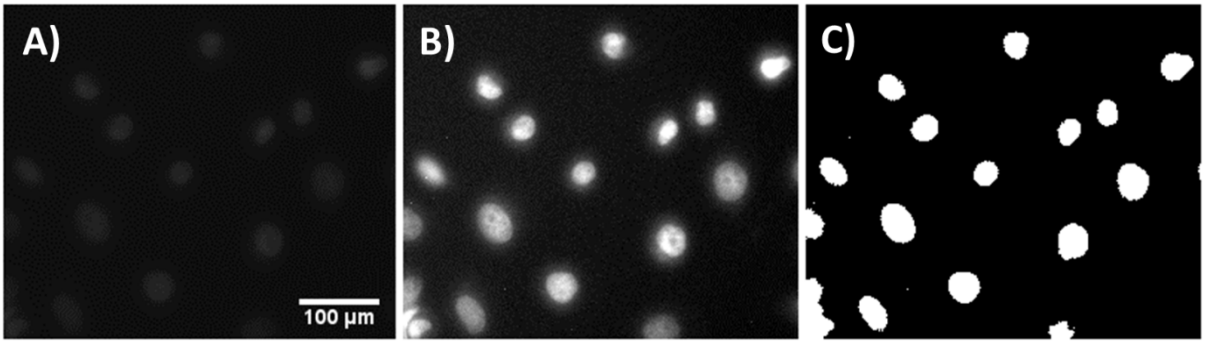

Figure 1.10 – Examples showing the effects of intensity normalisation (B) and Otsu thresholding (C) on a fluorescence microscopy image of a formalin-fixed H400 keratinocyte cell stained with DAPI (A). *A scale bar for all images is shown in A).*

Operations may also be applied to local neighbourhoods of each pixel as defined by a matrix termed a “kernel”: such operations are known as “convolution” [69]. The kernel is moved across the image and the value of each pixel is changed according to an operation applied to the pixels inside the kernel. Various operators on the kernel have different effects, and similarly, the size and shape of the kernel have an effect on the resultant image. Convolution-based operations, or spatial filtering, use the sum of weighted values in each pixel of the kernel operator. These range from discrete approximations to simple and rotationally symmetric mean (Figure 1.11A) and Gaussian filters, which have the effect of smoothing out image detail and removing noise, to anisotropic edge detection filters such as the Sobel [71] (Figure 1.11C) or Prewitt filters [72]. Other types of filters include histogram-based techniques applied locally to the kernel region, such as median filter also used for image smoothing [73], and variance filters used to enhance textural information [71].

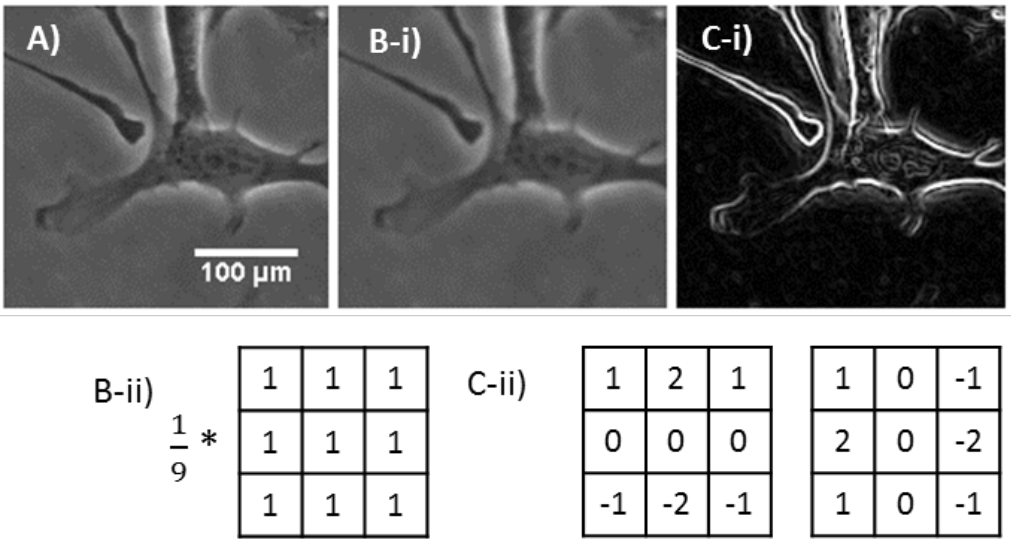

Figure 1.11 – Examples of 3x3 kernels used in image convolution and their effects on an example image. *A) An unfiltered phase contrast image of a 3T3 fibroblast cell. B-ii) Representation of a mean filter where each square represents one pixel in the image. The central square is the pixel upon which the kernel is acting. This filter finds the average intensity in the kernel and has the effect of blurring the image, as shown in B-i. C-ii) The set of Sobel filters which highlight horizontal (left) and vertical (right) edges in images and has the effect of highlighting edges as shown in C-i.*

Another image processing approach utilised is that of mathematical morphology (MM). MM was developed for use on binary images (although this approach can be extended to greyscale images) and considers a set of objects consisting of connected pixels on a background [74]. Analogous to the kernels used in convolution-based operations, a "structuring element" is applied to each pixel in the image. Typically, but not necessarily, this structuring element consists of the pixel in question and its immediate 8-connected neighbourhood, subsequently giving a 3x3 grid. For each pixel, if the structuring element contains both object and background intensities, the pixel will be redefined as background in the resultant image for an "erosion" operation, or as object for a "dilation" operation (Figure 1.12). Erosion and dilation are the two main operators of MM from which higher order operators are built [75]. This is considered a morphological or shape-based technique since these operators only take effect at the boundaries of objects. MM may be applied to

greyscale images by using the maximum and minimum greyscale values in the structuring element for dilation and erosion operators, respectively.

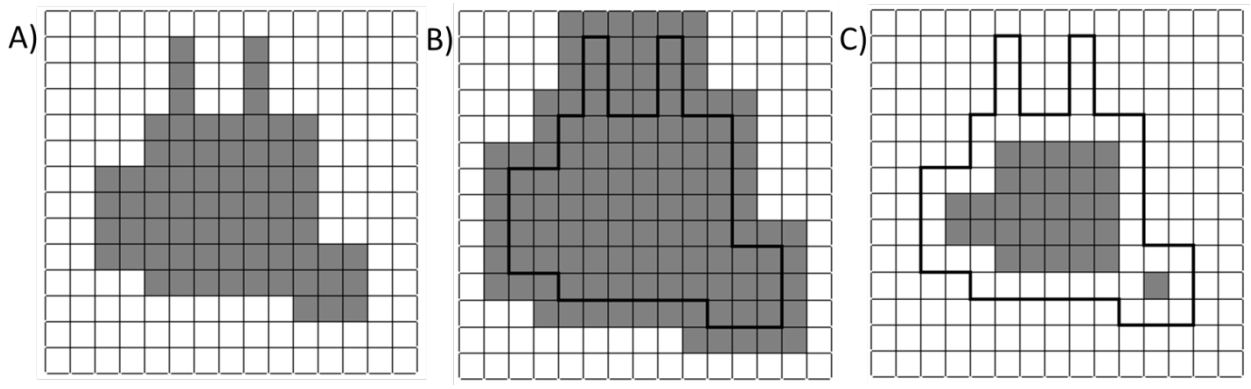

Figure 1.12 – Example showing the effects of erosion and dilation operators used in mathematical morphology. *A) A binary image of an object (grey pixels) on a background (white pixels). B) The object in A) was dilated using a 3x3 structuring element. C) The object in A) was eroded with the same element. The original object outline (in black) is shown for reference.*

A particular advantage of MM is that the fundamental dilation operator may be used to express a spatial logic called discrete mereotopology, in particular a spatial constraint language called discrete region connection calculus (RCCD) [76], [77]. RCCD is a set of logical statements that describe the possible parthood relations between two sets. Depending on the version of RCCD used, there may be up to eight different relations, and these are summarised in Figure 1.13. A version of RCCD with only five relations also exists in which tangential relations are subsumed into a more general parthood relation, for example, tangential proper parthood becomes only proper parthood. RCCD has been used previously to encode information about cellular structure into an automated evaluation of segmentation success in histological images and to classify malignant calcifications in MRI images of breast tissue [78], [79].

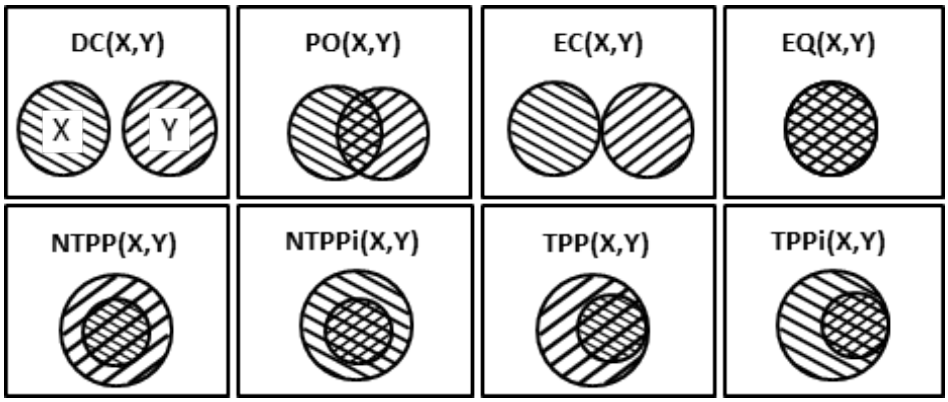

Figure 1.13 – Eight parthood relations between binary objects X and Y as described by the discrete region connection calculus spatial logic (RCC8D). *These are disconnection (DC), partial overlap (PC), external connection (EC), equivalence (EQ), non-tangential proper parthood (NTPP), inverse non-tangential proper parthood (NTPPi), tangential proper parthood (TPP) and inverse tangential proper parthood.*

1.6.2 Cell localisation and counting in microscopy images

A first step for counting cells from images is usually image segmentation, although cells are often segmented for other useful purposes, such as shape evaluation [80]. However, some segmentation algorithms may not be appropriate for cell counting. For example, some algorithms may be computationally expensive or may not be able to discriminate between multiple touching cells. If the aim of the analysis is to monitor cell numbers in cultures over time analytical methods must be able to detect cells in a high volume of images and at the range of cell densities typical of experimental conditions.

The sections below provide an overview of approaches for cell enumeration for each microscopy technique described in section 1.5 in the context of their appropriateness for application of counting cells across a range of densities.

1.6.2.1 Fluorescence microscopy

This approach potential provides the simplest modality from which to identify cells in images since the intrinsic contrast of fluorescent regions compared with background gives a

bimodally-distributed intensity histogram, thus cells in monolayers may be segmented using histogram-based threshold methods, such as the Otsu method (see Figure 1.10C). However, extra processing such as smoothing and background removal may be required to overcome problems such as low signal to noise ratio and uneven background illumination [51], [81], and MM techniques such as watershed segmentation [82] may be required to separate merged cells. Gradient-based techniques such as active contours have also been applied for cell segmentation; however the segmentation results of using such methods vary depending on initialisation [83] and the functions chosen to represent the image, and they often fail or require additional processing at high cell densities [84] since function boundary conditions do not automatically recognise borders between connected cells [85] .

1.6.2.2 Brightfield microscopy

Despite the problem of low contrast in brightfield microscopy images, approaches for cell detection in brightfield micrographs of live unstained cell cultures have nevertheless been attempted since the non-invasive nature of the technique provides the potential to longitudinally monitor cultures. Broadly speaking, these methods are separated into two types; contrast enhancement using defocusing methods, and classification of phase or textural features in focused images, although such approaches have been combined [86]. Edge detection and variance filters have been used to enhance textural features in brightfield images before segmentation through application of thresholds [87] or by contour based methods [88].

The technique of defocusing brightfield microscope images to gain contrast utilises the principle that when the imaging plane is moved slightly above the focal plane, contrast

increases such that cell centres become brighter than the margins due to constructive interference caused by scattering of light from the out-of-focus plane. The opposite contrast is observed when the imaging plane moves below the focal plane, i.e. cells become darker [52]. Cells may be located using multiple images of the same field of view; notably Dehlinger *et al.* used subtraction of two defocused images acquired with the objective lens displaced by a distance of 15 μm to count cells in a monolayer of epithelial cells [43]. A downside to this approach is that the requirement for multiple images increases the acquisition time, and the small, precise manipulations of focal plane required to acquire these images are difficult to achieve consistently without the use of costly automated microscope stage equipment.

1.6.2.3 Phase contrast microscopy

Combined with the low contrast between cell cytoplasm and background, the halo effect prohibits segmentation of cells from surroundings through the use of straightforward threshold-based methods. One approach for detecting cells is by reformulating the PC image contrast properties to generate an image in which the distributions of cell and background intensities are bimodal, enabling the segmentation of cells through application of thresholds. Yin *et al.* achieved this through deconvolution of PC images with a mathematical model of PC image formation in combination with image pre-processing to smooth cells and background [89]. This technique was most successful when applied to small images since the complexity of the mathematical model and the iterative optimisation of the pre-processing parameters require considerable computational power thus application to many large images is relatively slow. Furthermore the segmentation results are also dependent on user input of the accurate microscope phase ring dimensions in the model to correctly calculate the optical properties, which are not routinely specified by suppliers. An alternative is to use a

simplified model of the halo intensity with which to deconvolve the PC image, such as a difference-of-Gaussians [90]. The lower complexity of this model reduces computation time to a more suitable rate. However, this semi-automatic method requires user input in order to calculate the optimal Gaussian parameters.

Gradient-based techniques, such as active contours [91], marker-controlled watershed [92] and graph cuts [93] have been successful in cell segmentation of phase contrast images. Whilst these techniques are able to segment the outlines of individual cells, they are often unsuitable for processing images of densely-packed cell regions, since they require individual cell initialisation to distinguish between cells in contact, or are unable to distinguish between them at all. Furthermore, the accuracy of the segmentation is dependent on the accuracy of the initialisation and/or heuristic parameters selection.

An alternative to individual cell segmentation is to use bulk texture features to measure the culture confluency – the percentage of culture substrate covered by cells [94]. This approach is popular in wound healing assays where measurement of cell-free regions is the feature of interest [95]. However, cell confluency is not necessarily correlated to cell number due to cell spreading in the first 24 hours after seeding and reduction in cell size at high densities, thus this approach is inaccurate for monitoring cell growth rates [44]. The cell packing density for a confluent area has also been estimated using image features calculated using a series of derivative-of-Gaussian filters, although calibration with cell density measurements is required to be used to determine cell numbers [96].

1.7 Nanoparticles

Nanotechnology is the name given to the study and application of objects measured in the nanoscale, i.e. 1 nm = 10^{-9} metres [97]. Objects with one or more dimensions measuring between 1-100 nm are termed nanoparticles, and may take a number of different shapes, from a simple sphere or rod to more complex structures such as snowflakes, cones and chains [98]. A nanoparticle can be generated from different materials and composites, including metals and metal oxides, glass, polymers and ceramics [99], [100].

Since the laws of physics which govern objects at this scale can be different to those governing larger objects, nanoparticles often exhibit unexpected properties compared with the same materials on a bulk scale, including lower melting points, increased mechanical strengths and unusual optical properties [97]. More pertinently their interactions with biological matter are also different from those of bulk matter and this enables many biomedical applications of nanoparticles, including drug delivery, tissue engineering and bacterial infection control [101]. Silver nanoparticles (AgNP) are of particular interest for medical applications, in particular the antibacterial properties of silver have long been recognised, and evidence indicates that AgNP may also be effective in antimicrobial applications [102]. Furthermore, since silver is resilient to antibacterial resistance, AgNP offer an important alternative to traditional antibiotics in particular as antibiotic-resistant strains of bacteria are now becoming dangerously more common. Consequently, AgNP have been incorporated into wound dressings and toothpastes, and used as prophylactic coatings on catheters and other medical and dental implants [15], [103].

Whilst the novel properties of nanoparticles have resulted in significant research interest and commercial application, concomitant nanotoxicological studies appear somewhat lacking [100], [21]. Characterisation of the cytotoxicity of AgNP is especially important as it is estimated that these have a high commercialisation potential [104]. This section initially details methods for synthesising and functionalising AgNP, before discussing investigations into AgNP toxicity, including their use in *in vitro* culturing and assays as described in sections 1.3 and 1.4, with specific focus on the applications and effects on the tissues and bacteria of the oral cavity described in section 1.2.

1.7.1 Methods of silver nanoparticle synthesis and functionalisation

AgNP (also referred to in the literature as "nanosilver" [105], [106] or "SNP" [107], [108]) are generally synthesised using a "bottom up" approach [105]. The most common method of synthesis is through reduction of silver ions (Ag^+), often in the form of silver nitrate, to give uncharged Ag clusters using a chemical reducing agent, such as sodium borohydride, sodium citrate, tannic acid and ascorbic acid [20]. The byproducts of this reaction have the added function of providing stability for the prevention of NP aggregation through formation of a shell of ions, or "ion corona", which associates with the NP surface. Notably the choice of reducing agent affects the NP surface charge and level of stability, and consequently the cytotoxicity [20]. An alternative approach for synthesis of AgNPs is the use of so-called "green" synthesis methods, which use plant or bacteria extracts to reduce Ag^+ ions. This approach is gaining popularity due to its lower costs and reduced environmental impact compared with the reduction methods. There are however significant variations between chemical compositions of plant and bacteria samples collected from different countries, leading to variations between resulting nanoparticles [109].

AgNP stability may be increased by using capping agents such as polyvinylpyrrolidone (PVP) or polyethylene glycol, or other surfactants that reduce aggregation and enable dispersion across suspension [110]. AgNP can also be coated with functional groups, such as antibodies and carbohydrates, which may affect the levels of cellular uptake due to their interaction with cell membranes [111].

1.7.2 Current techniques for *in vitro* investigation of nanoparticles

AgNP cytotoxicity is commonly evaluated using fluorometric or spectrophotometric techniques (such as those described in section 1.4.2) which aim to determine cell viability [34]. However, certain properties of AgNP may cause erroneous readouts from these techniques. For example, aggregation of AgNP can cause visible dark regions to form in the culture, which could interfere with photometric measurements necessary for this type of analyses. Furthermore, AgNP have been shown to generate formazan in cell-free conditions in RPMI culture medium in a dose-dependent manner at concentrations above 10 μg/mL, whereas Ag^{+} alone did not [112]. The optical properties of AgNP can also cause artefacts in fluorescence-based assays, for example, quenching has been observed in fluorometric measurements of cell viability using GFP-tagged bacteria [113], [114]. AgNP interactions with specific enzymes can also cause unrepresentative biochemical readings. It is therefore recommended that each parameter of interest is investigated using multiple assays which generate different readout parameters. Generally, assays are performed between 3-48 hours [34], but since time-dependent toxicity has been observed [115] it is desirable to monitor cell number over as long a period as possible to give a full picture of the longer term effects of AgNP treatment.

Antibacterial activity of AgNP may be non-destructively evaluated using bacteria suspended in broth cultures through measurement of optical density [116], or in bioluminescent bacteria through fluorescence measurements [117]. However, as discussed previously, the optical properties and large aggregates of AgNP may interfere with spectrophotometric and fluorescent readings, thus corrective background subtraction measures must be implemented. An alternative approach for assay of antibacterial activity of AgNP is to measure growth on nanoparticle-treated culture agar, however this approach requires large amounts of AgNP, which may be difficult to synthesise in sufficient volumes. Alternatively colony counting or disc-diffusion methods can also be used in antibacterial investigations [118], [119].

AgNP uptake in bacteria and mammalian cells is another important factor which is regularly investigated alongside toxicity assays since amount and localisation of AgNP taken up by cells may provide insights into mechanisms of action. Uptake is typically measured qualitatively using electron microscopy and quantitatively using inductively coupled mass spectrometry / optical emission spectroscopy [112], or atomic absorption spectroscopy in treated samples digested with acid [120]. In mammalian cells, Ag uptake per cell may be calculated using a measurement of total culture cell number. This is typically estimated using a haemocytometer, either from the treated samples [120] or from separate cell cultures maintained specifically to be counted [121]. Both approaches have disadvantages; counting treated cultures adds an extra trypsinisation (the process used for chemical dissolution of samples) step to the processing method and the time taken to count cells may lead to sample degradation. However, culturing additional cultures for the sole purpose of counting consumes extra time and resources.

1.7.3 AgNP toxicity in human and bacterial cells

AgNP toxicity is currently not well understood and conflicting accounts are given as to the mechanisms of action involved: various reports contradictorily propose that toxicity is caused solely either by AgNP [122] or by the Ag^+ ions they release [123] or by a combination of both [104]. Many of the proposed mechanisms of AgNP toxicity are common to mammalian and bacterial cells due to shared cellular features or molecular pathways. Interestingly the following two mechanisms have been proposed for both cytotoxicity and antimicrobial activity:

- AgNP dissassemble into Ag^+ ions under oxidising conditions, which have high affinity to the thiol chemical groups present in many enzymes. These enzymes become inactivated upon interaction with Ag^+, inhibiting vital processes such as respiration and chemiosmosis (the movement of ions across cellular membranes) [124]. Ag^+ ions also interact with nucleosides and interfere with DNA replication [102]. It has also been proposed that uncharged AgNP act as a "Trojan horse" or delivery vehicle for Ag^+ to bypass cell membranes and cause increased damage than would be possible solely in ion form [125].
- AgNP inhibit antioxidant defences leading to increased levels of ROS in the cell, which cause damage to cell structures. Ag^+ may also contribute to elevated ROS levels by behaving as an electron-acceptor to generate increased ROS [126].

The proposed toxic mechanisms specific to bacteria are as follows: AgNP have been observed to adhere to and penetrate the bacterial cell membrane, causing damage which results in leakage of the cellular contents [127]. Indeed it has been shown that Gram-

negative bacteria are more susceptible to the effects of AgNP than Gram-positive strains. This differential effect is likely due to the thicker peptidoglycan layer characteristic of Gram-positive bacteria which provides extra protection from the penetration of AgNP and Ag^+ ions into the cell [118], [128]. The multifaceted antibacterial activity of AgNP is regarded as a significant contributor factor to their resilience to antibiotic resistance.

In terms of AgNP cytotoxicity mechanisms specific to mammalian cells, it has been proposed that AgNP particularly target mitochondria due to the higher levels of ROS produced by this oxidative organelle [34]. This targeting causes interruptions in ATP synthesis (a crucial step in cellular energy transfer), and subsequently AgNP cause a mitotic arrest rather than immediate cell death [129]. There is also evidence that AgNP cause damage to DNA, leading to an arrest in the cell cycle, followed by induction of apoptosis (a type of cell death) at relatively high concentrations [130]. Different cell lines also show differential responses, in particular cancer cells have been shown to be more susceptible to AgNP toxicity compared with primary cells, which has highlighted AgNP as potential anticancer agents [131].

Several AgNP characteristics reportedly play a role in their toxic action and differential concentrations appear effective in both mammalian cells and bacteria. An inverse size-dependence has been observed in many studies, and AgNP between 1-10 nm are understood to exert the greatest toxic effects [74], [117] . Potentially this is due to the increased surface areas from which Ag+ ions can be emitted and which interact with cell membranes although the opposite size-dependence has also been reported [19]. Notably, silver ions have generally been shown to exhibit greater toxicity than AgNP applied at the same silver concentration in a number of mammalian cell lines, including lung and kidney

cells, in spite of reportedly similar mechanisms of action and lower levels of Ag uptake [112], [120], [133]. Different cell lines also display different sensitivities to the actions of AgNP, potentially due to different rates of uptake [19]. AgNP shape has also been observed to effect toxicity in *E. coli*, and this is potentially mediated by surface-area mechanisms [116].

Nanoparticle toxicity is also strongly influenced by experimental conditions, for example, AgNP are prone to agglomeration in culture media as the salts present displace the ion corona surrounding the particle, particularly in unstabilised varieties of AgNP [20], [110]. This affects the levels of cytotoxicity observed as the aggregation effectively "locks away" many nanoparticles, so the dosage delivered to cell cultures by AgNP of the intended size is actually lower than predicted. Furthermore the resulting aggregates may have different cytotoxic potential due to the size-dependent effects discussed previously. Conversely the presence of proteins in the media, e.g. from FCS, may bind to the surface of AgNP and interact with the cell membrane, effectively providing the AgNP with "camouflage", leading to increased uptake and therefore toxicity [34]. Similarly, functionalised or capped AgNP, or AgNP synthesised with different methods will be taken up by cells at varying rates due to different surface charges and interactions with cell membranes, thus exerting varying levels of toxicity. To properly investigate AgNP toxicity alone, it has been advised that AgNP should be altered as minimally as possible during *in vitro* investigations [134], [135].

Whilst AgNP generally elicit a dose-dependent response, they have also been observed to induce a hormetic dose-response in some cell lines: that is to say low dose exposure stimulates growth, as opposed to the toxic response observed at higher doses. This stimulation of cell growth at low concentrations could prove useful in wound healing

therapies [136], [137], [138]. However low-dose hormesis has also been observed in AgNP-treated *E. coli* [123]. This is an important consideration when selecting the correct dose of AgNP for antibacterial applications, since sublethal concentrations may have the undesirable effect of increasing bacterial infection. There are currently few studies available which have observed or investigated this effect in bacterial or mammalian cells, and other studies have observed contradictory behaviour in the same cell lines at the same concentrations [131].

1.7.4 Oral exposure to silver nanoparticles

Alongside skin absorption and inhalation, oral ingestion is one of the main routes of AgNP entry into the human body. Furthermore AgNP are now being incorporated into products such as toothpaste and dental composites for their antibacterial properties [15], [139]. Whilst there have been numerous studies using lung [20], [129] and skin cell lines [20], [135] and studies on oral bacteria [140], [141], there appears minimal research on toxicity of AgNP within the oral epithelium although one recent study has reported that AgNP showed dose- and time-dependent cytotoxicity in the SCC-25 oral epithelial cell line [115].

AgNP have been shown to inhibit growth of a number of oral bacterial pathogens including *E. faecalis*, *P. gingivalis* and *Lactobacillus sp.*, and AgNP reportedly reduced oral biofilm attachment [15], [141], [142]. Determining AgNP antibacterial activity on *S. mutans* is particularly desirable due to its cariogenic properties alongside *lactobacillus*, as previously discussed in section 1.2.3. A number of approaches have been utilised to measure *S. mutans* susceptibility to AgNP in the context of dental materials, including adding AgNP to composite resins, incorporation into tissue conditioners (a treatment for trauma or damage from ill-fitting dentures) and its use in root canal irrigants [142], [143], [144]. However, given the

variability in toxicity between different synthesis and functionalisation methods, size and cell environment, it is desirable to evaluate the effects of AgNP on *S. mutans* using the simplest possible models before incorporation into other complex systems.

Table 1.1 provides a summary of previous *in vitro* studies undertaken on the antibacterial activity of AgNP on *S. mutans* through direct treatment of bacteria in terms of the minimum inhibitory concentrations (MIC) measured by each after 24 hours. Although a size-dependent effect was observed within a single study, there is no obvious trend apparent between studies, potentially due to the different synthesis methods used. Furthermore, none of the studies considered the cytotoxic side-effects of their AgNP on the surrounding oral tissues and cells.

AgNP synthesis method/ stabilisation	**AgNP size**	**MIC on S. mutans**	**Notes**
Reduction using Gallic acid [140]	8.4 nm 16.1 nm 98 nm	66.87 µg/mL 108.33 µg/mL 222.92 µg/mL	
Purchased from Sigma Aldrich as nanopowder and suspended in water/ broth [114]	50 nm	50 µg/mL	$AgNO_3$ MIC was less than 3.125 µg/mL on equivalent cultures
Reduction using $NaBH_4$ and PVP-stabilised [145]	20 nm	4.86 µg/mL	
Reduction using bacterial supernatant [146]	10 nm	9.5 µg/mL	AgNP also enhances the effect of traditional antibiotics

Table 1.1 – Four previous studies determining the minimum inhibitory concentrations (MIC) of AgNP on S. mutans.

1.8 Aims and objectives

The aim of this project is to develop a method that could be used to non-invasively monitor cell growth in *in vitro* cultures of oral epithelial cell monolayers through image analysis of

phase contrast images, and subsequently apply this method to the investigation of silver nanoparticle toxicity.

The first objective is to develop a novel image analysis-based method for cell counting using phase contrast microscopy. Current commonly used cell counting methods suffer various disadvantages such as subjectivity errors, large time or resource costs, or incapacity for longitudinal studies. Therefore, the key requirements of the image analysis development objective are as follows:

- Non-invasiveness – the imaging method should be purely image analysis based so as not to require stains or sample destruction to enable multiple measurements to be made from the same sample, thus enabling longitudinal study.
- Accessibility – it is desired that this method could be undertaken by anyone with access to commonly used laboratory equipment, namely a microscope and a computer for image analysis.
- Objectivity – human intervention should be minimal to reduce the effects of subjectivity on cell count results. Specifically, the image analysis method should automated wherever possible, including algorithm parameter selection.

Once the image analysis method is developed, the second objective will be to undertake investigations into the experimental conditions, including fixation and staining protocols, appropriateness of a variety of cell cultureware in experimental set-up, and applicability to different cell lines, in order to determine the optimal operating conditions and define any limitations of the image analysis method.

The third objective is to validate the results of the cell counts provided by image analysis by comparison with those achieved by other image analysis algorithms and current routinely-used laboratory methods for evaluating cell number and monitoring cell growth to determine whether similar results can be achieved.

The limitations in current commonly used techniques for monitoring cell growth in response to treatment of nanoparticles as described in section 1.7.2 could be overcome or offset through incorporation of such an image analysis-based method into nanotoxicological investigations. The final objective is therefore to utilise the developed image analysis cell counting methods as part of a multimodality approach for analysing the effects of synthesised silver nanoparticles on an *in vitro* model of the oral epithelium. The key outcomes of this objective are as follows:

- Characterisation of silver nanoparticle size and aggregation status, including dispersion in culture media and broth.
- Evaluation of size-, dose- and time-dependent effects, plus comparison of nanoparticulate and ionic silver, of AgNP on H400 cells used as a model for the oral epithelium.
- Evaluation of the same parameters on cariogenic *S. mutans* treated with AgNP using the same samples of nanoparticles, and subsequent comparison and evaluation of the response of H400 cells and *S. mutans* to AgNP.

2 MATERIALS AND METHODS

Unless stated otherwise all chemicals, media and reagents used in this study were obtained from Sigma Aldrich, UK.

2.1 Mammalian cell culture

2.1.1 Cell lines

2.1.1.1 H400 cells

The H400 oral epithelial cell line was derived from the oral squamous cell carcinoma of a 55 year old female patient (cells were a kind gift from Prof. S. Prime, University of Bristol, UK) [36]. Characterisation of the H400 keratinocytes has previously demonstrated they can provide an appropriate model *in vitro* to study oral epithelial cell behaviour [38].

H400 cells were cultured in Dulbecco's Modified Eagle Medium nutrient mix (DMEM) (Biosera, UK) supplemented with 10% (v/v) heat-inactivated foetal calf serum (FCS) (Biosera, UK), 0.4 mg/mL hydrocortisone, and 10 mL/L penicillin-streptomycin.

2.1.1.2 OKF6 cells

The OKF6 cell line originated from a biopsy from the oral epithelium of a healthy 57 year old male. Immortality in the OKF6 cell line was generated by retroviral induced expression of the human telomerase catalytic subunit (hTERT), followed by a spontaneous mutation reducing p16 protein. The OKF6 cell line demonstrates typical responses to keratinocyte control mechanisms, such as epidermal growth factor treatment, also making it appropriate for *in vitro* modelling of oral epithelial cell phenotype [35].

OKF6 cells were maintained in DMEM/F12 supplemented with 25 µg/mL bovine pituitary extract (BPE), 0.2 ng/mL epidermal growth factor (EGF), 0.4 mM $CaCl_2$ and 4 mM L-glutamine (Gibco, UK).

2.1.1.3 U2OS cells

The U2OS human bone epithelial osteosarcoma cell line was derived from bone tissue of a 15 year old female patient [147]. U2OS cells are commonly used to model osteoblast behaviour *in vitro* [148].

U2OS cells were maintained in McCoy's 5A Modified Medium with L-glutamine and sodium bicarbonate supplemented with 10 mL/L penicillin-streptomycin and 10% FCS.

2.1.1.4 3T3 cells

The 3T3 fibroblast cell line originated from primary Swiss albino mouse embryo tissue and was established through maintaining a strict subculture regime involving low seeding density and regular passage. Although the 3T3 cell line exhibits chromosomal differences from the cells from which it was derived, it does demonstrate a similar cellular phenotype to the parent cells [149].

3T3 cells were maintained in DMEM medium supplemented with 10% FCS and 10 mL/L penicillin-streptomycin.

2.1.2 Cell culture techniques

2.1.2.1 Subculture

Cultureware and working volumes used in this study are presented in Table 2.1. All mammalian cell cultures were incubated at 37 °C and 5% CO_2 in a Galaxy S+ incubator (Scientific Laboratory supplies, UK). All techniques used on live cell cultures were performed using aseptic technique in a class II biosafety cabinet. Media changes were performed every 2 days. Subculture was performed approximately every 3-4 days once cultures reached approximately 90% confluency. Culture medium was removed from the cultureware and the

cell monolayer was washed with fresh culture media to remove cell debris. Cultures were then incubated in 37 °C pre-warmed 0.25% trypsin-ethylenediaminetetraacetic acid (EDTA) (Gibco, UK) for 5-10 minutes with agitation until the monolayers had detached from the cultureware, as determined by inspection using a microscope. The volume of trypsin-EDTA used for different cultureware is provided in Table 2.1. The resulting cell suspension was added to an equal volume of pre-equilibrated culture medium in a 15 mL Falcon tube (Fischer, UK). The suspension was centrifuged at 800 revolutions per minute (rpm) in a Jouan B4i centrifuge for 4 minutes. The supernatant was removed and the cell pellet resuspended in appropriate media for the cell line (section 2.1.1). Cells were mixed by vortexing or vigorous pipetting to ensure a homogeneous distribution for counting using techniques described in section 2.1.3 and for further culture. Unless otherwise specified, cells were seeded at a density of 5×10^4 cells/mL for use in downstream experiments. The centrifugation and resuspension steps were omitted if cell density of suspension was being determined as the experimental end point and cells were not required for further culture.

Cultureware (& supplier)	Diameter/ surface area	Working volume of media	Working volume of trypsin-EDTA
T75 (ThermoScientific, UK)	- / 75 cm^2	10 mL	5 mL
T25 (ThermoScientific, UK)	- / 25 cm^2	5 mL	3 mL
35 mm culture dish (Sarstedt, UK)	35 mm/ 9 cm^2	2 mL	0.5-1 mL
6-well plate (Corning, UK)	35 mm/ 9 cm^2	2 mL	0.5 mL
12-well plate (Corning, UK)	22.1 mm/ 4 cm^2	1 mL	N.A.
24-well plate (Corning, UK)	15.6 mm/ 2 cm^2	0.5 mL	N.A.
48-well plate (Iwaki, Japan)	11.0 mm/ 0.7 cm^2	0.25 mL	N.A.
96-well plate (Corning, UK)	6.4 mm/ 0.3 cm^2	0.1 mL	N.A.

Table 2.1 – Cultureware used for culturing cells, imaging and cell growth analysis. *Diameters of cultureware, volume of media used to seed cells into each type of cultureware and volume of trypsin-EDTA used to detach cultures are shown. N.A. indicates that trypsin-EDTA was not used on this cultureware.*

2.1.2.2 Cell cryopreservation

For long term storage, cells were frozen in liquid nitrogen vapour (-196 °C). A confluent T75 flask was subcultured, cells were detached as described previously and pelleted cells were resuspended in 1 mL media containing 20% (v/v) FCS and 10% (v/v) dimethyl sulfoxide (DMSO). This suspension was stored at -80 °C overnight in a U535 Innova Ultra Low Temperature freezer (New Brunswick, UK) before being transferred to liquid nitrogen.

To revive cells after cryopreservation, the suspension was rapidly thawed using a PC-42OD hot block (Corning, UK) at 37 °C and transferred to the appropriate 10 mL pre-equilibrated media in a T75 flask. Cells were allowed to adhere to the plasticware overnight before removing DMSO-containing culture media and replacing with fresh media.

2.1.3 Cell counting

2.1.3.1 Haemocytometer chamber

For counting using an improved Neubauer haemocytometer chamber (Hawksley, UK) (Figure 2.1A), a coverslip was firstly attached by pressing firmly onto the clean, moistened haemocytometer. 50 µL of the cell suspension (as described in section 2.1.2.1) was pipetted at the edge of the gap between haemocytometer and coverslip, and drawn into the chamber by capillary action until the entire grid was covered. This loading process was repeated for both sides of the haemocytometer.

Cells in the outer larger four corner squares of each grid (Figure 2.1B) were counted and values averaged to determine the number of cells per 10^{-4} mL of suspension. To calculate the total number of cells from the density, the cell concentration was multiplied by the total volume of suspension. To ensure consistency in the counting technique, cells overlapping top and right edges were included in the count and cells overlapping the bottom and left edges were not (Figure 2.1).

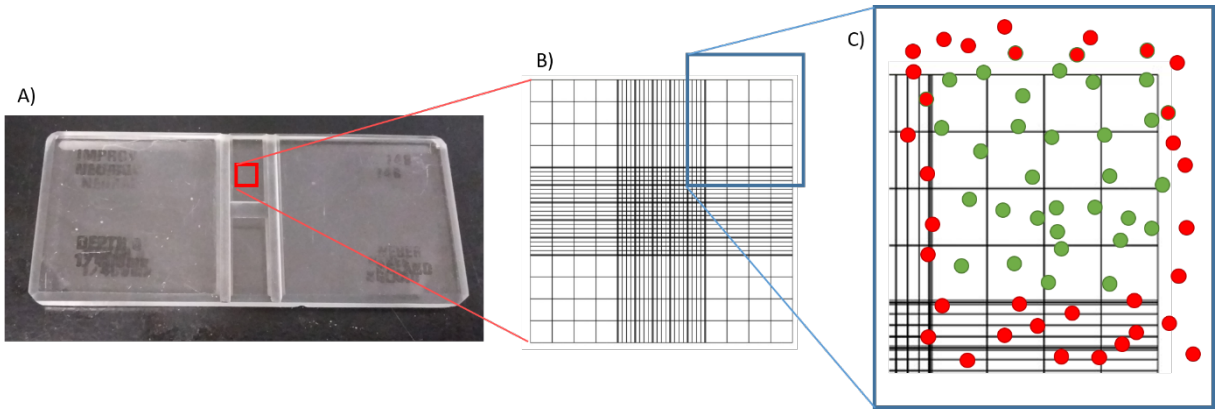

Figure 2.1 – The Neubauer haemocytometer chamber. *A) Image of an improved Neubauer haemocytometer, indicating the location of one counting grid. B) Schematic figure of a haemocytometer grid. Cells in the centre of the square and those overlapping with the top and right edges are counted (represented in C) by solid green circles). Those overlapping the bottom and left edges were not counted (represented by solid red circles). The average of four squares provided the number of cells per 10^{-4} mL of suspension.*

2.1.3.2 LUNA™ automated cell counter

The LUNA automated cell counter (Logos Biosystems, UK) operates using the same principle as the haemocytometer chamber, except the number of cells in a grid is determined automatically using the proprietary image analysis software included with the instrument.

To count cells using the LUNA device, 50 µL of the cell suspension was pipetted into the counting chamber at each end of a LUNA cell counting slide (Logos Biosystems, USA) prior to insertion into the counter (Figure 2.2A). For each sample, both chambers of two slides (four readings in total) were averaged to determine the number of cells per 10^{-4} mL of suspension. The focus on the device was adjusted manually following inspection of the image of the slide on the screen/viewer (Figure 2.2B). Image analysis settings for cells in suspension were adjusted manually and are shown in Table 2.2. The values selected had been previously optimised for H400 cells using knowledge of the morphology and probable range of cell sizes in suspension (data not presented).

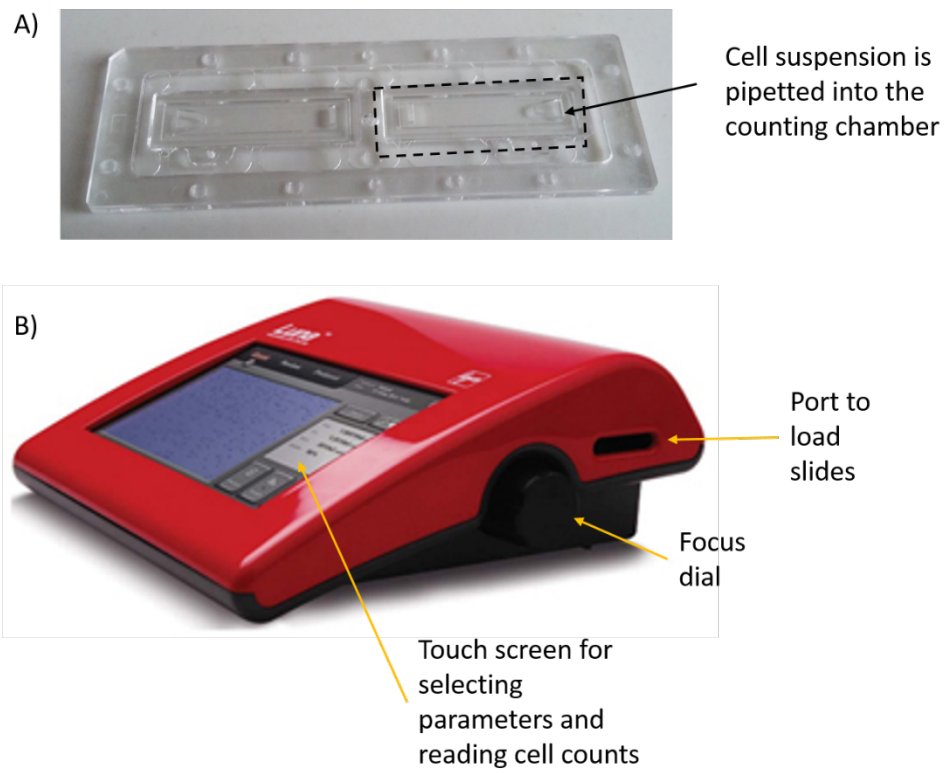

Figure 2.2 – The LUNA Automated Cell Counter. *A) Photograph of slide indicating the counting chamber (dotted line) where cells in suspension are loaded for counting (arrow). B) Annotated photograph of the LUNA Automated Cell Counter indicating the location of port to load slides, the focus dial and the touch screen used for selecting parameters and reading cell counts. Image B) acquired from the Logos Biosystems website* [150].

Parameter	Description	Set Value
Noise reduction	Level of background smoothing. Ranges from 0 to 9, where 9 indicates large background reduction	9
Roundness	Roundness threshold for detection	60%
Minimum cell size	Smallest acceptable cell size for detection	10 µm
Maximum cell size	Largest acceptable cell size for detection	50 µm
Dilution factor	The factor by which stock has been diluted	1

Table 2.2 – Parameters of the LUNA cell counter and values used for counting H400 cells in suspension.

2.1.3.3 MTT assay

The MTT assay measures the mitochondrial respiration rate of cells, which can be related to cell number (see section 1.4.2). This assay requires the addition of 3-(4,5-dimethylthiazol-2-yl)-2,5-diphenyletetrazolium bromide (MTT) substrate to cell cultures, which is reduced to purple water-insoluble formazan by the mitochondrial dehydrogenase enzyme produced in living cells during respiration [41].

A MTT stock solution of 5 mg/mL was generated in phosphate buffered saline (PBS) and agitated to solubilise. The PBS used in all methods described here consisted of 7.75 g NaCl, 0.2 g KH_2PO_4 and 1.5 g K_2HPO_4 dissolved in 1 L of reverse osmosis (RO) purified water prior to autoclaving. The MTT stock solution was stored in the dark at 4 °C to avoid degradation. For MTT assay, cells in media were seeded in a flat clear bottomed black-walled 96-well plate (Table 2.1) with 4 replicate wells per condition. After incubating overnight under the conditions described in section 2.1.2.1 to allow cell adherence, MTT stock was added to wells at a volume of 10% of the culture media (Table 2.1) and further incubated for 4 hours. Subsequently, the media was removed, taking care to avoid disturbing the crystals formed on the substrate. 50 µL of DMSO was then added to each well and agitated briefly until the crystals had dissolved. The amount of formazan salt produced was determined spectrophotometrically by acquiring optical density (OD) readings at 570 nm for each well using an ELx800 universal microplate reader (Bio-Tek Instruments, Cole-Parmer, UK). Background readings were acquired by seeding wells with cell-free media and treating identically to cell-containing wells (n = 2 per treatment condition). The average cell-free reading was subtracted from all OD readings to remove background.

A calibration curve was generated to determine the relationship between the MTT assay OD values to cell numbers determined from cells cultured under parallel conditions. Specifically, the known number of cells was determined by counting with a haemocytometer (see section 2.1.3.1) and making a serial dilution of these in a 96-well plate before immediately performing the MTT assay and plotting optical density against cell number (Figure 2.3).

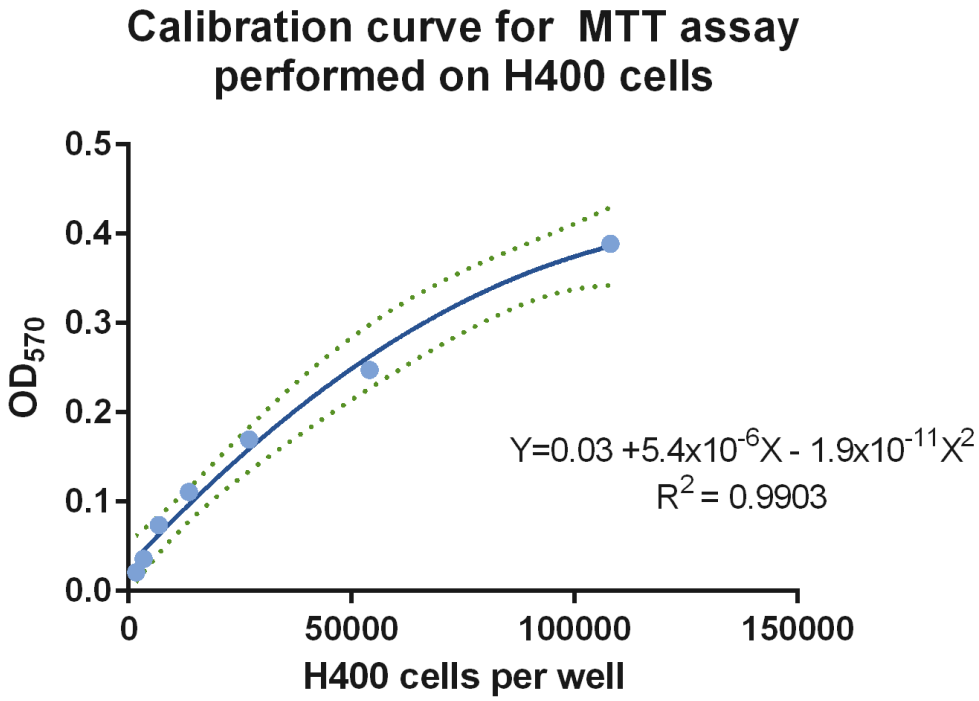

Figure 2.3 – Calibration curve for MTT assay performed on H400 cells. *Curve used to calibrate optical density at 570 nm of solubilised formazan generated in live cells after treatment with MTT plotted against number of cells in the culture as determined using the haemocytometer approach. The fitted curve is shown in blue alongside equation. Green dotted lines indicate 95% confidence intervals.*

2.2 Cell staining

Cells stained with fluorescent nuclear dyes were used as a ground truth in the development of image analysis techniques for phase contrast microscopy, the details of which can be found in chapter 0. A number of staining approaches were investigated. To avoid

photobleaching, all fluorescent stains were stored in the dark and fluorescently stained cultures were incubated in darkness.

2.2.1 DAPI

4',6-diamidino-2-phenylindole (DAPI) is a nuclear stain which becomes fluorescent when bound to the minor groove of DNA, particularly in regions containing high densities of A-T base pairs. DAPI is most commonly used to stain fixed cells, although it can also be used to stain live cells despite exhibiting lower fluorescent intensity due to reduced uptake. DAPI has an excitation peak at 358 nm and an emission peak at 461 nm [151]. An example of a cell stained with DAPI can be seen in Figure 1.10A).

The two protocols described immediately below were used for staining with DAPI. The first protocol described used DAPI in powder form dissolved in distilled water to generate a 1 mg/mL stock solution which was stored at -20 °C.

Protocol 1: The stock solution was diluted in distilled water to 1 µg/mL. Cultures were immersed in excess DAPI solution and incubated for 20 minutes in the dark at room temperature prior to washing three times with PBS. Cells were immersed in PBS whilst imaging to avoid cultures becoming desiccated.

Protocol 2: This protocol used Prolong Gold Antifade mountant with DAPI (Thermo Fisher Scientific, UK), a mounting medium used for fluorescence microscopy to prevent photobleaching. The mount medium was added dropwise directly to fixed cells prior to a glass coverslip being placed directly over their surface. Samples were incubated overnight at room temperature to cure the mount medium prior to image capture (details described in section 2.4).

2.2.2 Hoechst staining

Hoechst 33342 is a nuclear stain analogous to DAPI in that it fluoresces strongly upon binding to the minor groove of A-T rich regions of DNA, and has similar peak excitation and emission wavelengths of 361 nm and 486 nm, respectively [152]. An example of a Hoechst stained cell can be seen in Figure 4.4G.

NucBlue® Live ReadyProbes® Reagent (Thermo Fisher Scientific, UK) is a commercially available Hoechst stain. One drop of this per mL of media was added to live cell cultures, which were incubated for 15 minutes at 37 °C prior to image capture.

2.3 Cell fixation for fluorescent staining

A number of fixation techniques were investigated for use alongside fluorescent staining as described in section 2.2. Unless stated otherwise, adherent cell cultures in 6-well plates (Table 2.1) were washed three times with 2-3 mL PBS before application of the fixative (as described below), and incubated for 15 minutes at room temperature. Once the fixative was removed by aspiration, the samples were washed with PBS three times for 15 minutes.

A number of fixation techniques were investigated for use alongside fluorescent staining as described in section 2.2. Adherent cell cultures in 6-well plates (Table 2.1) were washed three times with 2-3 mL PBS before immersion in (Leica, UK), glutaraldehyde (as described in section2.3.2) or 4% paraformaldehyde (PFA) (as described in section 2.3.1), and incubation for 15-30 minutes at room temperature. In cultures fixed with methanol (Fisher Scientific, UK), the same protocol was followed except the fixative was pre-equilibrated to -20 °C and cultures were incubated at -20 °C. An alternative protocol for PFA used an 8% solution applied directly to an equal volume cell media to give a final concentration of 4% PFA, i.e.

without previous culture washing to avoid disturbances to the cells due to the washing step. In all cases, once the fixative was removed by aspiration, the samples were washed with PBS three times for 15 minutes.

2.3.1 Paraformaldehyde fixative

The PFA solution was synthesised to the required concentration by adding PFA powder to 100 mL of PBS (e.g. 4 g to give a 4% solution). The solution was stirred for 3 hours at 70 °C using a magnetic stirrer on a PC-42OD hotplate (Corning, UK) until it became clear. Finally, the PFA solution was filtered through a 0.22 µm syringe filter (Merck Millipore, UK) to remove any remaining undissolved particles.

2.3.2 Glutaraldehyde fixative

2.5% glutaraldehyde was prepared by mixing 6 mL distilled water, 7.5 mL 0.1 M sodium cacodylate buffer and 1.5 mL 25% glutaraldehyde solution. 0.1 M sodium cacodylate buffer was prepared by adding 4.28 g of sodium cacodylate trihydrate to 100 mL of distilled water. The pH was measured using a Beckman 40 pH-meter and adjusted to 7.4 by the dropwise addition of 50% NaOH or HCl solutions to increase or decrease pH respectively. Cultures were immersed in glutaraldehyde for at least 30 minutes at room temperature in a fume hood prior to further analysis.

2.4 Microscopy and Image processing

2.4.1 Microscope

Phase contrast and epifluorescence images were obtained using a TE300 microscope (Nikon, UK) with a x10 objective lens. Fluorescent stains were illuminated using a pE-100 excitation light source (CoolLED, UK). Plasticware lids were removed before imaging to reduce contrast

degradation due to condensation. Images were acquired inside a microscope enclosure chamber sterilised with 70% ethanol prior to image capture to reduce the risk of contamination.

2.4.2 Image capture

Culture images were captured using either a Nikon D40 digital camera (Nikon, Japan) or a Retiga-2000R CCD camera (Qimaging, Canada). Images captured using the CCD camera were imported directly to a computer using Micro-Manager software for ImageJ [153], [154]. All images were converted to 8-bit greyscale TIFF format prior to any further processing being performed.

2.4.3 Image scale calibration

To calculate the equivalent units of physical measurement corresponding to one pixel, an image of a 0.1 mm stage micrometer (Graticules Ltd., UK) was acquired. On this image, a line was drawn over a known distance in millimetres using the ImageJ line drawing tool, and from this a conversion factor was calculated using the length of the line in pixels. This approach was repeated for each camera used as described in section 2.4.2 [153].

2.5 Microbiological cell culture

2.5.1 Bacteria

2.5.1.1 Escherichia Coli

E. coli is a Gram-negative, facultative anaerobic, rod-shaped bacterium, normally commensal in the human lower intestinal tract. It forms rounded, translucent-white colonies when grown on horse blood agar. Due to the relative ease of culturing *E. coli in vitro* and its potential for both aerobic and anaerobic growth *E. coli* is used commonly as a model

organism for laboratory testing, including investigation of the properties of potential antibacterial treatments [127], [155]. *E. coli* was cultured at 37 °C under aerobic conditions in a Swallow incubator (LTE Scientific, UK). The strain used for this work was National Collection of Type Cultures (ATCC 10536) (Fisher Scientific, UK).

2.5.1.2 Staphylococcus aureus

S. aureus is a Gram-positive coccus commonly found on the skin, respiratory tract and oral cavity of humans, it is commonly associated with wound infection. When grown on horse blood agar it forms round colonies, which are golden yellow to white in colour. Similarly to *E. coli*, its robustness during culturing makes it a frequently used model organism for investigation of the properties of Gram-positive bacteria, including the response to potential antibacterial treatments [155].

The strain used for the studies presented here was ATCC 9144 (Fisher Scientific, UK). *S. aureus* was incubated in aerobic conditions at 37 °C for all experiments.

2.5.1.3 Streptococcus mutans

S. mutans is a Gram-positive coccus predominantly found in the oral cavity, which forms punctiform white colonies when grown on horse blood agar. It has been shown that the presence of *S. mutans* contributes to dental caries in humans [156].

The strain of *S. mutans* used in all the work presented here was ATCC 25175 (Fisher Scientific, UK). Cultures were maintained at 37 °C in a 5% CO_2 atmosphere in a NAPCO 5600 incubator (Richmond Scientific Ltd, UK).

2.5.2 Bacterial culture and analysis

2.5.2.1 Long term storage

For long term storage, bacteria were cryopreserved by inoculating cyopreservative fluid (ProLab, UK) with bacteria and inverting to mix in a cryovial containing porous beads (ProLab, UK). Excess cryopreservative was aspirated before storing cryovials at -40 °C prior to use. To revive bacteria from frozen, a single bead was spread across the surface of a pre-prepared agar base no.2 with 7% v/v horse blood agar plate (Fischer, UK) with a sterile inoculation loop (Technical Service Consultants Ltd., UK) using the streak plate technique (see section 2.5.2.2) and incubated at 37 °C for at least 24 hours under the appropriate atmosphere for the strain as specified in section 2.5.1. Plates were assessed to ensure purity of colonies before storage at 4 °C and all further experiments using a particular strain were established from a single colony from this master plate.

2.5.2.2 Streak plate technique

To ensure a sufficiently low concentration of all bacteria to enable single colony formation, a standard streak plate technique was applied. Using a sterile plastic loop, the bead (or a bacterial colony) was streaked back and forth along a third of the plate. The agar plate was then rotated by 90°and a second sterile loop drawn through the streaked region into the plate. The plate was subsequently rotated by 90° and a third sterile loop was drawn through the second streaked region (Figure 2.4).

Figure 2.4 – Photograph showing the streak plate technique. *90 mm horse blood agar plate inoculated with E. coli showing streak plate pattern generated to enable individual colony isolation.*

2.5.2.3 Bacterial growth in broth culture

Brain-heart infusion (BHI) broth powder (Oxoid, UK) was dissolved in distilled water at 37 g/L and autoclaved at 121 °C for 10 minutes in a steam steriliser (Prestige Medical, UK). Culture broth was allowed to equilibrate to room temperature prior to use.

A single representative bacterial colony (derived from an individual clone) for all strains studied was selected from the agar plate (as described above) using a sterile inoculation loop. This was used to inoculate 20 mL of BHI broth, before incubation overnight at 37 °C in an aerobic atmosphere on a shaking incubator stage (N-Biotek Inc., S. Korea) rotating at 100 rpm.

2.5.2.3.1 Bacterial growth analysis

The presence of bacteria in the broth results in culture turbidity, which translates as an increase in optical density (OD). To set up bacterial growth experiments, bacteria in broth was diluted to a low density by measuring the OD at 600 nm using a Jenway 6300 spectrophotometer (Jenway, UK) in a 1 mL disposable cuvette (Sarstedt, UK), and adding broth until an initial OD of 0.05 was achieved. The spectrophotometer was calibrated to zero using a sample of uninoculated broth. Bacteria in broth were subsequently seeded into an opaque-walled 96-well plate at a volume of 100 µL per well.

To generate a growth curve, OD measurements at 630 nm were obtained at multiple time points up to 24 hours following exposure using an ELx800 universal microplate reader (Bio-Tek Instruments, Cole-Parmer, UK). OD readings for *S. mutans* were acquired at fewer time points than for *E. coli* and *S. aureus* cultures to minimise the time spent outside the desired CO_2 conditions. Furthermore culture dishes were carefully agitated before OD readings were obtained in order to generate homogeneous mixtures for OD reading.

The OD of 4 replicate wells was averaged at each time point to determine the bacteria growth response following different treatment exposures. To remove background readings, the OD of additional wells (n=2) containing 100 µL of uninoculated broth were treated identically to inoculated wells and the average readings from these were subtracted from the average of the inoculated broth readings.

Dose-response curves were plotted using the OD readings of bacteria exposed to serially diluted treatment, measured after the 24 hour incubation period.

2.5.2.3.2 Bacterial growth on agar

To determine the presence of viable bacteria in treated cultures for which there was no change in OD observed after 24 hours incubation, 10 µL of broth was spread with a sterile inoculation loop over a segment of horse blood agar plate and inspected for colony growth after overnight incubation. A sample from an untreated well containing bacteria and an untreated and uninoculated well were also plated to serve as positive and negative controls for growth. For an example see Figure 6.15.

2.5.2.4 Gram staining

Gram staining aids confirmation of the identity of the strains of bacteria being studied. Gram's method uses a succession of stains to distinguish between two types of bacterial cell structure. Gram-positive bacteria appear purple as the initial crystal violet dye is retained after washing with acetone due to a thick peptidoglycan layer at the cell wall that entraps the stain. Conversely, the crystal violet is not retained by the thinner peptidoglycan walls of Gram-negative bacteria, which subsequently appear red-pink upon inspection due to the presence of the carbol fuchsin counter stain [157].

2.5.2.4.1 Gram stain reagents

Crystal violet stain was prepared by dissolving 10 g crystal violet in 100 mL of 95% ethanol (Fisher Scientific, UK). 20 mL of this solution was then combined with 90 mL of 1% ammonium oxalate and diluted with distilled water.

A 1:9 dilution of carbol fuchsin (BDH, UK) was also prepared in distilled water.

2.5.2.4.2 Gram staining method

A single bacterial colony was isolated from an agar plate using a sterile loop and incorporated with a single drop of BHI broth on a glass microscope slide (CellPath, UK). The bacteria were fixed by passing the slide through a Bunsen burner flame until the suspension appeared dried. The sample was initially immersed in crystal violet solution for 30 seconds and rinsed with tap water. The sample was then immersed in Lugol's iodine solution for 15 seconds, rinsed with tap water, flooded with acetone, and rinsed again with water. Finally, the sample was immersed in the carbol fuchsin stain for 15 seconds and rinsed for a final time with water. Once dry, the slide was viewed with a Motic oil immersion microscope using an x100 objective (Scientific Laboratory Supplies, UK). Images were acquired using an Olympus BX50 microscope and a Retiga 2000 R Camera with F-adaptor and RGB LCD filter.

2.5.2.4.3 Gram stain images

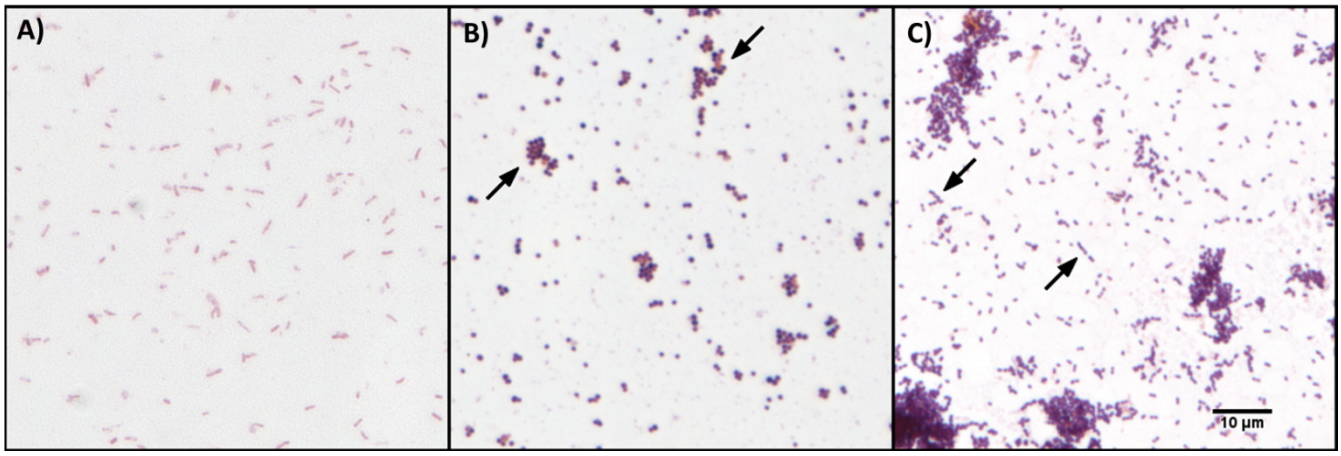

Figure 2.5 – Photomicrographs showing Gram-stained bacteria used in this study. *A) Gram-negative E. coli showing distinctive bacillus morphology. B) Gram-positive S. aureus. Arrows indicate grape-like clustering which is characteristic of staphylococcal bacteria. C) Gram-positive S. mutans. Arrows indicate chains of spherical bacteria, characteristic of streptococcal bacteria. Scale bar for all images is shown in C).*

2.6 Silver Nanoparticles

2.6.1 10 nm nanoparticle synthesis

Silver nanoparticles (AgNP) were synthesised by reduction of silver nitrate ($AgNO_3$) with sodium borohydride ($NaBH_4$), as follows:

$$\mathrm{AgNO_3 + NaBH_4 \rightarrow Ag + \frac{1}{2}H_2 + \frac{1}{2}B_2H_6 + NaNO_3} \qquad \textit{[Equation 1]}$$

AgNP were synthesised according to the method described by Creighton *et al.* [158]. 50 mL of 1 mM $AgNO_3$ was added dropwise to 150 mL of 2 mM $NaBH_4$ at a rate of approximately 1 drop per second using a Minipuls 3 peristaltic pump (Gilson, UK) whilst stirring rapidly with a magnetic stir bar to aid monodispersity [158]. All solutions were prepared with deionised water and chilled on ice prior to, and during, mixing to slow the reaction and promote homogenously sized and shaped nanoparticles. The reaction was performed in the dark to prevent photodegradation. Stirring was halted immediately after all $AgNO_3$ had been added to avoid irreversible AgNP aggregation. The resulting final solution was a deep yellow colour and was stored at room temperature in a dark bottle to avoid photodegradation.

2.6.1.1 Concentration of silver nanoparticle solution

The concentration of nanoparticles after synthesis was calculated stoichiometrically from the known mass of $AgNO_3$ added to the reaction. The molar concentration of Ag^+ is equal to that of $AgNO_3$. Using the atomic weight of Ag (107.8682 g/mol) and 1 mM = 10^{-3} mol/L, the Ag concentration in the initial $AgNO_3$ solution may be expressed in terms of g/L:

$$10^{-3}\ \text{mol/L} \times 107.8682\ \text{g/mol} = 0.107862\ \text{g/L of Ag+} \qquad \textit{[Equation 2]}$$

Multiplying by the ratio of $AgNO_3$ solution volume to the total volume as per the conservation of mass rule gives the concentration of Ag in the final volume of AgNP solution:

$$\frac{50}{200} \times 0.107862 \text{ g/L} = 0.026965 \text{ g/L} = 26.965 \text{ µg/mL} \qquad \textit{[Equation 3]}$$

To increase the concentration of AgNP, 2 mL aliquots of the solution were centrifuged in a 5415C centrifuge (Eppendorf, UK) at 15000 rpm for 1 hour until a pellet of AgNP had formed (Figure 2.6). Approximately 1.8 mL of supernatant was removed from the aliquot and the AgNP was resuspended in the remaining supernatant using ultrasonication for 10 seconds in an Vitasonic In-Ceram ultrasonicator bath. Aliquots were combined and the resultant AgNP solution (Figure 2.6C) was stored in the dark at room temperature prior to use. The concentration of the centrifuged AgNP was determined using UV-vis spectroscopy (section 2.6.4.1)

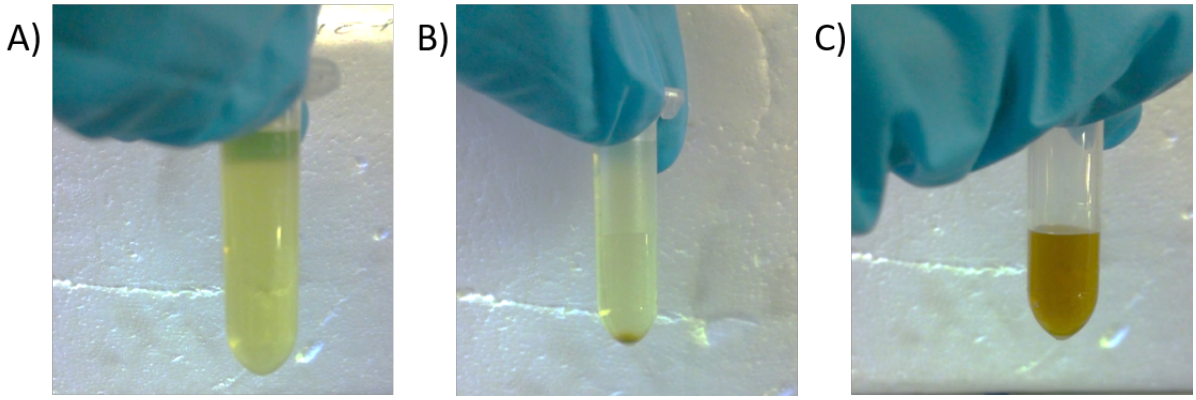

Figure 2.6 – Images showing the stages of AgNP concentration through centrifugation. *A) Image of the AgNP stock solution showing characteristic yellow colouration. B) AgNP stock solution after centrifugation at 15000 rpm for one hour. Note the dark pellet at the bottom of the aliquot and the lighter yellow colour remaining in the supernatant. C) Pellets from multiple aliquots were recombined to give the final concentrated AgNP stock solution. The dark yellow colouration is indicative of the increased density of nanoparticles in the solution.*

2.6.2 100 nm nanoparticle preparation

Nanoparticles purchased in powder form with nominal size <100 nm were suspended in water purified by reverse osmosis (RO water) at a concentration of 1 mg/mL to provide a stock solution. The stock solution was synthesised and stored in a glass vial since static attraction between powder and plasticware can impede accurate measurement and homogenous nanoparticle distribution in solution. The stock solution was mixed in a Vitasonic In-Ceram ultrasonicator bath for at least 45 minutes prior to use to ensure homogenous distribution of nanoparticles.

2.6.3 AgNP nomenclature

For simplicity AgNP synthesised as described in section 2.6.1 will be referred to nominally as 10nm AgNP, or “AgNP-10”. Those described in section 2.6.2 will be referred to as “AgNP-100”. The true size of all AgNP will be characterised using techniques described in the following section. Centrifuged AgNP-10 will be referred to as “AgNP-10 concentrate” and the primary synthesised sample will be referred to as “AgNP-10 stock”.

2.6.4 Nanoparticle characterisation

2.6.4.1 UV-vis spectroscopy

Light incident on a colloidal suspension of nanoparticles induces oscillations in the free electrons at the surface of the nanoparticles. There is a sharp increase in this oscillation when excited by electromagnetic radiation of wavelength specific to the size and shape of the nanoparticle, and this phenomenon is known as surface plasmon resonance (SPR). SPR results in a strong absorption band in the ultraviolet to visible (UV-vis) region of the electromagnetic spectrum. This may be characterised by UV-vis spectroscopy, a technique

that involves measuring the OD of the sample at a range of UV-vis wavelengths to create an absorbance spectrum. The size of nanoparticles in the sample determines the absorbance spectrum properties: larger particles shift the peak towards higher wavelengths and a more monodisperse sample displays a narrower peak [159].

A Cary 5000 UV-Vis spectrophotometer (Agilent, UK) was used to measure the UV-vis absorbance spectrum of nanoparticle samples using quartz cuvettes with a 10 mm path-length (Starna Scientific Ltd., UK). A blank sample of the deionised water solute was used to provide a background reading. The OD was measured at wavelengths between 200 nm and 800 nm at increments of 1 nm.

For optimal comparison of two samples, UV-vis spectra were first normalised to their respective peak value to account for differences in concentration. The full width at half maximum (FWHM) was calculated using the difference between wavelengths at half the peak intensity.

2.6.4.1.1 Calculation of AgNP-10 concentration

Not all AgNP-10 could be pelleted during centrifugation, as evidenced by the light yellow colour seen in the supernatant (Figure 2.6). Consequently, some nanoparticles were removed with the supernatant thus the concentration of the centrifuged sample cannot be determined arithmetically from the volume of supernatant removed. According to the Beer-Lambert law the intensity of the peak in the UV-vis absorbance spectrum is proportional to the concentration of AgNP in solution as follows:

$$A = \varepsilon lc \qquad \textit{[Equation 4]}$$

where A is absorbance at the peak value (398 nm), ε is the molar absorption coefficient, l is the optical path length and c is the concentration of AgNP in solution [160]. ε and l are constant for a given material measured using the same cuvette, therefore a standard curve was plotted by measuring the absorbance intensity (A) of the peak at varying concentrations of the stock solution (c) (Figure 2.7).

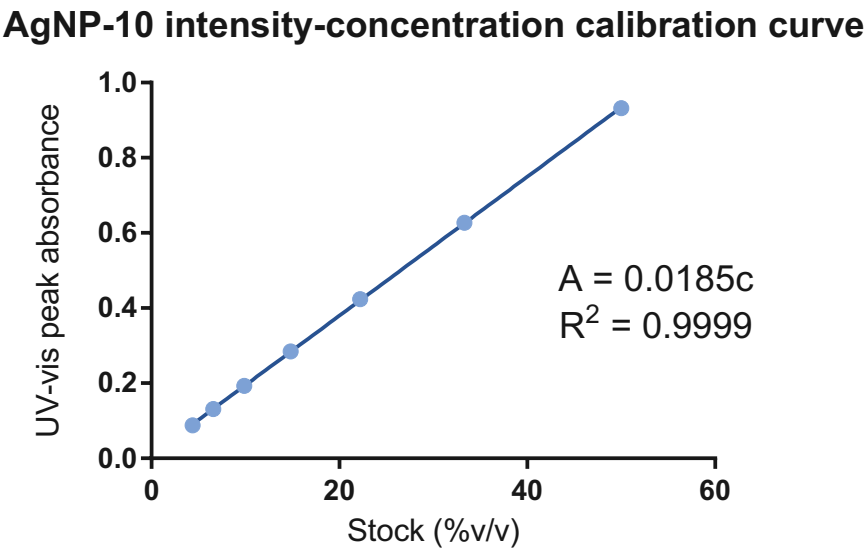

Figure 2.7 – Graph showing increase in UV-vis peak absorbance (398 nm) with increasing concentration of synthesised AgNP-10 stock.

The equation of the standard curve is:

$$A = 0.0185c \qquad \textit{[Equation 5]}$$

Concentration of centrifuged AgNP-10 (concentrate) was calculated by acquiring a UV-vis spectrum after dilution to a known concentration, $c_{concentrate}$. The peak absorbance was used in *[*Equation 5 to find the concentration of stock, c_{stock}, with the same absorbance. The ratio of $c_{concentrate}$ to c_{stock} gave the concentration factor: the average of 6 dilutions of

AgNP concentrate was used to calculate this. AgNP-10 concentrate was found to be 6.95 times the concentration of stock AgNP-10, giving a final concentration of 186.75 μg/mL.

2.6.4.2 Dynamic Light Scattering

Dynamic light scattering (DLS) utilises the principle that small particles dispersed in a solution will scatter incident light. Due to Brownian motion of the particles, the intensity of the scattered light from a polarised, monochromatic source gives rise to a speckle pattern due to interference effects. The intensity of the pattern varies randomly over time with a decay frequency related to the hydrodynamic diameter of the particles (smaller particles have a faster decay frequency) [161]. DLS is able to measure particle sizes between 0.3 nm to 10 μm [162]. DLS was used to determine the hydrodynamic diameter of AgNP in suspension.

A Zetasizer Nano ZS DLS system (Malvern Instruments, UK) was used with corresponding Zetasizer software, and 1 mL of diluted sample was loaded into a disposable polystyrene cuvette (Sarstedt, UK). The standard operating procedure used a refractive index of 1.33 for silver dispersion nanoparticles [163]. Twelve measurements were obtained per analysis and the average of three runs was used to determine nanoparticle hydrodynamic diameter.

2.6.4.3 Transmission Electron Microscopy

Images are created using transmission electron microscopy (TEM) by directing a beam of electrons onto a specimen. Regions in the sample containing elements with high atomic number block the transmission of electrons, and these manifest as dark regions in the resultant image; the background subsequently appears bright [164]. For an example image

refer to Figure 5.6. Nanoparticle size was therefore measured directly using TEM using image analysis (section 2.6.4.3.1).

AgNP samples in solution were air-dried onto Formvar/carbon-coated copper grids (Agar Scientific) before imaging with a JEOL JEM-1200EX microscope operating at 80 kV. Images were acquired with a Gatan multiscan camera and DigitalMicrograph 1.8 software (Gatan, USA).

2.6.4.3.1 TEM image analysis

Analysis of TEM images was performed using ImageJ version 1.48v [153]. To estimate AgNP size from TEM images, images were first converted to 8-bit and the background was removed using a rolling-ball filter with a 50 pixel radius [165]. Images were then smoothed before thresholding using Bernsen's method; a range of values for the radius of the local set and mid-grey level were tested and the final values used were a radius of 15 pixels and mid-grey level 30 [166]. The watershed algorithm was applied to separate merged segmented regions before the Particles8 plugin was applied to calculate various morphological properties of the resulting binary regions [167]. The maximum Feret diameter (the largest distance between two points on the binary object edge) was used to describe nanoparticle sizes.

2.6.4.4 Inductively-coupled plasma optical emission spectrometry

Inductively-coupled plasma optical emission spectrometry (ICP-OES) is used to quantify the presence of elemental ions in a solution by first passing the nebulised sample through an ionised argon plasma. When passing through the high temperature of the plasma, atoms in the sample become ionised and thermally excited, and emit light at wavelengths

characteristic of the element. The amount of a given element in the sample is determined by measuring the intensity of these characteristic wavelengths [168]. ICP-OES was used to verify the ratio of silver concentrations in AgNP-10 stock and concentrate as calculated with UV-vis spectrometry.

Thirty µL of sample was digested overnight in 1.5 mL of 20% nitric acid (BDH, UK) and subsequently diluted to 2% with RO water. 5 dilutions of silver standard solution (VWR Chemicals, UK) were made and digested similarly to give final concentrations between 500 ppb and 6.6 ppb for the generation of a standard curve. Triplicate samples were analysed on a Perkin Elmer Optima 8000 ICP-OES (Perkin Elmer, UK) (with the assistance of Eimear Orgill at the School of Geography, Earth and Environmental Sciences, University of Birmingham). Samples were prepared in triplicate and the mean value was used to plot a standard curve.

2.6.5 Cellular nanoparticle localisation and quantification

2.6.5.1 TEM

TEM was used to localise the destination of AgNP in H400 cells and bacteria and to inspect cellular structural integrity following AgNP exposure. After detachment from the substrate using Trypsin-EDTA, samples were fixed by suspension in 2% glutaraldehyde in phosphate buffer and overnight incubation at room temperature before being stained by suspension in 1% osmium tetroxide solution for 1 hour. Samples were dehydrated with a series of ethanol washes, increasing in concentration from 50% to 100%, before washing with propylene oxide to remove residual ethanol. Cells were embedded in epoxy resin (Agar Scientific, UK) and ultrathin sections (50-100 nm) were obtained using a diamond knife before mounting onto

copper grids, as described in section 2.6.4.3. Samples were stained and mounted by Theresa Morris at the Centre for Electron Microscopy, University of Birmingham, UK. Unexposed control cultures were prepared identically for each cell type processed. For an example image refer to Figure 6.7.

2.6.5.1.1 H400 cells

H400 cells were seeded at a density of 5×10^4 cells/mL into T25 flasks and incubated overnight to enable adherence, at which point cultures were treated with 5.4 µg/mL of AgNP-10 stock or AgNP-100. After 24 hours incubation cultures were washed three times with PBS to remove residual AgNP and cells centrifuged as described in section 2.1.2.1 prior to fixation.

TEM images of H400 cells were acquired as previously described in section 2.6.4.3.

2.6.5.1.2 Bacterial suspensions

Bacterial cultures in HBI broth were diluted as described in section 2.5.2.3 and treated with 4.5 µg/mL of AgNP-10 and 100 µg/mL of AgNP-100. Bacteria were incubated on a shaking incubator at 37 °C for 2-3 hours, after which time they were washed twice in PBS before fixation (described in section 2.6.5.1) and mounting on copper grids (described in section 2.6.4.3). TEM images of bacteria were acquired using a JEOL JEM-2100 microscope operating at 80 kV.

2.6.5.2 Energy dispersive spectroscopy

Energy dispersive spectroscopy (EDS) is a method for elemental analysis which uses X-rays to excite electrons bound to atoms to higher energy levels. Elements may be detected by

examining the emission spectrum for characteristic peaks caused by electrons decaying back down the unique energy levels in each element (example spectra are shown in Figure 6.16).

TEM images of bacteria control samples showed the stain had caused small round artefact regions in the image. Since these were not obviously distinguishable from nanoparticles upon visual inspection, EDS was used to test potential nanoparticle locations for the presence of silver. An INCA EDS system (Oxford Instruments, UK) was used to acquire EDS spectra for selected sub-regions inside TEM images acquired as described in section 2.6.5.1.2. EDS was performed with assistance from Theresa Morris at the Centre for Electron Microscopy, University of Birmingham, UK.

2.6.5.3 ICP-OES

ICP-OES as described in section 2.6.4.4 was used to quantify cellular uptake of nanoparticles. H400 cells were seeded into 3 wells of a 6-well plate at a density of 1.2 x 10^5 cells/mL, and an equal volume of cell-free media was added to the remaining 3 wells to act as controls to account for any silver adsorption to substrate. Cultures were incubated overnight and all wells were treated with 5.4 µg/mL AgNP-10 stock or 8.5 µg/mL (equivalent silver concentration) $AgNO_3$ for 3 hours, subsequently images of cell cultures were captured for cell count analysis (further details of the imaging process are presented in section 6.2.3.2). Media was subsequently removed and all plates were washed three times with PBS, ensuring thorough removal of PBS after the final wash step. 0.5 mL of sub-boiled nitric acid was added to each well and plates were incubated at room temperature for 1 hour. 0.4 mL of nitric acid digest was then diluted with RO water to a final concentration of 2% nitric acid

and added to a 15 mL falcon tube. Instrument calibration is described in section 2.6.4.4 and samples were stored at 4 °C until further processing as described in 2.6.4.4.

2.7 Computational and statistical analysis

2.7.1 Software

ImageJ version 1.48q was used for image processing and parameterisation [153]. Additional externally sourced and freely available plugins are referenced in the relevant sections. Matlab versions 13a and 15a including the Image Processing and Statistics and Machine Learning Toolboxes were used for data visualisation and further processing such as object classification for noise removal [169]. Statistical testing and associated graphs were generated using GraphPad Prism version 6 for Windows [170].

2.7.2 Statistical tests

In all cases, a p-value of less than 0.05 was used to indicate statistical significance. Varying degrees of significance were indicated through the use of asterisks as shown in Table 2.3.

Significance level	Indicator
p>0.05 (not significant)	n.s.
p<0.05	*
p<0.01	**
p<0.001	***
p<0.0001	****

Table 2.3 – Levels of significance are indicated in graphs by the different numbers of asterisks.

Student's t-test was used to identify differences between the means of two groups of data. One-way analysis of variance (ANOVA) was used to test for differences in the means of more than two groups of measurements. Additionally for experiments with a control for which ANOVA returned a statistically significant result, the Tukey test was used to identify

significant differences between mean values in all pairwise comparisons, or the Dunnett post-hoc method was used to test each group mean for significant difference to the control mean [171], [172].

2.7.3 Dose-response curve analysis

In samples treated with a range of stimulus concentrations, all values were normalised to the control and a sigmoidal dose-response curve was fitted of the form:

$$y = y_{min} + \frac{(y_{max} - y_{min})}{1 + 10\hat{}[(\log(IC_{50}) - x)h]} \qquad \textit{Equation 6}$$

where y is cell viability as a percentage of the control, y_{max} and y_{min} are the highest and lowest possible values respectively and x is the log of the treatment concentration [173]. Parameters of particular interest are: IC_{50}, the midpoint of the curve, which gives the concentration at which viability is reduced to 50%, and h, the hillslope of the curve, which indicates the rate of decrease in inhibition with increase in treatment concentration. Since data was normalised with background subtracted, y_{max} and y_{min} were constrained to 100 and 0, respectively. Nonlinear regression was used to optimise the parameters IC_{50} and h for each treatment.

2.7.4 Classification and dimensionality reduction techniques

2.7.4.1 Principal component analysis

The PCA method of dimensionality reduction wherein the feature space was re-expressed as linear combinations of features, or 'principal components' [174]. Principal components are ordered such that the first component, C1 contains the combination of variables that explain the greatest variance of the data, C2 has the second greatest, and so on until the last

principal components, which mainly describe statistical noise. This means the majority of information is contained within a smaller number of features, and the lower ranking components may be discarded to leave a smaller, more manageable dataset without losing a great amount of information. PCA assumes all variables are linearly related and variables are normally distributed, although violations of this assumption are tolerated in the case of large sample sizes (> 25 data points) such as the datasets used here. PCA is performed by eigendecomposition of the data covariance matrix to give eigenvectors (principal components) and corresponding eigenvalues. Elements of the eigenvector contain the contribution weight of each feature to the principal component, and eigenvalues indicate the proportion of variance explained by its corresponding eigenvector, and are used to rank the principal components. PCA was performed in ImageJ using the Morphological_PCA plugin [167], [175], [176] or using the Matlab eigenvalue decomposition function 'eig' [169].

2.7.4.2 K-means clustering

K-means clustering is an unsupervised learning technique that partitions the feature space into k regions, where k is the number of clusters of interest [177]. The feature space is first partitioned into k regions by randomly initialising data cluster centroids. The space is then re-partitioned by assigning all objects to the nearest cluster centroids according to some distance metric. The cluster centroids are re-calculated and the process is iterated until convergence. The algorithm implemented in all work described here employs a Euclidean distance metric, i.e. the sum of squares. To remove effects caused by differences in scale, features are standardised by re-centering the population mean feature values to 0 and normalising the standard deviations to 1. K-means was performed in ImageJ using the Morphological_Clustering macro [167], [178] or the Matlab 'kmeans' function [169].

2.7.4.3 Discriminant analysis

Linear discriminant analysis (LDA) is a supervised machine learning method which uses the training data to fit the parameters of a Gaussian distribution for each class [179]. This method assumes the data have a Gaussian mixture distribution, i.e. that all features are normally distributed within their classes and all features have the same variance. Predictions may be made from the fits by training a classifier to choose the class with the smallest misclassification cost.

Regularization is the process of finding a subset of features that can achieve a higher classification results. The two options examined here (both from the Matlab Statistics and Machine Learning Toolbox [169]) are “Diagonal covariance”, which uses all predictors and “Auto”, which automatically selects the optimal subset of features.

2.7.4.4 Support vector machines

Support vector machines (SVM) use data from a training set to define a plane in the feature space which optimally separates objects in each class [179]. A schematic example is shown in Figure 2.8 using a two dimensional feature space. The eponymous support vectors are those objects in the training set which lie closest to the boundary between two classes (outlined in black in Figure 2.8). In the case of linearly separable classes, SVM defines the hyperplane as that which separates these support vectors with the largest margin. However, since classes are not generally separable in the feature space considered in work described here, a “soft-margin” is used. In this case there is a trade-off between objects which may be found on the incorrect side of the hyperplane.

SVM classification was implemented with Matlab using the Statistics and Machine Learning Toolbox [169]. A linear hyperplane was used to avoid over-fitting.

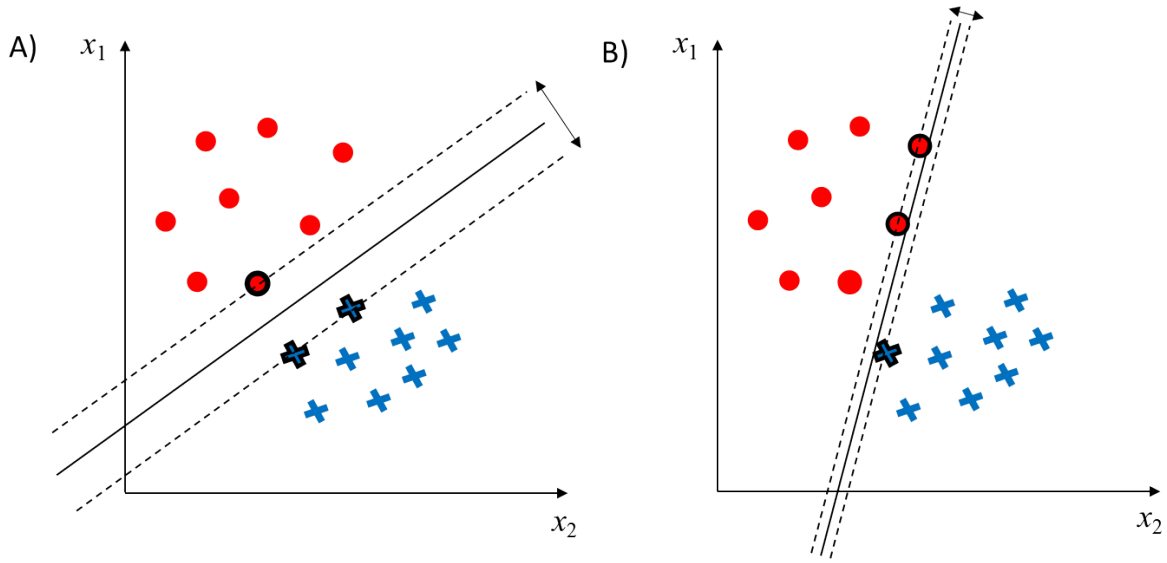

Figure 2.8 – Schematic diagram demonstrating the separation of object classes with support vector machines. *Two classes of objects (red circles and blue crosses) are separated in a 2-dimensional feature space by a linear plane (solid black line). The support vectors are outlined in black and support vector machine classification selects these such that the groups are separated with the largest possible margin (indicated by dashed lines). Graphs A) and B) show two possible partitions of the feature space but A) is favoured since the margin between two groups is larger.*

2.7.4.5 Decision trees

This method uses recursive partitioning to separate objects into classes [180]. At each node in the tree, the "impurity" of the object set is calculated – this value is 0 when all objects are of the same class and maximum when classes are evenly represented. The impurity is also calculated for each feature, and each possible threshold of this feature to find that which yields the greatest impurity gain at that node. The objects are then split according to this feature threshold and passed to new nodes to be split again, or reach an endpoint when the node is sufficiently pure (Figure 2.9).

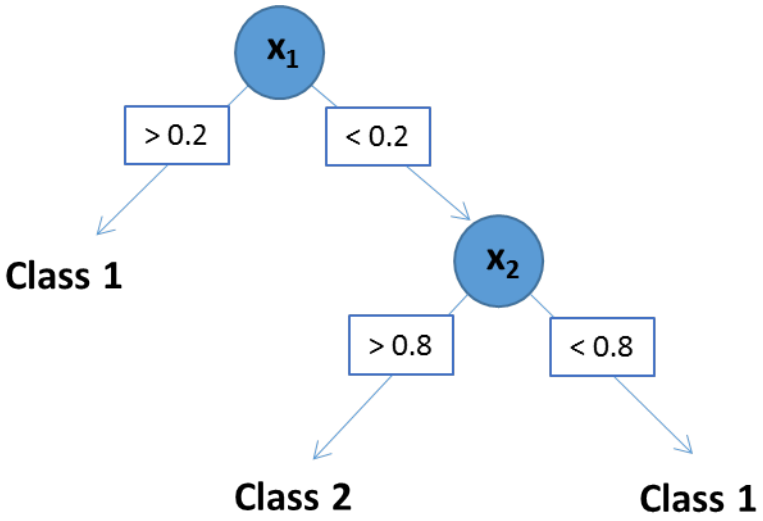

Figure 2.9 – Example diagram of a decision tree. *The data is split at each node (represented by a blue circle) by testing all thresholds on all variables to find that which gives the greatest impurity gain. The data may then be passed to a new node for further splitting (for example, if $x_1 < 0.2$ at the first node) or classified ($x_1 > 0.2$ at the first node).*

Decision Tree classification was implemented with Matlab using the Statistics and Machine Learning Toolbox [169]. The maximum number of splits (nodes) was limited to 4 and Gini's diversity index was used as the impurity measure [181].

2.7.5 Validation of Classification

2.7.5.1 Classification metrics

The success of classification of objects into a class, X was measured through a number of metrics calculated using four possible classification outcomes [182]. These are as follows:

- true positive (TP) – the classifier correctly identifies an object as X
- true negative (TN) – the classifier correctly identifies an object as not X
- false positive (FP) – the classifier incorrectly identifies an object as X
- false negative (FN) – the classifier incorrectly identifies an object as not X

Classification precision (p) indicates the fraction of objects correctly classified as X out of the total number of objects classified as such, and was calculated as follows:

$$p = \frac{TP}{TP + FP}$$

Classification recall (r), or sensitivity, indicates the fraction of objects correctly classified as X out of all true X objects, and was calculated as follows:

$$r = \frac{TP}{TP + FN}$$

r and p were expressed as percentages.

The F_1 score is the weighted average of precision and recall and serves as a convenient single measure of classification success that takes both parameters into account. An F_1 score of 0 indicates no agreement between classification labels and true values, and 1 indicates complete agreement. F_1 was calculated as follows:

$$F_1 = 2\left(\frac{pr}{p + r}\right)$$

2.7.5.2 Cross-validation

In the case of classification using supervised learning techniques, a five-fold cross validation was employed to evaluate classification success using the training data. Firstly, the labelled training set was randomly partitioned into 5 equal subsets, or 'folds'. The classification model is subsequently trained on 4 of the folds and the remaining fold used to validate classification [179]. This approach was repeated so that each of the folds was used for validation and the results were averaged to give the final estimations for classification success.

3 DEVELOPMENT OF AN IMAGE ANALYSIS METHOD FOR CELL DETECTION IN PHASE CONTRAST IMAGES

3.1 Introduction

This chapter details the development of a segmentation-based method for counting cells from phase contrast images of oral epithelial cell cultures. As discussed in the introduction (section 1.6.2.3), phase contrast microscopy images provide the potential for a non-invasive method of counting cells in live cultures if appropriate image analysis methods can be developed to achieve this. The use of image defocusing bright field microscopy has previously been used to count cells without the use of stains and it was proposed that a similar approach could be applied in phase contrast microscopy [43]. The effects of defocusing on PC microscope images were investigated in order to examine the properties of defocused PC images and the results were subsequently utilised in the conception and development of a novel image analysis-based cell counting approach. The various stages of development are described in this chapter, starting with the initial development of the image analysis algorithm, moving to the testing of parameter selection methods and concluding with refinement through evaluation of a number of noise removal techniques. This chapter concludes with the final method to be used for all further analyses undertaken.

3.2 Defocusing in phase contrast microscopy

To investigate the effects of defocusing in PC microscopy, a series of images of a monolayer of H400 cells were acquired using the set up described in section 2.1.2. The first image was in focus, i.e. the focal plane, h, was level with the object plane ($h = 0$). The focal plane was subsequently moved in 10 µm steps as measured by the graticule on the fine focus dial to 100 µm above and below the object plane, and an image captured at each increment.

Pixels were manually selected in the cell cytoplasm and at the cell boundary and the greyscale intensity recorded. The greyscale intensity of ten pixels at both cytoplasm and boundary were averaged to account for intensity variations due to noise and the presence of subcellular features. Figure 3.1 demonstrates the average intensity variation at two points inside a cell and at a cell boundary as the focal plane was moved. Contrary to the dark and bright images observed in bright field defocusing microscopy when the focal plane was moved above and below the object plane respectively, the pixel intensity at the cell boundary demonstrated a sharp peak at the object plane due to the halo effect, however when the image was defocused slightly, this became darker in both directions of defocus. Conversely, the pixel intensity inside the cell increased as the focal plane was moved away from the object plane, due to divergence of the halo light at the cell edges into this region.

Figure 3.1 A and B show how this change in contrast affected the image properties. The image in focus exhibited the characteristic bright cell edges from the halo artefact and darker cell interiors, whereas the defocused image appeared darker at the cell boundaries compared with the cell centres.

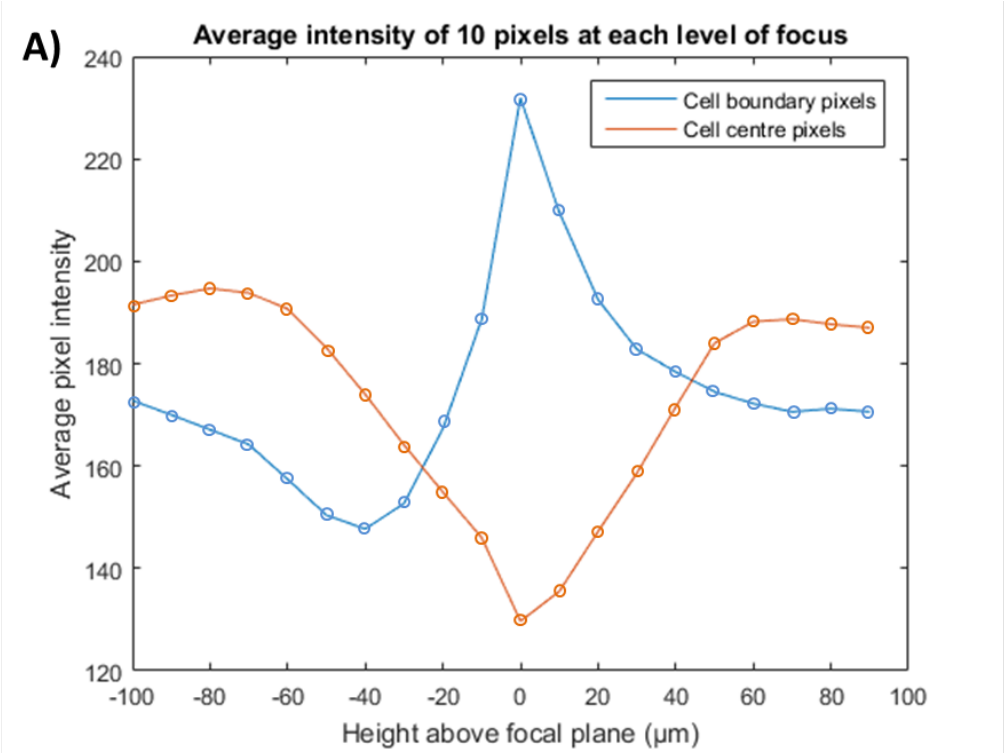

Figure 3.1 – Demonstration of the changes in PC image contrast after defocusing. *A) Graph plotting the average pixel intensity as the imaging plane was varied at 10 cell boundary pixels (blue line) and central cell pixels (red line). Examples of such pixels are highlighted by the correspondingly coloured arrow in B) the focused image and C) an image acquired at 40 µm below the focal plane. Scale bar for both images is shown in B). Note that the cell boundary becomes relatively darker when defocused, whilst the cell centre becomes relatively brighter.*

As discussed in the introduction, Dehlinger *et al.* (2013) used the direction dependent contrast changes upon defocusing brightfield microscopy images to locate cells through subtraction of a pair of images acquired above and below the object plane to create an image in which cells could be segmented using a threshold-based technique [43]. Since the

contrast change in PC microscopy showed the same trend in both defocusing directions, the greatest intensity difference was achieved by subtracting a defocused image from the in-focus image. The inner cell intensity exhibited a maximum at 80 µm below the focal plane, thus the image at this point had the greatest intensity difference from the in-focus image. Figure 3.2B shows this image subtracted from the in-focus image (Figure 3.2A) and thresholded using the Otsu method [70]. Each segmented region corresponded with a single cell, with the exception of a relatively few noise regions. Figure 3.2C shows the segmentation when an image defocused to 40 µm was used in this process – in this image there are fewer noise regions compared with the image defocused to 80 µm, although cell segmentations are merged.

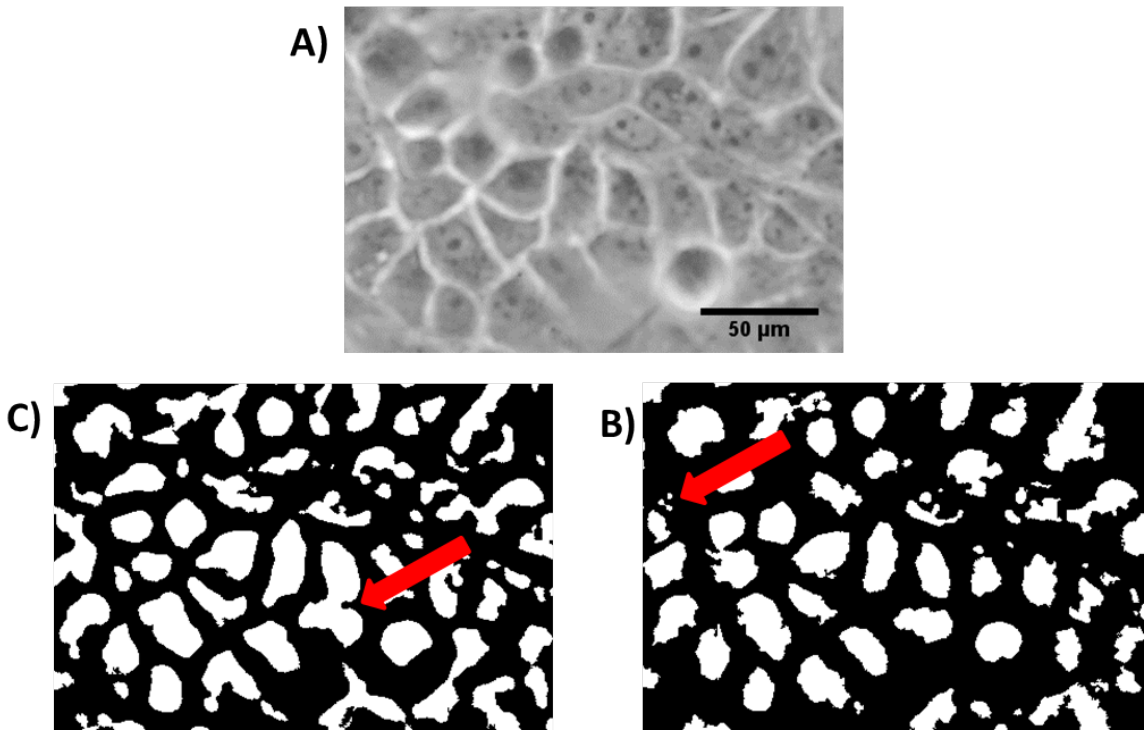

Figure 3.2 – Examples of cell segmentation using PC images defocused to different levels. *A) In-focus greyscale image of H400 cells acquired using PC microscopy. B) Mask acquired when image defocused to 80 µm below the focal plane was subtracted from original image. Arrow highlights some small regions. C) – as B but using image defocused to 40 µm. Arrow highlights merged cells. The scale bar for all images is shown in A.*

These examples show there is potential for the application of defocusing techniques in PC microscopy for the development of a method to locate cells for counting. However, it would be necessary to carefully select the defocusing level to achieve accurate cell counts, and the microscope stage height would have to be carefully manipulated to achieve the correct defocus each time an image pair is acquired. Without the use of an automated microscope stage, this would be an inaccurate and prohibitively time-consuming approach.

3.3 Use of morphological operators to mimic defocusing contrast

Rather than obtaining the contrast changes described in section 3.2 by precise and laborious manual manipulation of the focal plane, morphological mean filters were investigated to determine whether the same effects could be achieved from a single image in post-processing. Mean filters replace each pixel's intensity with the mean value in a neighbourhood region, or "kernel" centred on the pixel [183]. The mean filter was considered in particular due to the equal contribution of each pixel across the filter kernel to the final intensity value. In principle this should mean that when considering a pixel inside a cell, the resulting intensity will be lower if the filter kernel is small enough to be entirely contained within the cell cytoplasm than if it is large enough to include the high intensity halo pixels in the calculation of the mean. It was postulated that through careful selection of kernel size, mean filters have the potential to mimic the contrast changes observed in defocusing microscopy. Unless otherwise stated, the morphological mean filter used in the work presented here had a circular kernel of radius r.

3.3.1 Proof of concept

A set of images were acquired by applying mean filters with kernel radii, $2 < r < 47$, to the in-focus image in the dataset discussed in section 3.2. Ten pixels were manually selected to represent cell cytoplasm intensity. Average pixel intensity changes were examined as a function of object plane height as the images were defocused (Figure 3.3A), and compared with the pixel intensity changes in filtered images as a function of kernel radius (Figure 3.3B). The same trend in average pixel intensity was observed in both cases. The intensity increased to a maximum, although the change in pixel intensity was not as large in the case of the mean filtered image: the intensity at the maxima was only increased to 134% of the original value, compared with 150% in the defocused image.

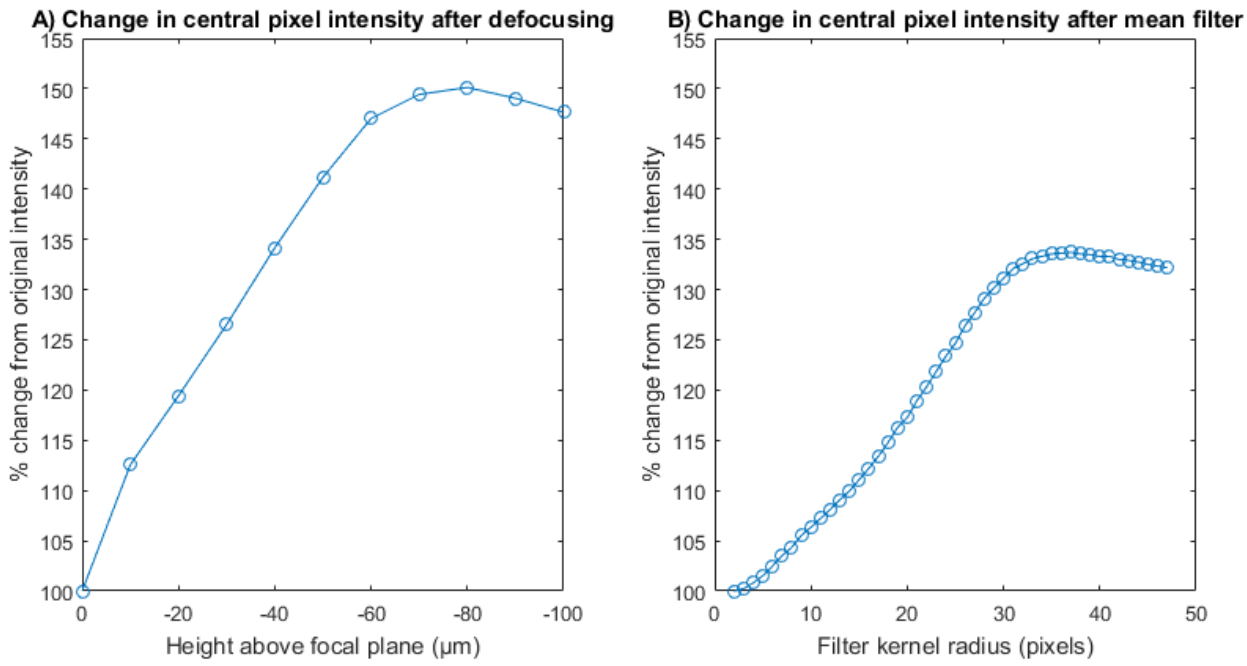

Figure 3.3 – Comparison of pixel intensity changes after defocusing and application of a mean filter. *Graphs showing the average change in intensity of 10 pixels located in the central cytoplasm of a cell after A) defocusing by moving the focal plane below the image plane and B) mean filtering with a range of kernel radii. Note how both increase to a maximum.*

This approach translated to an image with cell centres slightly higher in intensity than surrounding areas (Figure 3.4). This was similar to the defocused images, although due to the smoothing effect of the filter and the lower overall intensity change, the spatial resolution was much reduced.

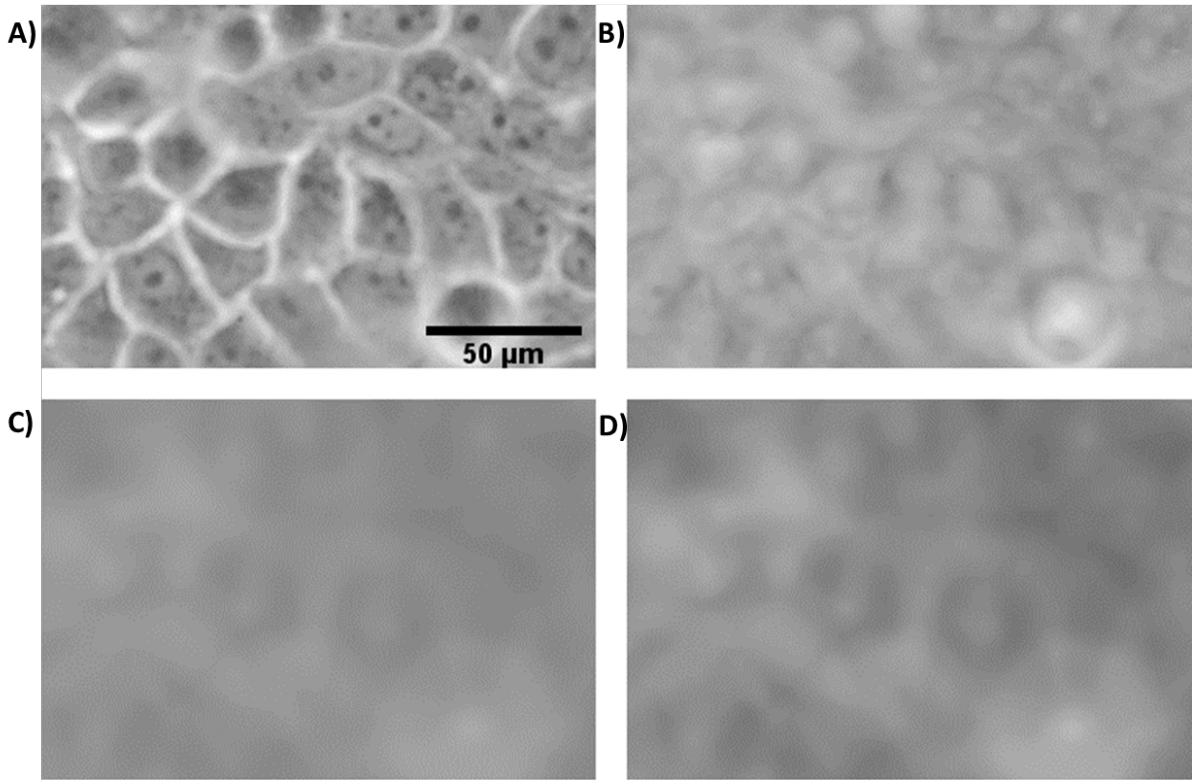

Figure 3.4 – Comparison of contrast changes in PC images after defocusing and mean filtering. *A) In-focus PC image of H400 cells. B) Image A defocused below the focal plane. In this image cells become blurred and intensity inside cells is increased compared with cell edges. C) Image A mean filtered with kernel radius,* $\boldsymbol{r = 34}$ *pixels, the radius at which the maxima is observed in the intensity change graph (Figure 3.3B) Similarly to the defocused image, intensity is higher inside cell regions, although cell resolution is lower. Image D) provides a contrast-enhanced version of C for clarity. The scalebar for all images is shown in A.*

Since mean filters were shown to achieve similar image properties to defocused images, it was proposed that cells may be roughly segmented for counting through subtraction of two PC images each with a mean filter applied with radii such that r_{small} smoothed fine detail inside cells but with minimal increase in intensity and r_{large} caused the intensity inside cells

to increase to its brightest point, to achieve an image to which a threshold-based segmentation approach may be applied.

The proposed algorithm is shown in the workflow in Figure 3.5. The Otsu threshold method was chosen as it did not require selection of extra parameters. Since some shape metrics required for downstream processing (section 3.3.3) could not be calculated for objects with low numbers of pixels, a minimum area condition was implemented to remove such objects. This value was chosen empirically to be 8 pixels. The number of segmented regions was taken as the number of cells.

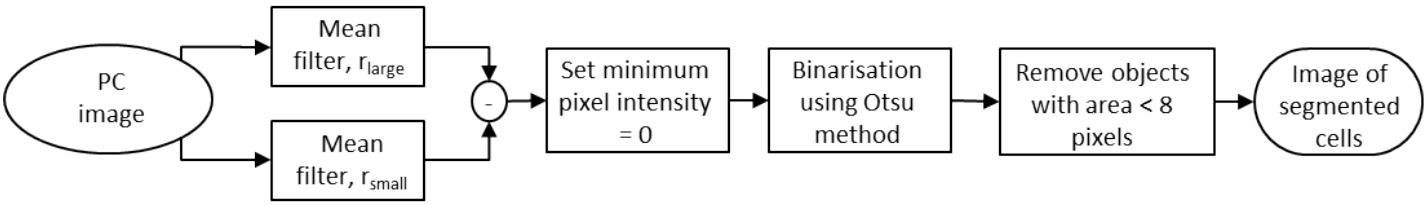

Figure 3.5 - Workflow for segmentation of cells in PC microscope image. *The cell number is determined by the number of binary objects in the final segmented image.*

3.3.2 Parameterisation

The aim of this work package was to develop a method for accurately counting cells from phase contrast images by segmentation through the use of mean filters as described in the previous section. Since the number of binary objects detected in the segmented image gave the image cell count, in the ideal case there would be a single segmentation per cell. However, a number of potential mis-segmentation events could occur, which lead to incorrect counts. These are as follows:

- "miss" – occurs when a cell is not segmented and thus is unaccounted for in the cell count (Figure 3.6A)

- “noise” – occurs when a region is segmented that does not correspond with a cell, for example due to image noise or edge effects caused by filters at low cell densities, causing an overestimation of the cell count (Figure 3.6B)
- “merge” – occurs when two or more individual cells are segmented as a single region, causing an underestimation of the cell count (Figure 3.6C)
- “split” – occurs when a single cell is segmented into multiple regions or when a noise region additionally overlaps with the nucleus causing an overestimation of the cell count (Figure 3.6D)

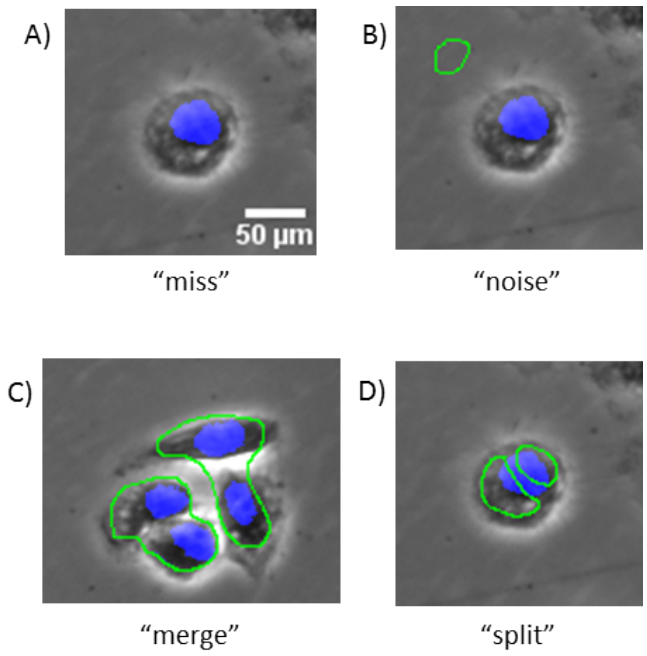

Figure 3.6 – Examples of potential errors in cell detection using the mean filter approach. *Manual example cell segmentations are shown in green and nuclei stained with DAPI and thresholded as described in section 3.3.2.2 are shown in blue. A) “Miss” – cell is undetected. B) A “noise” region, arising from image noise or spurious regions of high pixel intensities caused by filters at the edges of low density cells. C) “Merge” - multiple cells are detected as one. D) “Split” – a single cell is split into multiple segmentations. Scale bar for all images is shown in A).*

To optimise the number of correct cell detections, a robust parameterisation method for selecting r_{small} and r_{large} was required since the values of these filter radii affected the rate of occurrence of mis-segmentation events. For example, merge and split events occurred if r_{small} smooths the image too much or too little, and miss events occurred if r_{large} was not optimised to give the brightest region inside cells.

Therefore, an exhaustive search was used to find optimum parameters, which involved applying a range of r_{small} and r_{large} combinations to example PC images and comparing the cell counts achieved to a ground truth value. Sections 33.3.2.1 and 3.3.2.2 describe the methods investigated for defining the ground truth. Cultures of H400 cells were used for all developmental testing of the image analysis cell counting approach.

3.3.2.1 Manual cell count as ground truth

For this method the total number of cells in an image was used as the ground truth with which to compare the number of regions segmented by parameter pairs. Ten images of H400 cells cultured in 35 mm dishes representing a range of levels of confluency were acquired using the PC microscope described in section 2.4.2 and images captured with the Nikon D40 camera. Cells were counted by manual selection by an experienced microscopist using the 'ginput' function in Matlab and the number of 'clicks' was taken to be the total number of cells. For each image, the number of regions segmented for each combination of parameters was compared with the manual count.

A graph was generated indicating the number of images which gave a segmented cell count within 10% of the manual count, for each parameter combination (Figure 3.7). A value of 10% was chosen since this was the lowest margin of error which could be simultaneously

achieved in all images using the same set of parameters. The centre of the region indicated by the solid black rectangle was selected as the most suitable parameters since the cell count was within 10% in all images tested and the accuracy was more robust for small changes in parameter values, compared with the region indicated by the dotted rectangle. The parameters selected were $r_{small} = 14$ pixels (5 µm) and $r_{large} = 80$ pixels (31 µm).

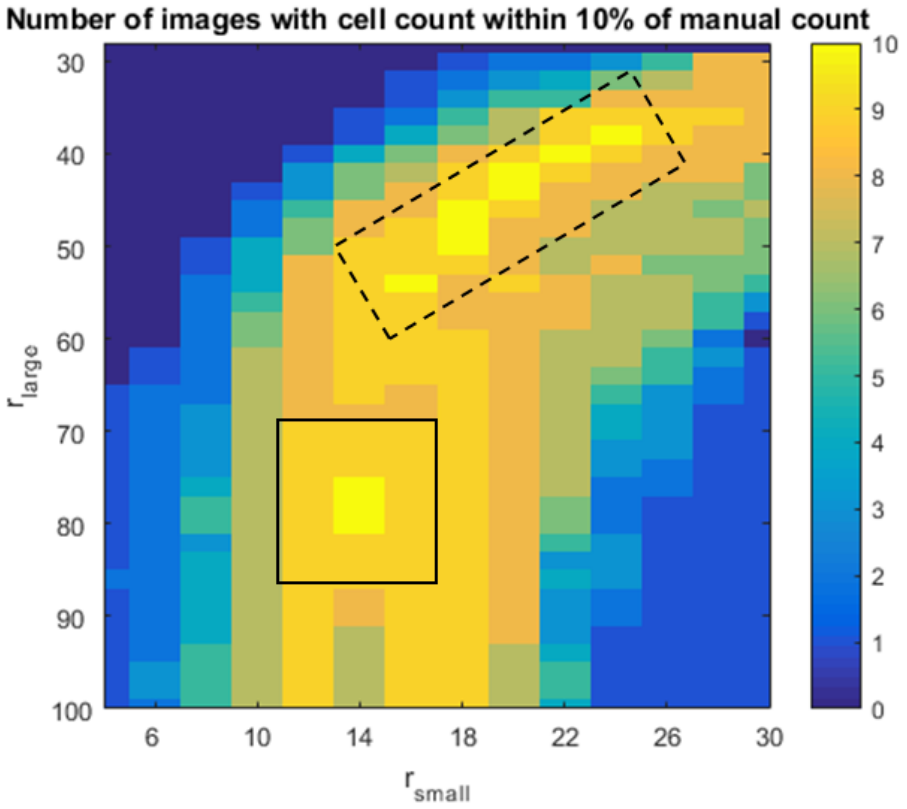

Figure 3.7 – Parameterisation graph generated using manual cell count as ground truth. *The colour map indicates the number of ground truth images (10 in total) for which the segmented count was within 10% of the manual count. The solid black box indicates the region from which final parameters were selected due to robustness to small changes in parameter values, compared with other high scoring regions, indicated by the dotted box.*

3.3.2.2 Stained cell nuclei as ground truth

A disadvantage of using total cell number as the ground truth was that this did not provide any spatial information, thus there was no guarantee that the regions segmented by a given set of parameters corresponded with the true locations of cells in images. Thresholded

images of stained cell nuclei acquired alongside PC images were identified as a candidate for use as a ground truth which incorporated information about cell location in PC images. In order to utilise this spatial information, correct cell detections were defined by their spatial relationship with nuclei using the RCC5D implementation of discrete mereotopology, shown schematically in Figure 3.8.

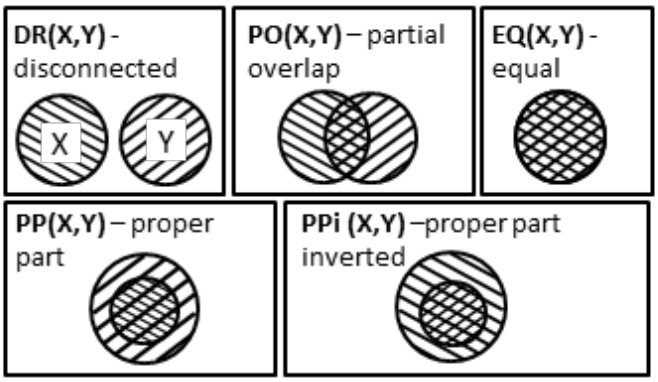

Figure 3.8 – The RCCD5 relationship set. *Five possible parthood relations between binary objects X and Y are defined by the RCCD5 set. The abbreviations may be read as follows: DR(X,Y) – "X is disconnected from Y", PO(X,Y) – "X partially overlaps with Y", PP(X,Y) – "X is a proper part of Y", PPi(X,Y) – "X is a proper part inverted of Y", EQ(X,Y) – "X is equal to Y".*

Epithelial cells generally have a single nucleus, N, entirely contained within the cell cytoplasm, C, in this case represented by the segmented region (Figure 3.9). In the ideal case, the segmented region corresponds with the cell cytoplasm, thus the following conditions were used:

i. A nucleus relation to the segmented cell region should be either proper part PP(N,C), partially overlap PO(N,C), or equal EQ(N,C) the segmented cell region. PP(N,C) is the expected case, but the restriction was relaxed to include PO(N,C) and EQ(N,C) relations to account for cases when the cell was a slightly under-segmented region but still detected.

ii. There should be an exclusive one-to-one relationship between segmented cell regions and nuclei (i.e. our definition does not include the less common case of multi-nucleated cells).

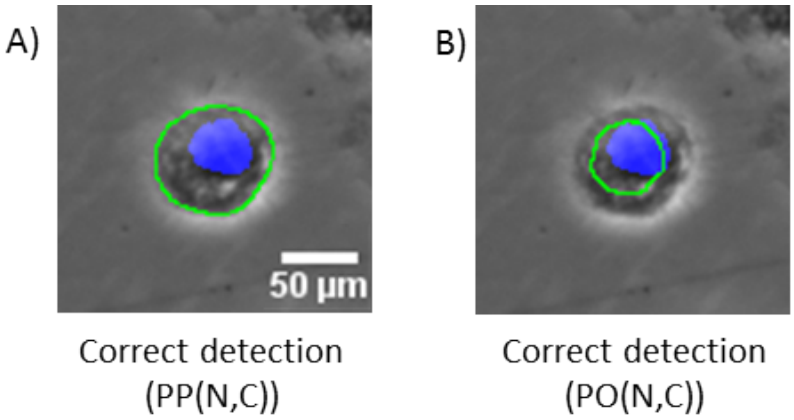

Figure 3.9 – Examples of acceptable cell detections. *PC images of H400 cells with manual example cell segmentations shown in green and nuclei stained with DAPI and thresholded as described in section 3.3.2.2 shown in blue. Image A) indicates the expected case for a correct detection – the nucleus is a proper part of the cell segmentation (green outline). B) Due to cell undersegmentation the condition is relaxed to include a partial overlap relation. Scale bar for both images is shown in A).*

A ground truth data set was acquired by staining live H400 cells in at a range of confluencies in 35 mm dishes with Hoechst dye as described in section 2.2.2 and acquiring concurrent images with PC and epifluorescence microscopy. (The benefits and disadvantages of various types of fluorescent stains and fixatives are discussed in chapter 4.) Images were acquired using the set up described in 2.4.2 with a QImaging Retiga-2000R camera.

Epifluorescence images of cell nuclei for the ground truth were segmented before use in parameter selection. This was done by first smoothing to reduce noise using the ImageJ 'Smooth' function (a mean filter with a 3x3 kernel, the smallest filter) and enhancing image contrast by normalising the intensity histogram to the full range of 8-bit image values. Due to uneven background illumination, a range of local threshold techniques and parameters

were evaluated using the ImageJ “Auto Local Threshold” function. Ultimately the mean local threshold method was selected and applied with a kernel radius of 20 pixels. A watershed function was applied to separate densely packed nuclei and the resultant binary objects were eroded twice to remove small protrusions and ensure nuclear regions were not over-segmented. Since correct nuclear segmentations were of utmost importance for correct parameter selection, images were inspected visually for incorrect segmentations and manually corrected if necessary using the ImageJ paint tool. Figure 3.10 indicates the result of each step of the segmentation process.

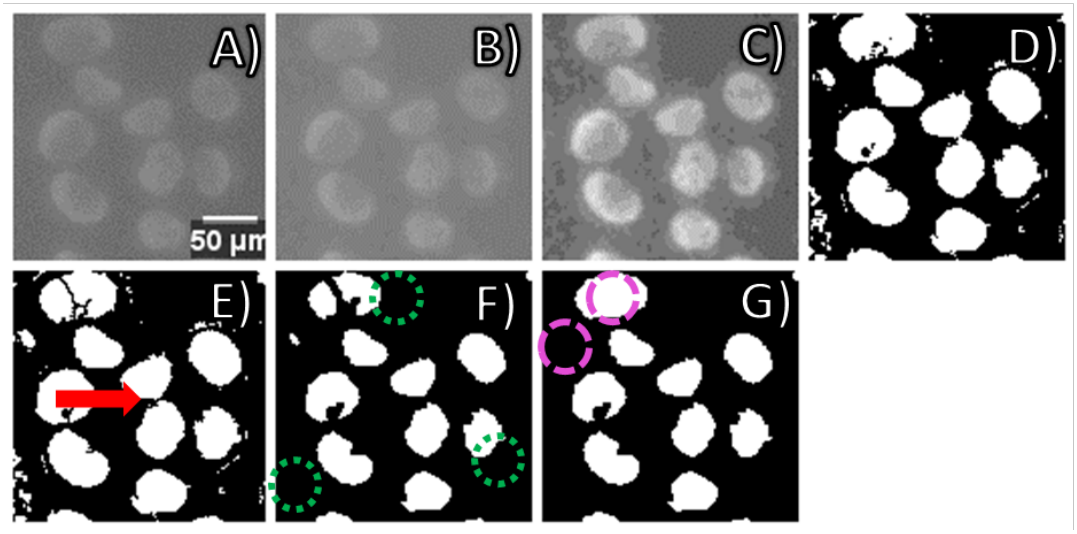

Figure 3.10 – the stages of the segmentation method for fluorescently stained cell nuclei. *A) The original epifluorescence image. B) Image smoothed using 3x3 Gaussian filter. C) Contrast enhanced using a normalised intensity histogram. D) Mean local threshold applied with a kernel radius of 20 pixels to binarise image. E) Watershed function applied to separate connected nuclei (example indicated by red arrow). F) Erosion to remove small regions and protrusions, e.g. those indicated by green dotted circles. G) Manual correction of incorrect segmentations (such as those indicated by pink dashed circle) to ensure highest possible accuracy.*

Subsequently an exhaustive search was performed using a range of r_{small} and r_{large} to segment the PC images corresponding to the epifluorescence image of cell nuclei, and the number of correct detections (as defined by comparison of segmentations in the PC image to

the corresponding cell nuclei image) achieved in the segmentation by each parameter pair was calculated and represented in a contour map in Figure 3.11. In total there were 1354 cells across 4 images in the ground truth dataset. The parameter pair with the highest percentage of correct detections (87.1%) was $r_{small} = 7$ pixels (6 µm) and $r_{large} = 22$ pixels (20 µm). The workflow for parameter selection using the nuclear ground truth method is shown in Figure 3.12.

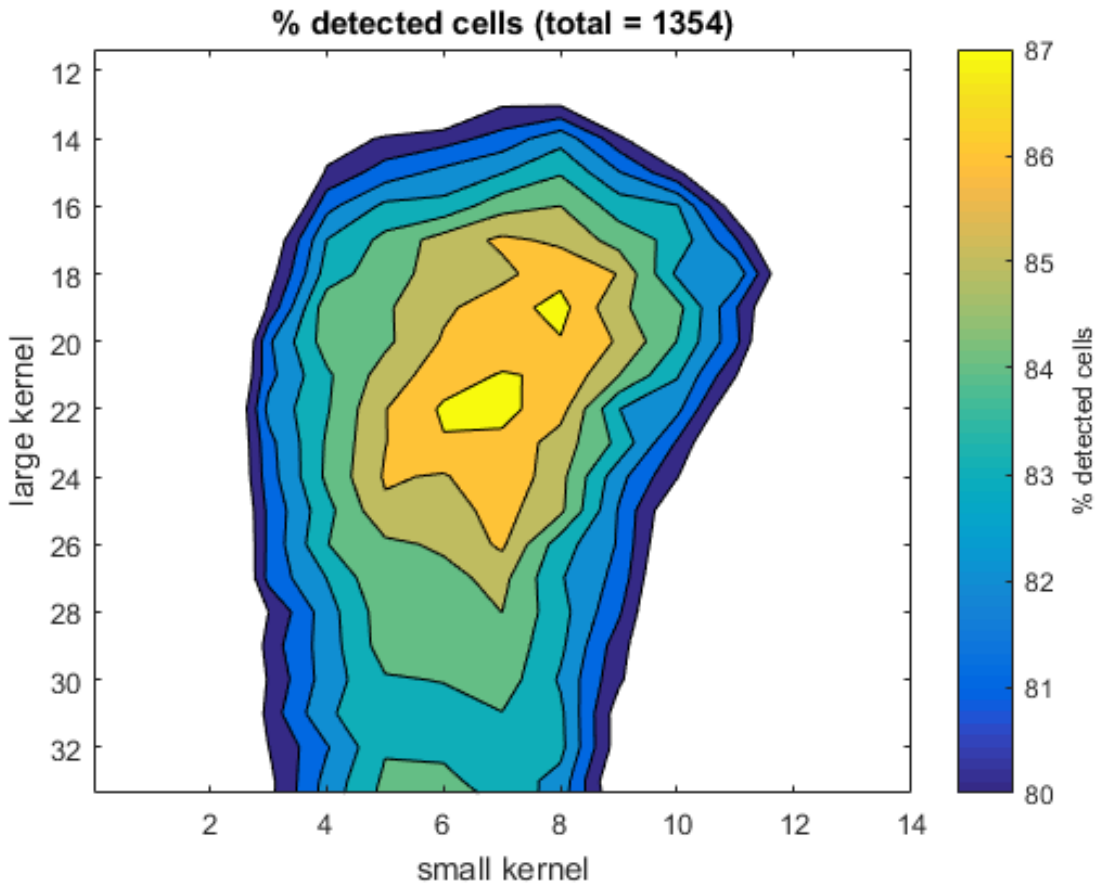

Figure 3.11 – Contour map showing the percentage of 1354 H400 cells correctly detected in 4 phase contrast images (as defined through comparison with the corresponding nuclei ground truth image as described in Figure 3.9), for a range of parameter combinations.

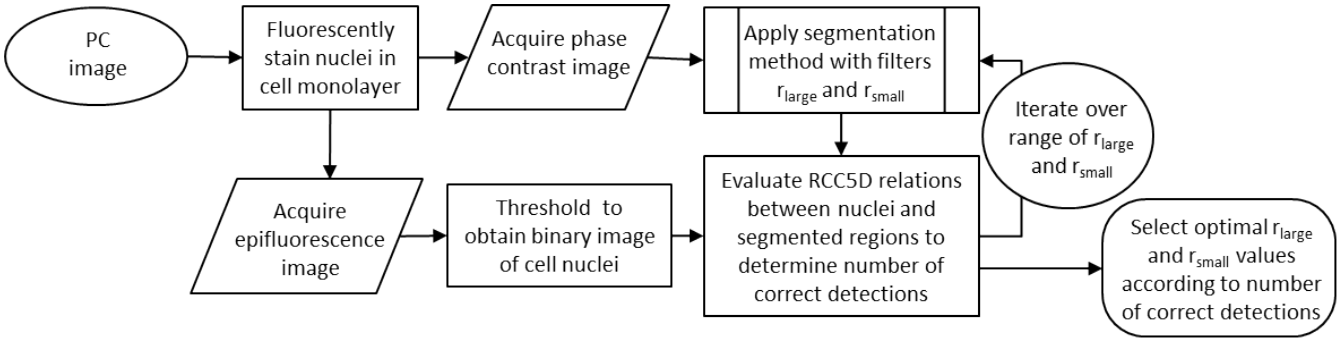

Figure 3.12 – Workflow for selection of parameters using fluorescently stained nuclei as ground truth. *The segmentation method workflow is given in Figure 3.5.*

3.3.2.2.1 Further investigation of mis-segmentation events

An advantage of using segmented nuclei for parameterisation ground truth is that specific mis-segmentation events may also be defined in terms of how the correct cell detection conditions are broken, and thus they may be quantified. For example, “miss” events are defined as nuclei DC with all segmentations (Figure 3.6A) and vice versa, “noise” events are defined as segmentations DC with all nuclei (Figure 3.6B). Split events are defined as multiple segmentations PO with a single nucleus (Figure 3.6C). Similarly, merge events are defined as segmented regions with more than one associated PO or PP nucleus (Figure 3.6D).

Figure 3.13A provides information in a pie chart indicating how each of the cells used in the ground truth dataset were labelled using the final selected parameters. The majority of incorrectly detected cells were due to splitting, merging and missing segmentations, and a very small fraction were identified as PPi(Nucleus, Cell). Whilst PPi events are erroneous segmentations that should not be included in the definition of cell detection for parameterisation, they do not cause errors in the cell count since they meet the exclusive one-to-one relationship condition between nucleus and segmentation. Furthermore, they

accounted for only 0.44% of cell segmentations. Consequently, these were not considered further as a candidate for noise removal.

The percentage error for each mis-segmentation type, including noise is shown in Figure 3.13B. It is clear that noise segmentations had the largest effect, increasing the cell count by 24%.

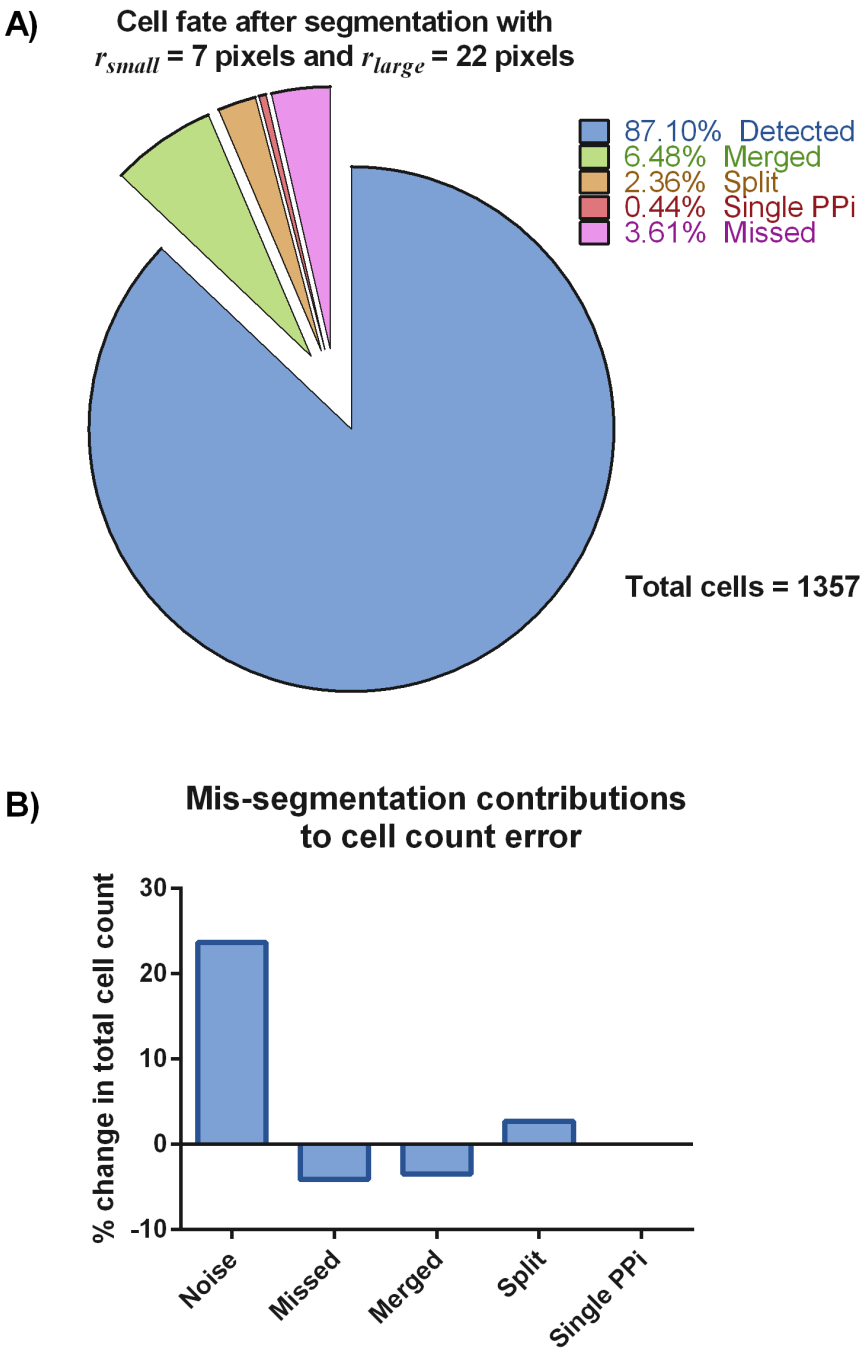

Figure 3.13 –Cell fates and mis-segmentation rates for H400 cells segmented using r_{small} = 7 pixels and r_{large} = 22 pixels. *A) Pie chart showing how each cell in the parameter training set is labelled using the final parameters of r_{small} = 7 pixels and r_{large} = 22 pixels. B) Bar chart showing the types of error leading to count error and their contribution to the change to the true count. Noise segmentations are the biggest contributor to errors in the cell count.*

3.3.2.3 Discussion of parameterisation methods

Using only a cell count as the ground truth is inadequate for use in the selection of image analysis parameters in a number of ways. Firstly, manually determining cell number from a PC image is a laborious and error-prone process, particularly for images of confluent monolayers where cell numbers can be in the thousands.

Furthermore, considering the total number of segmented regions as the sole measure of cell detection success does not guarantee that the regions have any spatial correspondence with the true cells. This can be shown by comparing the selected parameters using each technique applied. Since different cameras were used to acquire each set of data, optimal parameters selected by each technique were converted to µm for direct comparison. The value of r_{small} for both techniques was consistent at 6 µm. However, using the manual ground truth method a value of 31 µm was selected for r_{large} compared with 20 µm using the nuclear ground truth. The reason for this difference is elucidated using a labelled dataset generated by the nuclear ground truth method to compare the number of noise objects segmented by both parameter combinations. For r_{large} = 22 µm noise objects contributed 22% to the total segmented regions, putting this figure well outside the 10% accuracy limit applied in the manual count method. For r_{large} = 31 µm, noise regions contributed only 13%, however the percentage of correctly detected cells using these parameters was only 83.6% compared with 87.1% using r_{large} = 22 µm. The inclusion of noise regions in the cell count offset the reduction in count due to missed and merged cells. Since contributions to the final count from noise regions were substantial after parameterisations using both methods, additional techniques to remove this were required in both cases, thus the nuclear ground truth was preferred due to its increased detection rates.

Aside from increased cell detection rates, incorporating structural and spatial information using nuclear ground truth offers many other advantages. Firstly, it removes subjectivity from the number or location of cells in the ground truth, and cuts the manual processing time since no user-defined count is required in accordance with the aims set out in the introduction. Secondly, although it is not possible to achieve 100% correct detection rates, complexities such as merged and split cells may be quantified, and these values used to estimate error on the final count. Thirdly, the use of the ground truths and DM conditions on the segmentations with the optimal parameters provides an automatically labelled sample for training and validating classifiers for noise removal, as will be investigated in section 3.3.3.2.

Whichever parameterisation method is used, optimal r_{large} and r_{small} size values will vary according to a number of factors, including camera resolution, cell type and magnification, so re-parameterisation must be performed if any are changed. The applicability to other cell lines is investigated in chapter 4.

Epifluorescence images of cell nuclei for use in parameterisation were segmented empirically and segmentation accuracy was subsequently verified manually to ensure correctness. Whilst this would not be an efficient method for large image sets with vast numbers of cells, the method was employed on the relatively small dataset used for parameterisation proof of concept due to the crucial requirement of accuracy to ensure selection of the optimal possible parameters for the automated method. In future more efficient methods such as signal envelope estimation for background subtraction [81] could be validated for use on the ground truth set of fluorescent nuclear images.

3.3.3 Noise removal methods

Figure 3.13B shows that incorrect noise segmentations were the largest contributor to errors in the final cell count for the H400 training set. In order to improve the cell count, noise must be removed from images segmented using the final r_{large} and r_{small} values. To accomplish this, a number of classification techniques were investigated for labelling each segmented region as a correct detection or otherwise. In general, classification is based on the presumption that objects belonging to different classes may be distinguished by differences in the measurements of some or all features i.e. classes will populate different regions in the feature space. In this case the features were morphological properties of the binary segmentations and/or greyscale properties in the corresponding regions of the original PC image. For this purpose the Particles8 plugin for ImageJ was applied to segmented images [167]. This plugin considers individual regions in a binary image and for each calculates 25 morphological features and 11 greyscale features as listed in Table 3.1.

The aim of all noise removal methods investigated here was to maximise the detection of noise regions for removal whilst minimising the misclassification of correct cell detections. A number of noise removal methods using some or all of the features listed in Table 3.1 were investigated and are described in this section.

	Feature	Description
Morphological properties	Perimeter (P)	Length of region boundary
	Area (A)	Area inside perimeter
	Feret diameter (F)	Length of the longest region
	Breadth (B)	Length of the widest region perpendicular to Feret axis
	Convex hull (C_{hull})	Perimeter of the smallest convex polygon enclosing the object
	Convex hull area (C_{area})	Area of the convex hull
	Minimum radius (R_{min})	Radius of the inscribed circle centred at the centre of mass
	Maximum radius (R_{max})	Radius of the enclosing circle centred at the centre of mass
	Minimal bounding circle radius	Radius of smallest circle enclosing the object
	Aspect ratio	F/B
	Circularity	$4\pi A/P^2$
	Roundness	$4A/\pi F^2$
	Area equivalent diameter	$\sqrt{4A/\pi}$
	Perimeter equivalent diameter	P/π
	Equivalent ellipse area	$\pi FB/4$
	Compactness	$\left(\sqrt{4A/\pi}\right)/F$
	Solidity	A/C_{hull}
	Concavity	$C_{area} - A$
	Convexity	C_{hull}/P
	Shape	P^2/A
	R factor	$C_{hull}/\pi F$
	Modification ratio	$2R_{min}/F$
	Sphericity	R_{min}/R_{max}
	Area of bounding box	FB

	(A_{box})	
	Rectangularity	A/A_{box}
Greyscale properties of corresponding PC image	Greyscale integrated density	
	Minimum greyscale value	
	Maximum greyscale value	
	Modal greyscale value	
	Median greyscale value	
	Average greyscale value	
	Greyscale average deviation	
	Greyscale standard deviation	
	Greyscale histogram skewness	
	Greyscale histogram kurtosis	
	Greyscale entropy	

Table 3.1 – Features calculated for segmented objects for use in noise removal techniques using the ImageJ Particles8 plugin.

3.3.3.1 K-means clustering

Parameterisation by comparison to a manual count as described in section 3.3.2.1 results in segmented areas with no ground truth labelled set, so an unsupervised classification approach such as k-means clustering which does not require a labelled training set was most appropriate. However, ground truth classifications for 10 images were generated for validation of this classification method through comparison of each segmented region overlaid onto the original image and manual labelling of each as either cell or noise. Additionally, each image was examined visually for cells completely undetected by the segmentation process.

Principal component analysis (PCA) was applied to the set of features detailed in Table 3.1 before classification using k-mean to reduce the number of features and thus computation time.

Four principal components retained 86% of data variance and was the lowest number of components that was able to distinguish cells and noise when k-means clustering was applied. Using k-means on the first 4 principal components for the dataset segmented using the manual count ground truth ($r_{small} = 14$ pixels (5 µm) and $r_{large} = 80$ pixels (31 µm)) gave an average F_1 score for cells per image of 0.94 and cell recall of 96%.

The same approach was used on the dataset segmented with $r_{small} = 7$ pixels (6 µm) and $r_{large} = 22$ pixels (20 µm) automatically labelled using the nuclear ground truths as discussed in section 3.3.2.3. Maximum cell recall was 96.5% and the corresponding F_1 score was 0.91.

However in both cases the success of k-means clustering was sensitive to the random initialisation. When the algorithm was evaluated 20 times on the second dataset, three distinct minima became apparent. Two minima had F_1 scores greater than 0.9 and were observed in 65% of cases, however the remaining 45% of cases had an F_1 score of 0.53, indicating clustering had failed to successfully classify cells and noise. This indicates that the classification results of k-means clustering with random initialisation must be confirmed before application to datasets for the purpose of noise removal.

3.3.3.2 Use of labelled dataset

The automatically labelled datasets were used as training sets for supervised learning techniques to investigate the possibility of training classifiers to distinguish between cell,

noise, merged and split regions. Success of each technique was evaluated using 5-fold cross-validation. The images of cell nuclei used as ground truth in the parameterisation method described in section 3.3.2.2 were used to automatically label the binary objects in the final segmented image according to the appropriate DM conditions for cells and noise. The dataset contained 1175 cell objects, 41 merge objects, 70 split objects and 280 noise objects. In cases where only two classes were considered (noise and cells), merged and split objects were re-labelled as cells. This approach was employed as the morphological and greyscale properties of merge and split objects were more likely to be similar to cells than to noise.

3.3.3.2.1 Use of area threshold for noise removal

Histograms of object area were observed to be bimodal as shown in Figure 3.14, and visual inspection of images identified noise objects as often being smaller in size than cell objects. It was hypothesised that noise could be removed by setting a threshold for object area.

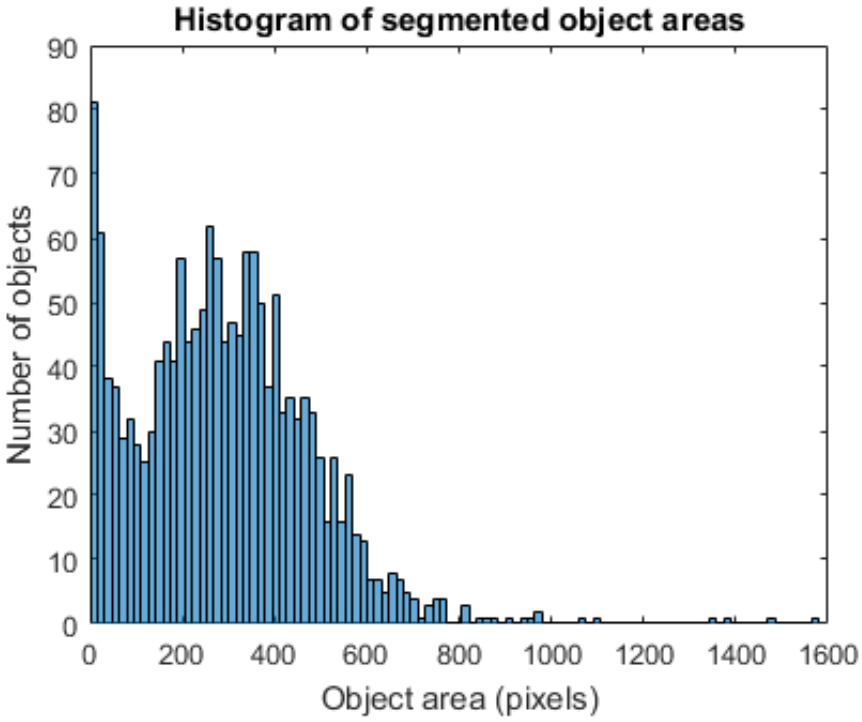

Figure 3.14 – Histogram showing the bimodal distribution of segmented object areas for the training set of H400 cells as obtained using automatically labelled ground truth dataset. *Visual inspection of images indicated that the peak at smaller object area could correspond to noise regions, and the peak at larger area to cells.*

The empirical cumulative probability function (CPF) of areas of segmentations meeting the correct detection criteria, CPF_{cells}, was compared with the CPF of regions that did not, CPF_{noise}. An appropriate size threshold for removing noise, which maximised noise removal whilst minimising removal of true cell segmentations, was selected by identifying the object area size for which the difference between CPF_{noise} and CPF_{cells} was maximised. This maximum occurred at 137 pixels, at which point 78.96% of noise was removed at the expense of 11.39% of cells.

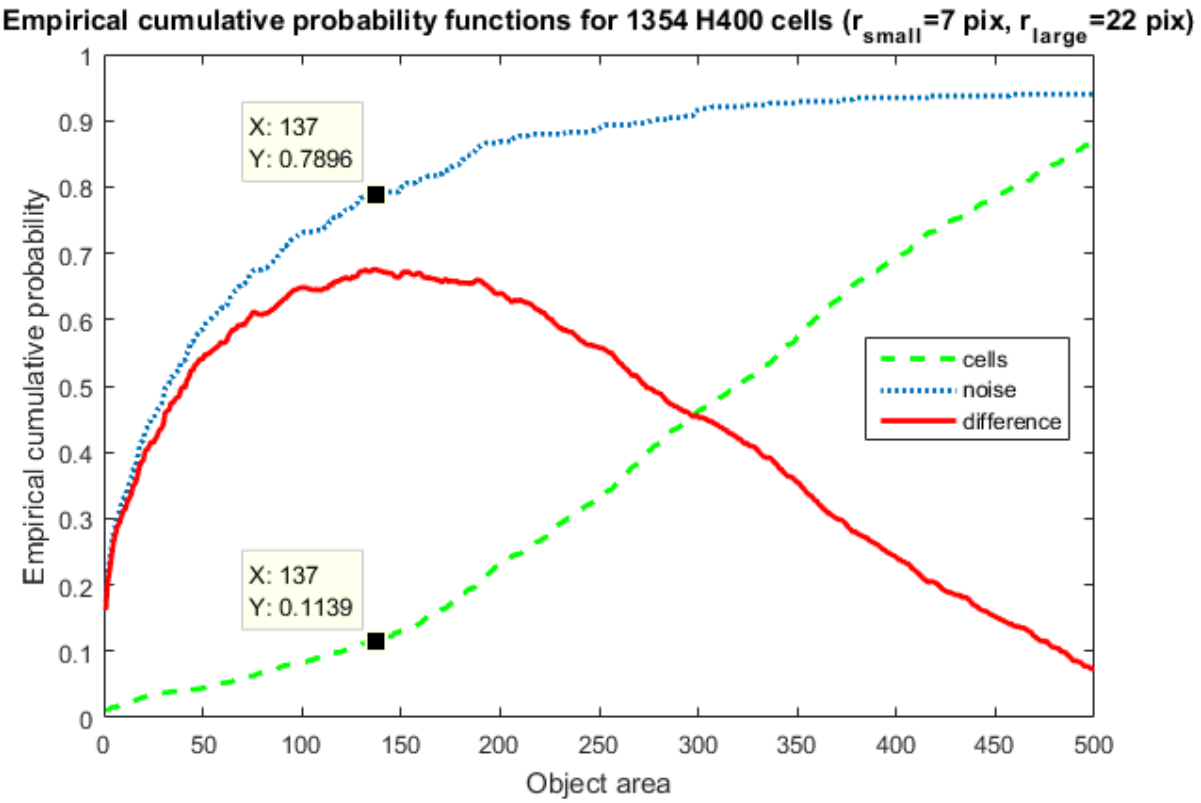

Figure 3.15 – Empirical cumulative probability functions showing the frequency of objects with a given area. *The green dashed line shows the CPF of cell segmentation areas and the blue dotted line shows the CPF of noise segmentation areas. The difference between these values is shown by the red solid line. The black squares indicate the values in the cell and noise CPFs corresponding to the maxima of the red line.*

3.3.3.2.2 Supervised learning techniques

Supervised learning techniques tested for classification were: linear support vector machine (SVM), a simple decision tree (simple tree), linear discriminant analysis using diagonal covariance (LDA_diag) and using automatic regularisation (LDA_auto). These were selected because of their ease of interpretation and fast calculation and prediction times [179].

To investigate the possibility of identifying merge and split objects in addition to noise objects, all 4 classes were considered and the results are shown in Table 3.2. Although SVM exhibited the best overall accuracy and highest recall for both cells and noise, misclassification was relatively high for split and merged objects compared with LDA_diag,

which achieved the best recall for merged and split objects but performed the worst overall in terms of accuracy.

Classifier	Overall accuracy (%)	Cell recall (%)	Noise recall (%)	Merge recall (%)	Split recall (%)
Simple tree	86.3	97.1	75.4	0	0
LDA_diag	73.2	76	70.1	**65.9**	**40**
LDA_auto	86.8	95.1	77.5	36	12.9
SVM	**87.6**	**97.2**	**80.7**	7.3	1.4

Table 3.2 - Results of classification of H400 segmentations into "cell" class and "noise", "merge" and "split" mis-segmentation classes. *The highest scoring results in each category are indicated in bold text.*

Since noise regions have the greatest detrimental effect on the total cell count (Figure 3.13B), removing these whilst retaining the maximum correct cell detections were given priority over detecting merged and split objects. To this end, merged and split objects were relabelled as cells and the classifiers were retrained using only two classes. Table 3.3 shows the results from this classification. Although LDA_auto did not achieve the highest recall rates for cells or noise, it achieved the greatest trade-off between precision and recall as indicated by the F1 score, only marginally outperforming SVM.

Classifier	Overall accuracy (%)	Cell recall (%)	Noise recall (%)	F1 score
Simple tree	92.1	**96.8**	70.7	0.953
LDA_diag	91.3	93.1	**83.2**	0.946
LDA_auto	**93.3**	96.4	78.9	**0.959**
SVM	93	96.3	77.9	0.957

Table 3.3 - Results of classification of H400 segmentations into "noise" and "cell" classes. *The highest scoring results in each category are indicated in bold text.*

To determine the possibility of distinguishing between cell, noise and split objects, the classifiers were trained on the data with all noise objects removed (Table 3.4). Once again there was a substantial trade-off between correct cell retention and merge and split recall.

Classifier	Overall accuracy (%)	Cell recall (%)	Merge recall (%)	Split recall (%)
Simple tree	**91.8**	98.6	24.4	17.1
LDA diag	75	75.7	**68.3**	**67.1**
LDA auto	90.9	95.9	41.5	35.7
SVM	91.3	**99.3**	0	5.7

Table 3.4 – Results of classification of noise-free segmented H400 cell data into "cell", "merge" and "split" classes. *"Merge" and "split" segmentations were subsumed into the "cell" category. The highest scoring results in each category are indicated in bold text.*

3.3.3.3 Discussion of noise removal methods

K-means clustering was able to distinguish between cell and noise segmentations, with an F1 score of 0.91 in the automatically labelled dataset. However judicious initialisation would be required before any meaningful implementation since random initialisation causes cluster means to converge to local minima, leading to incorrect labelling. Unsupervised learning methods are useful in the case when no training set is available but since the nuclear segmentation parameterisation method was proven to be the more successful, the labelled training set may be exploited to make use of one of the more successful supervised techniques.

Setting an area threshold for removing noise performed poorly compared with the supervised learning techniques since a relatively high number of cells were below the threshold to be removed compared with supervised learning techniques. For example, 96.4% of cells were correctly identified using LDA_auto on two classes (Table 3.3) compared

with 88.6% using an area threshold, with the same level of noise identification (78.9%). These data indicate that object area alone was insufficient to reliably distinguish between cells and noise.

All supervised techniques achieved the highest classification results when distinguishing between two classes, linear discriminant analysis with auto-regularisation in particular had the most favourable compromise between cell retention and noise removal (Table 3.4).

No methods were satisfactorily able to identify merge or noise objects and even those that performed best did so at large cost to the cell recall. This is understandable, since these segmentations will have many of the same morphological and greyscale properties as cells – ultimately they are simply cell segmentations that have some small discrepancy causing them to become merged/ split. However the parameterisation step quantifies these small contributions to the total cell count (Figure 3.13B), which allows quantification of the total cell count error.

3.4 Conclusion and final method

It was shown that cells may be segmented through use of mean filters using the method described in Figure 3.5. Selection of appropriate parameters for this method using the nuclear segmentation ground truth method was by far the superior technique and as such was used to select parameters for any future applications, and the parameters selected for H400 cells as described in section 3.3.2.2 was used the analysis of all further images acquired with the same camera and microscope as used in development. After cell segmentation according to the workflow shown in Figure 3.5, segmented regions were classified as noise or cell regions, and the noise regions discarded to give the final cell count.

Linear discriminant analysis using auto-regularisation was chosen as the best method for this purpose since it gave the highest F1 score and thus the greatest trade-off between cell retention and noise removal.

4 IMAGE ANALYSIS VALIDATION AND OPTIMISATION

4.1 Introduction

The ability to count cells from images using the technique developed in chapter 0 provides a method for non-destructively generating growth curves by acquiring images at intervals during culturing. However, in order to successfully utilise this technique, it is important to firstly consider how the experimental protocols may be optimised and determine what limitations the experimental setup may pose to successful application. This chapter describes a number of investigations into protocols for use in image acquisition and parameter optimisation.

The results from image analysis methods must also be compared with those obtained by other routinely used laboratory cell counting techniques to ensure that the method is able to provide comparable results. This chapter describes the results of experiments comparing cell counts and growth curves obtained using the image analysis method developed in this work compared with those determined manually using a haemocytometer, a LUNA automated cell counter and the MTT assay. The ability of the image analysis method to distinguish between the growth rates of cells cultured under different conditions is also validated by generation of growth curves for H400 cells supplemented with varying amounts of foetal calf serum (FCS) [184].

Finally, investigations into the potential for wider application of the image analysis method for use with cell lines, other than the H400 cell line for which it was initially developed, are described.

4.2 Determining the total number of cells in a culture from images

H400 cells grow in discrete colonies on the substrate prior to development of confluent monolayers causing small variations in the number of cells detected in images acquired at different locations. An image acquired at a random location in the culture dish provides a random subsample of the culture. To account for small variations in cell density, multiple images at random locations were acquired. The mean number of cells per image, N_{image}, was then used to estimate the total number of cells in the culture using the ratio of substrate area and image area. For example, in the case of an image of a culture in a 35 mm dish acquired using the Retiga-2000R camera the calculation used was as follows:

$$\boldsymbol{N_{total} = \frac{A_{total}}{A_{image}} \times N_{image} = \frac{962.11\ mm^2}{1.06\ mm^2} N_{image} = 907.65 \times N_{image}} \qquad \textit{Equation 7}$$

where A_{total} is the total area of the vessel, A_{image} is the area of substrate included in a single image and N_{total} is the total number of cells in the culture. As the area included in the image set tended towards the total surface area of the culture vessel, the accuracy of estimated N_{total} should approximate the true value. However, increasing the number of images acquired required the sample to be outside the desired incubation conditions for longer periods of time and that also increased the risk of exposure to infection. To investigate how the mean cell number per image changed as the number of images n increased, sets of 20 images were acquired at random locations in H400 cell cultures in 3 35mm culture dishes. Eighteen image sets were acquired at multiple time points to include cultures of different levels of confluency. The magnitude of the difference between the mean cell count calculated using n images and $n-1$ images, ΔC, was averaged over the 18 image sets and plotted against n (Figure 4.1). This graph demonstrated an initial rapid

reduction in ΔC as more images were added to the calculation of the mean, before stabilisation to approximately 1.5% at $n = 11$. After this point there were minimal improvements in ΔC, indicating that 11 images was the minimum required.

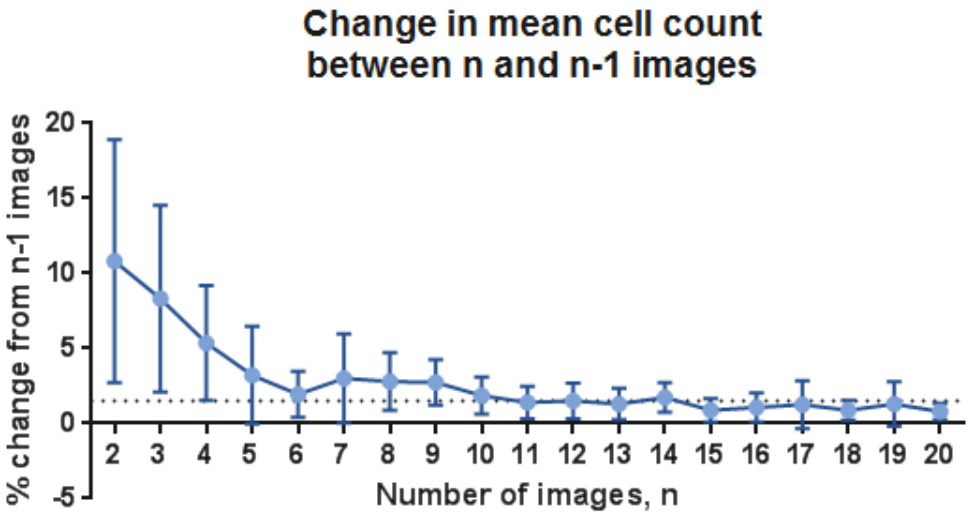

Figure 4.1 – The magnitude of the change in mean cell count per image, ΔC, ***when the number of images included in the mean count calculation was increased from*** $n - 1$ ***to*** n***.*** *ΔC was calculated as the average of 18 image sets and the error bars indicate standard deviation. As more images were added to the calculation of the average number of cells, ΔC tended towards a value of $\Delta C = 1.5$ as indicated by the dotted line. This indicates there was little benefit in acquiring more than 11 images in terms of stability of the average cell number.*

The approximate average length of time required to acquire 20 images was four minutes, or 12 seconds per image on average, thus the minimum time to acquire a viable set of 11 images is ~2 minutes. However, when imaging cultures in 12-well plates the culture remains outside the desired incubations conditions for the length of time required to image all wells, and this increases the image capture period to a maximum of 24 minutes. To reduce the time spent outside the incubator for cultures in 12-well plates, when more than 12 cultures were required for an experiment, these cultures were distributed evenly across two plates to reduce the imaging time-per plate, and control cultures were present on both plates. The

number of imaging time points for generation of growth curves was restricted to twice per day to further reduce the time spent outside the desired incubation conditions.

4.3 Experimental set up

4.3.1 Minimum well diameter

The problem of path length interference as discussed in section 1.5.2.2 is a particular problem for cultures in small dishes as the small well diameter causes variation in light path length and therefore contrast within the surface area corresponding to one image. In order for the image analysis procedure to be successful, the contrast must be consistent across the entire image. It has previously been shown that image quality in PC microscopy is problematic when using 96-well plates (well diameter 6.4 mm) [58]. Other multi-well plates may also be subject to image contrast degradation due to the meniscus, depending on the magnification and size of the image captured. To determine the minimum well-size for the microscopy set-up used here, PC images were acquired of H400 cells in 12-, 24-, and 48-well plates (well diameters 11 mm, 15.6 mm and 22.1 mm, respectively) using the microscope set up as described in section 2.4.1 using a x4 objective lens (Figure 4.2). The area that would be captured by the x10 objective (used in method development and all experiments) is indicated by an overlaid rectangle. In the case of 48- and 24-well plates, poor contrast was observed inside the x10 image due to meniscal interference (as discussed in section 1.5.2.2). However, this was not observed for the image acquired in the 12-well plate, thus this was the smallest well used in subsequent experiments.

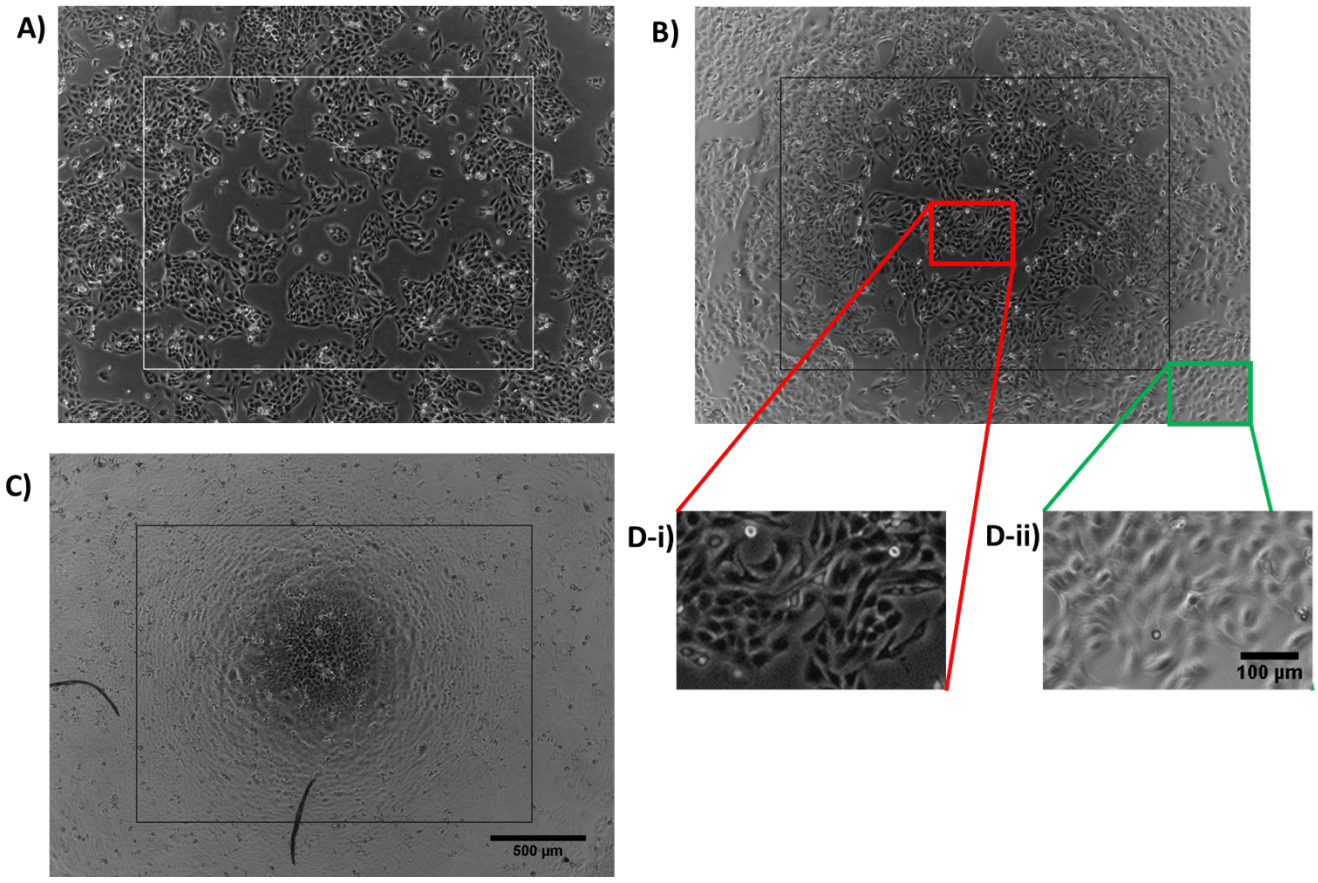

Figure 4.2 – PC images showing the effect of the meniscus formed by cell media in cultureware of various sizes. *Images of H400 cell cultures captured using a x4 objective in the wells of A) a 12-well plate, B) a 24-well plate and C) a 48-well plate. The superimposed rectangles in each image indicate the area that would be included in a concentric image acquired using a x10 objective. Note how the contrast at the edges of images for 12- and 24-well plates is decreased (D-ii) compared to that at the centres (D-i). The scale bar for images A-C is indicated in C and scale bar for images D-i and D-ii is indicated in D-ii.*

4.3.2 Condensation on cultureware

When cultures are removed from the incubator for imaging, exposure to the lower ambient temperature outside the incubator leads to the formation of condensation on the inner surface of the cultureware lid, or upper internal surface in the case of larger flasks used for general cell culture (e.g. T25 or T75 flasks), during the course of the image acquisition process. Condensation accumulation has the potential to cause a variation in image contrast due to scattering of light by the condensation layer, which could result in a reduction in

image analysis performance (especially since that greyscale properties are used in classification for noise removal). To determine whether condensation had a significant effect on the contrast of images, the mean and standard deviation of greyscale intensities in the first and last four images in datasets acquired from T25 flasks and a 35 mm culture dishes were recorded and an unpaired t-test was performed to determine differences between groups. All images used were 8-bit greyscale images, i.e. the range of intensities was between 0 and 255 (black and white).

In the case of images obtained from T25 flasks, no significant differences in greyscale mean or standard deviation were observed (Student's t-test, $p>0.05$). However, in the case of images captured from 35 mm dishes, Student's t-test measured a significant increase in mean greyscale intensity from 102.6 to 114.8 ($p<0.01$) and decrease in mean greyscale standard deviation from 18.83 to 12.58 ($p<0.001$). This could be due to an increased condensation build-up compared to the T25 flask due to the lower vessel volume which evaporated media may occupy relative to the surface area of the lid. Consequently, all images of cells cultured in 35 mm dishes were acquired with the lids removed. Images were acquired as quickly as possible inside a microscope enclosure chamber, sterilised with 70% ethanol to reduce the risk of culture contamination during the imaging process.

4.4 Cell growth curves from larger culture flasks

Experiments carried out in larger volume cultureware such as T25 or T75 flasks are less prone to volume-dependent effects compared to smaller cultureware, but they are utilised less frequently since the large volume and surface area incur higher costs of reagents and stimuli, particularly when using destructive viability assays. The ability to non-invasively

monitor cell number in such cultureware therefore offsets the higher costs of reagents and stimuli required. The high volume of these flasks are also favourable in experiments in which large, consistent numbers of cells are required, for example in DNA extraction for quantitative polymerase chain reaction, thus the ability to non-invasively monitor cell number until the desired density is reached would be advantageous. Additionally, regular monitoring of cell appearance and growth is an essential part of culture maintenance and this is normally performed by visual inspection. However, the ability to generate growth curves of cultures in flasks without destroying the culture has potential utility, for example, to ensure that cell growth characteristics are consistent over long periods of culturing, or to ensure that cell proliferation rates have been restored after a period of cryopreservation [185].

To investigate the potential for generating growth curves from larger culture flasks, H400 cells were seeded in a T25 flask at an initial number of $5x10^5$ cells. 30 images were acquired at random locations at 24 hour intervals post-seeding and the average number of cells per image used to generate a growth curve (Figure 4.3). The growth curve shows the expected initial phase of rapid growth followed by a reduction in cell proliferation rate after three days in culture as cell contact and diminishing availability of nutrients begin to inhibit growth. These data support the use of the image analysis procedure for growth curve generation in T25 flasks.

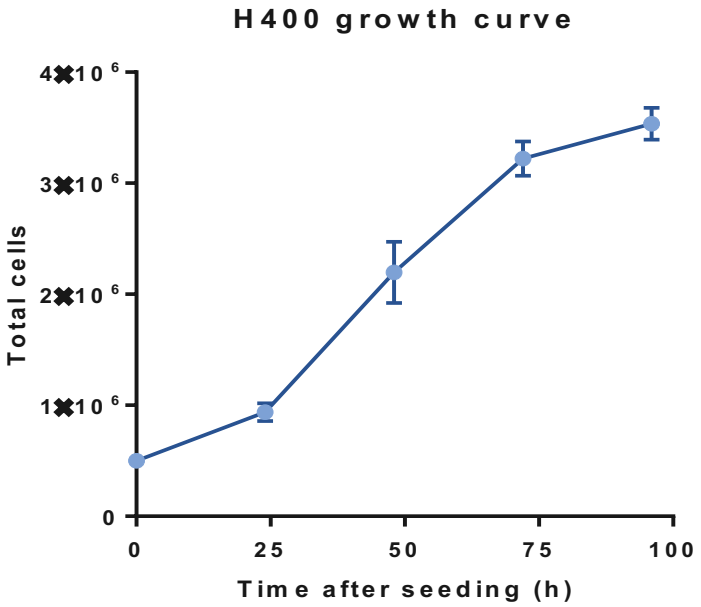

Figure 4.3 – Growth curve of H400 cells cultured inside a T25 flask, imaged at 24 hour intervals after seeding. *Data points show the average cell count using 30 images, error bars show standard deviations. The shape of the growth curve is similar to that which is expected – a rapid initial growth followed by a slowing down of growth after 3 days culture.*

4.5 Effects of fixative and stain on cell monolayer morphology

In section 3.3.2, use of segmented nuclei corresponding to a PC image was shown to be the optimal ground truth for selecting parameters for use in the image analysis cell counting method. Using an image of cell nuclei as the ground truth for parameterisation requires staining of cell monolayers with a fluorescent nuclear dye. Two commonly-used dyes for this purpose are DAPI and Hoechst. These dyes may be applied to live cells, although cultures are often fixed before staining, particularly in the case of DAPI, due to the increased permeability of cell membranes compared with live cells, which allows greater dye uptake and therefore improved image contrast [60], [64]. As discussed in the introduction in section 1.5.3.2, fixation techniques rarely preserve morphology perfectly and different techniques may cause artefacts in cell structure. It is essential to choose a technique which preserves the appearance of live cells in the PC images used for parameterisation, as these images

must be representative of all further images to which the analysis method will be applied. Differences between stained and/or fixed images used for parameterisation and live unstained images may lead to the selection of parameters that are not correctly optimised, or give a false representation of the detection rate.

To determine which staining and fixation protocol, could provide the closest to the true representation of live H400 monolayer morphology, cultures of H400 cells in 6-well plates were fixed using formalin, PFA at either 4% or 8%, methanol or glutaraldehyde (protocols are described in section 2.2). Unless otherwise stated, fixation was followed by staining with powder form DAPI as described in Protocol 1 (section 2.2.1). Additionally, unfixed cultures were stained using Hoescht due to its increased permeability in live cells compared with DAPI. Representative images of cells fixed and/or stained with these protocols are shown in Figure 4.4.

Cells fixed with methanol appeared with dark rings surrounding the nuclei after the stain was applied (Figure 4.4C-i). This divergence from the morphology of live cells (see Figure 4.4G-i) means that this fixative is inappropriate for use in cultures intended for parameterisation. In cultures fixed with an aldehyde-based method cells appeared more rounded than live cells, likely due to the characteristic cell shrinkage caused by aldehyde-based fixation methods (Figure 4.4 A, B, E and F) [67]. This often resulted in an increase in brightness of the halo, due to the change in angle of the cell edge with the culture dish, which is critical in the formation of the halo (see section 1.5.2.2).

An exception to this was the culture fixed using the 8% PFA protocol, in which cells appeared relatively similar to the unfixed culture (Figure 4.4D). This protocol did not require the initial

washing step since the fixative was added directly to the cell media. This could have resulted in a decreased rate of fixation and reduced shrinkage compared with other aldehyde-based methods, or the lack of washing step could have reduced any potential disruption to cell adhesion before fixation and caused cell shape to appear more similar to live cells (Figure 4.4D-i). In any case, when cell cultures were subsequently stained with DAPI, the entire cell appeared fluorescent rather than only the intended nuclear region (Figure 4.4D-ii). Indeed this was the case for all cultures stained using DAPI protocol 1, except those fixed using methanol, which showed the expected localised nuclear staining. As it was essential that nuclei were distinguishable both from each other and the rest of the cell to enable the DM conditions applied in the parameterisation to be applicable, staining using DAPI protocol 1 was deemed unsuitable.

Conversely, DAPI protocol 2 (section 2.2.1) gave a high contrast stained image with localised nuclear staining (Figure 4.4F-ii), albeit with a lower signal intensity, potentially due to the fixed concentration of DAPI in the pre-manufactured stain. However, the cell-rounding phenomenon from culture fixation was still observed.

Live cells stained with Hoechst exhibited the most typical cell morphology in the PC images as cultures were not disturbed by a fixation step (Figure 4.4G-i). Additionally, the nuclei were distinct and there was no superfluous staining of cell cytoplasm (Figure 4.4G-ii), although the nuclear fluorescent intensity was much lower due to the lower permeability of live cells to the nuclear dye. This protocol was therefore selected as the most appropriate for use in parameterisation, and was therefore used to select H400 culture analysis parameters as described in section 3.3.2.2.

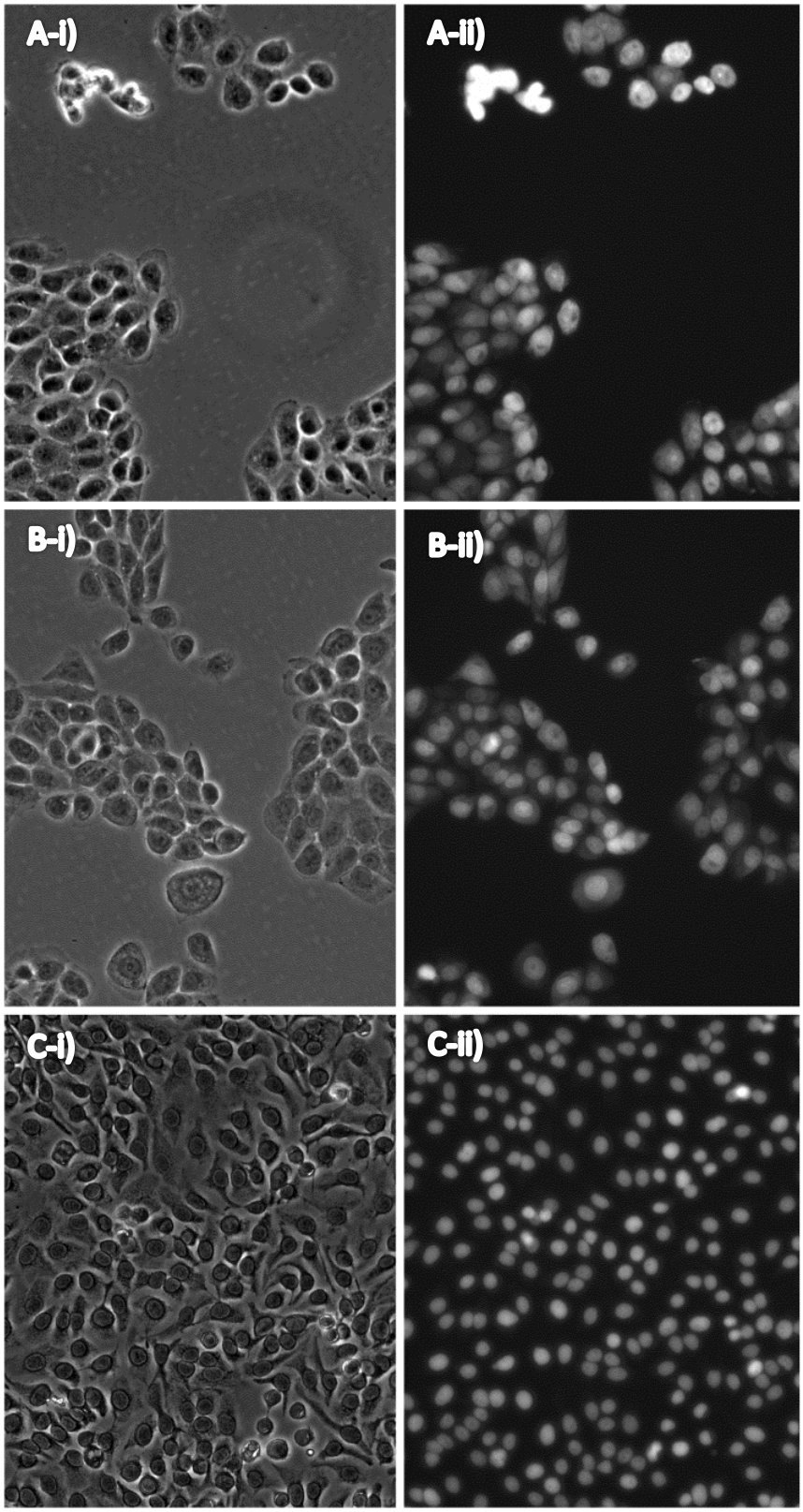

Figure 4.4 – Pairs of concurrently acquired PC (i) and epifluorescence (ii) micrographs of H400 cells using a range of fixation and staining methods. *(Continued on next two pages, figure description follows final image on page 129).*

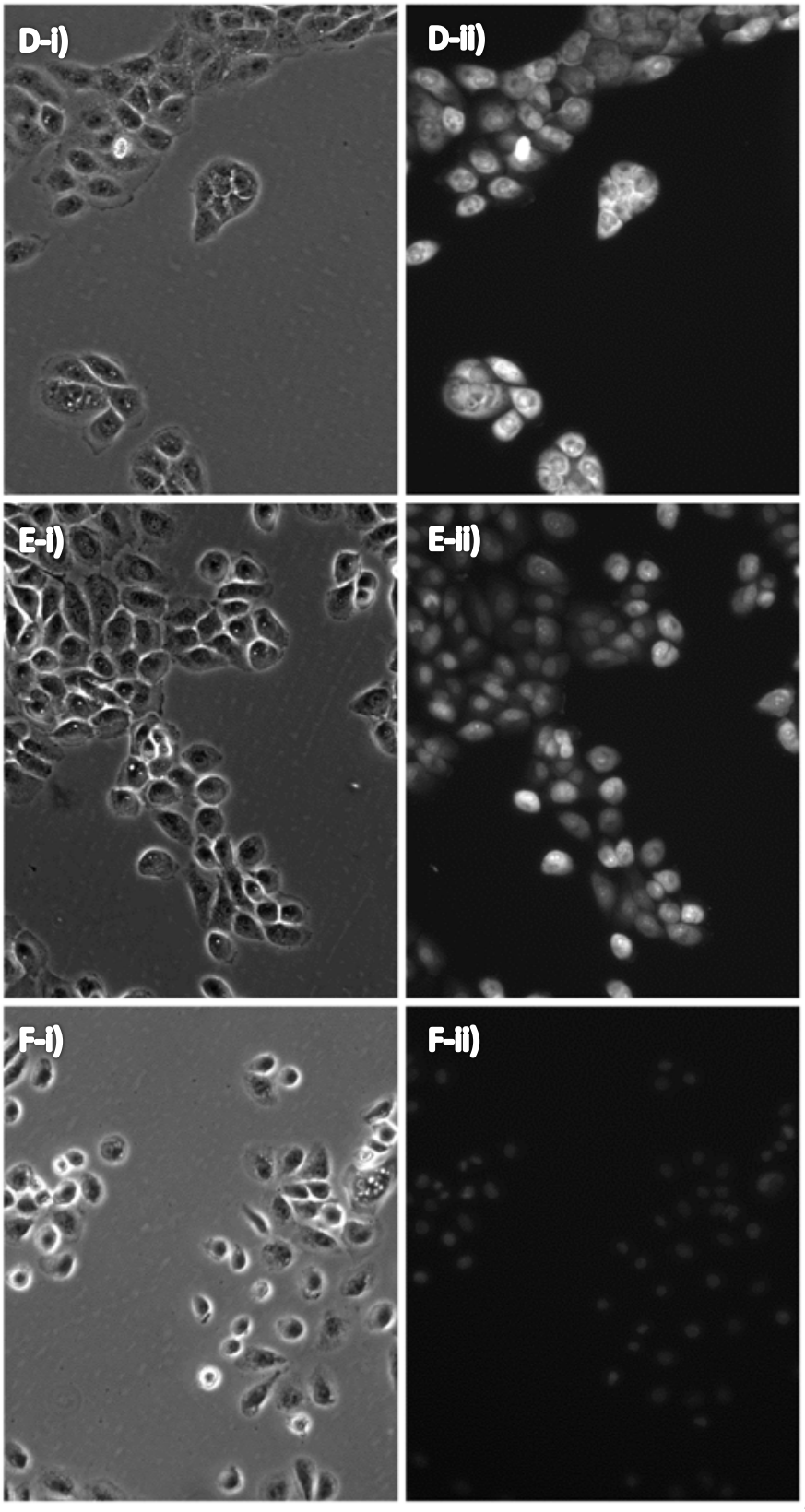

Figure 4.4 cont.

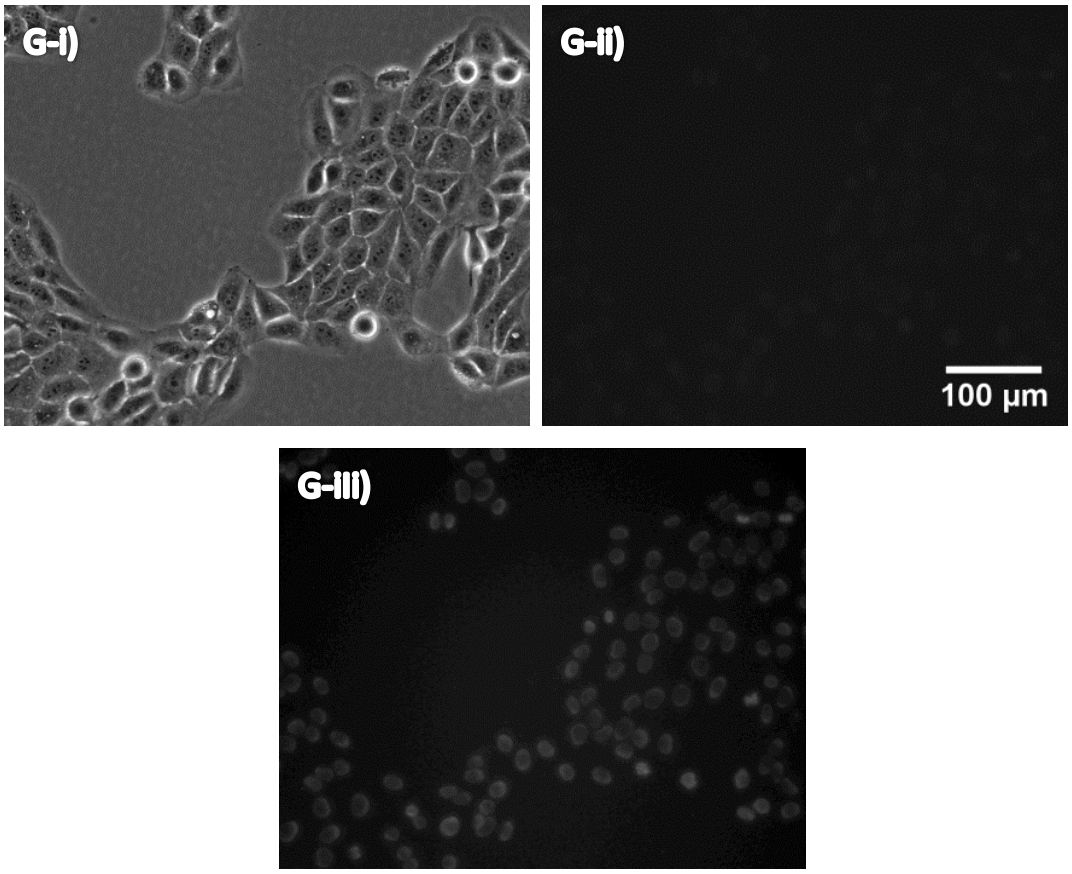

Figure 4.4 cont. *The samples in A-E were fluorescently stained using DAPI protocol 1, F was stained using DAPI protocol 2 and G was stained using Hoescht. The following fixatives were used on each sample: A) 4% PFA, B) and F) formalin, C) methanol, D) 8% PFA, E) glutaraldehyde, G) none (live, unfixed culture). The scale bar for all images is shown in G-ii. Note the dark rings around cell nuclei in methanol-fixed cells (C-i) and the cell rounding in washed and aldehyde-fixed cultures (A, D, E, F -i) compared with live unfixed cells (G-i). Also note the leakage of fluorescent stain into cell cytoplasm in cultures fixed aldehydes and stained with DAPI protocol 1 (A, B, D and E-ii). Conversely the unfixed samples display isolated nuclear staining, but show markedly lower contrast (G-ii). Image G-iii shows G-ii with enhanced contrast for clarity.*

4.5.1 Comparison of parameterisation results using live and fixed samples

Formalin-fixed cultures stained with DAPI protocol 2 provided clear resolution of individual nuclei, although fixation artefacts affecting cell morphology may cause errors if this protocol were used for parameterisation (Figure 4.4F). In particular, the rounding of cells caused by fixation and consequent brighter halo may make individual cells easier to distinguish compared with live cultures, which may have exhibited unclear boundaries between cells.

This could lead to an unrepresentatively high cell detection rate. To investigate the effects of fixation artefacts on parameterisation and cell detection rates, the nuclear ground truth parameter selection method was performed using images of H400 cultures fixed and stained using this protocol (1425 cells). The optimal parameters were compared with those obtained using the live culture stained with Hoechst described in section 3.3.2.2.

The optimal parameters for the fixed cultures were determined as described in section 3.3.2.2 on a sample of 1425 H400 cells from images of cultures representing a range of cell densities, which had been fixed and stained using DAPI protocol 2. These parameters were found to be $r_{small} = 7$ pixels (6 µm) and $r_{large} = 18$ pixels (16 µm), and which gave a 91.4% correct cell detection rate compared with the live cell method which gave the optimal parameters to be $r_{small} = 7$ pixels (6 µm) and $r_{large} = 22$ pixels (20 µm), with a detection rate of 87.1%. As predicted, the fixed H400 cells achieved a higher maximum detection rate compared with unfixed cells in the procedure applied. Whilst r_{small} was found to be the same for both techniques, the optimal r_{large} value was smaller for fixed cells. This may also have potentially been explained by a slight decrease in average size caused by cell rounding. However, this difference in parameter values did not have a significant effect detection rate as the detection rate in live cells using these parameters was 85.8%. Consequently, cell cultures fixed and stained in this way may be suitable for approximating optimal parameters when no vital nuclear stain is available, however the detection rates may not be representative of those achieved when these parameters are applied to segmenting live cultures.

4.6 Validation of method using foetal calf serum supplemented H400 cultures

In vitro eukaryotic cell cultures are commonly supplemented with FCS to provide a source of growth factors and proteins required for survival and proliferation. Serum starved cell cultures enter cell cycle arrest thus it was expected that cells exposed to lower levels of FCS would show a lower rate of growth [186]. Cultures supplemented with the FCS maintenance concentration level of 10% and reduced levels of 5% and 2.5% were used to validate whether the cell counting method was able to differentiate different cell growth rates and show the expected dose-dependent response.

H400 cells were seeded in 35 mm dishes at an initial number of $5x10^4$ cells and supplemented with 10%, 5% or 2.5% FCS (in triplicate cultures). Cultures were imaged at multiple time points between 48 and 98 hours post-seeding and growth curves generated from the average cell counts at each time point. The image analysis method was able to demonstrate the expected dose-dependent growth rate of H400 cells with FCS supplementation (Figure 4.5).

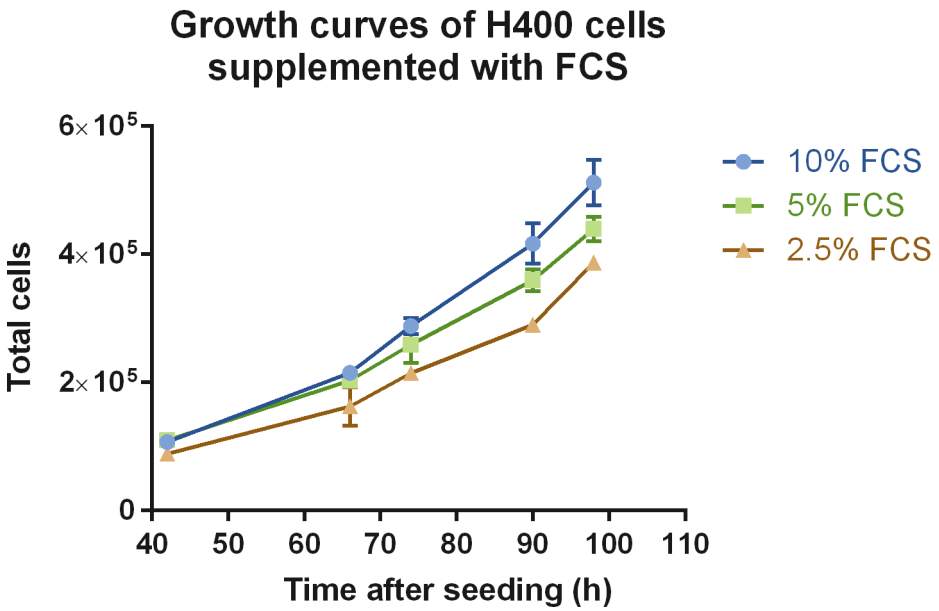

Figure 4.5 – Growth curves of H400 cells supplemented with 10%, 5% and 2.5% FCS as measured using the image analysis cell counting method. *The mean of triplicate plates is plotted at multiple time points and error bars show standard deviations. The expected reduction in growth rate is observed in cultures supplemented with lower volumes of FCS.*

4.7 Comparison of image analysis method with other computational methods

The aim of this section is to compare the image analysis cell counting method developed in chapter 3 with other image analysis methods. It should be borne in mind that the main purpose of the algorithm developed in this thesis is for cell counting rather than cell segmentation; whilst cell segmentation is a step in this process, the veracity of the segmentation compared to the true shape of the cell is not important so long as the criteria for a correct detection are met (section 3.3.2.2). Therefore, comparison to a manual outline using metrics such as the Jaccard index were unsuitable for evaluation of algorithm success, since this considers overlap between algorithm-generated segmentation with a ground truth segmentation rather than the number of cells present in the image. Instead each method was first evaluated to determine whether cells in PC images of H400 cells could be

approximately segmented. Where this was possible, the ground truth data set described in section 3.3.2.2 was segmented using a variety of possible parameters, and the number of correctly detected cells used to enable direct comparison between methods.

The segmentation methods considered here are: global thresholding techniques [187], graph cut [93] and Chan-Vese active contours [85]. Further methods were considered for comparison but were precluded by the unavailability of their source code. These include smart markers for watershed-based cell segmentation [92], basic image features [96] and restoration of images through reversal of phase contrast artefacts [89], [90].

4.7.1 Global threshold methods

Segmentation by global threshold methods convert images to binary by selecting an intensity value to distinguish foreground and background regions. There are a number of techniques to calculate the threshold value. Sixteen methods were tested using the ImageJ Auto Threshold function [187] to examine suitability for use in segmentation for cell counting. The methods tested were: Default (the ImageJ default method) [176], Huang [188], Intermodes [189], IsoData [190], Li [191], MaxEntropy [192], Mean [193], MinError(I) [194], Minimum [189], Moments [195], Otsu [70], Percentile [196], RenyiEntropy [192], Shanbhag [197], Triangle [198] and Yen [199]. Details of each method may be found in reference [187].

Figure 4.6 shows an example phase contrast image of H400 cells with each of the threshold methods applied. It is clear methods for setting a single threshold value to binarise images is inappropriate for segmenting such images, since the similarity in intensities between cell

cytoplasm and background causes them to be indistinguishable. Consequently, such methods are unsuitable for use in cell counting.

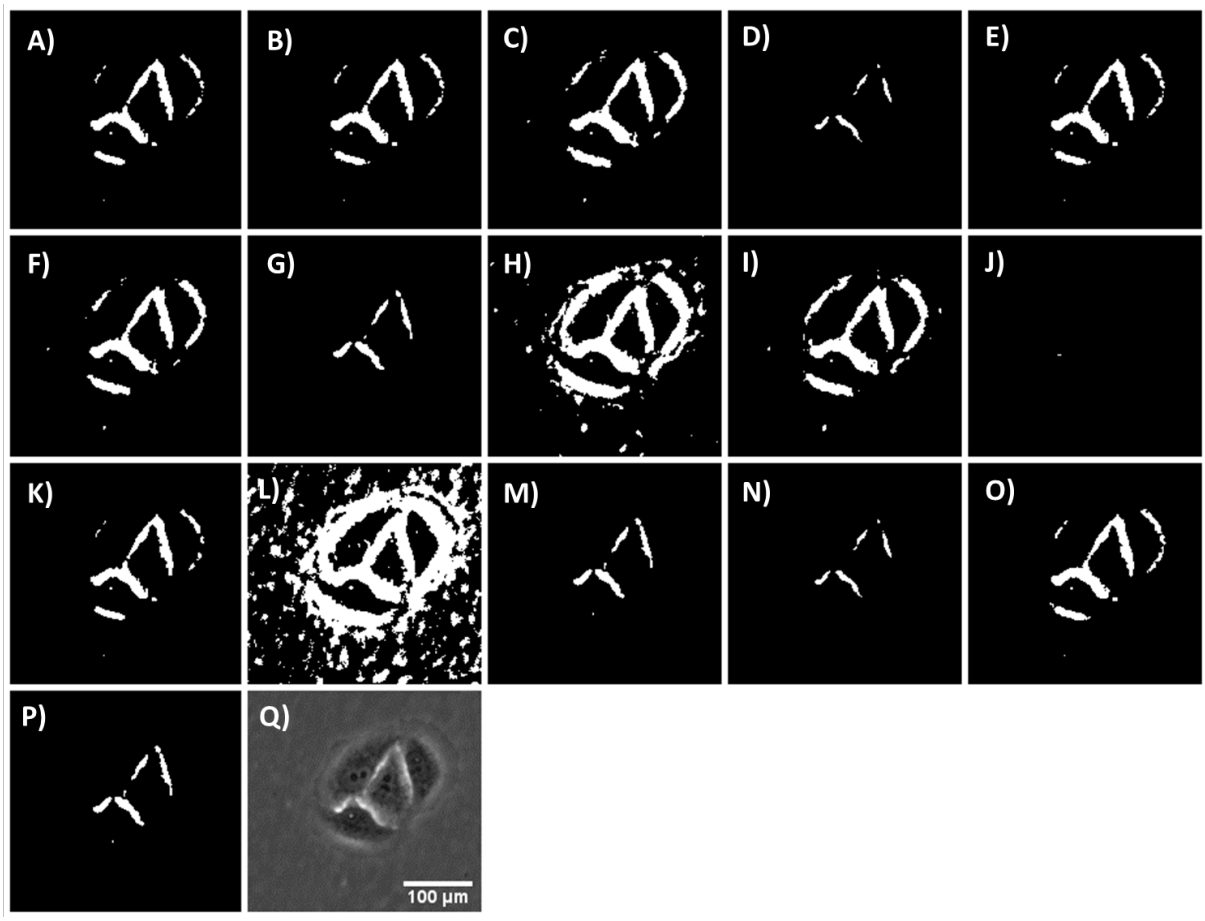

Figure 4.6 – Examples of PC images of H400 cells segmented using a variety of global threshold techniques incorporated in the ImageJ Auto Threshold function*: A)Default, B) Huang, C) Intermodes, D) IsoData, E) Li, F) MaxEntropy, G) Mean, H) MinError(I), I) Minimum, J) Moments, K) Otsu, L) Percentile, M) RenyiEntropy, N) Shanbhag , O) Triangle, and P) Yen. Q) Shows the original PC image of H400 cells with scale bar. No methods are able to distinguish the cell cytoplasm from the background due to their similar intensities, and only the bright halo regions are segmented.*

4.7.2 Graph cut with asymmetric boundary costs

The graph cut method segments images by first creating a graph linking each pixel with the background, B, and the foreground, F, regions. The link between each pixel and either region is assigned a value, or 'weight' depending on the similarity of the pixel properties with those

of B or F. Links are also created between pixels and assigned weights according to the similarity of the properties of the linked pixels.

This graph is described in an energy function with two terms: the region (pixel-region) term and the boundary (pixel-pixel) term. The region term is weighted by a factor, λ, and the boundary term is controlled by a smoothing factor, σ. For the purpose of segmentation, the objective is to cut the links with the lowest cost possible energy cost i.e. the energy function is minimised. A full mathematical explanation can be found in reference [200].

The method by Bensch *et al.* is adapted for use on phase contrast images of cells through use of asymmetric boundary term in the energy function as a means of compensating for intensity gradients caused by the halo effect [93]. The method was originally intended as a cell tracking algorithm which initially segments cells before tracking across multiple time points. The initial segmentation algorithm uses a maxflow graph-cut algorithm [201] with asymmetric boundary costs. This method requires training of the graph cut algorithm using manually-selected foreground (cell centre regions) and background regions, and setting 4 parameters: the size of a Gaussian filter for pre-processing (σ_{bgr}), a minimum cell size for removal of small objects (a_{min}) for post-processing, and min-cut parameters σ and λ.

In Bensch's paper, the optimal values for σ and λ were found by an exhaustive search using comparison of segmentations acquired with each parameter set with a manually segmented cell using a pixel-wise F-score as defined in section 2.7.5. However, to reflect that the desired purpose of this work is count cells rather than achieve accurate segmentations, the total number of cells present in the image was used as a ground truth for the purpose of parameterisation. Parameter pairs between σ = 0.001 to 0.02 and λ = 0.01 to 0.3 (the same

used in the original paper) were used to segment the image and the number of segmented regions present in the resultant image was compared with the known number of cells in the image from the nuclear ground truth (as described in section 3.3.2.2). The remaining parameters were selected manually to be the same as those chosen in the original paper: σ_{bgr} = 20 pixels and a_{min} = 500 pixels. Figure 4.7 shows the number of binary objects segmented by each parameter pair in terms of percentage of the true cell number.

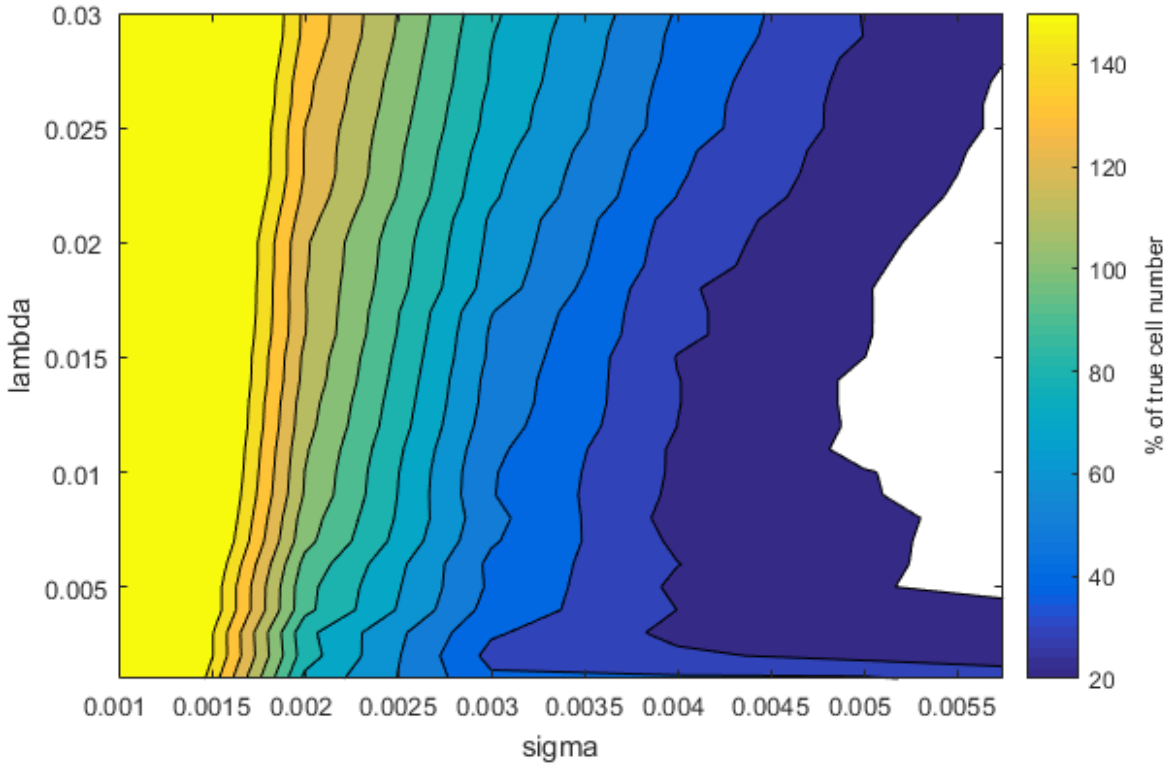

Figure 4.7 – Contour map showing segmentation success of a range of σ and λ values for the graph cut with asymmetric boundaries segmentation method on a PC image with known cell number as a ground truth. *The number of segmentations achieved by each parameter pair are given as a percentage of the ground truth cell number. No maximum value was achieved so there was no obvious best parameters.*

No maximum value was observed for any parameter pair and inspection of the segmented images using the parameters achieving the highest rate of correct cell detections (σ = 0.001 and λ = 0.029) (Figure 4.8) showed that this was because the method was unable to segment individual cells from monolayers of contacting cells. This precludes the use of the graph cut

method for counting H400 cells from phase contrast images, therefore results cannot be directly compared to the results from the cell counting method developed in this thesis.

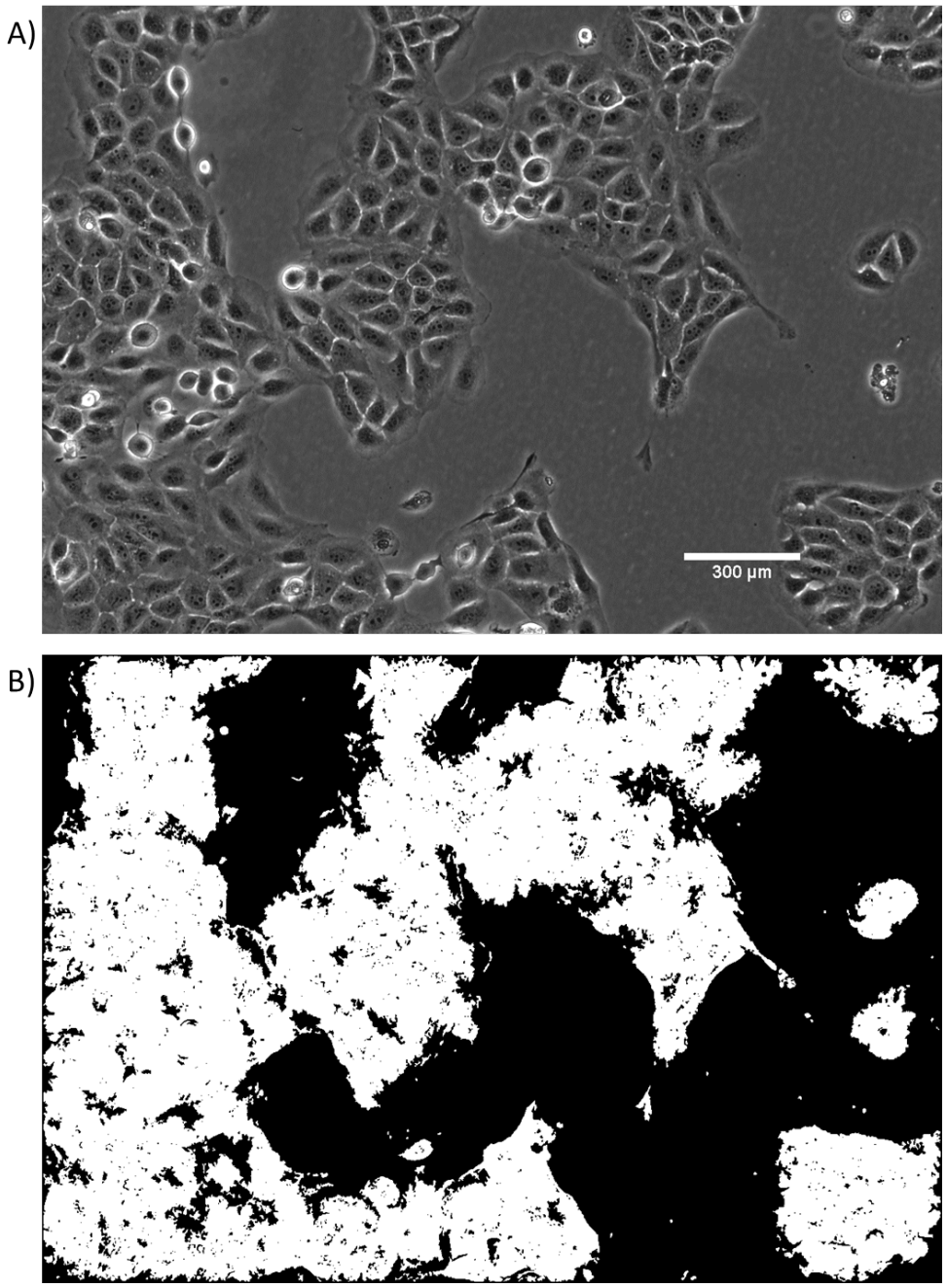

Figure 4.8 – A) PC image of H400 cells and B) the result of segmentation of this image using the graph cut method with asymmetric boundary costs. *Sigma and lambda parameters were chosen as the best performing from the parameter search (σ = 0.001 and λ = 0.029). The method using these (or any) parameters was unable to distinguish between individual cells as required for use in a cell counting method.*

4.7.3 Active contours

Active contour methods segment objects in an image by deforming an initial contour according to some constraints such that the curve aligns with the edges of the object, resulting in a segmentation. There are a number of proposed methods for contour evolution [202]; an implementation of the Chan-Vese method [85] by Lankton [203] is used in this work due to its relative speed [202]. The Chan-Vese method treats images as a set of foreground and background regions that exert opposite forces on the contour, modelled by an energy function. Each point on the contour is iteratively moved according to the forces acting upon it until the forces are balanced and the energy function is minimised i.e. on the boundary between regions. The method requires specification of an initial contour on which the energy function acts, and a smoothing parameter, α. A full mathematical description may be found in reference [85].

It is known that the shape of this initial contour has strong effects on the result of the segmentation [83]. Two initialisations were considered using an initial smoothing parameter of $\alpha = 0.2$ to determine which, if either, was most appropriate for the purpose of segmenting H400 cells in PC images for the purpose of cell counting: these were a single rectangle (Figure 4.9D) and a grid of circles (Figure 4.9B). The results of these initialisations after iteration to convergence are shown in Figure 4.9 E and C respectively. The rectangle initialisation was unsuccessful at distinguishing between individual cells in the centre and edges of the image, thus was not considered further for the purpose of counting cells. Despite a high degree of merging segmentations (as indicated by a red circle in Figure 4.9C), the grid of circles initialisation was able to identify some individual cells (as indicated by a green circle in Figure 4.9C) thus had the potential for use as a cell counting method. This

initialisation was therefore used in investigations into the optimal value of α for the purpose of cell counting.

The PC images of H400 cells with corresponding nuclear ground truth images as described in section 3.3.2.2 were segmented using the grid of circles initialisation and α varied between 0.2 and 0.7. Each image was subsequently compared to the nuclear ground truth to determine the number of correctly detected cells according to the definition in section 3.3.2.2. None of the α values tested were able to correctly detect more than 45.6% of cells in the ground truth images, compared to 87.1% obtained using the method developed in this thesis (Figure 4.10).

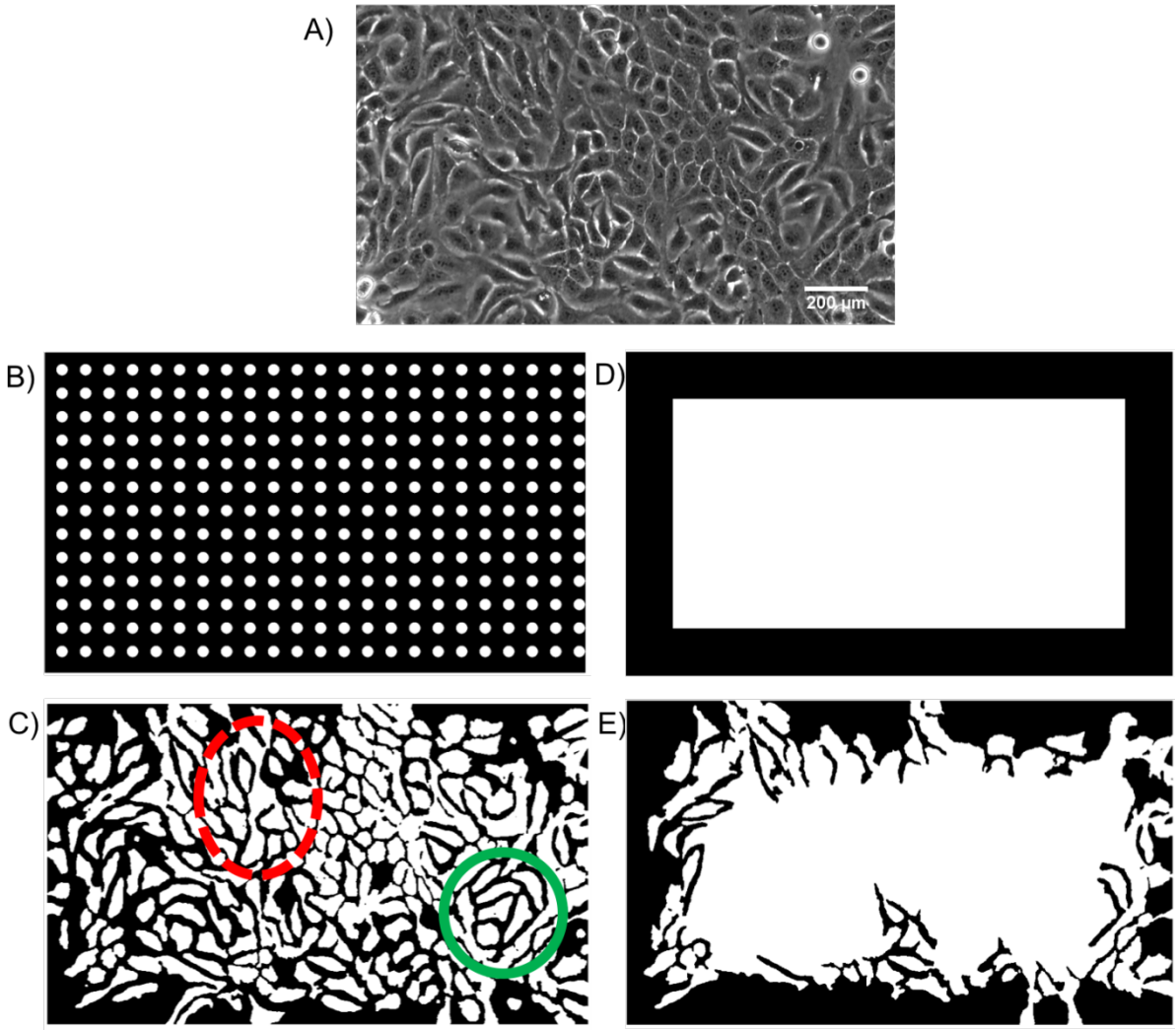

Figure 4.9 - The effects of the initial contour on the results of level set segmentation on a PC image of H400 cells when iterated until convergence using smoothing parameter 0.2. *A) The original PC image. B) Initial contour consisting of a grid of equally spaced circles of radius 10 pixels, and C) the result of this initialisation. D) Initial contour consisting of a single rectangle, and E) the result of this initialisation. The rectangular initialisation was unable to distinguish cell boundaries in the centre and edges of the image and is thus unsuitable for use for cell counting. The grid of circles initialisation was able to detect some individual cells (green circle) but cell regions were merged in other cases (red broken circle). The scale bar for all images is shown in A).*

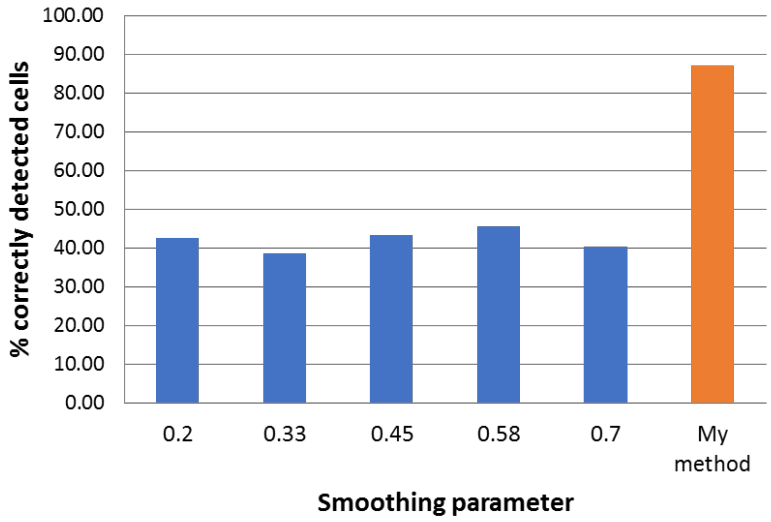

Figure 4.10 – Graph showing the percentage of correct detections achieved from 1354 cells in the ground truth dataset using the Chan-Vese active contour segmentation with a range of smoothing parameter values (blue bars) and the method developed in this thesis (orange bar). *The method developed here achieved higher detection rates than any parameter used in the active contour method.*

4.8 Comparison of image analysis cell counting with other laboratory cell counting approaches

4.8.1 Comparison of image analysis method with cell suspension methods

The cell counts obtained by the image analysis method were compared with other commonly used cell counting methods: counting from suspension using the haemocytometer method and LUNA automated cell counter. For this purpose, H400 cells cultured in 35 mm dishes were seeded at an initial density of $5x10^4$ cells and image sets acquired at a range of time points of between 24 and 100 hours to account for a range of cell densities. Following image acquisition cells were detached from the plate and resuspended in media for counting using either a haemocytometer or the LUNA automated cell counter as described in sections 2.1.3.1 and 2.1.3.2, respectively.

The cell number obtained for each dish using image analysis and haemocytometer or LUNA was plotted against each other. A curve of the following form was fitted using linear regression to examine whether the two methods were linearly correlated (Figure 4.11):

$$Count_{image} = gradient \times Count_{suspension}$$

where $Count_{image}$ was the total cell count as measured by image analysis and $Count_{suspension}$ was the total culture cell count as measured using either of the suspension methods. Whilst the cell count using the image analysis method was linearly proportional to the count measured by both cell suspension methods, in both cases the gradient was less than 1, indicating that the image analysis count was systematically lower than the suspension methods (Figure 4.12).

To determine the extent of systemic differences between methods Bland-Altman plots were generated by plotting the mean cell count reading obtained by the two methods against the difference in counts for each culture (Figure 4.12). The magnitude of the systematic difference between methods was indicated by the line of average difference (solid black line); this value was 4.9 x 10^4 for the haemocytometer method and 10.7 x 10^4 for the LUNA automated counting method. The distribution of points about line of average difference did not indicate any systematic increase or decrease as the average count increased. Although the image analysis method was subject to a systematic reduction in counts compared with the suspension methods, linear proportionality holds thus the image analysis provided an equivalent measure of relative changes in cell number.

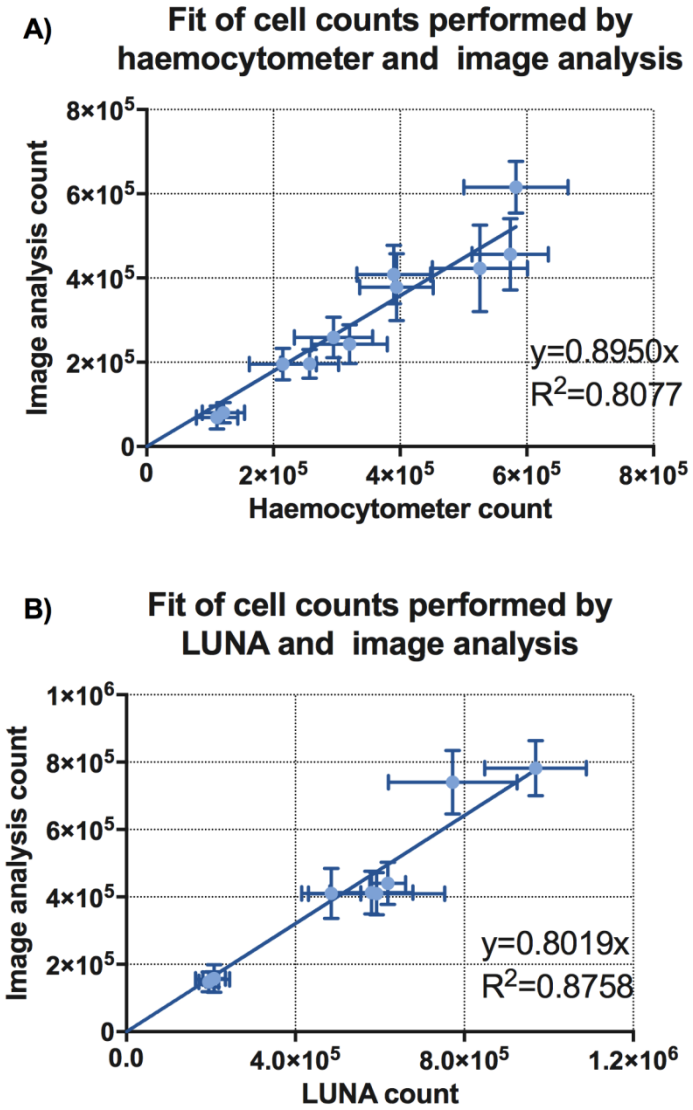

Figure 4.11 – Correlation of image analysis cell counts with A) haemocytometer method and B) LUNA automated cell counter. *Each point corresponds to a single culture and error bars indicate standard deviations of multiple measurements carried out on each sample (n=11 for image analysis, n=8 for haemocytometer, n=4 for LUNA). This indicates that cell counts by the image analysis method are systematically lower than those obtained from the same cultures by the haemocytometer or LUNA methods.*

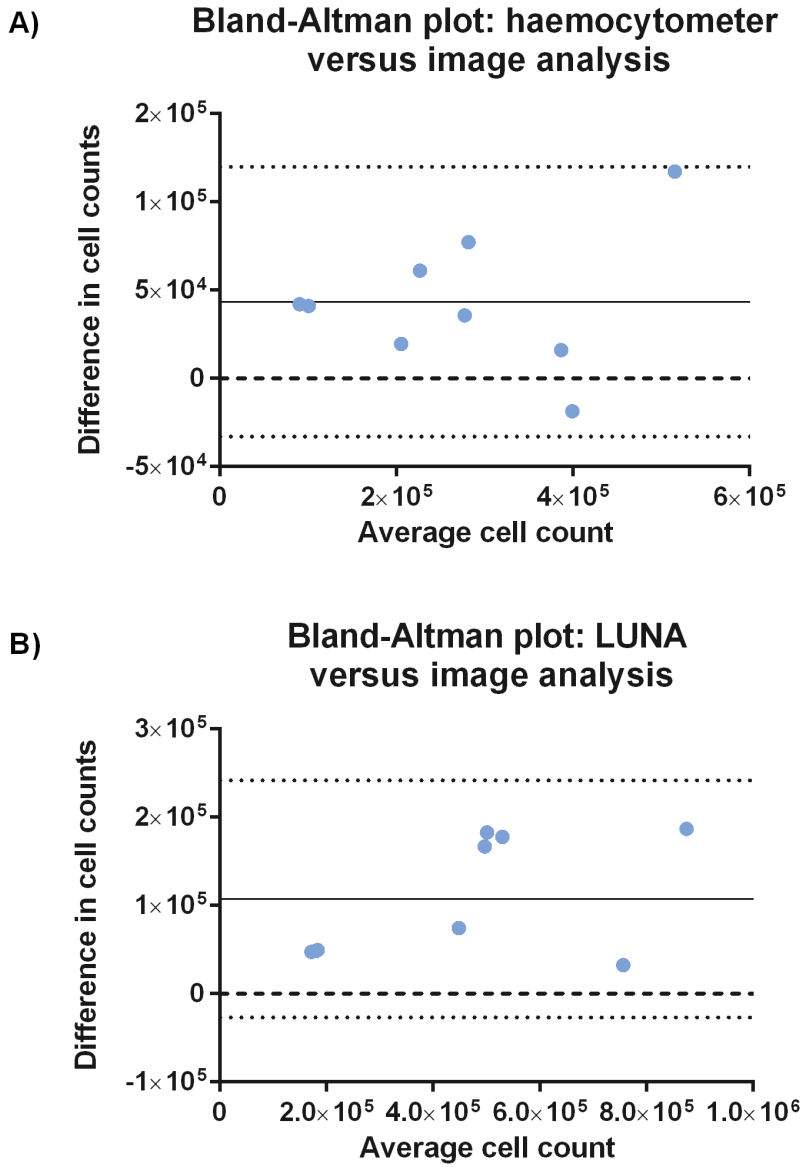

Figure 4.12 – Bland Altman plots comparing the image analysis cell count with cell counts from the same cultures using A) the haemocytometer method and B) the LUNA automated cell counter. *The solid line in the Bland-Altman plot indicates the average difference between measurements by the two modalities (image count subtracted from other modality count) and the dotted lines indicate the 95% limits of agreement (the limits within which 95% of readings should fall). The dashed line indicates the line of zero average difference.*

4.8.2 Sensitivity of methods for distinguishing between different culture conditions

FCS supplementation as described in section 4.6 was used to compare the ability of multiple cell counting techniques to differentiate between cell growth under different culture conditions. H400 cells were seeded in 35 mm dishes at an initial number of $5x10^4$ cells. Triplicate cultures were supplemented with 10, 5 and 2.5% FCS and imaged for analysis at 72 hours after seeding. Cultures were subsequently re-suspended in 1 mL media. For each sample, half of the suspension was centrifuged at 1000 rpm for 5 minutes, re-suspended in 100 µL media and added to a 96-well plate and an MTT assay performed. The other half of the suspension was used to perform haemocytometer and LUNA automated counting. All cell counts were converted to cells/mL to enable direct comparison between methods.

When cell numbers were evaluated using image analysis and MTT assay after 72 hours incubation, the predicted dose-dependent response to FCS supplementation was observed (Figure 4.13). However, cell counts using the haemocytometer method and the automated LUNA cell counter did not show the expected dose-dependent response. Due to the relatively long periods of time required to serially undertake the haemocytometer and LUNA counting methods for three triplicate samples, cells were left in suspension outside the ideal incubator conditions for up to two hours after trypsinisation. During this time it was possible that there was some cell degradation or settling of the cells in the suspension despite agitation before counting, which lead to errors in counts. These results highlight a disadvantage of cell counting techniques which require cells to be in suspension compared with techniques which count cells directly in the *in vitro* environment.

While showing the same dose-dependent growth rate response to FCS, the cell counts from image analysis and MTT assays did not indicate the same cell density at each time point, particularly at 2.5% and 5% FCS concentrations. One potential reason for this is the fact that the MTT assay is a measure of metabolic activity, which is only partially dependent on the number of cells – other factors such as rate of cell division also affect the levels of metabolic enzymes present to form the formazan measured in the assay. Low serum conditions have previously been shown to cause cell cycle arrest, resulting in a higher population percentage of quiescent cells [186]. Since quiescent cells have a lower metabolic activity compared with dividing cells, this could be the cause of the discrepancy between cell number and MTT activity observed in Figure 4.13 [204].

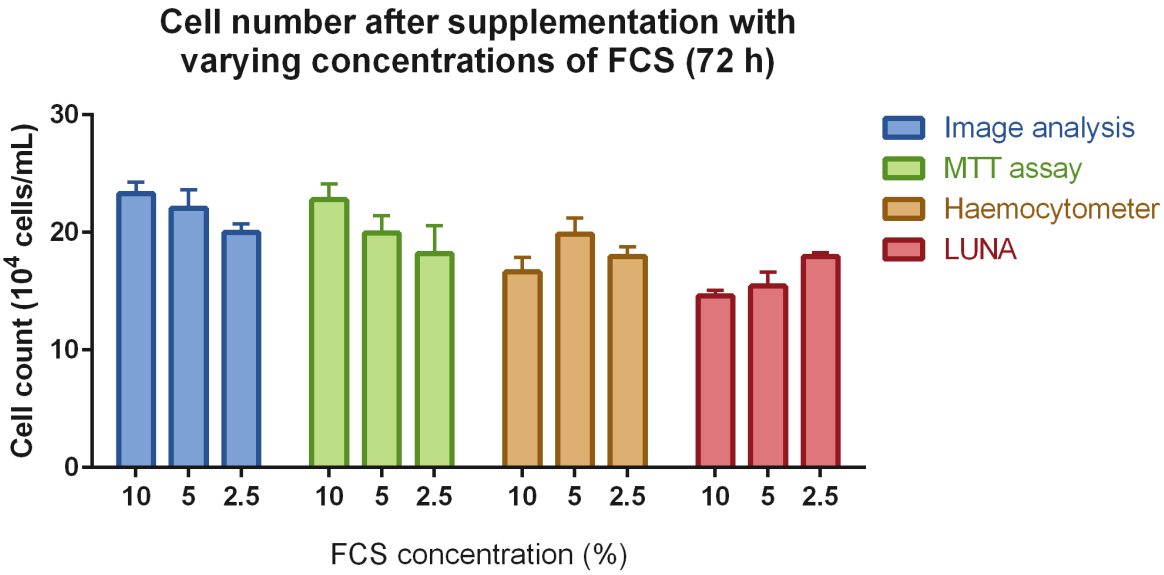

Figure 4.13 - Graph showing cell numbers in H400 cultures supplemented with a range of FCS concentration after 72 hours incubation, as determined by cell counting using image analysis, MTT assay, haemocytometer or LUNA. *Image analysis and MTT methods show the expected dose-dependent response, whereas haemocytometer and LUNA methods did not. Each point is the mean measurement of triplicate culture analysis and error bars show standard deviations.*

One-way ANOVA was performed on counts obtained using the MTT assay and image analysis and in both cases these showed significant differences in mean cell numbers between cultures treated with different FCS doses ($p<0.05$). Dunnett's multiple comparison test was used in each case to identify significant reductions in cell growth when FCS% levels were reduced below the standard 10% maintenance level. 2.5% FCS supplementation showed a significant reduction ($p<0.05$) in growth whereas 5% FCS supplementation did not ($p>0.05$).

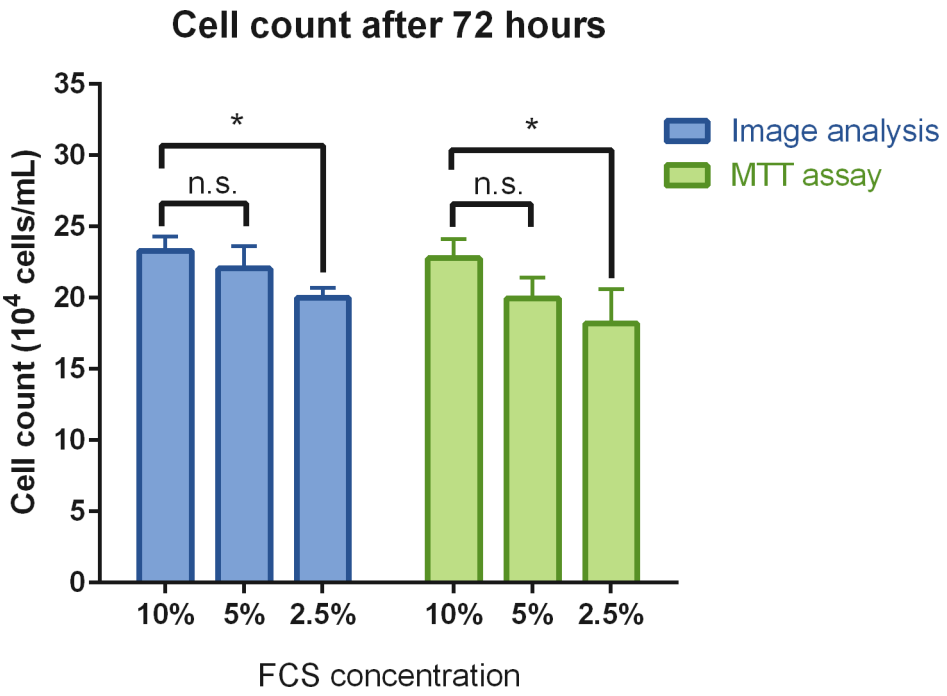

Figure 4.14 – Cell counts in cultures of H400 cells supplemented with 10%, 5% or 2.5% FCS after 72 hours incubation as determined by image analysis and MTT assay. *One-way ANOVA showed significant differences in the means between supplementation levels and Dunnett's multiple comparison test showed cell count after supplementation with 2.5% was significantly lower than the 10% maintenance level. The mean of triplicate cultures is plotted and error bars indicate standard deviation. * indicates $p<0.05$.*

4.8.3 Intrinsic haemocytometer error analysis experiments

Due to its relatively low cost and simplicity, counting cells using the haemocytometer method is a commonplace laboratory technique. However, as has been demonstrated in section 4.7, there was potential for experimental errors using this technique, which could

also have contributed to the systematic difference between cell counts determined by this method and the image analysis method, as presented in sections 4.8.1 and 4.8.2. These errors may occur in the sample preparation stage or be the result of user subjectivity whilst counting. This section details experiments to determine the source and extent of such errors when using the haemocytometer method.

4.8.3.1 Operator variability

Human error in affixing the coverslip to the haemocytometer or loading the sample onto the grid, or ineffective compensation for cell settling in suspension before loading the sample may contribute to errors in cell counts. Each haemocytometer operator may have particular preferences for performing the haemocytometer counts, for example, choice of pipette, use of a cell counting "clicker", which may cause systematic differences between operators through under-mixing of the sample after sedimentation or under/over filling of the chamber during the preparatory phase, or mis-pressing of the clicker or losing count of cells during counting phase. Indeed, variation could occur between multiple readings by the same operator if techniques are not standardised.

Seven independent operators with one year or more of experience using a haemocytometer were requested to count cells from the same sample of H400 cells in suspension. They were instructed to load both sides of the haemocytometer and count the cells in the four large corner squares (as demonstrated in Figure 2.1B) of both sides to generate one "reading"; each operator performed four readings from the same sample of suspended cells. Aside from being instructed to thoroughly aspirate the sample between readings to ensure a homogenous cell distribution, the operators were free to use the haemocytometer as they

would under standard laboratory conditions. The operators were sequentially assigned a unique identity number.

Operator variability was evaluated by performing one-way ANOVA on the four readings taken by each operator. Of the seven operators, one exhibited significant differences between the mean counts of their readings ($p<0.05$); the difference between their largest and smallest average reading equated to 22.75 x 10^4 cells/mL. The remaining operators exhibited no statistically significant difference between their readings (Figure 4.15). The average coefficient of variation (ratio of standard deviation to mean count) of all operators was 18.6%.

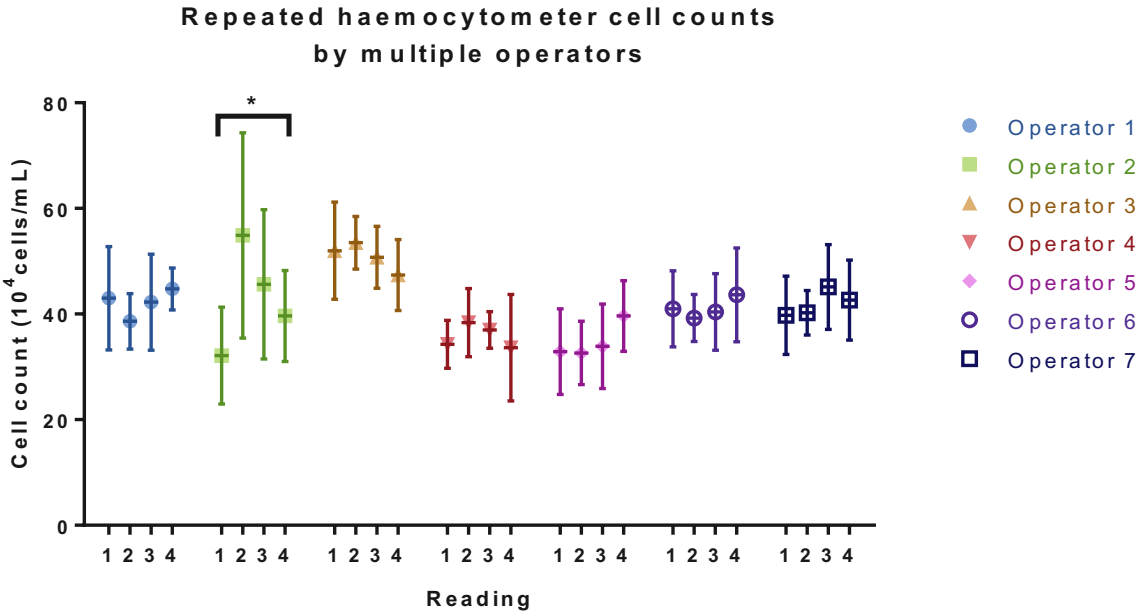

Figure 4.15 – Sets of four haemocytometer readings generated by seven independent operators from the same sample of H400 cells in suspension. *Operator 2 exhibited statistically significant difference mean counts between readings. Each point indicates the average cell count in the 8 large corner squares in the haemocytometer grid, error bars indicate standard deviation. * indicates p<0.05.*

Inter-operator variability was evaluated by performing one-way ANOVA on the average of the four repeats for each operator (Figure 4.16), and statistically significant differences in

the means were identified ($p<0.001$). Tukey's multiple comparison test showed that the mean cell count recorded by operator 3 was significantly higher than those recorded by operators 4 and 5 ($p<0.01$ and $p<0.001$ respectively). However, there did not appear to be a time-dependent effect on operator count, indicating that the cell suspension did not degrade significantly over the course of the experiment (approximately 1 hour). The difference between the highest and lowest average count was 16.2 x 10^4 cells.

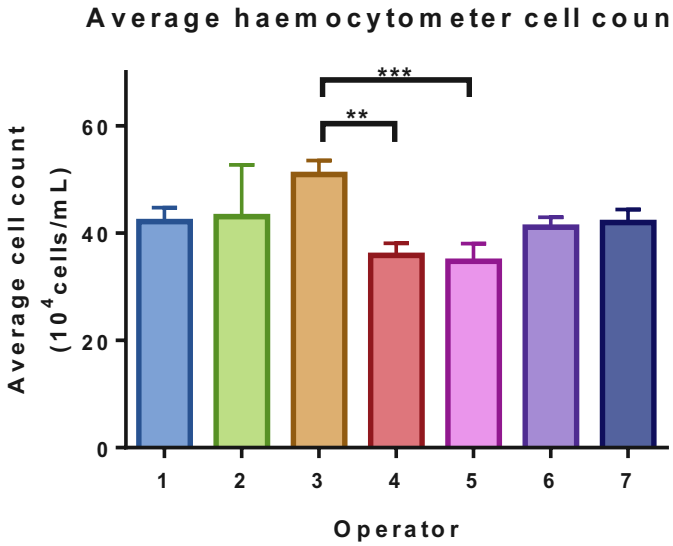

Figure 4.16 – Average count of four repeat readings by seven operators from the same sample of H400 cells in suspension. *Operators were assigned a number chronologically. The mean count by operator 3 was significantly higher than those by operators 4 (** indicates $p<0.01$) and 5 (*** indicates $p<0.001$). Error bars indicate standard deviation.*

4.8.3.2 Error due to subjectivity in counting

As with all measurements performed by human judgement, there is a degree of subjectivity in counting the number of cells in a haemocytometer grid, as demonstrated in Figure 2.1B. Cells that overlap with the lines of the haemocytometer grids are a particular source of ambiguity and haemocytometer operators generally use systematic approaches to ensure consistency in including or rejecting such cells in the count. The default strategy used in all other experiments in this thesis is to include cells overlapping the top and right-most edges

of the grid and reject those overlapping bottom and left (Figure 2.1C). Other operators may use different systematic approaches, but the accuracy of the technique relies upon the operator's consistent application of the system and ability. This becomes more difficult at high cell densities, where the potential to lose track of the cell count increases.

To isolate any effects of subjectivity in cell counting, one side of a haemocytometer was pre-loaded with a sample of H400 cells in suspension and six operators with prior haemocytometer experience were requested to count the cells in all nine large squares (Figure 2.1B). The operators were instructed to count the cells as they usually would during their own study protocols, i.e. no instructions were provided regarding how to account for cells overlapping the edges of the grids. The use of cell counter clicker was optional.

The number of cells per square was generally similar when counted by each operator; in particular an outlier in one of the grid squares was clearly identifiable in the counts from all operators (Figure 4.17). However, a maximum difference of 23 cells from a single square was observed by two subsequent operators in square 6, equivalent to a difference of 2.3×10^5 cells per mL. Despite this, one-way ANOVA performed on the dataset showed that the mean counts by each operator were not significantly different ($p>0.05$).

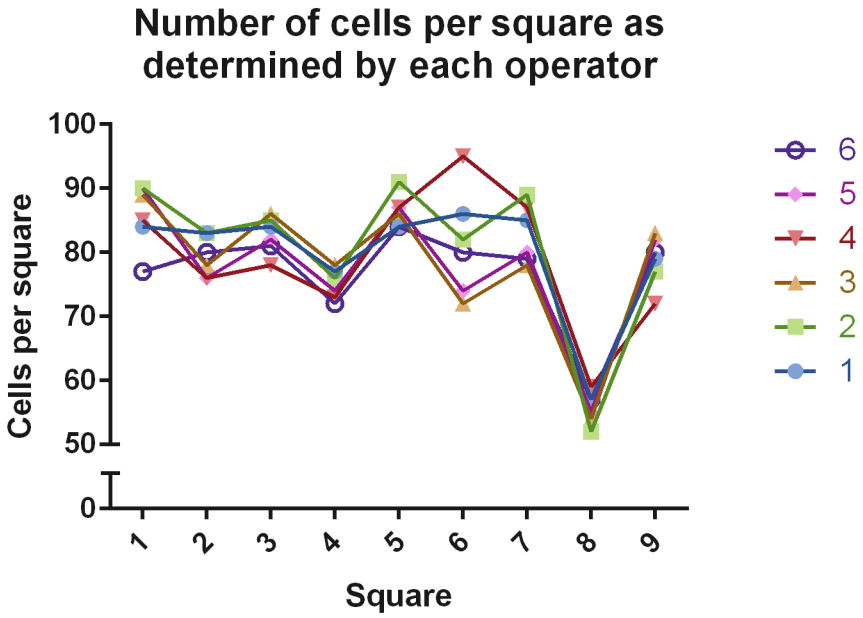

Figure 4.17 – Scatter plot showing the cell counts of each square in one side of a loaded haemocytometer as performed by six different users. *Each user is represented by different coloured points. One-way ANOVA detected no difference in the inter-operator means (p>0.05). Haemocytometer square 8 contained an outlying number of cells, which was clearly identified by all users. The square with the greatest difference between counters was square 6 (23 cells difference).*

4.9 Suitability of the image analysis approach for cell counting in different cell lines

The H400 cell line was used during all stages in the development of the image analysis method however the potential for use of the method for cell counting in other adherent cell lines was investigated through application to OKF6 oral keratinocytes, 3T3 fibroblasts and U2OS osteosarcoma cells.

For each cell line used, co-localised PC and epifluorescence images of stained nuclei were acquired and, where possible, the parameterisation method using nuclear ground truth as described in section 3.3.2.2 was applied and the noise removal methods evaluated.

4.9.1 OKF6 cell line

OKF6 keratinocytes were initially used to test the potential wider application of the image analysis cell counting procedure since they are also a human oral epithelial cell line (as described in section 2.1.1.2) [205]. Despite this, substantial differences compared with H400 cells were observed in OKF6 cultures in terms of both morphology and growth characteristics. Identification of individual OKF6 cells in PC images was extremely difficult due to the formation of tight cell colonies, which resulted in cell boundaries being unclear (Figure 4.18A). Inspection of the corresponding images of cell nuclei also revealed that OKF6 cells overlapped with neighbouring cells (Figure 4.18B). The image analysis method in chapter 0 was developed under the assumption that cells grow in a two-dimensional monolayer (i.e. non-overlapping). Since this assumption was not valid for OKF6 cells, it was not possible to consider this cell line for further analysis.

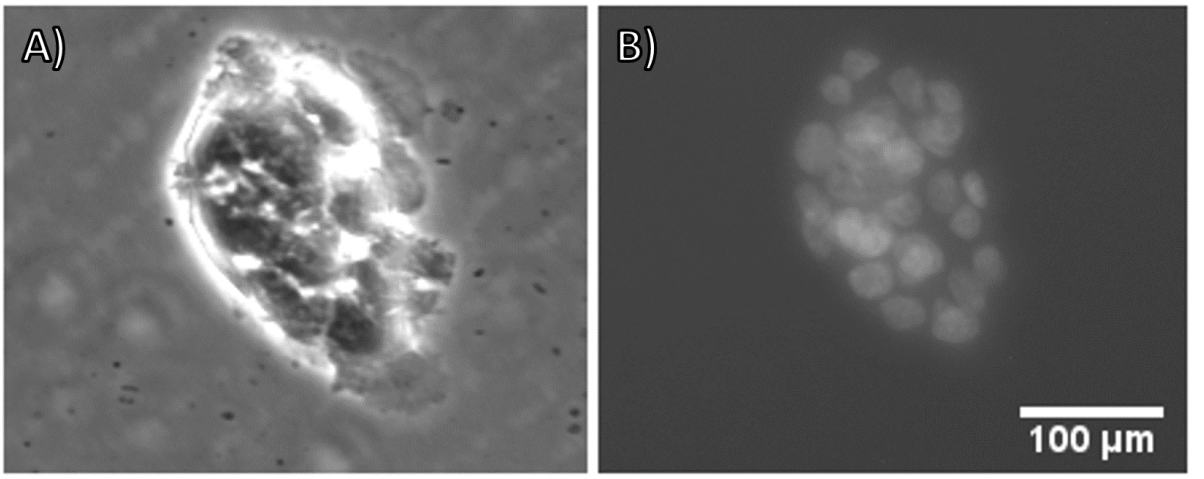

Figure 4.18 – Representative PC and epifluorescence microscopy images of OKF6 cells fixed with 10% formalin and stained with DAPI. *A) PC microscopy image showing it is not possible to distinguish individual cells from one another since the cell edges are not clearly delineated. B) The corresponding epifluorescence microscopy image of DAPI-stained cell nuclei showing that cells overlap with one another. Scale bar for both images is shown in B).*

4.9.2 3T3 cell line

The 3T3 fibroblast cell line is commonly cultured *in vitro* and used both as a model for fibroblast behaviour and to facilitate the cultivation of other cell lines [205], [206]. Importantly, unlike OKF6 cells these cells remain highly sensitive to contact inhibition, thus tend to form single-layer sheets when cultured *in vitro* unlike many other cell lines established *in vitro* from primary tissue [207]. However, unlike H400 epithelial cell morphology, which is generally polygonal, fibroblast morphology may become bi- or multi-polar, or they may extend lamellipodia to display stellate or fusiform morphology (refer to Figure 4.21 for an example showing 3T3 morphology). Additionally, 3T3 cell morphology is heterogeneous in size and shape compared with typical H400 morphology, which tends to be more regular in appearance. The 3T3 cell line was selected for investigation to explore whether the image analysis method could effectively count cells with such heterogeneous morphological features.

When parameterisation using the nuclear ground truth method was applied to 608 3T3 cells, a peak in the graph of correct cell detections for each parameter pair was observed similarly to H400 cells (Figure 4.19). However, the maximum detection rate for 3T3 cells was lower than that achieved for H400 cells (81.91 % compared with 87.1%). The parameter pair with the highest percentage of correct detections was found to be $r_{small} = 7$ pixels (6 µm) and $r_{large} = 25$ pixels (23 µm), and these values were selected for further use on images derived from 3T3 cultures.

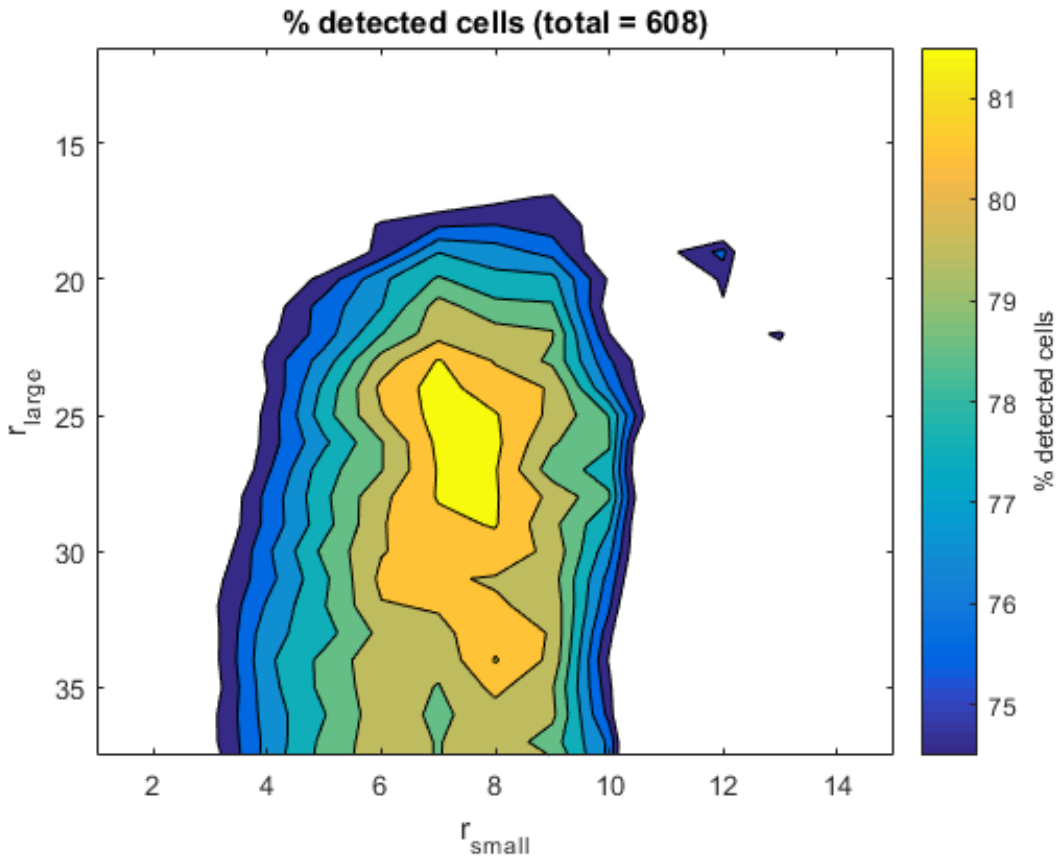

Figure 4.19 – Contour map showing the percentage of 608 3T3 cells correctly detected as defined by comparison with corresponding nuclear ground truth for a range of parameter combinations. *A maximum was observed at $r_{small} = 7$ pixels and $r_{large} = 25$ pixel, indicating these were the optimal parameters.*

Mis-segmentation events were quantified using the selected parameters on the ground truth set as described previously (section 3.3.2.1). Figure 4.20A indicates how of each of the cells in the ground truth dataset were labelled with the final selected parameters. The reduction in detection success compared with H400 cells could mostly be explained by an increase in the number of cells labelled as split: 8.7% for 3T3 cells compared with 2.4% for H400 cells.

The percent contributions to the cell count error for each type of mis-segmentation are shown in Figure 4.20B. Similar to H400 cells, noise segmentations are the largest contributor, however in the case of 3T3 cells the effect of noise is much greater, increasing the cell count

by 83%, compared with only 23% for H400 cells. The contribution from split cells is also substantially increased, from 2.7% to 21%.

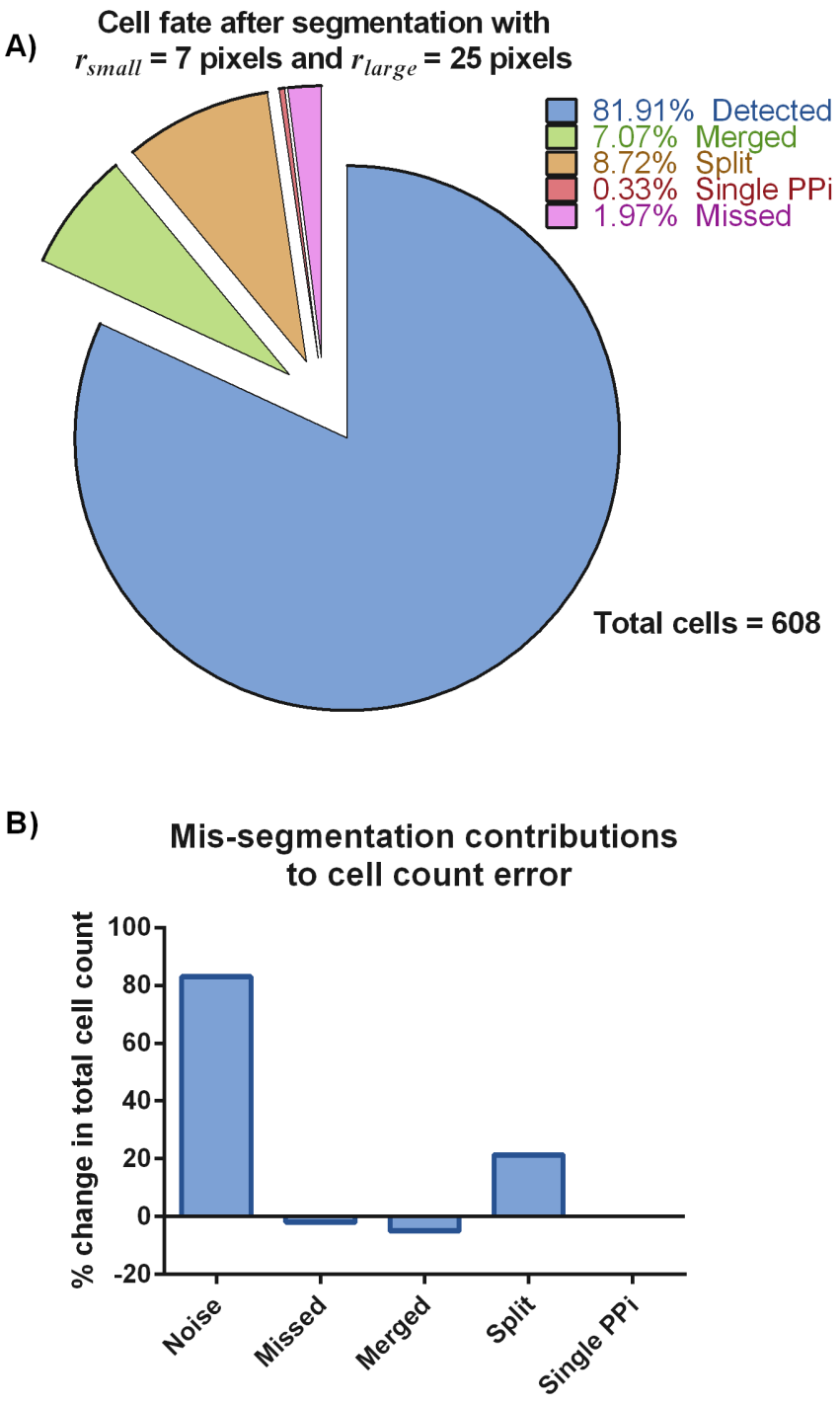

Figure 4.20 – Cell fates and mis-segmentation rates for 3T3 cells segmented using r_{small} = 7 pixels and r_{large} = 25 pixels. *A) Pie chart showing how each cell in the 3T3 parameter training set is labelled using the final parameters of r_{small} = 7 pixels and r_{large} = 25 pixels. B) Bar chart showing the types of error leading to count error and their contribution to the change from the true count. Noise segmentations are the biggest contributor to errors in the cell count, although split cells also contribute a large change in cell number.*

The labelled dataset with morphological and greyscale features of each region was used to train the supervised learning techniques described in section 3.3.3.2.2 to identify mis-segmented regions. As for H400 cells the priority was to remove noise regions, however the substantial contribution to error from split cell segmentations means that it was now important to also identify these regions for correction, thus the possibility of training classifiers to identify merge and split objects in addition to noise was firstly investigated. The data presented in Table 4.1 show that none the classification techniques tested were able to identify merged and split cells without substantial reductions in the cell recall rate. Relabelling of split and merge mis-segmentations as cells in an attempt to target identification of noise regions was also unsuccessful – none of the techniques improved noise recall rate and at least 16% of cells were misclassified as noise in all cases (Table 4.2).

Classifier	**Overall accuracy (%)**	**Cell recall (%)**	**Noise recall (%)**	**Merge recall (%)**	**Split recall (%)**
Simple tree	75.9	82	91.9	0	0
LDA_diag	67.9	69.1	76.8	**53.3**	**30.8**
LDA_auto	76.3	84.8	85.7	20	14.6
SVM	**78.6**	**87.9**	**92.3**	0	0

Table 4.1 - Results of classification of 3T3 cell segmentations into 4 classes. *The highest scoring results in each category are indicated in bold text.*

Classifier	Overall accuracy (%)	Cell recall (%)	Noise recall (%)	F1 score
Simple tree	82.2	80	85	0.83
LDA_diag	82.4	78.8	**86.7**	0.83
LDA_auto	84.2	83.8	84.8	0.85
SVM	**84.7**	**84**	85.5	**0.86**

Table 4.2 – Results of classification of 3T3 cell segmentations into "noise" and "cell" classes. *The highest scoring results in each category are indicated in bold text.*

Closer inspection of the segmented cells showed that the irregular and inconsistent shape of the fibroblasts contributed considerably to the high rates of noise and split mis-classifications cells, since long protrusions in 3T3 cells were often segmented into multiple disconnected regions. As exemplified in the image shown in Figure 4.21, correct cell detections (indicated by white arrows) occurred either in cells with smaller cell bodies and few protrusions, or in cells with long protrusions when only one of the segmented regions overlapped with the nucleus. In this case the remaining disconnected cell segmentations were detected as noise (indicated by black arrows). When more than one segmented region was partially overlapping with the nucleus, the cell was labelled as a split mis-segmentation (green dashed lines). These types of mis-segmentation also explain the lower success rate when using morphological and greyscale features to train classifiers to identify noise regions – many "noise" regions comprise cell regions disconnected from the nucleus, thus they have similar features as those cells that are connected to the nucleus and are unable to be distinguished using these techniques.

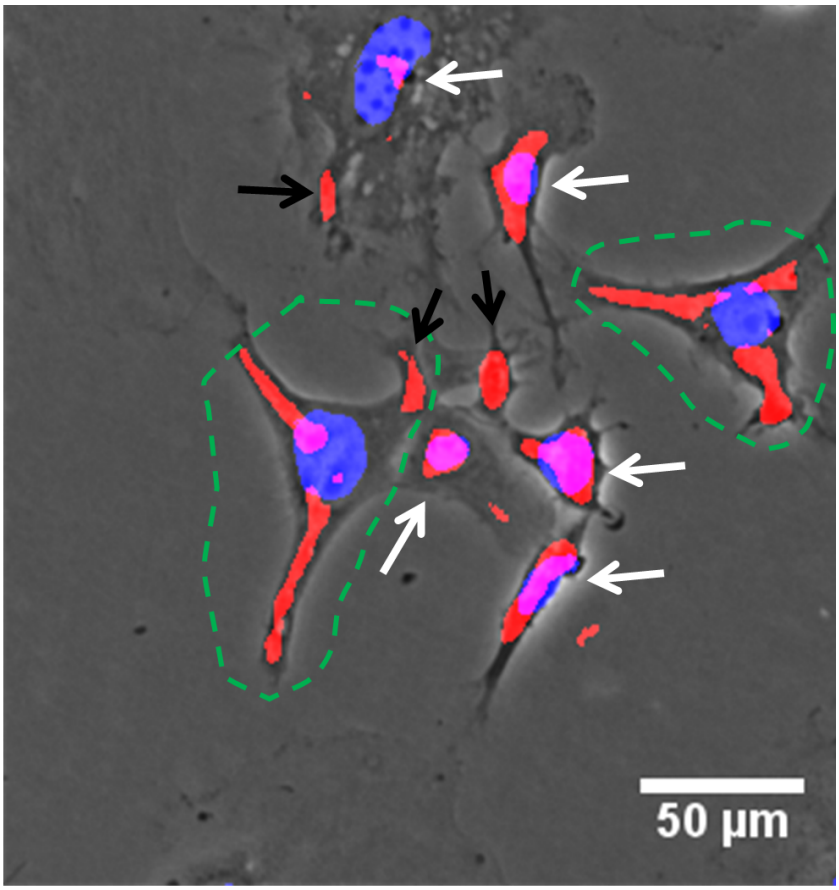

Figure 4.21 – Representative PC image of 3T3 fibroblast cells overlaid with stained and segmented nuclei in blue and segmentations obtained using $r_{small} = 7$ pixels (6 µm) and $r_{large} = 25$ pixels (23 µm) in red. *White arrows indicate correct cell detections, black arrows indicate parts of cells that have been segmented but that are registered as noise due to being disconnected from the nucleus. Green dashed lines indicate cells which are registered as "split" mis-segmentations.*

Low cell detection rates and high noise levels coupled with unsatisfactory performance of noise removal techniques lead to the conclusion that the image analysis technique was unsuitable for counting cells in cultures of 3T3 fibroblasts.

4.9.3 U2OS cell line

U2OS cells were selected for experimentation since, like H400 cells, this cell line displays regular epithelial morphology and forms non-overlapping monolayers when cultured *in vitro* (Figure 4.22), and are often used as a model for bone tissue [148], [208].

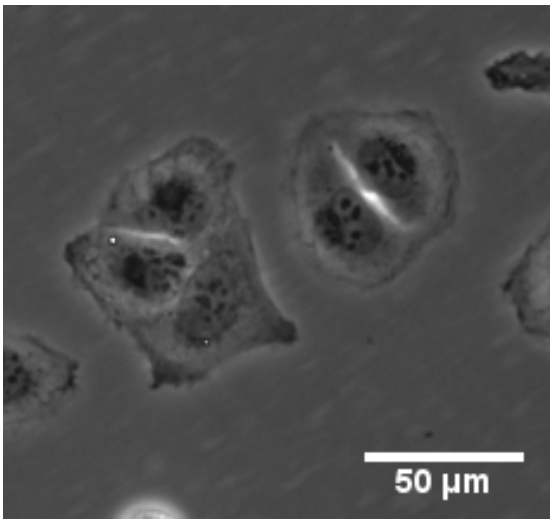

Figure 4.22 - Phase contrast microscopy image showing morphology of U2OS cells. *The morphology is more rounded and regular in size and shape, similar to the H400 cell line (Figure 4.4G-i) and unlike the 3T3 cell line (Figure 4.21).*

When parameterisation was performed, the correct cell detection rates were found to be higher than that for H400 cells – the peak detection rate was 92% compared with 87.1%. Additionally, the cell detection rate had a smaller dependence on r_{large}, i.e. there was not an obvious peak region in the parameter map but rather a range r_{large} values that gave similar detection rates (Figure 4.23). The parameters selected were $r_{small} = 9$ pixels (8 µm) and $r_{large} = 30$ pixels (27 µm).

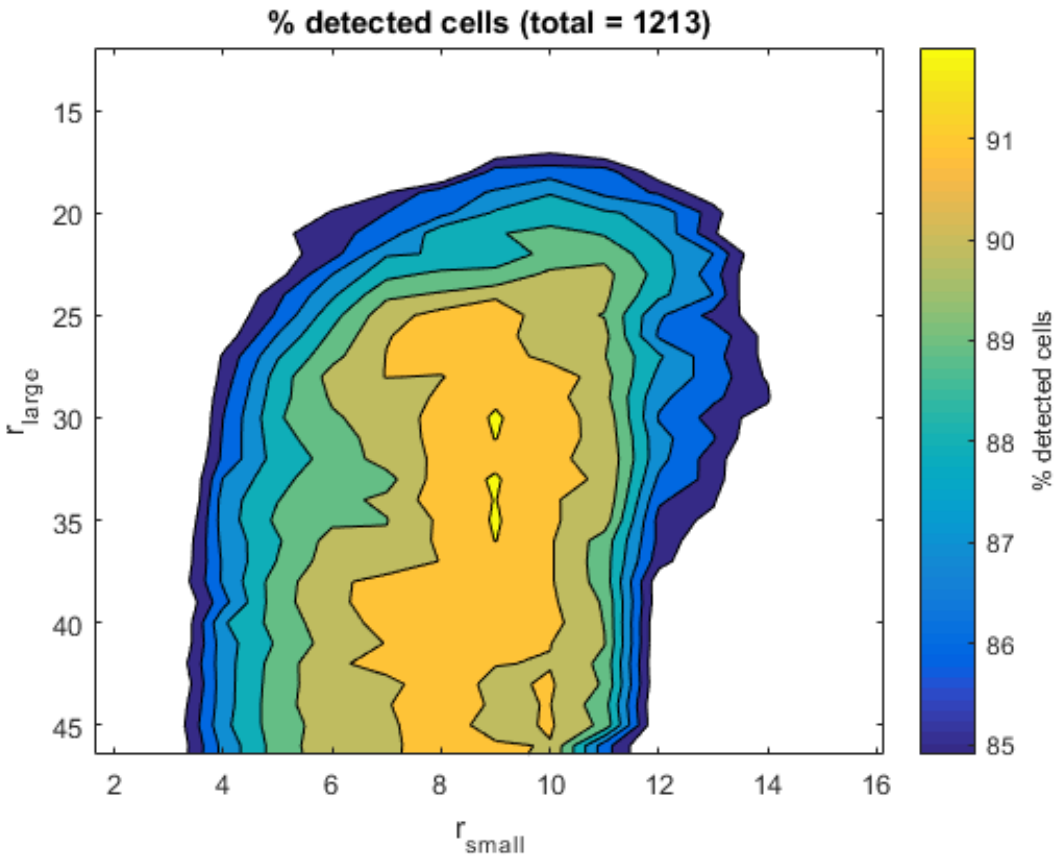

Figure 4.23 – Contour map showing the percentage of 1213 U2OS cells correctly detected as defined by comparison with corresponding nuclear ground truth for a range of parameter combinations. . *A maxima was detected at* $r_{small} = 9$ *pixels and* $r_{large} = 30$ *pixels.*

The increase in detection rate compared with H400 cells was due to a decrease in the percentage merge and split mis-segmentations (Figure 4.23A). However, similarly to H400 and 3T3 cell lines, noise mis-segmentations still contributed considerably to the error in the cell count (Figure 4.23B), thus approaches to identify these regions for removal were necessary. The supervised classification techniques were investigated as described in section 3.3.3.2.2, and the data presented in Table 4.3 to Table 4.5. It was not possible to distinguish merge and split mis-segmentations from cell segmentations, so these categories were subsumed into the cell category. In this instance three out of the four methods tested gave high F1 scores of 0.97. Of these SVM and LDA with auto-regularisation achieved the joint-

highest overall accuracy. LDA was chosen since it achieved a higher rate of noise classification of 78.2% and this was used for noise removal in applications to cell counting.

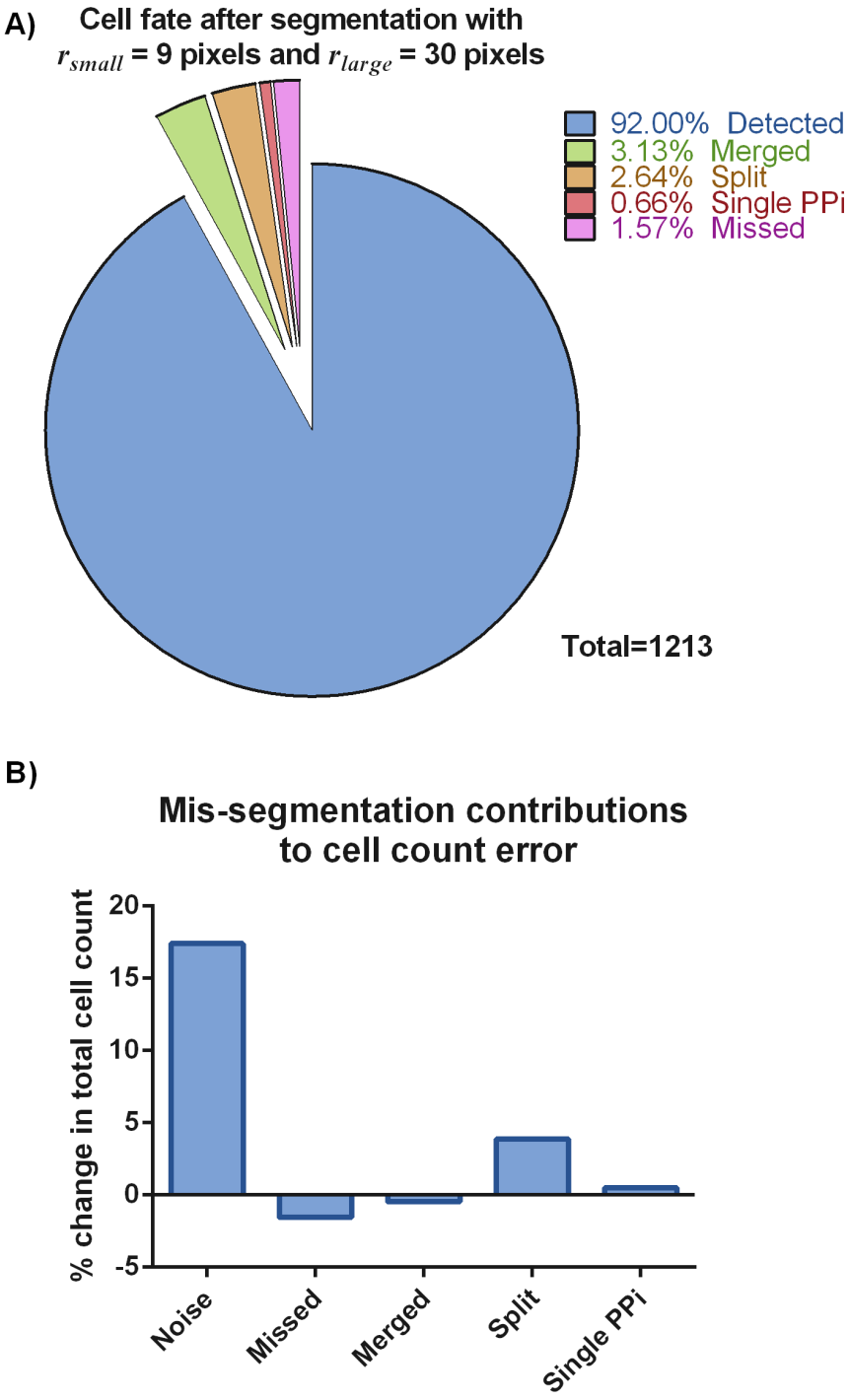

Figure 4.24 – Cell fates and mis-segmentation rates for U2OS cells segmented using r_{small} = 9 pixels and r_{large} = 30 pixels. *A) Pie chart showing how each cell in the parameter training set is labelled using the final parameters of r_{small} = 9 pixels and r_{large} = 30 pixels. B) Bar chart showing the types of error leading to count error and their contribution to the change to the true count. Noise segmentations are the biggest contributor to errors in the cell count.*

Classifier	Overall accuracy (%)	Cell recall (%)	Noise recall (%)	Merge recall (%)	Split recall (%)
Simple tree	91.9	97.4	**80.1**	0	0
LDA_diag	79.3	82.1	71.6	**50**	**38.3**
LDA_auto	90	95.4	75.8	16.7	10.6
SVM	**92.5**	**98.3**	79.6	0	0

Table 4.3 – Results of classification of U2OS cell segmentations into "cell" class and "noise", "merge" and "split" mis-segmentation classes. *The highest scoring results in each category are indicated in bold text.*

Classifier	Overall accuracy (%)	Cell recall (%)	Noise recall (%)	F1 score
Simple tree	94.9	97.9	75.4	**0.97**
LDA_diag	93.5	95.7	**79.1**	0.96
LDA_auto	**95.1**	97.7	78.2	**0.97**
SVM	**95.1**	**98.1**	75.4	**0.97**

Table 4.4 – Results of classification of U2OS cell segmentations into "noise" and "cell" classes *"Merge" and "split" segmentations were subsumed into the "cell" category. The highest scoring results in each category are indicated in bold text.*

Classifier	Overall accuracy (%)	Cell recall (%)	Merge recall (%)	Split recall (%)
Simple tree	95.7	**100**	0	0
LDA diag	78.4	78.7	**50**	**74.5**
LDA auto	93.1	95.9	16.7	23.4
SVM	**96.1**	**100**	0	0

Table 4.5 – Results of classification of noise-free U2OS cell segmentations into "cell", "merge" and "split" classes. *The best results in each category are indicated in bold text.*

4.9.3.1 Validation of cell counting method on U2OS cells

The image analysis method was applied using the parameters and noise removal methods described in the previous section to generate growth curves for U2OS cells in triplicate cultures supplemented with 10%, 5% and 2.5% FCS (35 mm dishes). Growth curves indicated that U2OS cells cultured with all levels of supplementation proliferated at similar rates until 67 hours after seeding, after which time a dose-dependent response was observed (Figure 4.25).

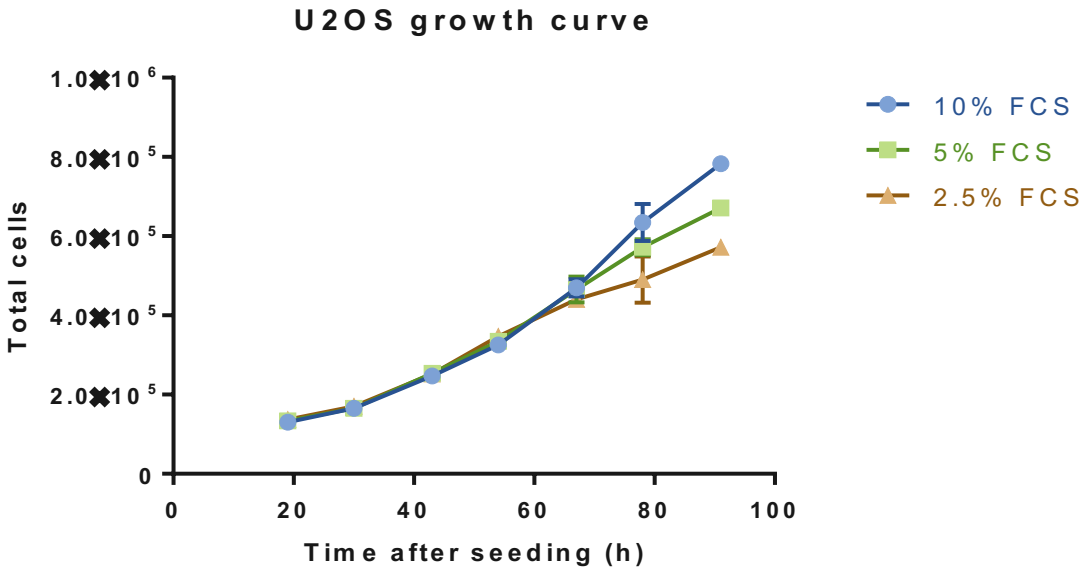

Figure 4.25 – Growth curves of U2OS cells supplemented with a range of concentrations of FCS as measured by the image analysis method. *The growth curves show the expected dose-dependent response after 67 hours incubation. No differences in culture growth were detected prior to this time point. Each point is the average of triplicate cultures and error bars indicate standard deviation.*

4.10 Conclusion

The first objective of the work detailed in this chapter was to establish optimal laboratory protocols for application of the image analysis cell counting method to generate accurate growth curves. It was determined that the image analysis method may be applied to cells

grown in wells of diameter of 22.1 mm (12-well plate) or greater without image degradation from menisci formed by media at well walls. Additionally, it was determined that at least 11 images should be acquired for an accurate estimation of total cell number whilst minimising image acquisition time, and that in small vessels images should be acquired without lids to avoid image degradation caused by media condensation.

A range of nuclear fixation and staining protocols were tested to determine which one(s) were most appropriate for use in application of the parameterisation method. Unfixed cells stained with the Hoechst nuclear dye was selected as the most appropriate protocol since it avoided the morphological artefacts caused by cell fixation. However, it was shown that when cultures fixed with 10% formalin and stained with Prolong Gold Antifade mountant with DAPI in the parameterisation step, the parameters obtained were similar to those achieved by live Hoechst-stained cultures, although detection rates were misleadingly high due to cell rounding caused by fixation.

The image analysis cell counting method was compared to other segmentation methods to determine whether results were comparable between algorithms. As expected, thresholding methods were found to be unsuitable for segmentation of cells in PC images due to the similarity in intensity between cell cytoplasm and unpopulated background regions, which caused both regions to be erroneously classified as the same region type. Whilst achieving success previously in accurate segmentation of single uncontacting cells in PC images [93], the graph cut method with asymmetric boundary costs was unable to distinguish between cells in a monolayer as is required for successful enumeration, therefore was not considered further for comparison. The Chan-Vese implementation of the level set method was found to

be highly susceptible to changes in initialisation as documented previously [83]. Whilst initialisation using a grid of circles was able to achieve some correct cell detections, the detection rate using the best performing smoothing parameter was approximately half that of the rate achieved by the cell counting method developed in this thesis. Other initial contours may give improved results, although the vast range of possibilities may be difficult to optimise, unlike the automated parameterisation for the method developed in this thesis. Other methods may give more comparable results but were not freely available thus could not be considered in the comparison.

Given the relatively poor cell counting results achieved by image analysis methods, a more suitable validation method is therefore to compare laboratory methods for cell counting. It was shown that image analysis counts were systematically lower than counts performed on the same samples using the haemocytometer method or LUNA by 4.9×10^4 and 10.7×10^4 cells/mL, respectively. In the case of haemocytometer counting, the source of this difference could be explained by operator bias – experiments comparing counts from the same sample by multiple haemocytometer operators showed the measured counts from a given sample were different by as much as 16.2×10^4 cells/mL. In extreme cases, inconsistencies in readings performed by a single operator alone were measured to be up to 2.28×10^4 cells/mL. The greatest contributor to such errors is likely to be due to ineffective homogenisation of the cell suspension rather than subjectivity in reading the sample, since differences in readings between operators when reading from the same pre-loaded haemocytometer were considerably lower. Furthermore the counts obtained using the LUNA automated image analysis method, also exhibited similar discrepancies. Errors in cell mis-segmentation and noise removal could also have contributed to the difference between

methods. Merge mis-segmentation errors are unlikely to have caused the discrepancy since the contribution to undercounting was largely balanced by split mis-segmentation (Figure 3.13B). Another source of error could be the 4% of cells which were removed as a byproduct of the noise removal method.

Despite these systematic differences, the counts are linearly correlated thus the image analysis method was able to measure relative cell count changes, as was validated through generation of growth curves in cultures supplemented with differing FCS levels.

Investigations into the application of the image analysis cell counting technique on other cell lines showed it performed poorly on the OKF6 cell line which grew in overlapping cell clusters, and in the 3T3 cell line which exhibited more irregular cell morphology. Conversely, the image analysis technique was applied successfully to the U2OS osteosarcoma cell line which displays regular rounded cell morphology and grows in single-layer sheets, even outperforming the rate of correct cell detection achieved for H400 cell cultures. Therefore it is recommended that the image analysis method performs best when analysing adherent, contact inhibited cell lines with epithelial-like morphology.

5 CHARACTERISATION OF SILVER NANOPARTICLES

5.1 Introduction

As discussed in the introduction, silver nanoparticles are increasingly common in dental applications for their antibacterial properties, however their effects on oral epithelial tissues have not yet been thoroughly characterised. The aim of the work presented in chapter 6 is to utilise the image analysis method developed and validated in chapters 0 and 4 as an assay for nanotoxicological studies. However, as discussed in section 1.7.3, AgNP have been shown to have both size and dose-dependent effects, and experimental conditions have also been shown to affect AgNP stability and toxicity. It is therefore critical to thoroughly characterise these features for each AgNP sample used to fully contextualise any nanotoxicity observed in cells or bacteria. This chapter describes the characterisation of the two sizes of silver nanoparticle used in the work described here (the synthesis of which is reported in sections 2.6.1 and 2.6.2) using a series of analytical techniques prior to investigations into their effects on H400 cells and bacteria.

5.2 Validation of stochiometrically calculated AgNP-10 concentration

The concentration of synthesised nanoparticles, or "AgNP-10", was calculated stoichiometrically from the known mass of silver nitrate used (section 2.6.1.1) and was determined to be 26.96 µg/mL. Synthesised samples were concentrated by centrifuging the colloidal AgNP-10 to form a pellet of nanoparticles, before removing the majority of the supernatant prior to resuspension.

The nanoparticle concentration increase after centrifugation was calculated using the ratio of the UV-vis spectroscopy peaks (section 2.6.4.1) and was determined to be 6.95. ICP-OES

(section 2.6.5.3) was used to verify this value and results of these analyses are presented in Figure 5.1.

Although the concentration of AgNP-10 stock measured with ICP-OES differed significantly from the stoichiometric calculation (17.84 µg/mL compared to 26.96 µg/mL), the concentration factor between stock and concentrate was similar to that calculated using UV-vis spectroscopy (6.58 compared to 6.95). This indicated that the error was systematic, perhaps introduced during the instrument calibration step. Subsequently the concentration values for AgNP-10 stock (26.96 µg/mL) and concentrate (187 µg/mL) calculated stochiometrically from the known mass of $AgNO_3$ used in synthesis and using UV-vis calibration curve were those that were used in all subsequent work.

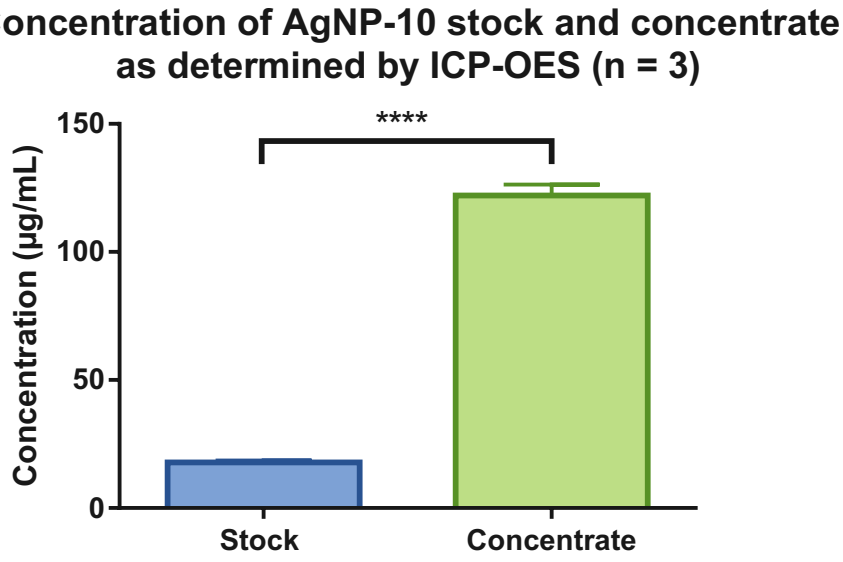

Figure 5.1 – Concentration of AgNP-10 stock compared with AgNP-10 concentrate as determined using ICP-OES. *The AgNP-10 stock was determined to be 17.84 µg/mL, and the concentrate 122.1 µg/mL, a concentration factor of 6.58. The concentrations determined were significantly different (**** indicates p<0.0001). The average of triplicate samples is plotted and error bars indicate standard deviation.*

The chemicals used in AgNP-10 synthesis, $AgNO_3$ and $NaBH_4$, were included as controls in all experiments testing antibiotic and cytotoxic properties. Concentrations of these chemicals equivalent to the AgNP-10 concentrate were calculated by multiplying the concentrations used in synthesis by the concentration ratio, 6.95. These values were 294 µg/mL for $AgNO_3$, 391 µg/mL for $NaBH_4$ – these will be referred to in further experiments as the "equivalent concentrations"

5.3 Maximum dose volume for treatment of H400 cell cultures

Since all nanoparticles and other treatments studied here were suspended in RO water, the maximum dose that could be administered to cell cultures was limited by the volume that could be supplemented into the culture media without inhibiting cell growth through media dilution. To determine the water concentration which limited cell growth, an MTT assay was performed using H400 cells at 24 hours after treatment with volumes of water between 2-50% of the total media volume (n=6). Dunnett's multiple comparison test showed water added at a volume of 20% or less of the total volume did not significantly reduce cell growth as compared with the controls ($p>0.05$) (Figure 5.2). Subsequently a maximum dilution of 1:5 was used in all future experiments, limiting the maximum possible treatment concentration of AgNP-10 to 31.1 µg/mL. The same volume of RO water was added to cultures to provide appropriate controls.

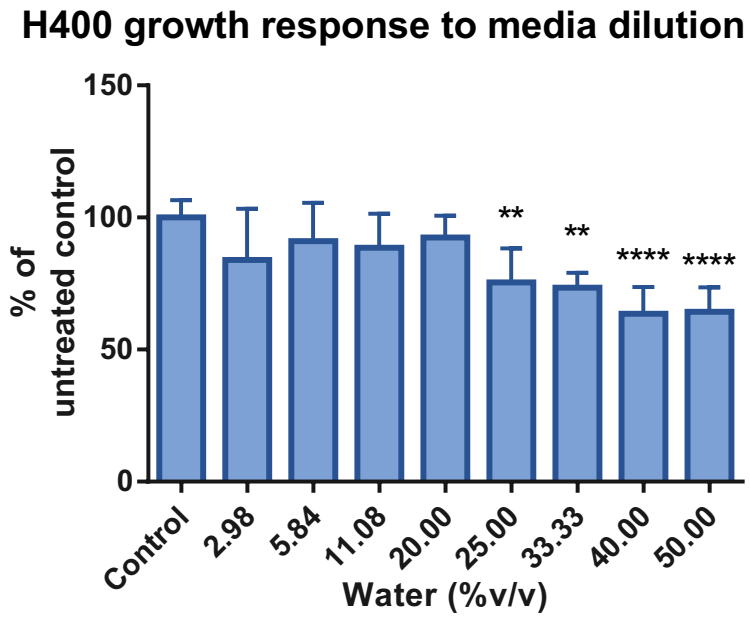

Figure 5.2 – H400 cells cultured in medium diluted with water and growth response analysed using the MTT assay. *Percentages of the untreated control are shown. There were no significant reductions in MTT levels in cultures diluted with 20% volume or less of water. The average of 6 replicate wells were plotted and error bars indicate standard deviation. (** indicates p>0.01, **** indicates p>0.0001)*

5.4 Characterisation of nanoparticle size distributions

Several approaches were used to characterise the size distributions of nanoparticles generated and to enable comparison of nanoparticle properties both in water and diluted with cell media or bacteria broth.

5.4.1 UV-vis spectroscopy

Although UV-vis spectroscopy was unable to provide a direct quantitative measurement of particle diameter, as discussed in section 2.6.4.1, the peak wavelength and spread of the absorbance spectrum was useful for comparing particle size distributions between two samples as there is a particle size-dependent relationship with absorbance wavelength.

The UV-vis spectra of AgNP-10 stock and concentrate are compared in Figure 5.3. The peak wavelength of the concentrate was similar to that of the stock [396 nm (concentrate)

compared to 398 nm (stock)], indicating that modal particle sizes were similar. However, the FWHM of the concentrate was greater than that of the stock (61 nm compared with 57 nm), indicating a wider distribution of particle sizes. Furthermore, there was an increase in absorbance between 450 nm and 550 nm (demonstrated by an arrow in Figure 5.3) indicating an increased presence of larger particles compared with the stock.

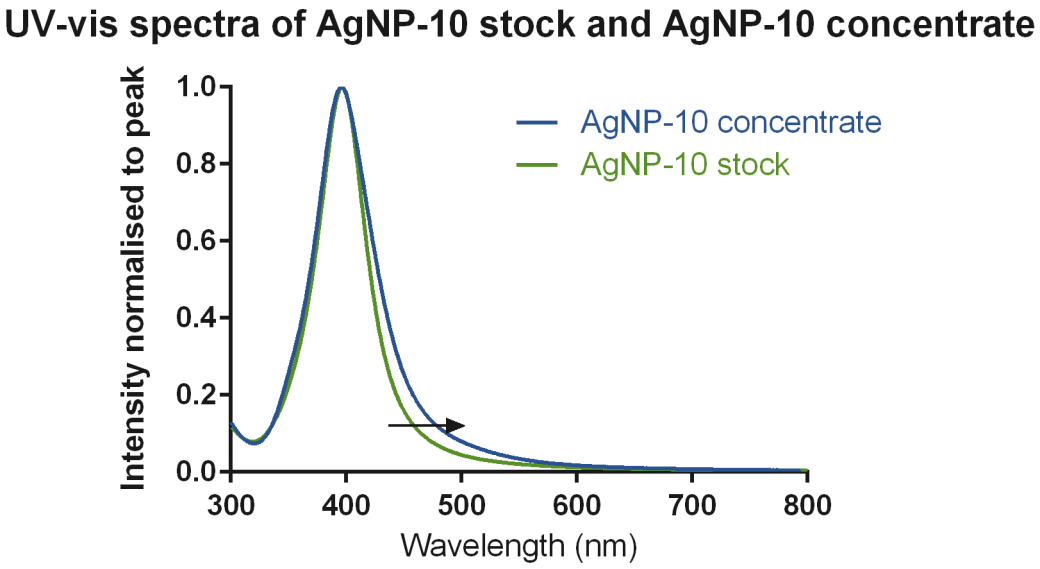

Figure 5.3 – UV-vis spectra for synthesised AgNP-10 stock (green line) and AgNP-10 concentrate (blue line). *For wavelengths between 450 – 500 nm there was a shift to higher absorbance (indicated by arrow) for the AgNP-10 concentrate. These data indicated an increased presence of larger particles in this sample.*

UV-vis spectra were acquired in DMEM media with 10% FCS and BHI broth treated with 20% AgNP-10 stock to evaluate the effects of AgNP interaction with salts and proteins on size distribution.

To correct for additional peaks in the UV-vis spectrum caused by the absorbance of cell media or broth, a background spectrum of DMEM cell media supplemented with 10% FCS or BHI broth treated with 20% water was acquired and subtracted from media treated with

20% AgNP-10. An example showing the background spectrum of supplemented DMEM media is shown in Figure 5.4A.

The spectrum of AgNP-10 diluted in media is compared with that of AgNP-10 stock only in Figure 5.4B. The peak intensity of the AgNP-10 in media was shifted from 398 nm to 407 nm, and the FWHM increased from 57 nm to 65 nm which indicated an increase in the average size of the nanoparticles and a wider size distribution. The increase in absorbance between 400-500 nm indicated a particular increase in larger particle presence, which could be caused by the presence of aggregated particles.

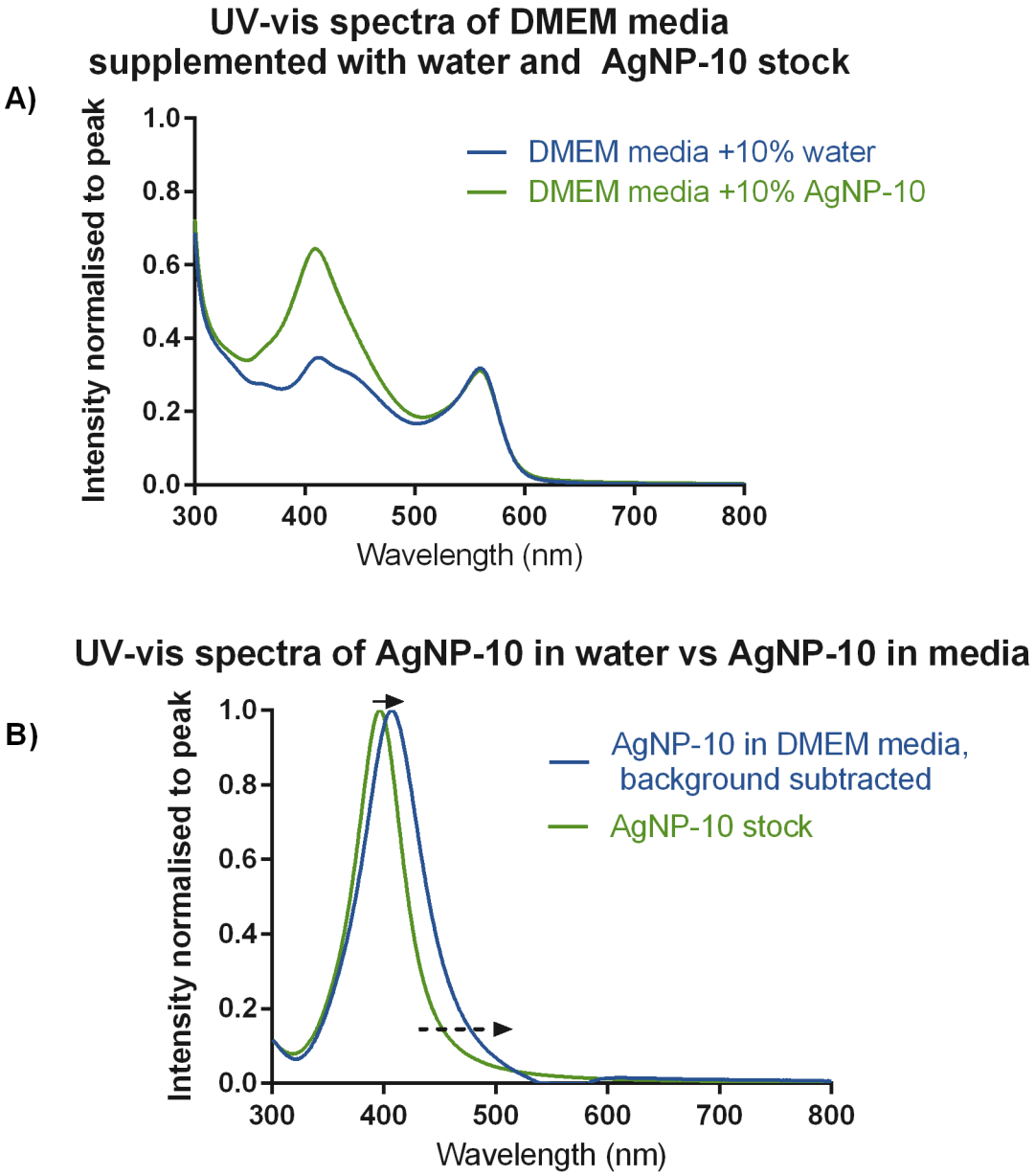

Figure 5.4 – UV-vis spectra for AgNP-10 in cell media. *A) DMEM cell media with 10% FCS treated with 20% AgNP-10 (green line) and 20% water (blue line). The water treated spectrum was used for background subtraction. B) UV-vis spectra of background-corrected AgNP-10 in DMEM media (blue line) and AgNP-10 stock (green line). There was a shift in the peak for AgNP-10 in media to a longer wavelength (solid arrow), and there was increased absorbance at wavelengths between 400-500 nm (dashed arrow), indicating the presence of larger particles in this sample.*

The peak wavelength for AgNP-10 in broth was shifted marginally compared with that of AgNP-10 stock from 398 nm to 400 nm, indicating a similar modal particle size (Figure 5.5).

The increase of FWHM from 57 nm to 74 nm indicated a wider distribution of particle diameters, with a particular increase in absorbance at higher wavelengths, which also indicated the presence of particle aggregates.

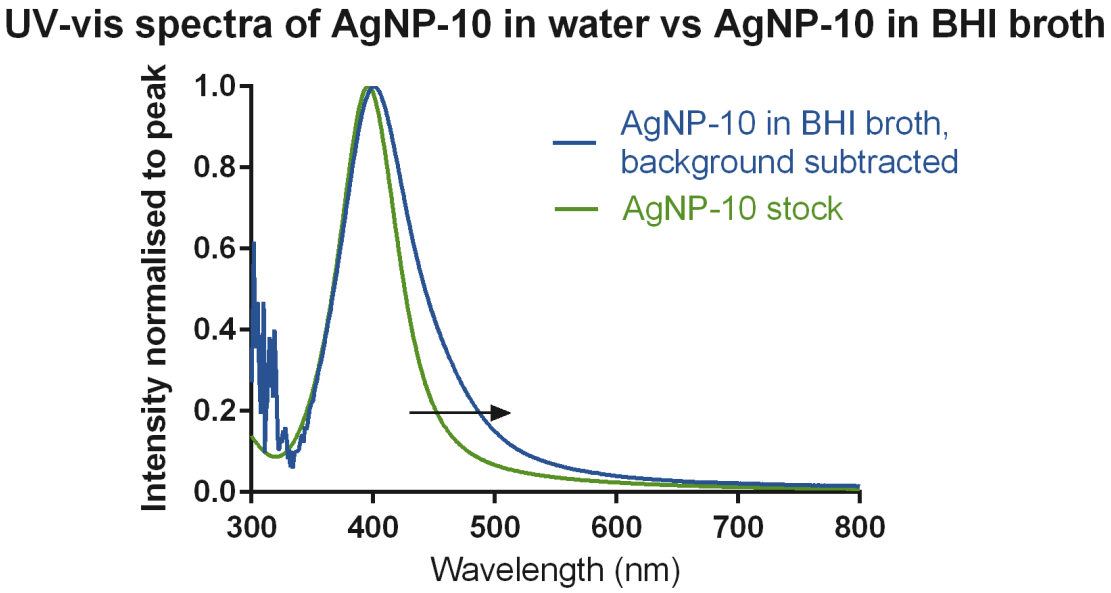

Figure 5.5 – UV-vis spectra of AgNP-10 in BHI broth. *Background-corrected spectrum of AgNP-10 in BHI broth (blue line) and AgNP-10 stock (green line). The peak absorbance occurred at similar wavelengths for both spectra, although there was increased absorbance at wavelengths between 400-600 nm for AgNP-10 in broth, as indicated by the black arrow, indicating the presence of larger particles.*

There was no plasma resonance detected for AgNP-100 at any concentration, it was therefore not possible to perform characterisation using UV-vis spectroscopy.

5.4.2 Transmission electron microscopy

Unlike UV-vis spectroscopy, TEM provides a method for direct measurement of nanoparticle size, and by measuring a large number of particles it allows statistical analysis between samples. However, the sample preparation method does not guarantee an even distribution

of particles, and this must be considered when comparing samples statistically. Additionally, very small nanoparticles (<10 nm) may not be resolvable against image noise.

Particle diameters were measured as described in section 2.6.4.3.1 and representative images for each sample are shown in Figure 5.6. The average particle diameter in AgNP-10 stock solution was 11.2 ± 8.7 nm and in the concentrated sample the average diameter was 10.5 ± 11.1 nm (Figure 5.6A and B). Both measurements showed a relatively large standard deviation compared with the mean, indicating the presence of large particles or aggregates, as indicated in the histograms showing particle diameter (Figure 5.7). Student's t-test showed the average particle diameter was not significantly different between samples ($p>0.05$). Figure 5.6C and D provide representative TEM images of 20% AgNP-10 stock dispersed in BHI broth and DMEM media with 10% FCS respectively. Neither of the mean diameters of 9.47 ± 4.97 nm or 11.5 ± 5.6 nm were significantly different to the AgNP-10 stock diameter of 11.2 nm (Student's t-test, $p>0.05$). The standard deviations were relatively small compared with the large values measured for stock. However, due to the lower concentration of nanoparticles in these samples, fewer particles were detected for imaging in the TEM samples. Thus any aggregates in the sample were obscured by the low particle numbers since they represent a lower proportion of the total particle population.

The average diameter of AgNP-100 dispersed in water was 32.91 ± 33.53 nm (Figure 5.6E). Most nanoparticles measured were found to be under the "<100 nm" guideline specified by the nanoparticle manufacturer [209], although similarly to AgNP-10 samples the standard deviation was high due to the presence of a relatively few much larger-sized aggregates.

AgNP-100 dispersed in DMEM media with 10% FCS were significantly larger than the diameter in water, with an average diameter of 107.1 ± 116.4 nm (Student's t-test, $p<0.0001$). However, histograms of particle diameter showed that the increase in average size was mainly due to the presence of very large aggregates (Figure 5.8). A representative image of AgNP-100 in DMEM media is shown in Figure 5.6F.

It was not possible to distinguish individual particles using the image analysis method in images of AgNP-100 suspended in BHI broth due to poor particle resolution (Figure 5.6G), thus an average particle size was not obtained. A possible explanation for this could be that the aggregates were sufficiently large to form substantial 3-dimensional structures which were not resolvable using TEM.

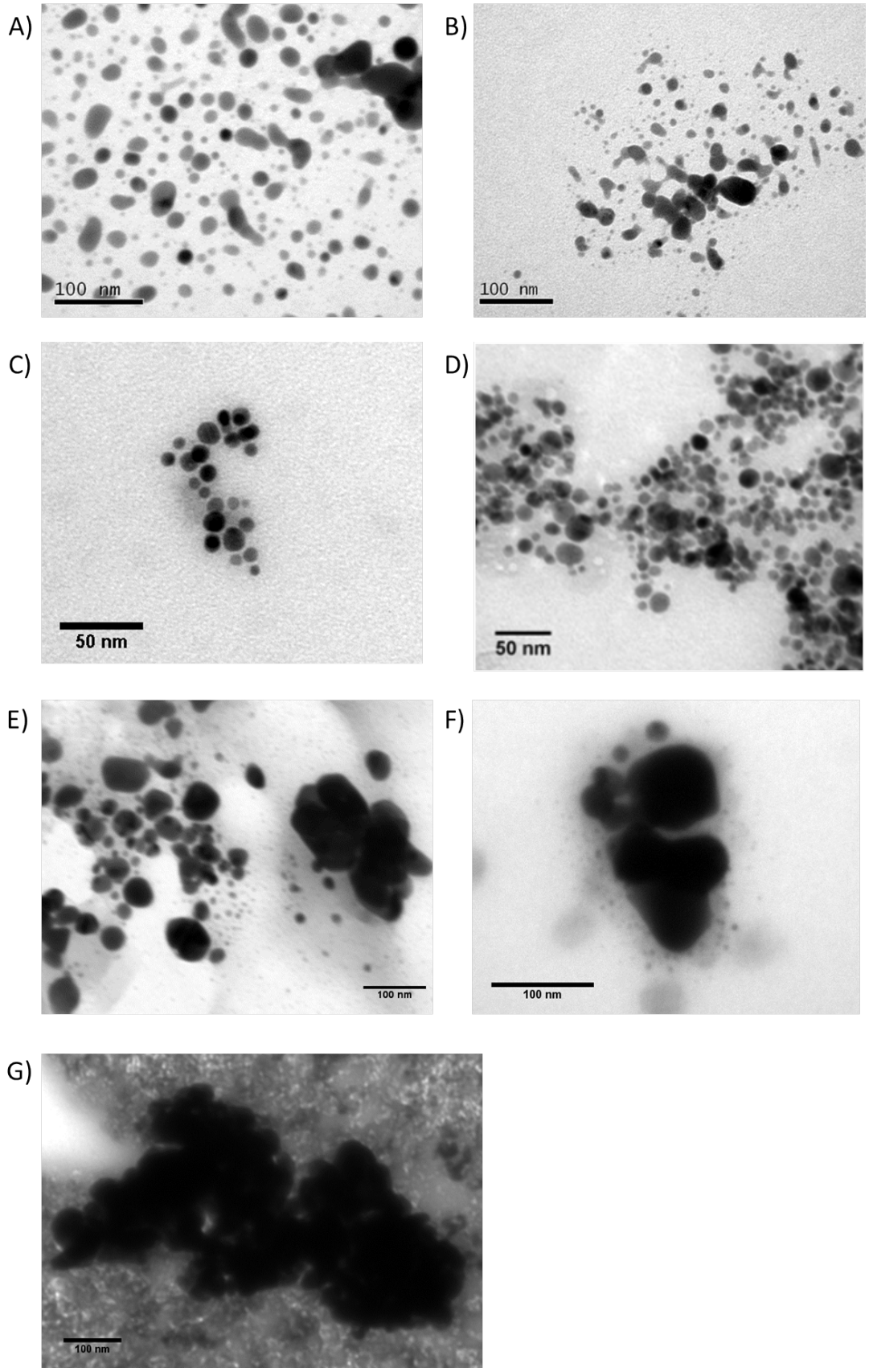

Figure 5.6 – Representative TEM images of AgNP samples. *A) AgNP-10 stock, B) AgNP-10 concentrate, C) AgNP-10 in DMEM media, D) AgNP-10 in BHI broth, E) AgNP-100 in water, F) AgNP-100 in DMEM media and G) AgNP-100 in BHI broth. Scale bars are shown in each image.*

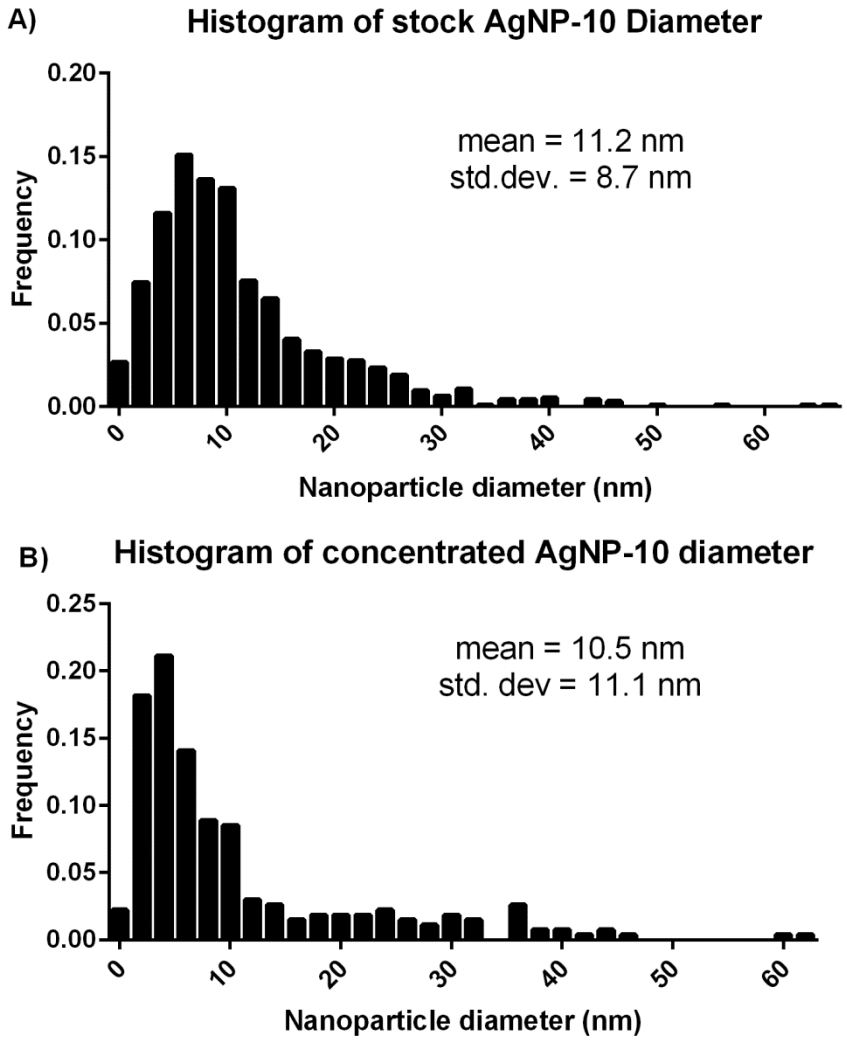

Figure 5.7 – Histograms of AgNP-10 diameters as determined by TEM. *A) AgNP—10 stock and B) AgNP-10 concentrate samples. Both distributions exhibit a similar distribution of particle diameters: the majority of nanoparticles have diameter less than 20 nm however some larger aggregates of 60 nm are observed in both samples.*

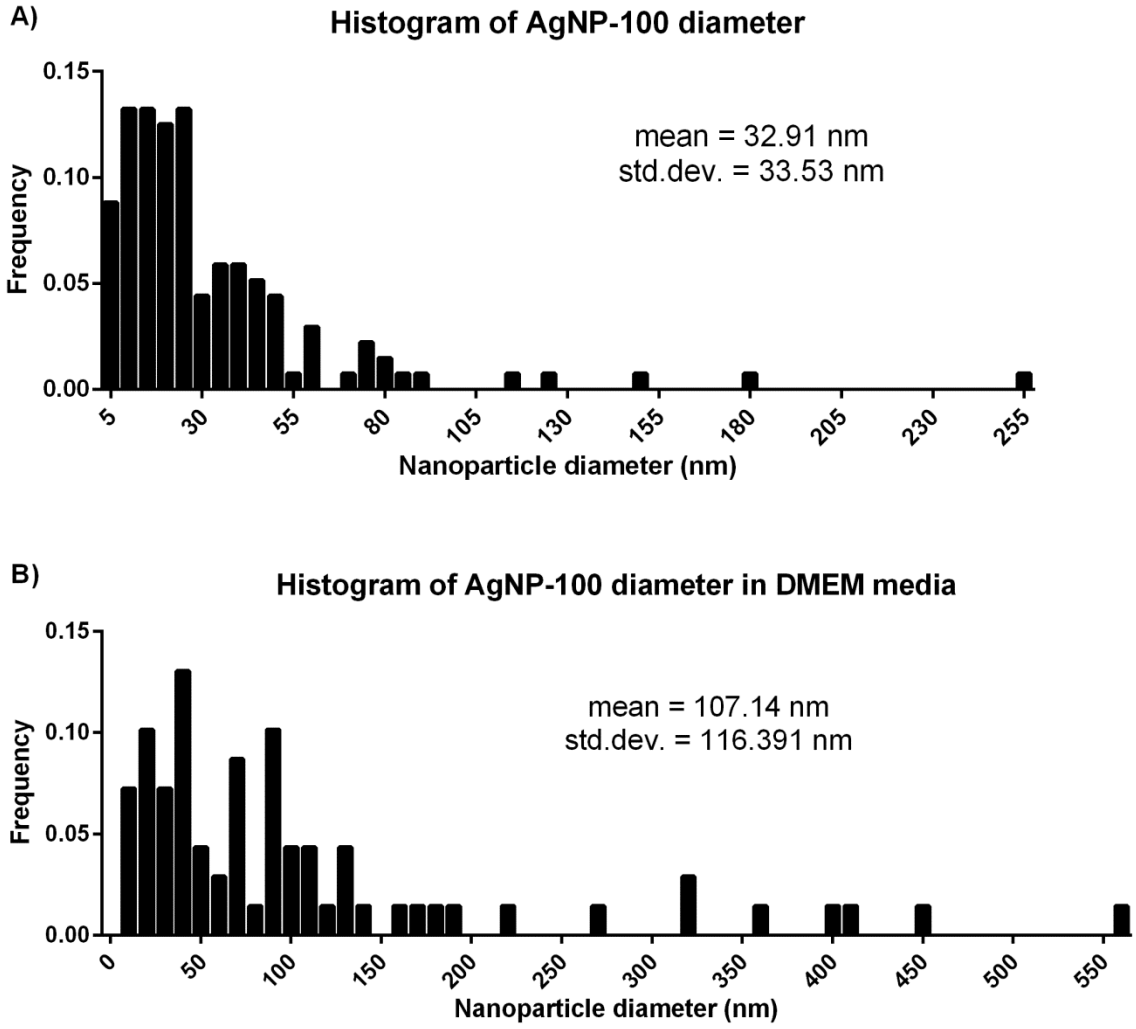

Figure 5.8 – Histogram distribution of AgNP-100 diameters as determined by TEM. *A) AgNP-100 in water and B) AgNP-100 in DMEM media with 10% FCS. Large aggregates were observed in both samples, particularly in the AgNP in media.*

5.4.3 Dynamic light scattering

DLS provides a method for measuring the size distribution of particles in a suspension. In the case of DLS, size refers to the hydrodynamic diameter of the particle, i.e. the diameter inclusive of the light ion corona surrounding the metallic core. Distributions are presented in terms of raw signal intensity thus peak height is not indicative of the number of particles in the sample of this size. AgNP were measured in water only since extraneous particulate

matter in the culture medium, including BHI broth, DMEM media and FCS, resulted in interference in the spectra.

The hydrodynamic diameter distributions of AgNP-10 stock and concentrate are shown in Figure 5.9A, and AgNP-100 data is provided in Figure 5.9B. AgNP-10 stock and concentrate distributions showed peak sizes at 15.8 ± 4.8 nm and 16.9 ± 4.8 nm, respectively, corresponding to the expected size of the nanoparticle. Each sample analysis also showed a further peak at a larger diameter, which likely corresponded with larger particle aggregates. The concentrated nanoparticle solution distribution showed an additional peak size at 3.4 ± 1.1 nm which was not observed in the stock distribution.

The AgNP-100 distribution showed nano-scale peaks at 270.2 ± 106.4 and 54.8 ± 10.8 nm, and another peak at 5034 ± 613.8 nm which corresponded to large aggregates of silver nano- and micro-particles.

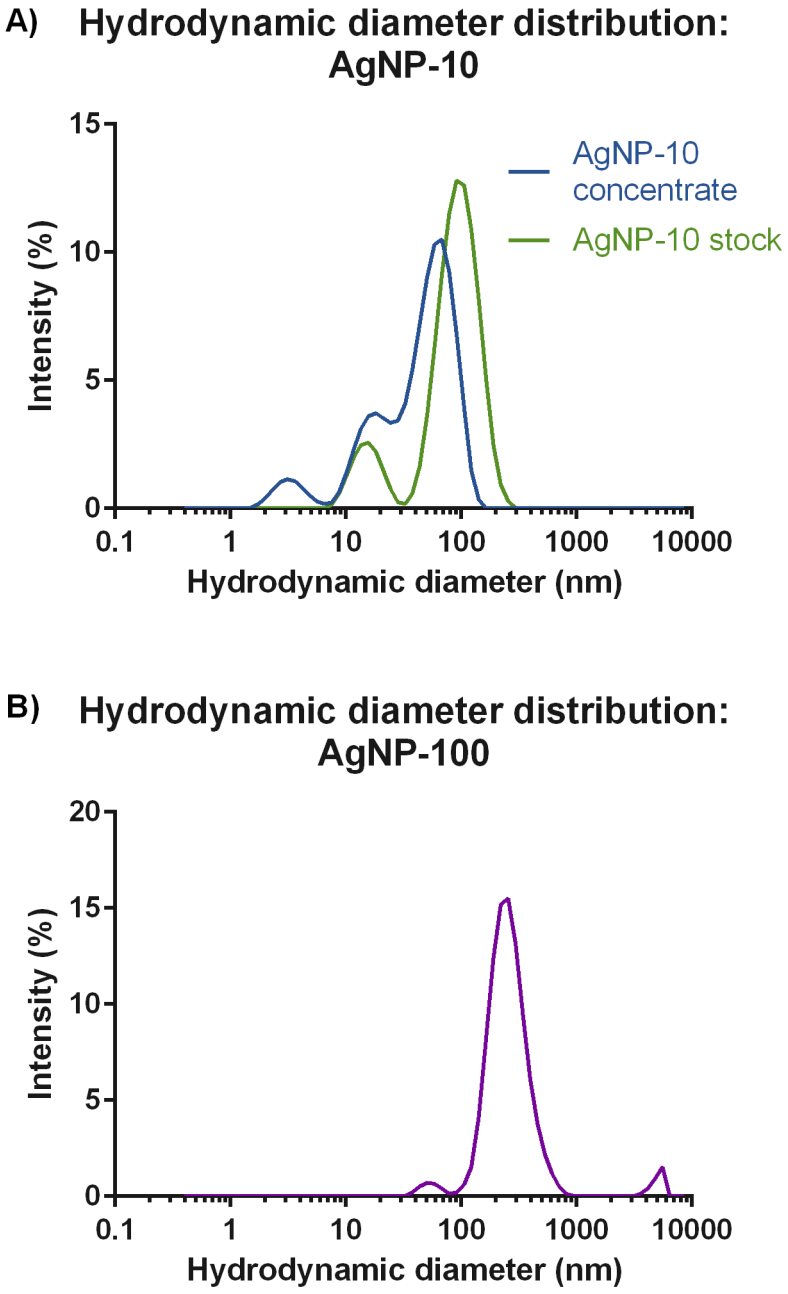

Figure 5.9 – Hydrodynamic diameter distributions of AgNP as measured using DLS. *A) Distribution of nanoparticle hydrodynamic diameter (in nm) of particles in AgNP-10 stock and concentrate. B) Distribution of hydrodynamic diameter in AgNP-100 in water. Measurements are the average of 3 readings performed on one sample.*

5.5 Conclusion

All nanoparticle characterisation techniques exhibit advantages and disadvantages. For example, UV-vis spectroscopy allows evaluation of the size distribution for a large sample of particles but does not provide quantitative measures of size. DLS provides estimates of the hydrodynamic diameter but is sensitive to interference from extraneous particulate matter. TEM enables visualisation and quantification of nanoparticle shape and size, but due to clustering of particles on the sample substrate, is not guaranteed to provide a representative sample analysis. Therefore, using all methods in conjunction with each other enables more complete characterisation.

Measurements from all three modalities showed that AgNP-10 stock and concentrate had distributions of nanoparticle size with the same mean diameter close to the expected value of 10 nm, and that stock and concentrate mean sizes were not significantly different [158]. However, TEM analysis demonstrated that larger particles of sizes up to 60 nm were also present. UV-vis spectroscopy showed AgNP-10 concentrate had a wider distribution of particle sizes, in particular an increased percentage of large particles. This is likely due to the centrifugation method applied: larger particles experience greater centrifugal forces than smaller particles, which are more likely to remain in the supernatant and subsequently be removed. Consequently, larger particles comprised a higher percentage of total particles in the concentrate than in the stock. As expected, when samples were evaluated using DLS, a hydrodynamic diameter peak slightly larger than the physical diameter as measured by TEM was observed. Peaks at larger sizes in the spectra also indicated the presence of larger particles as discussed previously.

AgNP-100 are advertised by the manufacturer as having size "<100 nm" and the mean diameter of AgNP-100 (32.91 nm) was determined using TEM to be similar to that measured elsewhere [114], [163]. Similarly to AgNP-10 there were also larger particles detected of up to 255 nm. The DLS spectra showed peaks corresponding to TEM particle measurements and an additional peak in the μm region. This indicated that some of the mass in aqueous AgNP-100 solutions aggregates into particles well outside the nanometre range. This means that when a solution is synthesised using a known mass of AgNP-100 powder, in reality the concentration of available nanoparticles is lower since silver mass is effectively "locked away" in these large aggregates.

It is also essential to evaluate the effects of media on AgNP, an aspect that is often overlooked in nanotoxicity studies. An increase in the FWHM was observed in the UV-vis spectra of AgNP-10 dispersed in BHI broth and DMEM media compared with the stock alone. There was a particular rise in this intensity at longer wavelengths, indicating an increased presence of larger particles and aggregates. The increase in density of larger particles when in media was likely due to destabilisation of the ion corona by salts present in the media and broth, leading to particle aggregation. However, evidence of these larger aggregates were not observed in the TEM images. It is likely that this outcome was because of the sparse distribution of nanoparticles in the TEM samples due to the limited maximum concentration, combined with the lower overall probability of observing larger particles.

6 CELLULAR AND BACTERIAL RESPONSES TO SILVER NANOPARTICLE EXPOSURE

6.1 Introduction

As discussed in the introduction, silver nanoparticles are increasingly common in dental applications for their antibacterial properties, however their potential side-effects on oral mucosal tissues has not been thoroughly characterised. Investigation into effects of AgNP on the H400 cell line is desirable since this cell line provides a model of the oral mucosal lining which may be exposed to AgNP. The image analysis cell counting method developed in chapter 0 could therefore provide a convenient, non-invasive method for monitoring the viability of H400 cells exposed to AgNP. Following the characterisation of two sizes of AgNP in chapter 5, this chapter describes investigations into the use of image analysis methods for studying the growth of H400 oral epithelial cells in response to AgNP exposure. Cells were also treated with $AgNO_3$ to compare the effects of ionic silver with nanoparticulate silver, as well as exposure to $NaBH_4$ to investigate whether the reducing agent played any part in the cellular response.

In addition, the antibacterial effects of AgNP, $AgNO_3$ and $NaBH_4$ were characterised through exposure to *E. coli, S. aureus* and *S. mutans*. The responses of *E. coli* and *S. aureus* to AgNP were used as models to study the effects on Gram negative and Gram positive bacteria, respectively, and compare these with the results of previous studies. *S. mutans* was studied to investigate the antibacterial potential of AgNP against these pathogenic oral bacteria. In particular, the effect of AgNP exposure on *S. mutans* and H400 oral epithelial cells was analysed to determine whether AgNPs could potentially be utilised as an oral antibacterial treatment whilst exerting minimal adverse effects on the oral epithelium. The results of experiments investigating the response H400 cells and bacteria to treatment with AgNP are

presented in sections 6.2 and 6.3 respectively. Combined this enabled a comparison of AgNP host cytotoxic and antibacterial properties in section 6.4.

6.2 H400 cell response to AgNP exposure

AgNP have been shown to have concentration and cell line-dependent effects on cells, ranging from cytotoxicity to growth stimulation [19], [132], [138]. However, the effects of AgNP on the H400 oral epithelial cell line have not been studied. This section initially details the results of experimental investigations into the viability response of H400 cells treated with AgNP-10 and AgNP-100 using the image analysis method that has been developed and validated in chapters 0 and 4. The next section details comparisons of the results obtained using the image analysis with counts performed using the MTT assay and standard haemocytometer counting. Following this, the results of investigations characterising silver uptake are presented.

6.2.1 Investigations into dose- and time-dependent responses to AgNP using image analysis

In all imaging experiments in this section, triplicate cultures of H400 cells were seeded in 12-well plates at as described in section 2.1.2.1 and the average number of cells per well was calculated from 11 images. Cultures were incubated overnight before treatment. Control cultures for each experiment were treated with identical volumes of RO water.

In initial investigations into the suitability of the image analysis approach for generating dose-response curves, H400 cells were treated with concentrations of AgNP-100 and $AgNO_3$ between 90 and 0.09 μg/mL and incubated for 24 hours prior to imaging ($AgNO_3$ and AgNP-100 were used rather than AgNP-10 since both were synthesised by dissolving powder in

water, which allowed a greater range of concentrations to be analysed.) In both cases, the maximum concentration that could be included in the analysis was 9 μg/mL; at 90 μg/mL exposure dead cells and dying cells with ruptured membranes displaying markedly different morphology to viable cells were predominant in the images captured, and detached cells obscured a relatively large proportion of the imaged area, similarly to the image shown in Figure 6.2B. Such objects were subsequently mis-segmented as cells and since the noise removal method was not initially designed to take into account the different morphology of detached cells or blebbing regions, these were erroneously counted as live cells. Dose-response curves were plotted for the remaining treated regions and a curve of the form shown in Equation 6 was fitted. Figure 6.1 shows these curves and a comparison of the fitted function parameters for each one.

The fitted hillslope for $AgNO_3$ was -2.7 and the IC_{50} was 7.8 μg/mL. The fitted IC_{50} (or the inhibitory concentration for which cell number is reduced by 50%) for AgNP-100 was 4.8 mg/mL. Since minimal reduction in growth was observed at the AgNP-100 doses tested the confidence intervals spanned several orders of magnitude, thus it was assumed this fit was unreliable. It was concluded that the image analysis approach was inappropriate for evaluation of the response of cells when there are high levels of cell death, since interferences in the images from dead and dying cells are not accounted for in the image analysis approach.

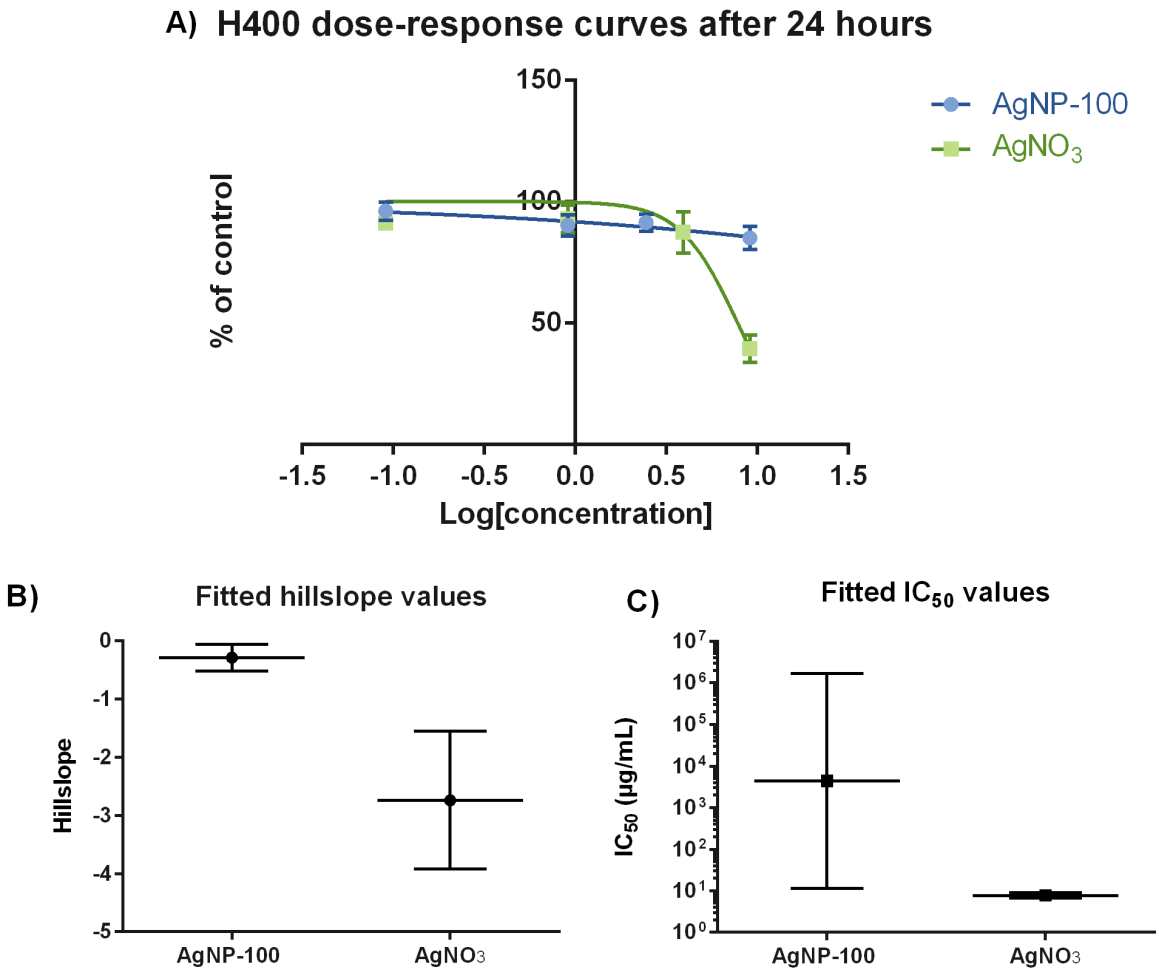

Figure 6.1 – Dose-response curves of H400 cells treated with $AgNO_3$ and AgNP-100 as measured using the image analysis assay. *A) The dose responses of H400 cells treated at concentrations between 9 µg/mL and 0.09 µg/mL for 24 hours with dose-response curves fitted of the form shown in Equation 6. Values are the mean of triplicate cultures and represented as a percentage of an untreated control. Error bars indicate standard deviation. B) The fitted hillslope values, h, and C) IC_{50} values converted from the fitted log(IC_{50}) of the dose-response curves for each treatment. Error bars in B) and C) indicate 95% confidence intervals. The $AgNO_3$ dose-response curve exhibits a steeper curve than AgNP, as reflected in the hillslope value. The high IC_{50} value for AgNP compared to the treatment values is likely to be unreliable.*

To determine whether the image analysis method could be used to investigate a dose-response relationship with H400 cells treated with the highest possible concentrations of AgNP-10, H400 cells were treated with AgNP-10 concentrate at concentrations of 17 µg/mL, 8.5 µg/mL and 4.25 µg/mL and imaged after 24 hours exposure. It was not possible to apply

image analysis for the highest concentration as all cells appeared dead following 24 hours incubation thus there were no cells detectable (a representative image is shown in Figure 6.2C). A small proportion of cells survived at 24 hours post-treatment with 8.5 µg/mL AgNP-10 concentrate, however there were high numbers of cells exhibiting ruptured membranes and dead cell debris obscured many of the images (Figure 6.2B). However, H400 cells treated with 4.25 µg/mL of AgNP-10 exhibited the same morphology as in control cultures (Figure 6.2A) thus image analysis was successfully applied. This cell count after 24 hours was only 76% of the control, which demonstrated a statistically significant decrease in cell numbers (Student's t-test, $p<0.01$). There were however higher levels of dead cells after 48 hour culture which prohibited application of the image analysis approach.

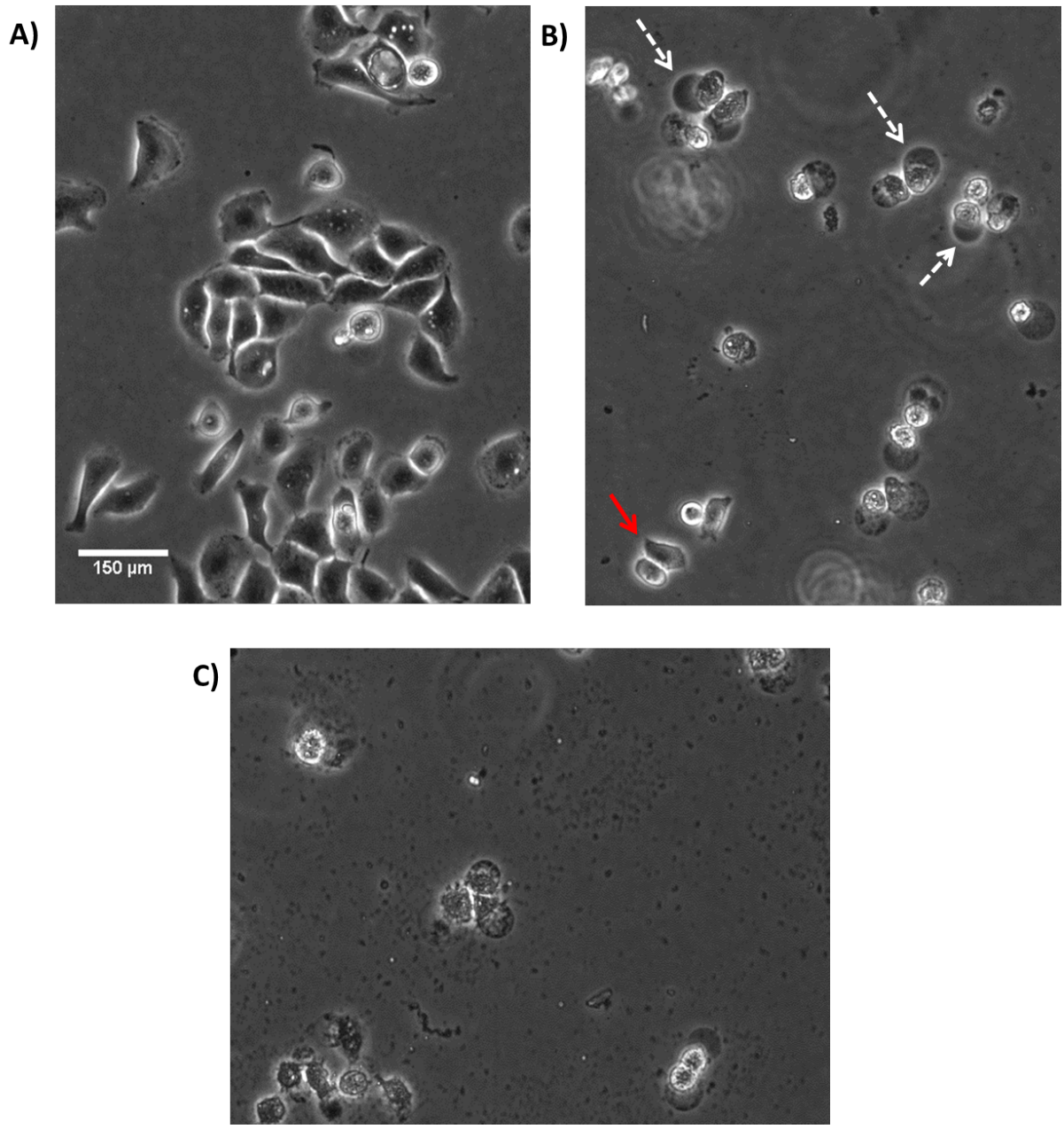

Figure 6.2 – Representative images of H400 cell cultures 24 hours after treatment with AgNP-10 *Triplicate cultures were treated with A) 4.25 µg/mL, B) 8.5 µg/mL and C) 17 µg/mL. Solid red arrow indicates cells that appear to be intact. White broken arrows indicate cells that have undergone cell membrane rupture. The scale bar for all images is shown in A).*

Lower concentrations of AgNP-10 were investigated using AgNP-10 stock to provide a final treatment concentration of 2.5 µg/mL. Cell morphology was similar to that in control cultures over the entire period of culture thus it was appropriate to apply image analysis to compare cell numbers and generate growth curves. To generate growth curves, images were

acquired between 8 and 48 hours after treatment with 2.5 µg/mL AgNP-10 or AgNP-100, or equivalents of $AgNO_3$ or $NaBH_4$. The resulting growth curves are provided in Figure 6.3. One-way ANOVA and Dunnett's multiple comparison tests were also performed on cell counts at after 24 and 48 hours to determine significant differences in viability compared with control.

After 24 hours only cells treated with AgNP-10 exhibited a significant inhibition in cell numbers ($p<0.05$). 48 hours incubation both sizes of AgNP show a significant reduction in cell numbers compared with the control (Figure 6.4). This indicates a time-dependent response of AgNP and highlights the importance of longitudinal studies. The growth curve for the $NaBH_4$ exposure overlaps continuously with the control curve, indicating no inhibitory effects on the cells. Cultures treated with $AgNO_3$ displayed a reduction in cell numbers compared with the untreated control, however this was to a lesser extent than those treated with AgNP-10.

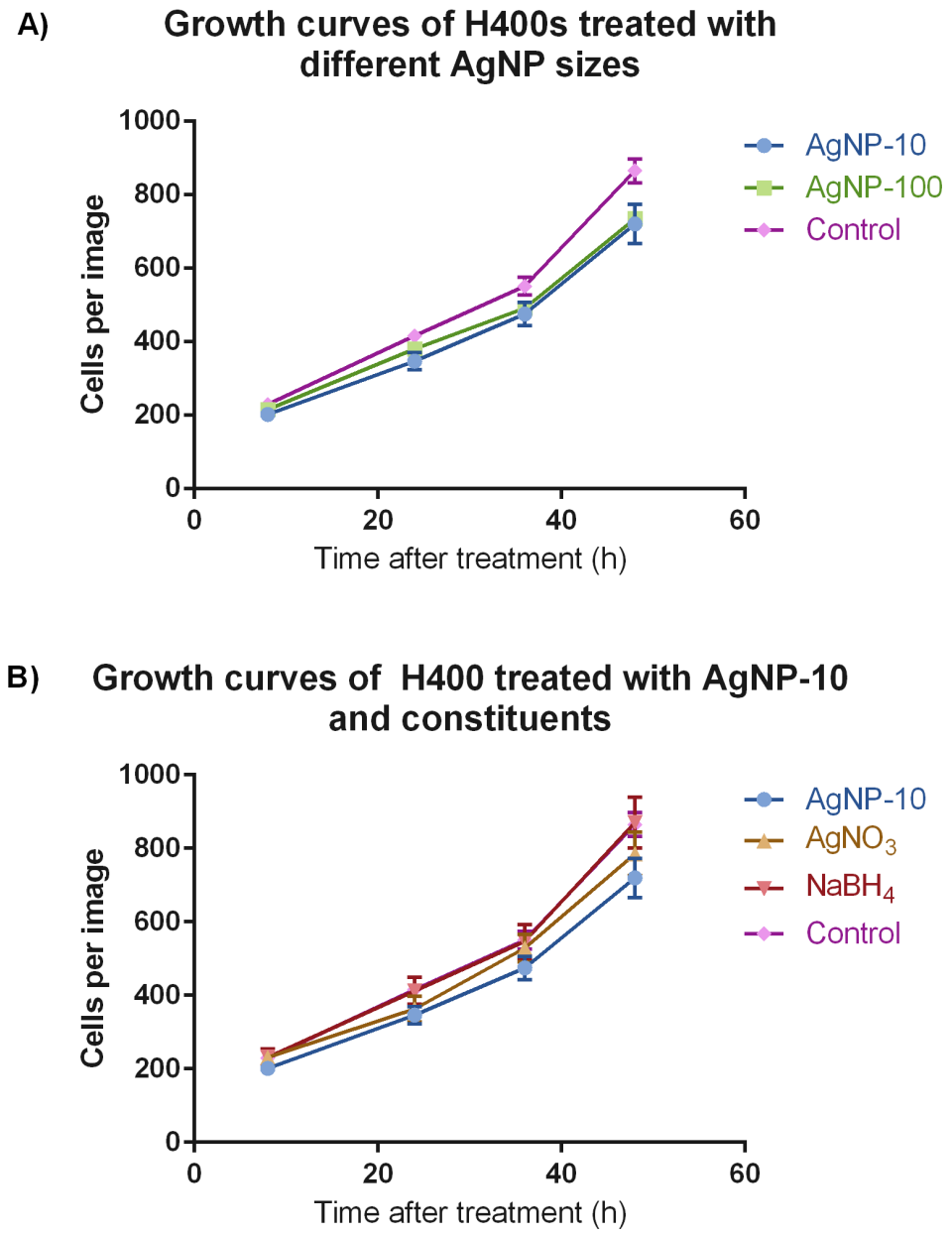

Figure 6.3 – Growth curves for H400 cells as determined using cell counts from images. *Graph A) shows cells treated with 2.5 µg/mL of AgNP of different sizes and B) shows growth curves of cells treated with 2.5 µg/mL of AgNP-10 compared to the constituent synthesis chemicals. The mean of triplicate cultures is plotted at each time point and error bars indicate standard deviation. AgNP-10 and $AgNO_3$ displayed reduced growth compared to the control, whereas $NaBH_4$ did not.*

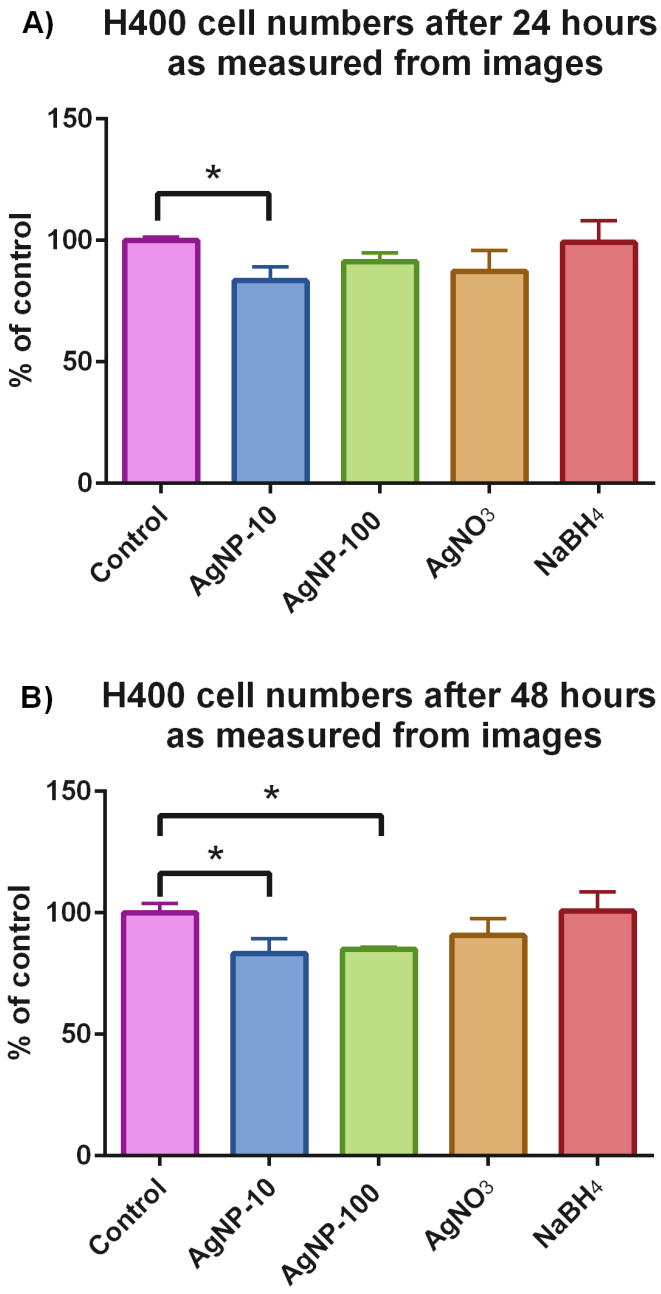

Figure 6.4 - H400 cell number analysis after incubation with 2.5 µg/mL AgNP-10 or AgNP-100 or equivalents of $AgNO_3$ and $NaBH_4$ as measured using image analysis approach. *Measurements made after A) 24 hours and B) 48 hours and normalised to a control. Cells treated with AgNP-10 exhibited a significant reduction in numbers compared to control after 24 hours and after 48 hours incubation both AgNP-10 and AgNP-100 showed significant reduction (* indicates $p<0.05$).*

6.2.2 Comparison of cell counts using different methods

To compare the dose-response curves generated by MTT assay with image analysis, H400 cells in 96-well plates (4 replicate wells) were treated with a range of concentrations up to 31.1 μg/mL of AgNP-10 (the maximum concentration-limited dose), up to 83 μg/mL of AgNP-100 (the dose was limited by high levels of background interference above this concentration from aggregates subsequently it was not possible to correct this through background subtraction approaches), and up to 190 μg/mL of $AgNO_3$ and $NaBH_4$. MTT assays were performed after 24 hours incubation. After background subtraction and normalisation with the water-treated control, a curve of the form shown in Equation 6 was fitted to the data points plotted. Figure 6.5 shows dose-response curves for H400 cells exposed to all treatments and graphs comparing the fitted IC_{50} and hillslope parameters.

Since no dose-dependent reduction in cell viability was observed for $NaBH_4$ exposure, it was not possible to fit parameters in this case. The fitted IC_{50} value was highest for AgNP-100 (158.4 μg/mL) followed by $AgNO_3$ (41.0 μg/mL, equivalent to 26.0 μg/mL silver) and the lowest was AgNP-10 (1.7 μg/mL). The fitted hillslope values were similar for both sizes of AgNP due to a gradual decrease in cell viability with dose, whereas the fitted hillslope value for the viability of H400 cells exposed to $AgNO_3$ was much steeper indicating a sharp increase in cytotoxicity past a threshold dose.

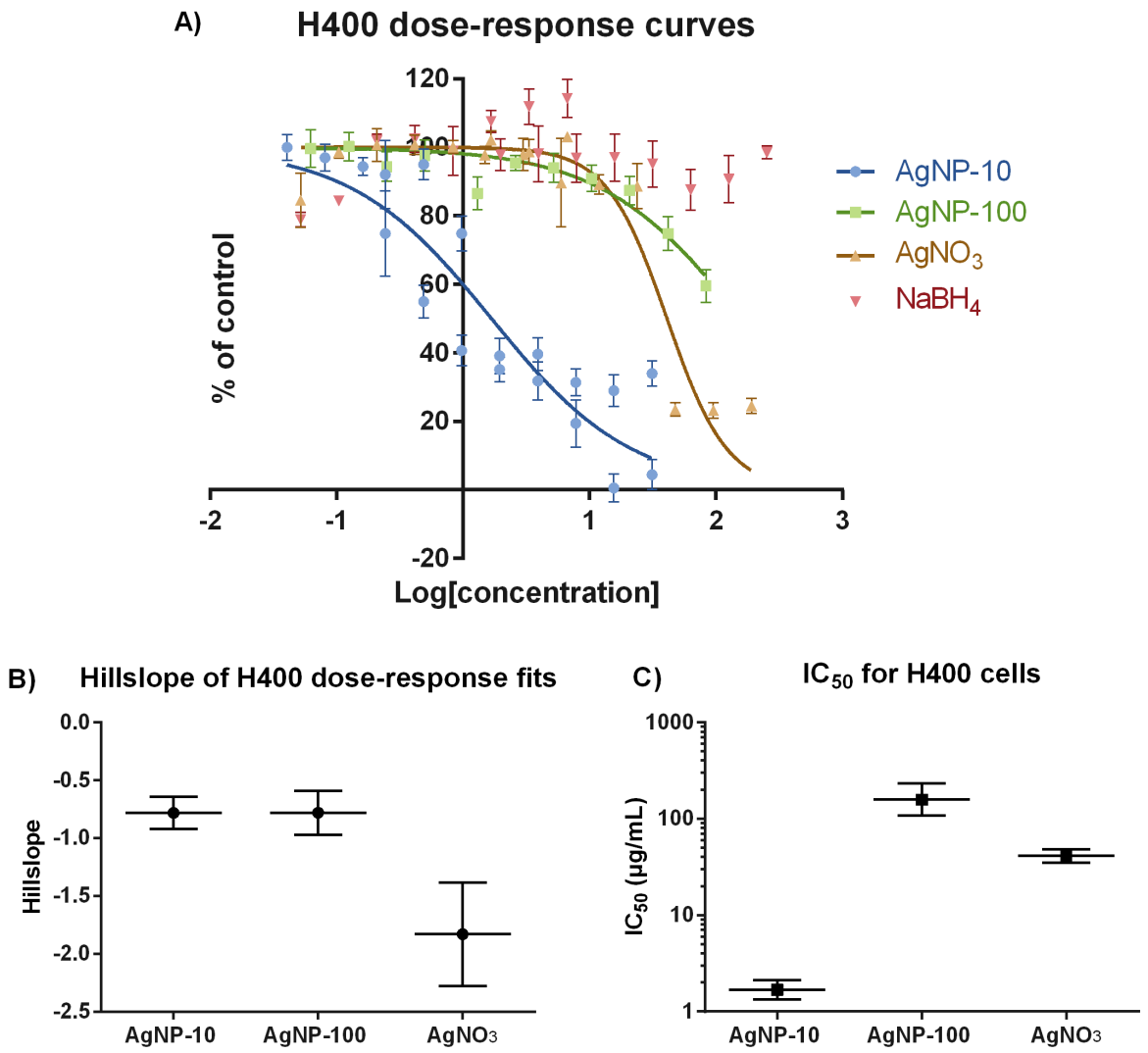

Figure 6.5 – The dose responses of H400 cells treated with AgNP-10 and equivalents of AgNP-100, $AgNO_3$ and $NaBH_4$ as measured using MTT assay. *A) Dose-response graphs with curves fitted where possible. Values are the mean of 4 replicate cultures and represented as a percentage of an untreated control. Error bars indicate standard deviation. B) The fitted hillslope values, h, and C) IC_{50} values for each treatment converted from the fitted log(IC_{50}) of the dose-response curves. Error bars in B) and C) indicate 95% confidence intervals. Note the relatively steep dose response curve for $AgNO_3$ compared to AgNP and $NaBH_4$.*

To directly compare the measurements of cell inhibition by image analysis with haemocytometer counting and MTT assay, the H400 cell cultures treated with 2.5 µg/mL AgNP-10 and equivalents of AgNP-100, $AgNO_3$ and $NaBH_4$, as described in the previous section (6.2.1), were detached using Trypsin after imaging at 48 hours incubation and subsequently re-suspended in DMEM media for counting using the haemocytometer

method as described in section 2.1.3.1. Simultaneously seeded and treated cultures in 96-well plate formats were used for MTT assay analysis (described in section 2.1.3.3). The results of cell viability compared with the untreated control at 48 hours as determined by image analysis are shown in Figure 6.4B, and Figure 6.6 shows the results as determined using the haemocytometer method and MTT assay. Image analysis and MTT assays both identified significant differences between treatments however the haemocytometer assay determined no significant difference (one-way ANOVA, $p<0.05$). Dunnett's multiple comparison test showed significant differences between AgNP-10 and the control were measured for both image analysis ($p<0.05$) and MTT assays ($p<0.001$) only the image analysis method showed significant reduction in cell numbers following AgNP-100 exposure ($p<0.05$).

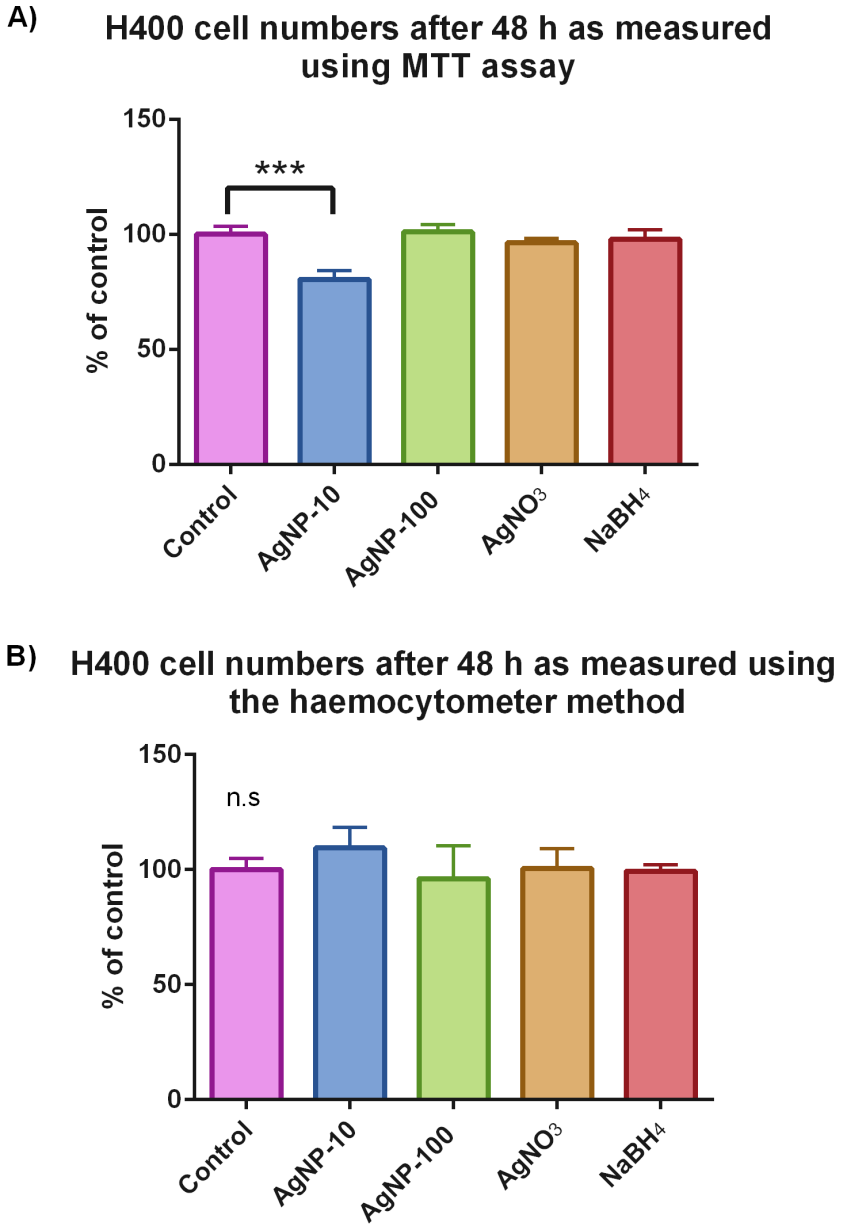

Figure 6.6 – H400 cell number analysis after incubation with 2.5 µg/mL AgNP-10 and equivalents of AgNP-100, $AgNO_3$ and $NaBH_4$ as measured using MTT assay or haemocytometer method*. Measurements were taken after 48 hours incubation using A) MTT assay (n=4) and B) haemocytometer method (n=3). Error bars indicate standard deviation. When counted using the haemocytometer approach cells showed no significant difference in numbers between treatments (n.s. = p>0.05). MTT showed a significant reduction in cell numbers following culture treatment with with AgNP-10 (*** indicates p<0.001).*

6.2.3 AgNP uptake and localisation

6.2.3.1 TEM

H400 cells were treated for 3 hours with 4.5 μg/mL AgNP-10 stock and AgNP-100. Their locations within cells after this time were investigated qualitatively using TEM. The representative image in Figure 6.7 shows that AgNP-10 were mainly associated with the cell membrane, with decreasing amounts present in the cell cytoplasm and nucleus.

Figure 6.8 shows TEM images of H400 cells treated with AgNP-100. Large micron-scale aggregates were observed inside several cells, as well as smaller nanoparticles present at cell membrane locations. However, the majority of cells appeared to show minimal or no evidence of AgNP-100 presence.

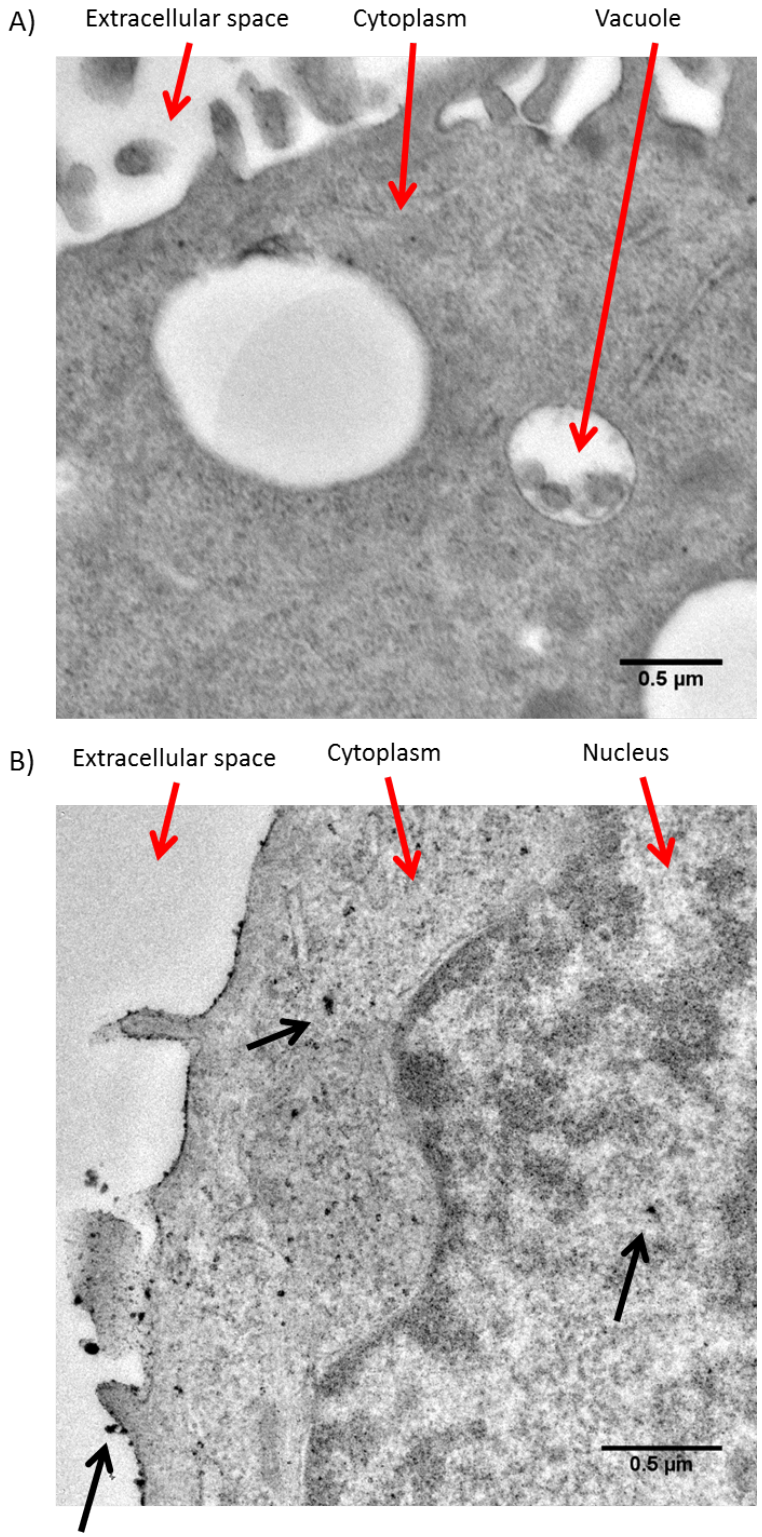

Figure 6.7 – Representative TEM images of H400 cells treated with AgNP-10. *A) An untreated H400 cell and B) a H400 cell treated with AgNP-10 for 3 hours. Red arrows indicate the structural features of the cell. Black arrows indicate the location of some nanoparticles on the cell membrane, in the cytoplasm and in the cell nucleus. AgNP-10 appeared mainly located with the cell membrane and cytoplasm. Scale bars are shown in each image.*

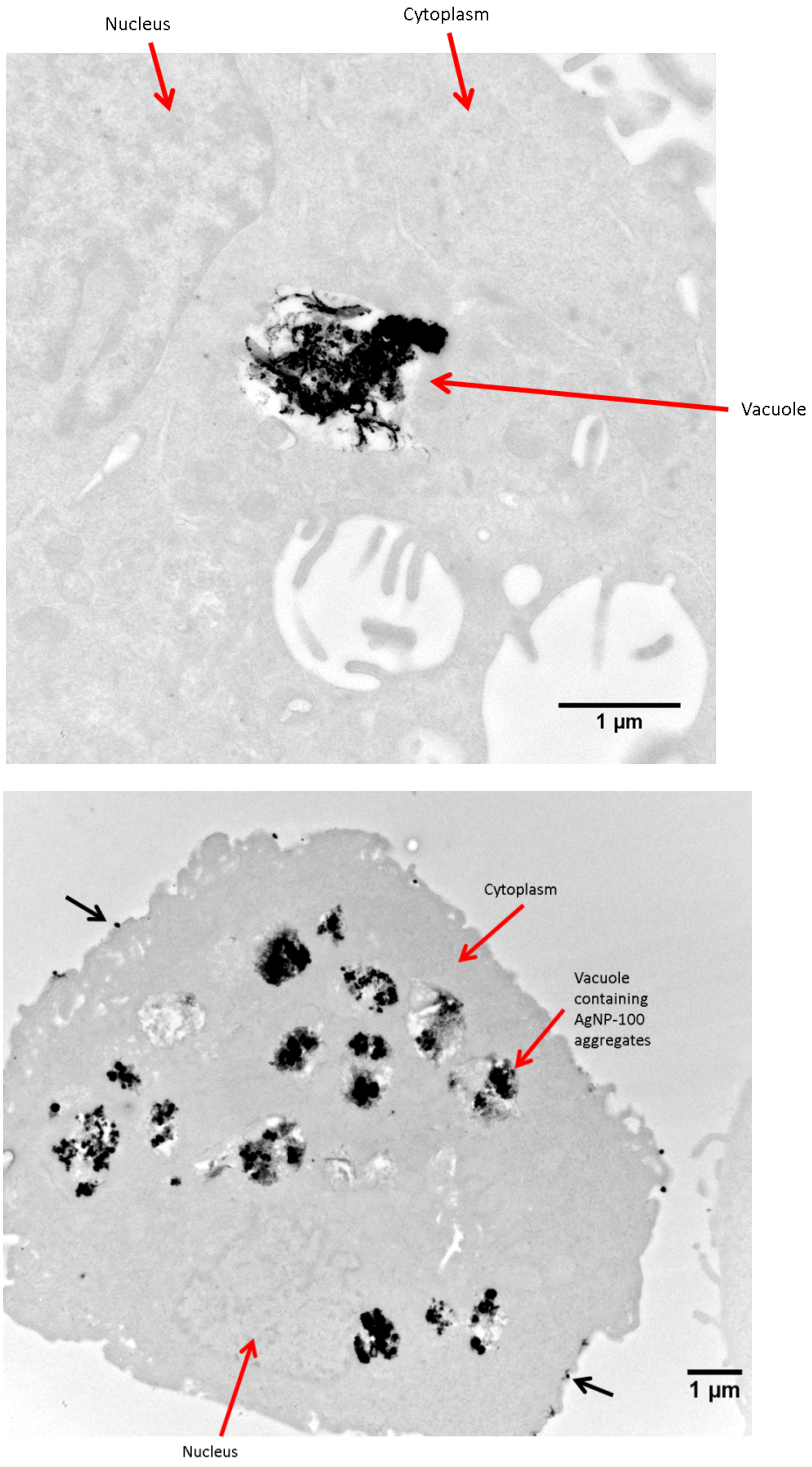

Figure 6.8 – Representative TEM images of H400 cells treated with AgNP-100. *Red arrows indicate cellular structures. Black arrows indicate some AgNP-100 associated with cell membrane. Scale bars are shown in each image. An image of an untreated control cell is shown in Figure 6.7A for reference.*

6.2.3.2 Inductively coupled plasma optical emission spectroscopy

The uptake of silver in H400 cells treated with 5.4 µg/mL AgNP-10 stock and $AgNO_3$ containing equivalent Ag^+ concentration was measured using ICP-OES. The amount of silver adsorbed to cultureware substrate was determined with identically treated cell-free blank wells; in each case this was determined to be lower than the detection limit of the ICP-OES technique, thus this was considered to be negligible. Figure 6.9 shows that cells treated with AgNP-10 exhibited a 52% uptake of available silver, compared with the significantly lower 20% of available silver from $AgNO_3$ (Student's test, $p<0.001$).

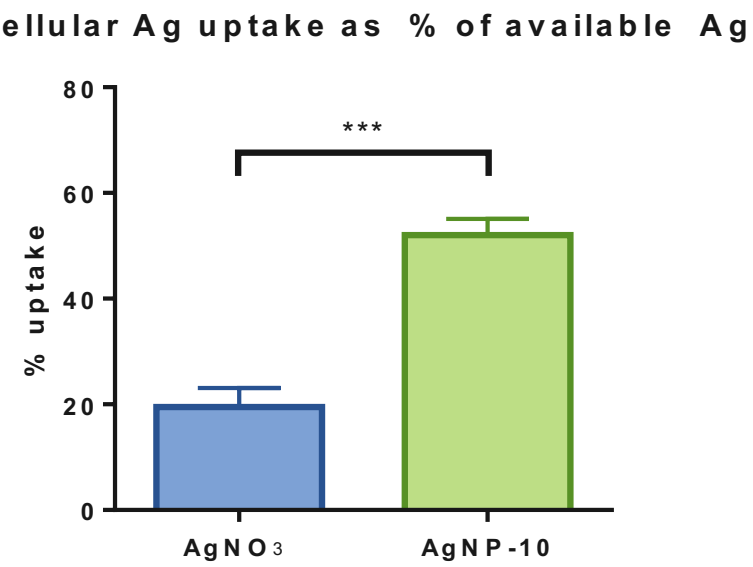

Figure 6.9 – Percent cellular uptake of silver in H400 cells treated with 5.4 µg/mL $AgNO_3$ and AgNP-10 with equivalent Ag mass concentrations. *The average of triplicate cultures is plotted and error bars indicate standard deviation. The Ag uptake for AgNP-10 was significantly higher than for $AgNO_3$ (*** indicates $p<0.001$).*

Cell counts were performed using the image analysis method using images captured immediately prior to using the cultures for ICP-OES preparation. The total number of cells per dish and the total Ag uptake per dish were used to calculate the silver uptake per cell. Data indicated that this was 11.18 ng/cell for AgNP-10 and 3.97 ng/cell for $AgNO_3$. Cell

numbers were not significantly different between each treatment group (Student's t-test, $p>0.05$).

6.3 Effects of AgNP on bacterial cultures

The section below details experiments performed to characterise the response of bacteria to AgNP. The effects of the constituent chemicals in the synthesis of AgNP-10, namely $AgNO_3$ and $NaBH_4$, were once again characterised in these assays to compare the effects of ionic silver to nanoparticulate silver and investigate any effects of the reducing agent on bacteria. *E. coli* and *S. aureus* were used as model organisms to test antibacterial effects of AgNP on Gram-negative and Gram-positive bacteria respectively under aerobic conditions. The response of *S. mutans* was also examined since this cariogenic bacteria is a potential target for the antimicrobial properties of AgNP-10. *S. mutans* was cultured under 5% CO_2 – the same conditions under which H400 cells were cultured, in order to compare effects. Whilst the effects of AgNP have been characterised on these bacterial cell lines previously, as discussed in the introduction section 1.7.4 it has been shown that AgNP synthesis method and functionalisation significantly affect the inhibitory concentrations, thus in order to usefully compare antibacterial and cytotoxic effects it is essential to use the same samples of AgNP.

In this section the results of experiments performed to characterise the antibacterial properties of AgNP are presented first, followed by TEM analysis to localise the AgNPs in treated bacteria.

6.3.1 Bacterial growth curves

Growth of bacteria in a suspension culture results in an increase in the turbidity of the broth in which it is grown. Bacterial growth was therefore investigated by measuring the change in OD measured at 630 nm of bacterial suspensions at intervals over a 24 hour period to generate growth curves as described in section 2.5.2.3.1. The relative power of antibacterial agents was investigated by comparing the growth curves for bacteria treated with each agent. Figure 6.10 shows growth curves for all strains of bacteria treated at a concentration of 31.13 µg/mL of AgNP-100 and AgNP-10 concentrate, and the equivalent concentrations of $AgNO_3$ and $NaBH_4$.

$AgNO_3$ showed the greatest inhibitory response out of all treatments tested, with no growth detected in *S. aureus* and *S. mutans*, and only a limited amount of growth after 24 hours in *E. coli*. Conversely, minimal change in turbidity compared with the control was observed after treatment with $NaBH_4$ for all strains tested. The smaller AgNP-10 elicited a larger inhibitory effect compared with AgNP-100 in all bacterial strains tested. In fact, *S. aureus* treated with AgNP-100 showed minimal change compared with the control.

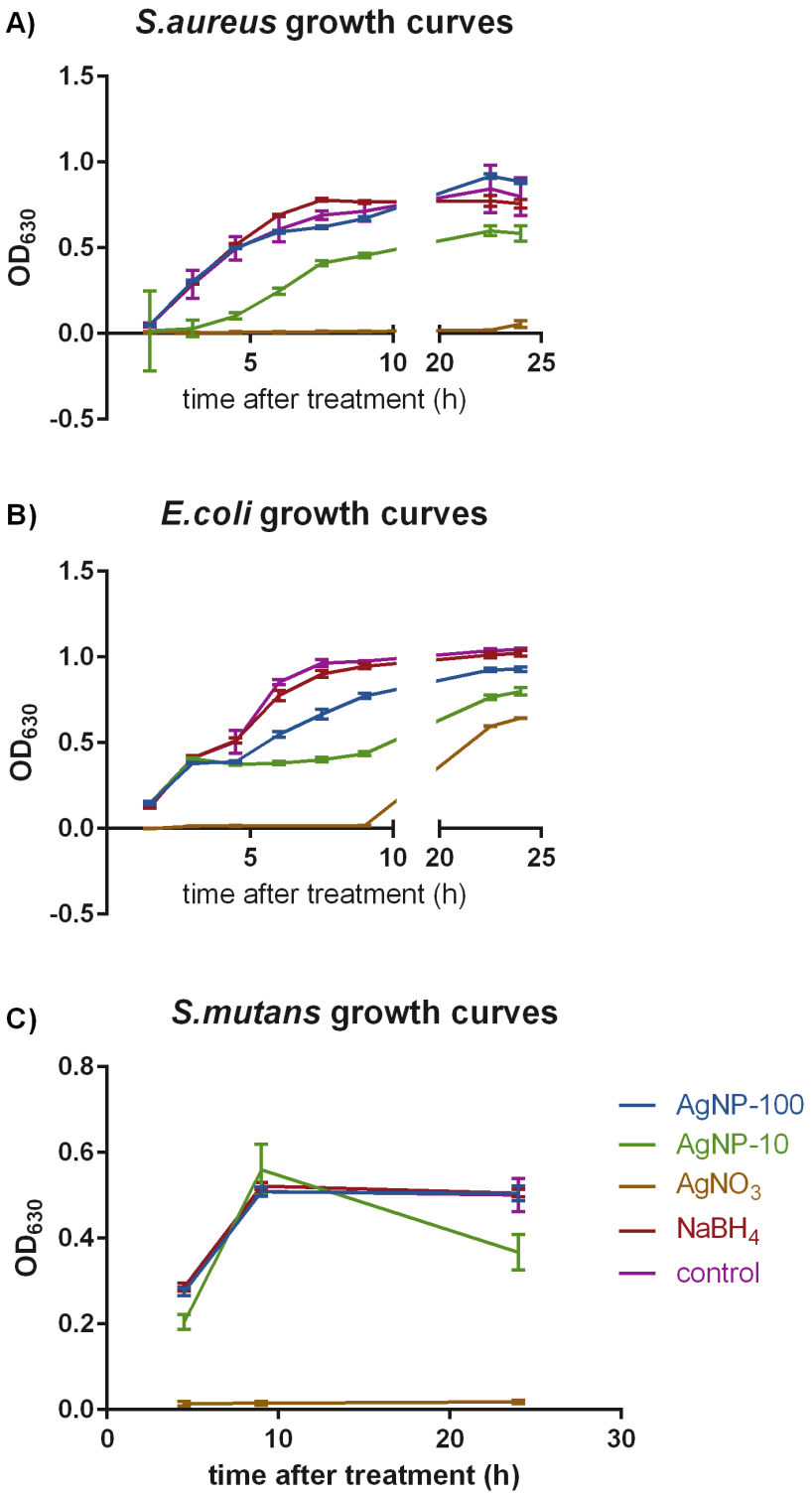

Figure 6.10 – Growth curves in bacteria treated with 31.13 µg/mL of AgNP-10 and AgNP-100, and equivalent concentrations of $AgNO_3$ and $NaBH_4$. *Cell number was measured using OD at 630 nm in A) S. aureus, B) E. coli and C) S. mutans. Each point represents the mean of four replicates with background subtracted, and error bars indicate standard deviation. The key for all plots is shown in C). In all cases $AgNO_3$ reduced growth by the largest amount compared to control, followed by AgNP-10. Note the unusual measurement for AgNP-10 in S. mutans, which could have been caused by the formation of a film layer in* this *culture, which can be seen in Figure 6.11.*

6.3.1.1 S. mutans continuous layer formation

It was observed that a continuous film layer had formed in *S. mutans* wells after 24 hours culture. It was noted the highest two concentrations of AgNP-10 exposure which caused this film to tear and fold (Figure 6.11). This phenomenon caused inaccurately high OD readings so wells containing *S. mutans* were homogenised by pipetting the bacterial culture prior to acquiring OD readings at 24 hours. Interestingly this phenomenon of continuous layer formation was not observed for any other treatments, nor at any other concentrations. It could potentially also explain the abnormally high OD reading obtained for AgNP-10 at 9 hours post-treatment, since wells were not homogenised before OD measurement at this time point (Figure 6.10C).

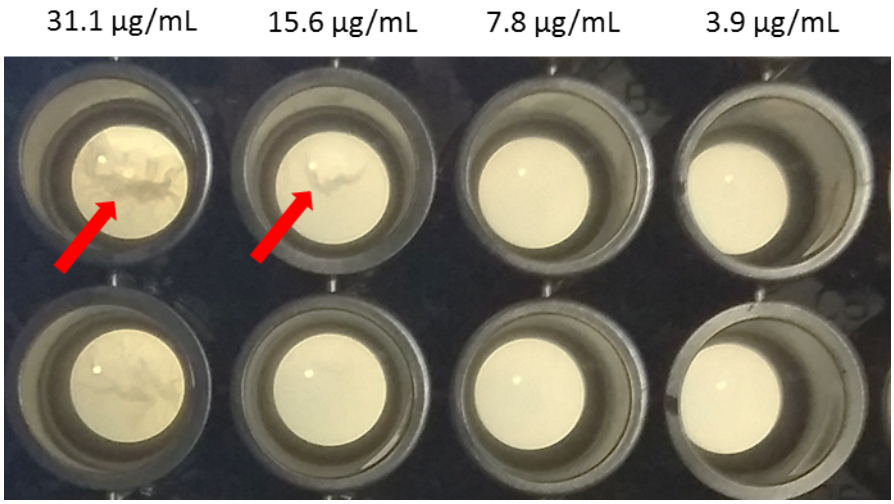

Figure 6.11 – Representative images of continuous films of bacterial growth formed in a 96-well plate after S. mutans was cultured in BHI broth for 24 hours and treated with AgNP-10. *Numbers above the image indicate the treatment concentration of AgNP-10 for each column of wells. Arrows indicate tears in the film that had formed, which were only observed in the highest two concentrations of AgNP-10.*

6.3.2 Dose-response curves

OD readings were acquired for bacteria treated with 31.1 µg/mL AgNP-10 and equivalents of AgNP-100, $AgNO_3$ and $NaBH_4$ after incubation for 24 hours. Once normalised to the control,

a curve of the form shown in Equation 6 was fitted to the data points. Figure 6.12, Figure 6.13 and Figure 6.14 show these curves and the parameters fitted for *S. aureus*, *E. coli* and *S. mutans,* respectively.

The fitting algorithm did not converge on values for $NaBH_4$ on *S. aureus* and *S. mutans* or AgNP-100 on *E. coli* indicating that there was no dose-dependent reduction in growth. In all cases for which a curve was fitted for both AgNP-10 and AgNP-100, the IC_{50} was higher for the smaller sized nanoparticles tested. However the values fitted for *S. aureus* are in the order of 100 mg/mL, and the 95% confidence intervals are very large, spanning two or more orders of magnitude, indicating an unreliable fit. The IC_{50} was lower for $AgNO_3$ than for AgNP-10 exposure in all cases, indicating inhibitory efficacy at a lower concentration. For all bacterial strains, the hillslope for $AgNO_3$ was considerably steeper than for AgNP treament, signifying a sudden sharp increase in antibacterial response rather than a gradual increase due to concentration.

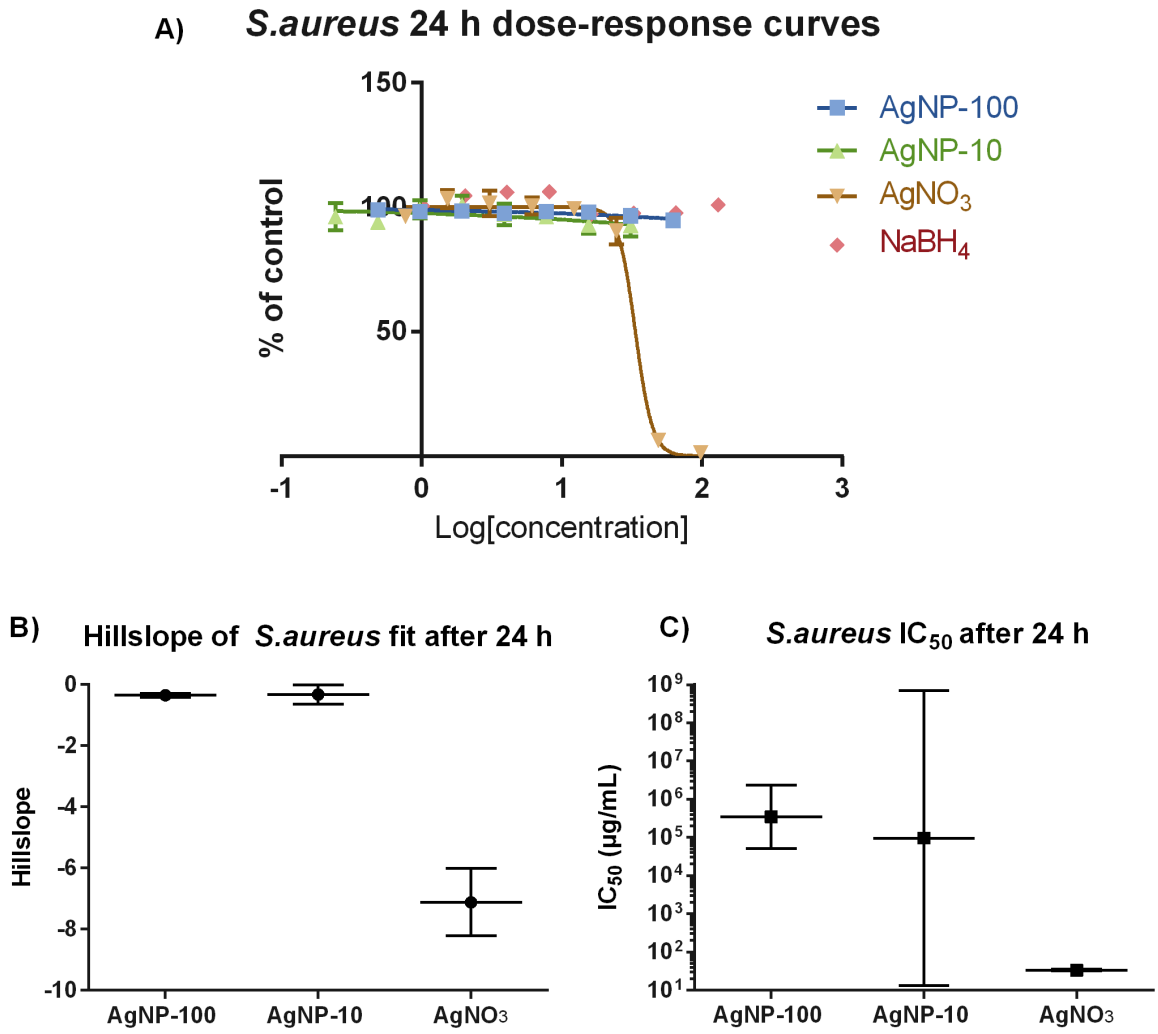

Figure 6.12 –The dose responses of S. aureus treated with AgNP-10 and equivalents of AgNP-100, $AgNO_3$ and $NaBH_4$ *A) Dose-response graphs with curves fitted where possible. Each point is the mean OD_{630} of four replicates with background subtracted, represented as a percentage of an untreated control. Error bars indicate standard deviation. B) The fitted hillslope values, h, and C) IC_{50} values for each treatment converted from the fitted log(IC_{50}) of the dose-response curves. Error bars in B) and C) indicate 95% confidence intervals. Note the relatively steep increase in cell toxicity for $AgNO_3$ in the dose response curve (A) compared to AgNP, which is reflected in a lower hillslope value (B).*

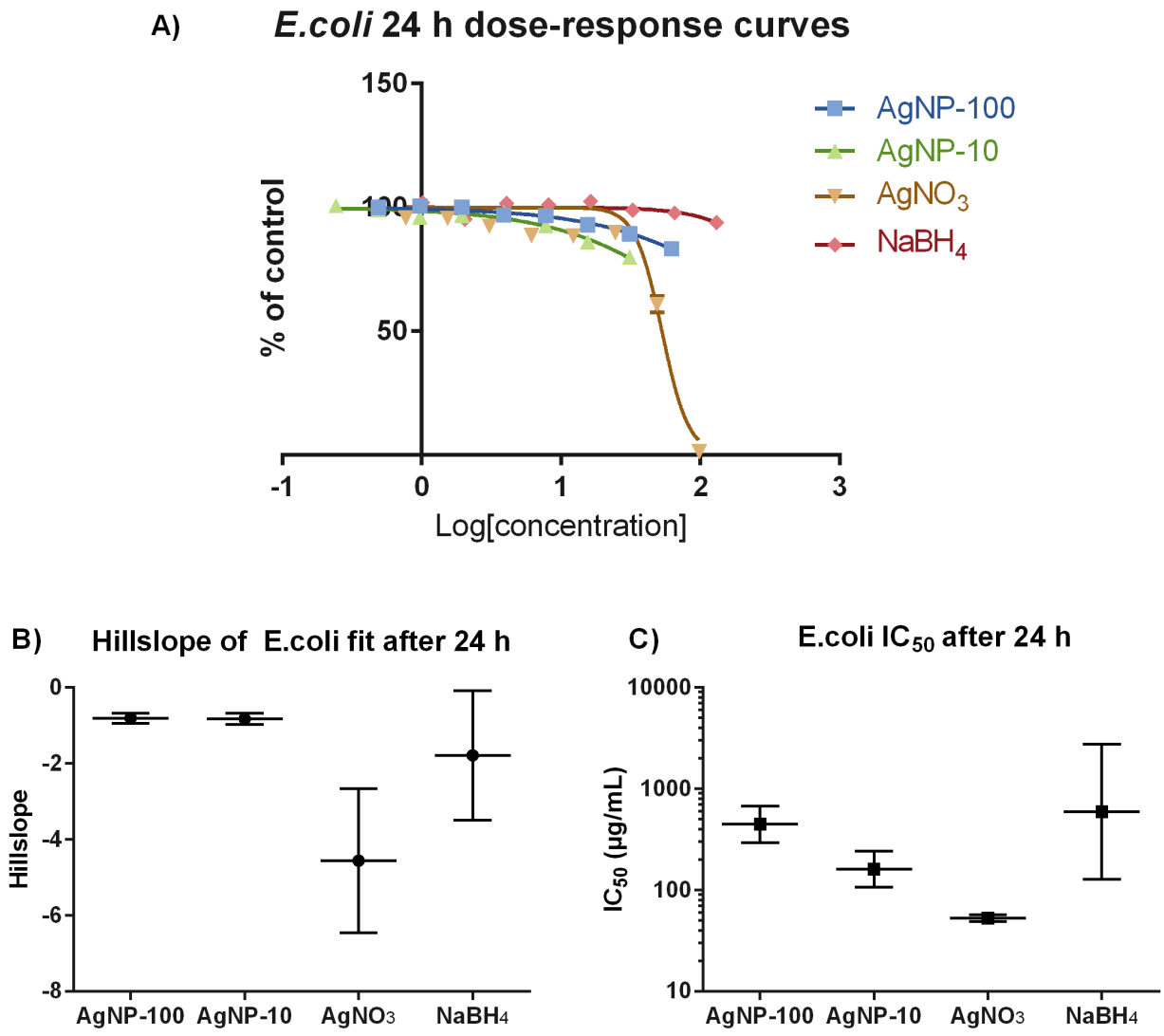

***Figure 6.13 - The dose responses of E. coli treated with AgNP-10 and equivalents of AgNP-100, $AgNO_3$ and $NaBH_4$** . A) Dose-response graphs with curves fitted. Each point is the mean OD_{630} of four replicates with background subtracted, represented as a percentage of an untreated control. Error bars indicate standard deviation. B) The fitted hillslope values, h, and C) IC_{50} values for each treatment converted from the fitted log(IC_{50}) of the dose-response curves. Error bars in B) and C) indicate 95% confidence intervals. Note the relatively steep increase in cell toxicity for $AgNO_3$ in the dose response curve (A) compared to AgNP, which is reflected in a lower hillslope value (B).*

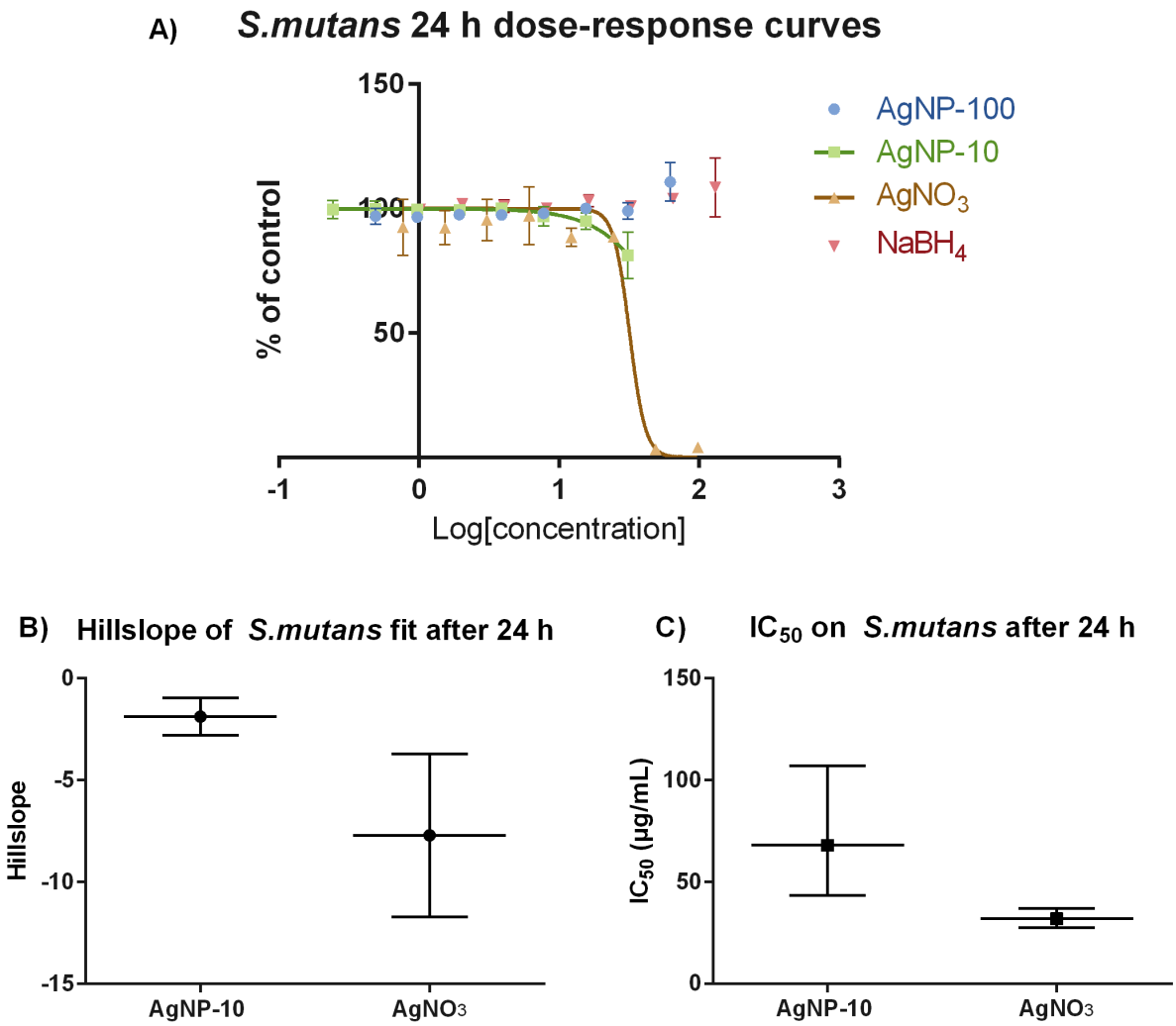

Figure 6.14 - The dose responses of S. mutans treated with AgNP-10 and equivalents of AgNP-100, $AgNO_3$ and $NaBH_4$. *A) Dose-response graphs with curves fitted where possible Each point is the mean OD_{630} of four replicates with background subtracted, represented as a percentage of an untreated control. Error bars indicate standard deviation. B) The fitted hillslope values, h, and C) IC_{50} values for each treatment converted from the fitted log(IC_{50}) of the dose-response curves. Error bars in B) and C) indicate 95% confidence intervals. Note the relatively steep increase in cell toxicity for $AgNO_3$ in the dose response curve (A) compared to AgNP, which is reflected in a lower hillslope value (B).*

6.3.3 Bacterial growth on agar

No change in the OD of a bacterial suspension after 24 hours incubation may indicate that the treatment has successfully inhibited the growth of bacteria, although there may still be some viable bacteria present. To determine whether treatments were bacteriocidal (bacteria were killed by treatment) or bacteriostatic (growth was inhibited but some bacteria were

still viable) bacterial suspensions with no change in OD were plated onto the agar culture substrate as and incubated for a further 24 hours to inspect for growth described in section 2.5.2.3.2. At 31.13 μg/mL AgNP-10 and equivalents, a substantial increase in OD was observed after 24 hours for all treatments except $AgNO_3$, thus only bacteria cultures treated with $AgNO_3$ were plated onto agar for further analysis. $AgNO_3$ at 97 μg/mL (double the AgNP-10 concentrate equivalent value) was also evaluated to determine approximate values for the minimum bacteriocidal concentration (MBC). Figure 6.15 provides images of the agar plates after 24 hours incubation and Table 6.1 summarises these results and estimates a limit for the MBC of $AgNO_3$ on each strain.

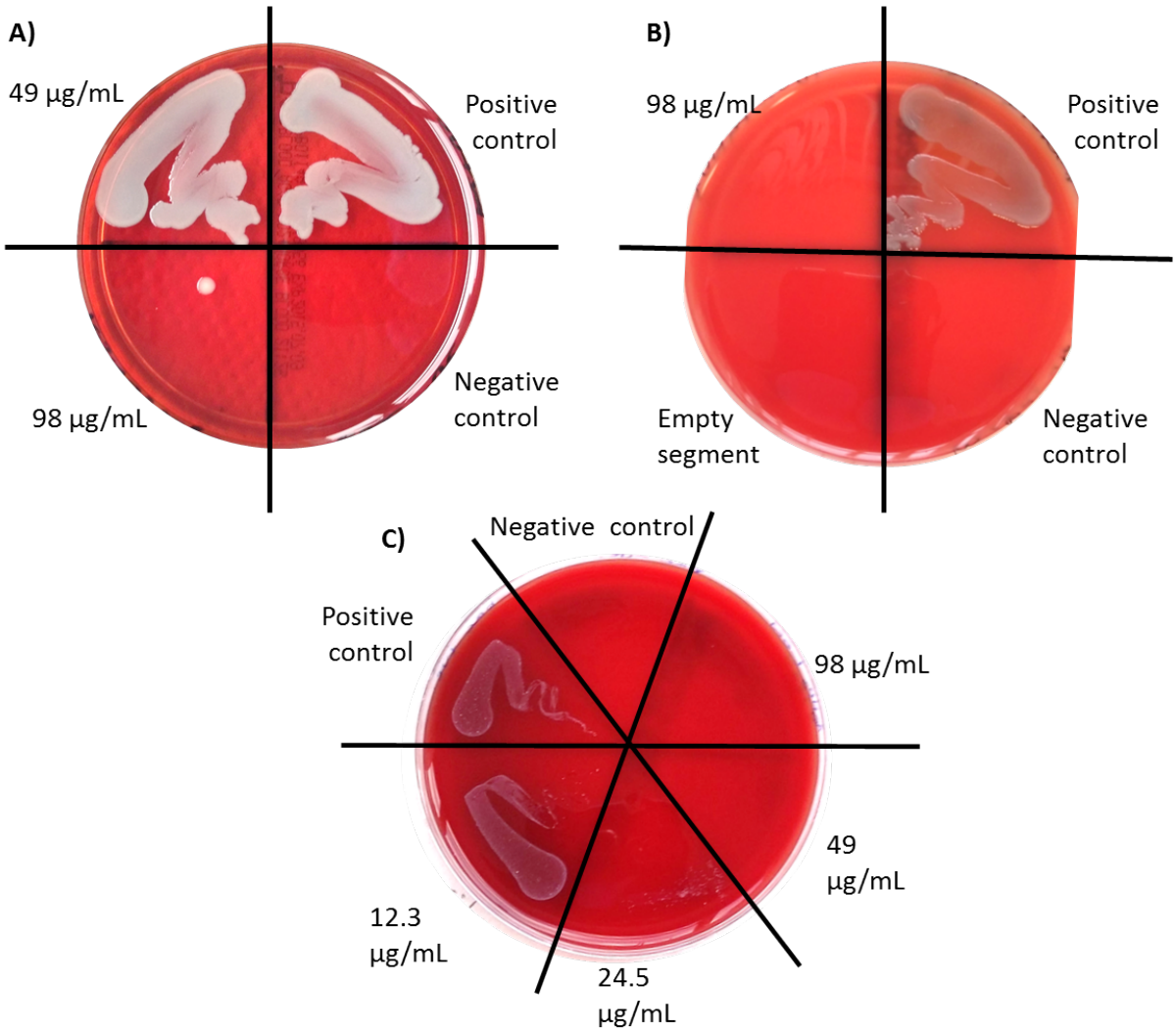

Figure 6.15 – Images of agar plates inoculated with bacteria incubated with $AgNO_3$ for 24 hours. *After 24 hours incubation with $AgNO_3$, bacterial suspensions that showed no increase in optical density were inoculated onto horse blood agar plates to determine minimum bactericidal concentration. Bacterial strains shown are A) S. aureus, B) E.coli and C) S. mutans. Treatment concentrations in each segment of agar are indicated in text.*

Bacterial strain	Growth observed at this concentration?			Estimate of MBC limits
	98 µg/mL	49 µg/mL	24.5 µg/mL	
S. aureus	1 colony	N/A	N/A	> 98 µg/mL
E. coli	No	Yes	N/A	< 98 µg/mL
S. mutans	No	No	Visibly reduced growth	< 49 µg/mL

Table 6.1 – Table demonstrating whether bacterial growth was observed on agar for each bacterial strain after 24 hours incubation with various treatments of $AgNO_3$. *"N/A" indicates that there was a visible increase in OD so the bacterial suspension was not assayed on agar. 49 µg/mL corresponds to the highest concentration of AgNP-10 concentrate tested.*

6.3.4 AgNP localisation in bacteria

Bacteria treated with AgNP were imaged using TEM to determine the destination of AgNP in treated bacteria. Initial observation using TEM as described in section 2.6.4.3 showed staining artefacts that were difficult to distinguish from AgNP. Consequently, EDS was used on these samples to test candidate regions for the presence of elemental silver (section 2.6.5.2). Figure 6.16 shows representative spectra of regions containing AgNP and artefact regions. Table 6.2 lists the other peaks observed and their sources.

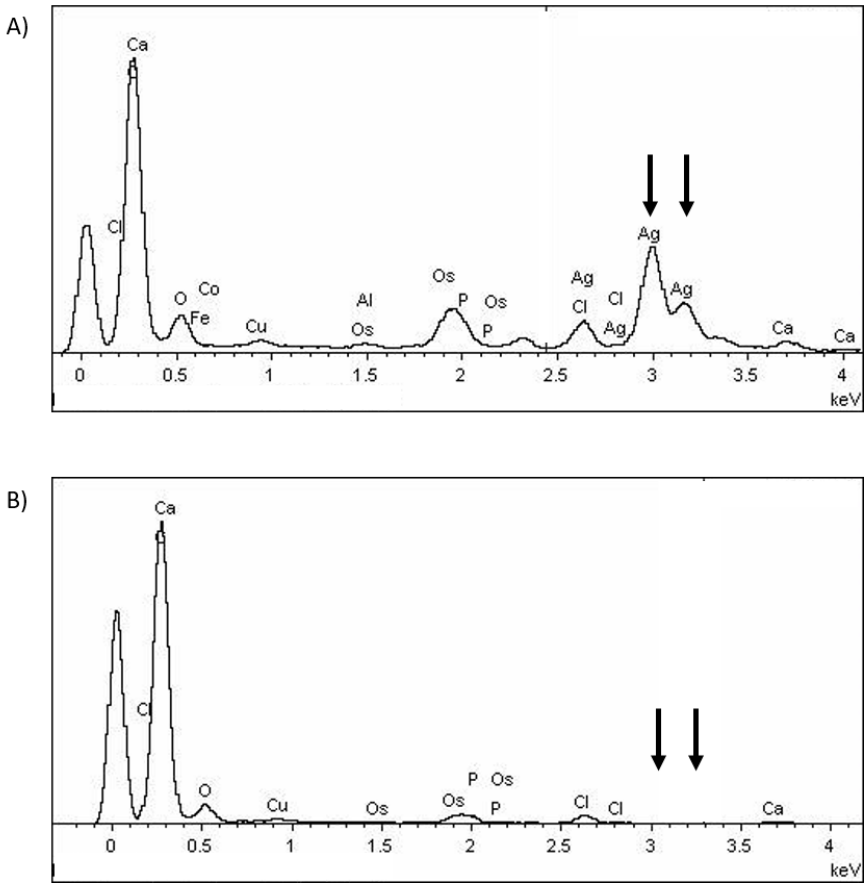

Figure 6.16 – X-ray emission spectra obtained using EDS. *A) Spectrum corresponding to a region in the sample containing silver. The two largest peaks in the energy spectrum that characterise silver are indicated by black arrows. B) Spectrum corresponding to a region containing no silver. There are no peaks at the characteristic energies of silver. Other elements are observed due to interference from sources such as the copper grid used to mount samples and the stain.*

Element	**Source**
Ag	Silver nanoparticles
Ca, P, O, C	PBS used to wash bacteria
Cu	Copper grid
Fe, Al, Co	Container used to mount grid in microscope
Os	Stain

Table 6.2 – Elemental peaks observed in the EDS spectra acquired in images of AgNP-treated bacteria and their sources.

No silver was detected in samples treated with AgNP-10, either inside bacteria or in the surrounding regions. Clusters of AgNP-100 were found in the substrate of all bacterial strains (Figure 6.17) however there were no detectable levels of silver inside cells.

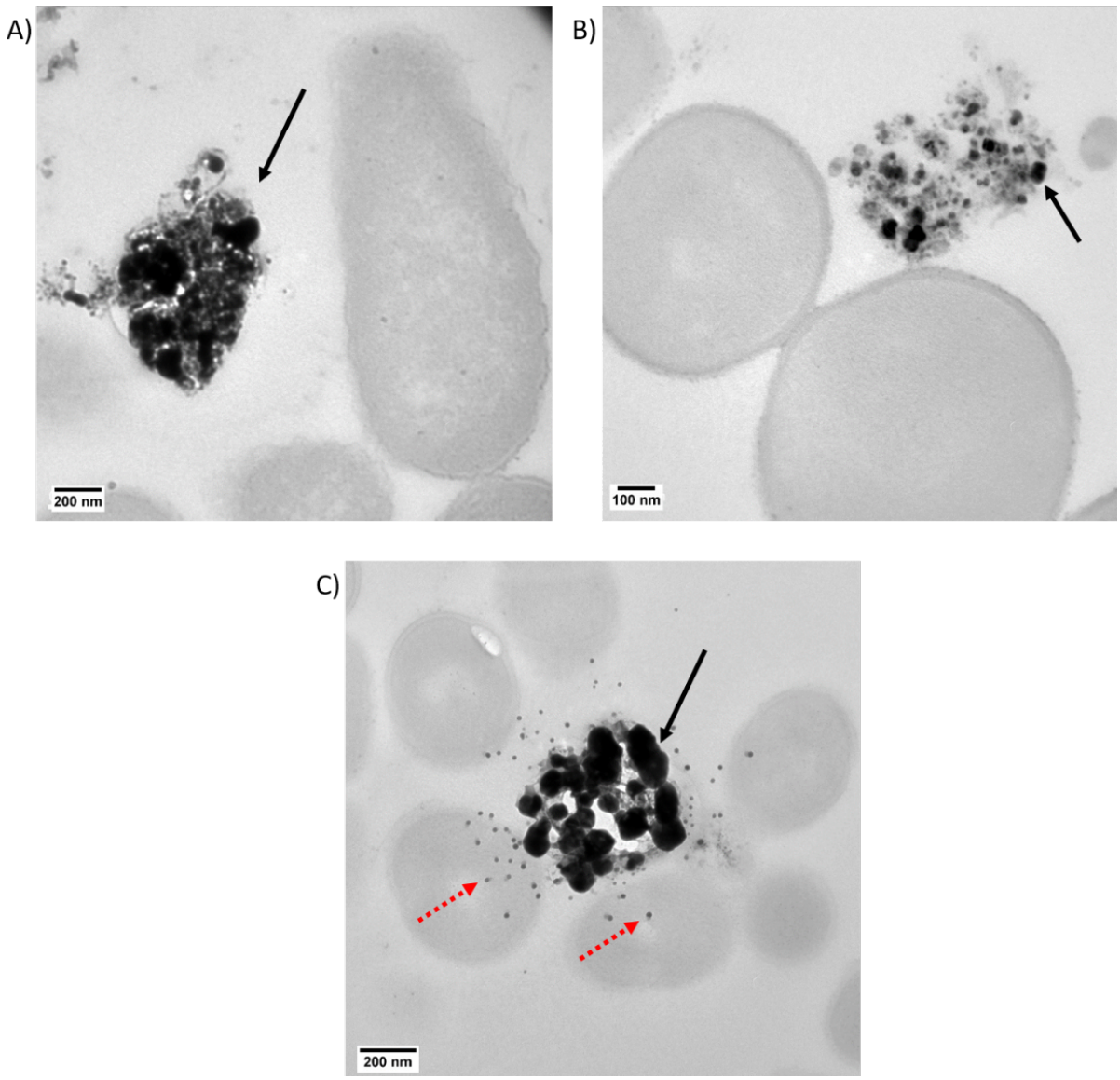

Figure 6.17 – TEM images of bacteria treated with AgNP-100. *A) E. coli, B) S. aureus and C) S. mutans. Regions marked with solid black arrows were verified as containing silver using EDS. Small regions such as those marked with red dotted arrows are staining artefacts rather than nanoparticles. No silver was observed inside cells for any strain.*

6.4 Oral epithelial cellular viability versus antibacterial activity on *S. mutans* after treatment with AgNP

Any treatment used to reduce the presence of bacteria in the oral cavity will also be exposed to the native tissues, thus any positive antibacterial effect must be balanced against cytotoxic effects. To evaluate these effects, the fitted curves for H400 cell viability and bacterial inhibition were compared for *S. mutans* treated with AgNP-10 and $AgNO_3$ (Figure 6.18). Inhibition as a percent of the control is given as:

$$I_{\%} = 100\% - V_{\%}$$

where $V_{\%}$is viability as a percent of the control. Neither AgNP-10 nor $AgNO_3$ inhibited *S. mutans* growth without significant cytotoxic effects on H400 cells. In particular, AgNP-10 caused a large reduction in H400 cell viability at concentrations that were well below those that exerted minimal inhibitory effect on *S. mutans* growth.

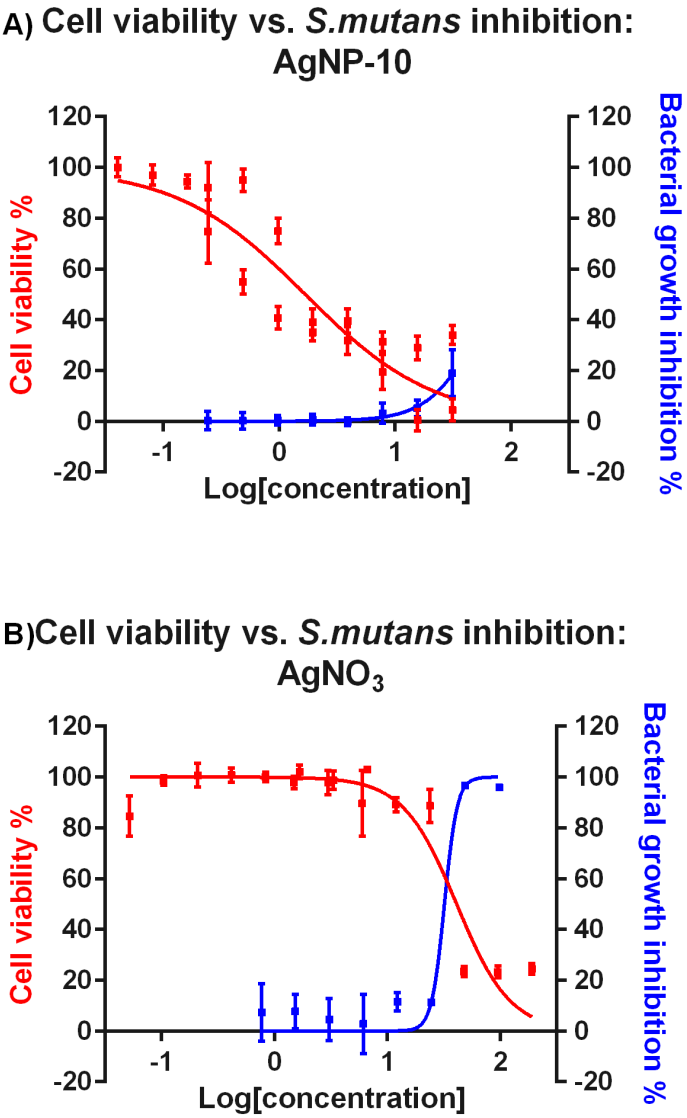

Figure 6.18 – Fitted curves for cell viability (red) as determined by MTT assay compared with S. mutans growth inhibition (blue) when treated with A) AgNP-10 and B) $AgNO_3$. *Interestingly, $AgNO_3$ displays a steeper curve than AgNP-10 for both bacterial inhibition and cell viability, although neither treatment inhibited* S. mutans *growth without significant cytotoxic effects on H400 cells*

6.5 Conclusion

The work in this chapter aimed to investigate the utility of the image analysis cell counting technique for determining the effects of AgNP on H400 cells. At concentrations at which many cells became detached from the culture substrate and/or died the image analysis method was unable to be reliably performed due to interference from cell debris. This limited the upper concentration to which the technique may be applied and as a result the

dose-response curve fitting did not achieve a realistic fit. Subsequently the MTT assay was better suited to generation of dose-response curves since this assay allowed a large number of concentrations to be rapidly tested, and the upper concentration limits were not restricted. Dose-response curves fitted to MTT data showed that Ag in the form of 10 nm nanoparticles has a lower IC_{50} on H400 cells than Ag in ionic form (from $AgNO_3$), but that $AgNO_3$ caused a relatively sharper increase in toxicity around the IC_{50} compared with the relatively shallow increase in toxicity caused by increased AgNP dose. The increased toxicity of AgNP-10 compared with $AgNO_3$ could be due to greater uptake of silver: ICP-OES indicated that H400 cells took up 22% more silver in the form of nanoparticles than in Ag^+ form.

When investigating lower concentrations of AgNP, the image analysis method proved to be superior to destructive methods such as MTT and haemocytometer counting, since its non-invasive nature enabled the generation of growth curves through longitudinal measurements over time of the same cultures. This approach was used to show that AgNP cause a time-dependent cytotoxic response in H400 cells. Furthermore, significant reduction in H400 growth after 48 hours incubation with AgNP-100 was only observed using the image analysis approach, suggesting it may have greater sensitivity in determining cell growth compared with the other approaches at this concentration.

Similarly to the cytotoxic activity data, dose-response curves in all bacteria exposed to $AgNO_3$ exhibited a characteristic relatively steep increase in toxicity compared with the more gradual increase in toxicity exerted by AgNP. However, conversely with the human cell analysis, ionic silver exhibited higher antibacterial activity compared with nanoparticulate silver in all strains as shown in both growth curves and dose-response curves. The difference

in cytotoxic and antibacterial IC_{50} doses could potentially be related to differences in the levels of salt in broth and media, causing different rates of AgNP aggregation. This was observed in TEM images of AgNP-100 (chapter 5), wherein suspension in broth caused relatively large aggregates of silver, whereas smaller nanoparticles were still distinguishable in images of AgNP-100 in media. However, the same effect was not observed in corresponding TEM samples of AgNP-10 due to the low particle numbers detected.

When the effects of AgNP-10 and $AgNO_3$ on *S. mutans* and H400 cells were compared, it was shown that neither AgNP-10 nor $AgNO_3$ inhibited *S. mutans* growth without causing significant cytotoxic effects on H400 cells. However, it was observed that AgNP-10 was able to disrupt a continuous thin film that formed. Since *S. mutans* is known to form biofilms in conjunction with other bacteria [144] this could be the cause of the thin film formation. However, without further analysis such as scanning electron microscopy (SEM) and live/dead staining it is not possible to confirm the presence of a biofilm and rule out other causes of formation, such as an accumulation of dead cells. This preliminary result suggests that whilst AgNP-10 may not be effective in inhibiting *S. mutans* growth, there may be potential for its use in biofilm prevention. However more work is required in this area, both to determine the nature of the film formation and the characterisation of AgNP interaction with this film.

AgNP-100 was generally less toxic than AgNP-10 and $AgNO_3$ in both bacteria and H400 cells. The characterisation in chapter 5 indicated that much of the mass of AgNP-100 was trapped in large aggregates with up to micron scale diameters, particularly when suspended in broth and media, which means the exposure to free nanoparticles was lower than intended. This could be the cause of the relatively low toxicity observed. This finding was corroborated in TEM images of all bacterial strains, where large silver aggregates were observed outside the

bacteria, but no detectable levels of silver were observed inside bacteria. TEM images of H400 cells treated with AgNP-100 showed a small number of cells with large aggregates, whilst many cells exhibited few or no associated nanoparticles. This suggests the silver became trapped in these few cells, whilst the rest of the population remained unaffected.

7 DISCUSSION

7.1 Introduction

This chapter provides an evaluation of the work presented in this thesis in the context of the objectives stated in the introduction section 1.8 and other previous studies. It subsequently proposes further work that could be undertaken to extend or improve this work, before concluding.

7.2 Evaluation of image analysis method and experimental applications

7.2.1 Experimental apparatus and protocols

Since phase contrast microscopy does not necessitate the use of staining or fixation to observe cells, it provides a method for non-invasively acquiring images of live cell cultures for analysis. Furthermore, since phase microscopes are commonly found in most research laboratories where cell culture is routinely performed and this approach does not require other costly additional equipment (e.g. automated microscope stages required for defocusing techniques), therefore the method presented exhibits obvious advantages and is widely accessible.

The image analysis method developed was applied to cells cultured in a range of cultureware. The lower size-limit for culture vessels was determined by the meniscus formed at the edges of culture dishes, which led to deterioration in image quality in wells with radii smaller than 22.1 mm (12-well plate) when imaged at x10 magnification that precluded the application of image analysis. There was no upper limit detected for the size of the vessel to which the method could be applied and growth curves were successfully measured for cells grown in 12-well plates up to T25 flasks. However, condensation build-up was observed on the underside of culture lids or upper surfaces of culture flasks due to the change in temperature when removed from the incubator. In smaller culture vessels this resulted in a

significant reduction in the image quality and contrast that could be obtained, therefore lids were removed prior to imaging in such vessels. Despite precautions put in place to minimise the risk of contamination, removing cultureware lids was undesirable leaving cultures vulnerable to microbial infection, therefore a sterile microscope chamber should be used where possible to reduce this risk.

7.2.2 Parameterisation and noise removal techniques

Using an image of fluorescently stained cell nuclei as the ground truth achieved the goal of providing an objective method for selecting optimal image analysis parameters. Additionally, it provided an automatically labelled ground truth that could be used to train classifiers for noise removal and to estimate cell detection rate errors. However, since image analysis parameters are specific to a given experimental setup, parameterisation and training of noise removal classifiers must be re-performed at the onset of each future experiment using a new camera, cell type or specific magnification. A x10 objective lens was used in the development and application of this method in all work described here, however lower magnification could provide a method for imaging larger areas of substrate in shorter times, thus reducing time spent outside incubator conditions. This approach should be considered in future investigations.

The method used for segmentation of nuclei from epifluorescence images used in this work was developed empirically, and included manual inspection and editing to ensure the vital criterion for individual nuclear segmentation was met to ensure the best possible parameterisation results. This was suitable for the relatively small dataset and the time taken for manual inspection for parameterisation would be offset in the long run by the time saved through use of image analysis method compared to, say, haemocytometer counting.

Furthermore, since parameterisation need only be performed once per experimental setup, the method need only be performed once. However, other more efficient segmentation methods may be considered in the future.

A disadvantage of using fluorescent images for the parameterisation ground truth is that it requires the user to have fluorescent imaging capabilities incorporated in their imaging microscopes. In instances where this is not possible, manual cell localisation, for example through 'clicking' on cell nuclei in images, could be investigated as an alternative approach. However, despite meeting the objective for accessibility more fully, this method would be more time-consuming than using fluorescent microscopy, and would be more prone to human error.

7.2.3 Application to different cell lines

Although developed for use on H400 epithelial cells, the principal cell line of interest, the image analysis technique was also applied successfully to the U2OS osteosarcoma cell line, even outperforming the rate of correct cell detection achieved for H400 cells. Conversely, the image analysis technique performed poorly on the 3T3 fibroblast cell line, and could not be applied at all to the OKF6 epithelial cell line. The key differences between successful and unsuccessful applications were due to cell morphology and growth characteristics. H400 cells cultured *in vitro* were generally homogeneously sized and polygonal in morphology, and following mitosis daughter H400 cells maintained cell-cell contact to form colonies of cells, which spread and merged together to form a sheet a single layer thick. OKF6 cells exhibited different growth characteristics and did not form single layers. The 3T3 cells exhibited a heterogeneous morphology ranging from polygonal cells similar to H400 cells through to fusiform or stellate shapes that resulted in a wider range of sizes. Conversely, U2OS cells

exhibited regular epithelial morphology and growth behaviour similar to that of the H400 cell line to form monolayers. It is therefore likely that the image analysis approach could perform well on other cell lines with similar characteristics, and the parameterisation method provides a way to quantify the success of this performance and compare it with the cell lines tested here.

7.2.4 Validation and comparison with other cell counting methods

The image analysis method was successfully shown to distinguish between cells cultured in different conditions by generating growth curves in H400 and U2OS cultures supplemented with a range of FCS concentrations. However, the image analysis method was not successful in cultures treated with relatively high levels of AgNP and $AgNO_3$ due to the presence of dead and dying cells. These lead to erroneous segmentation unable to be identified as such by the classifier (since the classifier was not trained on segmentations with these properties). As a consequence, the method was not suitable for generating growth curves for these toxicants on H400 cells, since it was not possible to measure a wide enough range of treatment concentrations.

Comparison of cell counts achieved with the novel cell counting method with other available segmentation algorithms (global thresholding, graph cuts and active contours) showed that the active contour method achieved vastly inferior results in terms of correctly detected cells for level sets (45.6% of cells in the nuclear ground truth images, compared to 87.1%), and the graph cut and thresholding methods were unable to segment enough individual cells to carry out a meaningful comparison. It is important to consider the known limitations of these methods and the purpose for which they were originally developed when considering their relatively poor performance. For example, segmentation using global thresholding has

great utility in images with different properties, such as fluorescent microscopy images, but is known to be inappropriate for PC images due to the similarity between cell cytoplasm and background. The original aim of the level set and graph cut methods is to accurately segment individual cells for the purpose of cell tracking and shape analysis. However such methods were found clearly to be unsuitable for adaptation for the purpose of longitudinal monitoring of cell number in cell cultures of contacting cells. This indicates the necessity of a novel method such as the one developed in this thesis for this specific purpose.

Cell counts obtained by the method were also compared with values derived using a haemocytometer and the commercially available LUNA cell counting method and demonstrated that the objective of providing equivalent results was successfully achieved: counts between methods were linearly proportional over a range of cell densities. However, counts obtained by using haemocytometer and LUNA approaches were systematically higher, likely due to ineffective homogenisation of the cell suspension used in these techniques caused by user error or sample degradation. Investigations into the intrinsic error of the haemocytometer method showed that the average user coefficient of variation of 18.6% was similar to those that have been typically reported previously (range 9-20%) [46], [48]. It was not possible to directly compare cell counts using the MTT assay since this is an inferred value obtained from spectrophotometry absorption, converted to cell numbers through calibration with haemocytometer counts, however both methods showed the same trend in H400 cell cultures treated with a range of supplementation concentrations of FCS.

Since all methods tested generated comparable results in terms of cell number, the inherent advantages and disadvantages of each technique must be considered when selecting the most suitable cell counting method. Table 7.1 provides a comparison of the properties of

each method. A particular advantage of counting cells using the image analysis approach over other methods is that cultures are undisturbed in the process of data collection, thus may be studied longitudinally to easily generate growth curves. This contrasts with the other techniques which may only be used as endpoint assays, necessitating additional cultures for generation of growth curves, adding further time and expense and introducing errors through variations between cultures. Consequently it is common to use these techniques to determine cell counts at only one or perhaps two time points, generally 24 and 48 hours [34]. However this may be insufficient to provide a true indication of time-dependent effects, for example the dose-dependent response of U2OS cells treated with FCS only became apparent after 72 hours culture (Figure 4.25). These data demonstrate the importance of monitoring cell growth over longer time periods. The capability to non-invasively count cells in a culture is also advantageous when cell number is not the only parameter of interest. For example, in experiments to determine AgNP uptake as described in section 6.2.3.2 cell number was directly measured from treated samples using the image analysis method, thus no additional cultures were required as necessitated in previous protocols [120], [121].

Despite being unable to apply the MTT assay to longitudinal studies due to its destructive nature, it does provide the simplest and most rapid way to process a relatively wide range of concentrations. However, the results of the MTT assay are affected by several factors, such as length of incubation period and residual cell media [210]. Furthermore it has been shown that some chemicals such as silver nanoparticles cause reduction of MTT readouts even when no cells are present, potentially leading to erroneous results [112], [135]. Consequently it has been proposed that the MTT assay should be performed in conjunction

with other methods to ensure reliability [34], [112], [135]. It is therefore proposed here that MTT and the developed image analysis approach may be best used together as part of a multimodality approach. For example, the MTT assay may be used to generate an initial dose-response curve from which appropriate concentrations may be identified to generate growth curves for study of time-dependent effects using the image analysis approach. Similarly, the image analysis approach may be used to validate results obtained using the MTT assay.

Method for cell counting	Cost	Accuracy and objectivity	Throughput	Invasiveness	Cell concentration range
Haemocytometer	Low one-off cost	Poor, subject to human error in cell counting and samples are subject to degradation	Low, cultures must be prepared and counted individually	Destructive	Wide range, although ideally >100 cells measured at a time
LUNA automated counter	High one-off cost of cell counting unit, lower ongoing cost of consumable slides	Medium, samples are processed automatically but suitable parameters are chosen manually and any limitations of proprietary software are unknown. Samples are subject to degradation	Low, cultures must be prepared and counted individually	Destructive	Wide range
MTT assay	Low but ongoing costs for consumables	Good, although cell number is inferred rather than directly measured and results may be affected by interference with other chemicals present	High, many samples processed at once	Destructive	Wide range
PC microscopy image analysis method	Low, if any cost, most laboratories already have PC microscopes and there are many freely available image analysis software packages	Good, if used on suitable cell line	Medium, cultures must be imaged individually but are computationally processed automatically	Non-invasive, individual cultures may be studied longitudinally	Wide range, although limited if high levels of cell debris are present

Table 7.1 – Table comparing the properties of several routinely used cell counting methods in comparison to the image analysis method developed here.

7.3 Silver nanoparticles

One of the key objectives of the work presented here was to take into account the behaviour of AgNP suspended in cell culture media and bacterial broth when interpreting results. Despite the known aggregation effects of AgNP interaction with salts in biological media, many other studies do not take these effects into consideration [211], [212]. It was shown that AgNP-100 in particular reacted with media, and especially broth, causing a significant increase in the average particle size and reducing the 'true' concentration doses by "locking away" silver in to large micron-scale aggregates. All toxicity experiments were therefore evaluated in the context of this knowledge.

For both cells and bacteria, results regarding size-dependence and a comparison of ionic and nanoparticulate silver are discussed in the following sections. Subsequently the comparison of AgNP effects in both bacteria and mammalian cells is discussed.

7.3.1 H400 cells

The effects of AgNP on the H400 oral epithelial cell line were investigated for the first time in this work. It was found that at treatment concentrations of 2.5 µg/mL of AgNP-10, significant reductions in H400 cell growth was observed, i.e. the low dose cell growth stimulation observed in other cell lines treated with similar concentrations of AgNP did not occur [136], [138].

AgNP-100 appeared to be generally less cytotoxic than smaller AgNP-10, in agreement with previous studies on mammalian cells, although growth curves indicated a time-dependent increase in toxicity of AgNP-100 [132]. However, all experiments showed that AgNP-10 exerted a greater cytotoxic effect than equivalent concentrations of ionic silver, contrary to

previous studies using mammalian cell lines, which generally show ionic silver to be more cytotoxic [120], [133]. In conjunction with ICP-OES data showing that H400 cells took up 22% more nanoparticulate silver than ionic silver, these data support the theory that AgNP provide a "Trojan horse" to facilitate delivery of silver across cell membranes where they may exert cell damage from within the cytoplasm [125]. Investigations into cell uptake using quantitative ICP methods at a range of concentrations could be used to investigate the Trojan horse theory by plotting cell uptake against treatment concentrations.

7.3.2 Bacteria

The IC_{50} concentrations of the AgNP-10 dose-response curves suggested AgNP-10 exerted a stronger antibacterial effect on Gram negative *E. coli* compared with Gram positive *S. aureus,* as has been reported previously [118], [128]. Interestingly, however, the IC_{50} for Gram positive *S. mutans* was lower than for *E. coli*, although comparisons must be made with caution since these strains were cultured under different CO_2 levels during incubation. The resulting differences in broth pH could have affected the rate of dissolution or aggregation of nanoparticles thus causing a differential response. It is also important to note that, unlike *S. aureus* and *E. coli*, *S. mutans* formed a continuous film layer during incubation thus the toxicity of AgNP may have been enhanced through entrapment in or interactions with this film layer. Additionally, it is interesting to note that tears in the thin film layer that had formed in the well were observed at high concentrations of AgNP-10. It has been suggested previously that silver is able to disrupt dental biofilm formation [144], and *S. mutans* is known to form biofilms *in vivo* in conjunction with other bacteria [15]. If the source of this layer was also formation of a biofilm matrix, this suggested that the antibacterial mechanism of AgNP-10 may have been via the biofilm matrix rather than

targeting bacterial cells, as has been suggested previously [15]. However further investigation is required to verify the nature of this film layer.

All studies showed that ionic silver was more toxic to bacteria than nanoparticulate silver in all strains tested, as has been observed in some previous studies [113], [114]. However, despite the greater antibacterial effect of $AgNO_3$, the "biofilm" tearing phenomenon observed in cultures treated with AgNP-10 was not observed for $AgNO_3$, potentially indicating different mechanisms of antibacterial action. This highlights the importance of the need for further investigations into the effects of AgNP on biofilm formation to potentially target oral bacteria using a different mechanism.

A size-dependent effect on nanoparticle toxicity was observed in all experiments, indeed it was observed in growth curves and dose-response curves that AgNP-100 minimally caused any reduction in bacterial growth in *S. aureus* and *S. mutans*. However, these results must be interpreted with caution as AgNP-100 had the most extreme aggregation reaction with broth, thus the effective concentration was likely much lower than intended. This could have been because this type of AgNP was purchased rather than synthesised in house, thus utilised a different stabiliser than AgNP-10 (PVP rather than sodium borohydride). It is therefore recommended that further studies on the size-dependence of nanoparticles use samples synthesised and stabilised as similarly as possible to enable better comparison.

7.3.3 Comparison of the effects of AgNP on H400 cells with *S. mutans*

The effective inhibitory concentrations of AgNP have been shown to take a wide range of values when applied to the same cell lines or bacterial species in different studies [145], [146], [213], and for some cell lines both stimulatory [138] and inhibitory [131] effects have

been observed at the same treatment concentrations in different. This is most likely due variations in AgNP synthesis and functionalisation methods, thus one objective of this work was to compare inhibition in H400 oral epithelial cells and S*. mutans* as accurately as possible by using the same samples of AgNP on each and culturing each cell type under the same atmospheric conditions (5% CO_2, 37°C). The comparison of cell viability versus bacterial inhibition however showed that AgNP-10 was not able to inhibit S. *mutans* growth without causing high levels of cytotoxicity in H400 cultures at the same concentration. As discussed in section 7.3.1 however, the H400 cell line is a cancer derived line, which may be more susceptible to the toxic effects AgNP than a primary cell line. Therefore further investigations should use a primary cell line for comparison of cytotoxicity with the antibacterial effects on oral bacteria since this would provide a more relevant model to evaluate the appropriateness of the use of AgNP for antibacterial applications.

Another barrier to the direct comparison between cells and bacteria was the differential effects that media and broth had on the aggregation levels of nanoparticles. This was observed most obviously for AgNP-100 samples, which demonstrated a large increase in average size when suspended in water compared with media, and an even greater increase in aggregation in broth to the extent where it was not possible to measure particle sizes at all. However it was likely that time-dependent effects during the length of incubation may also have affected AgNP-10 aggregation and dissolution – previous studies have shown the levels of silver ions released from AgNP change over time depending on factors such as the presence of salts [214]. Therefore in future studies time dependent characterisation of AgNP in media and broth may provide a greater understanding of the reasons behind any differences in *in vitro* toxicity performed in different types of cell media.

Furthermore it was interesting to note that the dose-response curves for both H400 cells and bacteria displayed a relatively steep curve for $AgNO_3$ but a shallower curve for AgNP. This could have been due to differences in the rate of uptake: if AgNP were taken up relatively easily by cells through the proposed "Trojan horse" method, they were able to inflict small amounts of cell damage at lower concentrations. Conversely, if Ag^+ ions were unable to easily penetrate cell membranes they may have been unable to inflict cell damage until their concentration was sufficiently high enough to break down the cell membranes completely.

7.4 Future work

It is envisaged that future work could be carried out to extend the image analysis method to overcome the limitations of the current method. For example, further investigations may determine the extent of the interference of condensation on cultureware has on the results of the image analysis method and identify whether computational adjustments to image contrast could be applied to overcome them.

Additionally, to extend the application of the image analysis approach to evaluating cells treated with substances causing high levels of cell death, classifiers could be trained to identify segmented regions corresponding dead cells in images using a similar discrete mereotopology approach to that used for parameterisation, in this case using a vital stain to automatically label dead cells for use in the classifier training set. If successful this would enable the image analysis approach to be used for generation of dose-response curves.

Additional work could be carried out to further validate the use of the image analysis method, for example, through application to other image resolutions/ magnifications, and

cell lines with different properties, such as non-adherent cell lines. The image analysis cell counting method described here was compared with routinely used laboratory methods for monitoring cell count since these are the most relevant methods currently used for the same purpose. However, future work could include comparison with other computational methods for cell segmentation in PC microscopy images to determine whether they were appropriate for this purpose, or to the defocusing brightfield techniques on which the conceptual development of the image analysis method was based.

AgNP have previously been shown to exert stronger inhibitory effects on cancer cell lines compared with primary cell lines [129], [131]. Further work should therefore involve comparison of the cytotoxicity of AgNP on the cancer-derived H400 cell line with a primary oral epithelial cell line to determine whether the same effect occurs in oral epithelial tissue. Data generated could open a new avenue of investigation into the use of AgNP as a novel treatment of oral SCC. In terms of nanotoxicological investigations, the complexity of the *in vitro* model of the oral epithelium may be increased by extending the culture to a 3-dimensional or organotypic culture model [215]. The advantage of such cultures is that they provide an environment which more accurately represents the structure of tissues and intercellular interactions of the *in vivo* epithelium and this would likely provide more information about AgNP penetration through layers of tissue. However, the improved structural relevance is at the cost of greatly increased difficulty of generating and maintaining such cultures. Similarly, *in vitro* models of oral biofilm could provide a more biologically relevant model of the oral environment on which to test the antibacterial activity of AgNP. Additionally, a biofilm model could also be used to further investigate the

observation that AgNP disrupted the formation of a potential *S. mutans* biofilm, since this may be a more effective method of antibacterial action for AgNP than bactericidal activity.

7.5 Conclusion

This thesis developed a novel image analysis based method for counting cells in epithelial cell cultures using phase contrast microscopy, inspired by the defocusing technique used in brightfield microscopy. This incorporated a novel application of mean filters from a single image to roughly segment cells for counting, and a novel application of RCC to enable automated filter radius selection and automated dataset labelling for training classifiers for noise removal.

Thorough testing and refinement of the experimental protocols showed that the method has potential application to multiple cell lines in a wide range of *in vitro* cultureware and experimental set ups. Comparison with other image analysis segmentation algorithms showed that the novel method delivered superior results for the purpose of cell counting. Validation against current commonly used laboratory cell counting techniques as the "gold standard" showed comparable results could be achieved but with the advantage of an objective and non-invasive technique.

The method was subsequently applied to investigate the effects of silver nanoparticles on oral epithelial cell cultures and compare this to ionic silver achieving success through combination with the MTT assay to exploit the advantages of each technique and deliver a multi-modal investigation of AgNP toxicity. It was found that AgNP and ionic silver have different toxicity profiles: Ag^{+} exhibited a characteristic relatively steep increase in toxicity compared with the more gradual increase in toxicity exerted by AgNP. Additionally, AgNP

were more cytotoxic at equivalent concentrations, potentially due to a greater uptake by cells. AgNP size- and dose- dependence were also observed in agreement with previous findings in the literature [19], [115].

Concurrent investigations into the antibacterial effects of AgNP showed that AgNP had lower toxicity compared to ionic silver, conversely to the effects observed on oral epithelial cells. Importantly, no antibacterial effects were observed without significant reductions in oral epithelial viability, highlighting a need for further nanotoxicological investigations before incorporation of nanoparticles into dental and oral hygiene products.

LIST OF REFERENCES

[1] C. A. Squier and M. J. Kremer, “Biology of oral mucosa and esophagus.,” *J. Natl. Cancer Inst. Monogr.*, vol. 52242, pp. 7–15, 2001.

[2] A. Nanci, *Ten Cate’s Oral Histology: Development, Structure, and Function*. Elsevier Health Sciences, 2007.

[3] B. Alberts, D. Bray, K. Hopkin, A. D. Johnson, J. Lewis, M. Raff, K. Roberts, and P. Walter, *Essential Cell Biology*, 4th ed. Garland Science, 2013.

[4] M. G. Newman, H. Takei, P. R. Klokkevold, and F. A. Carranza, *Carranza’s Clinical Periodontology*. Elsevier Health Sciences, 2011.

[5] J. K. Klarlund and E. R. Block, “Free edges in epithelia as cues for motility,” *Cell Adhes. Migr.*, vol. 5, no. 2, pp. 106–110, 2011.

[6] V. Mehrotra, P. Devi, T. V. Bhovi, B. Jyoti, and U. Pradesh, “Mouth As a Mirror of Systemic Diseases,” *Gomal J. Med. Sci.*, vol. 8, no. 2, pp. 235–241, 2010.

[7] Y. Jinbu and T. Demitsu, “Oral ulcerations due to drug medications,” *Jpn. Dent. Sci. Rev.*, vol. 50, no. 2, pp. 40–46, 2014.

[8] D. M. Williams, F. J. Hughes, E. W. Odell, and P. M. Farthing, *Pathology of Periodontal Disease*, 1st ed. Oxford University Press, 1992.

[9] dhealth, “Periodontal Disease,” 2016. [Online]. Available: https://www.dhealth.com.au/gum-disease-treatment/problems/periodontal-disease/. [Accessed: 10-Aug-2016].

[10] L. Feller and J. Lemmer, “Oral Squamous Cell Carcinoma: Epidemiology, Clinical Presentation and Treatment,” *J. Cancer Ther.*, vol. 03, no. 04, pp. 263–268, 2012.

[11] G. R. Ogden and A. J. Wight, “Aetiology of oral cancer: alcohol,” *Br. J. Oral Maxillofac. Surg.*, vol. 36, no. 4, pp. 247–251, 1998.

[12] T. Franco, S. Trapasso, L. Puzzo, and E. Allegra, “Electronic Cigarette: Role in the Primary Prevention of Oral Cavity Cancer.,” *Clin. Med. insights. Ear, nose throat*, vol. 9, no. 1, pp. 7–12, 2016.

[13] A. K. Markopoulos, “Current aspects on oral squamous cell carcinoma.,” *Open Dent. J.*, vol. 6, pp. 126–130, 2012.

[14] A. A. Ghashm, N. H. Othman, M. N. Khattak, N. M. Ismail, and R. Saini, “Antiproliferative effect of Tualang honey on oral squamous cell carcinoma and osteosarcoma cell lines.,” *BMC Complement. Altern. Med.*, vol. 10, no. 49, pp. 1–11, 2010.

[15] R. García-Contreras, L. Argueta-Figueroa, C. Mejía-Rubalcava, R. Jiménez-Martínez, S. Cuevas-Guajardo, P. A. Sánchez-Reyna, and H. Mendieta-Zeron, “Perspectives for the use of silver nanoparticles in dental practice.,” *Int. Dent. J.*, vol. 61, no. 6, pp. 297–301,

2011.

[16] J. D. Robertson and S. Orrenius, “Molecular mechanisms of apoptosis induced by cytotoxic chemicals,” *Crit. Rev. Toxicol.*, vol. 30, no. 5, pp. 609–627, 2000.

[17] M. Nair, Z. Kronfol, and S. Schwartz, “Effects of alcohol and nicotine on cytotoxic functions of human lymphocytes,” *Clin. Immunol. Immunopathol.*, vol. 54, no. 3, pp. 395–409, 1990.

[18] C. Chen, S.-S. Lee, H.-C. Yu, F.-M. Huang, and Y.-C. Chang, “Effects of nictine on cell growth, migration and production of inflammatory cytokines and reactive oxygen species by cementoblasts,” *J. Dent. Sci.*, vol. 10, no. 2, pp. 154–160, 2015.

[19] T.-H. Kim, M. Kim, H.-S. Park, U. S. Shin, M.-S. Gong, and H.-W. Kim, “Size-dependent cellular toxicity of silver nanoparticles,” *J. Biomed. Mater. Res. Part A*, vol. 100A, no. 4, pp. 1033–1043, 2012.

[20] J. Kaur and K. Tikoo, “Evaluating cell specific cytotoxicity of differentially charged silver nanoparticles.,” *Food Chem. Toxicol.*, vol. 51, pp. 1–14, 2013.

[21] A. Elsaesser and C. V. Howard, “Toxicology of nanoparticles,” *Adv. Drug Deliv. Rev.*, vol. 64, no. 2, pp. 129–137, 2012.

[22] J. A. Aas, B. J. Paster, L. N. Stokes, I. Olsen, and F. E. Dewhirst, “Defining the Normal Bacterial Flora of the Oral Cavity Defining the Normal Bacterial Flora of the Oral Cavity,” *J. Clin. Microbiol.*, vol. 43, no. 11, pp. 5721–5732, 2005.

[23] P. D. Marsh, D. A. Head, and D. A. Devine, “Dental plaque as a biofilm and a microbial community - Implications for treatment,” *J. Oral Biosci.*, vol. 57, no. 4, pp. 185–191, 2015.

[24] M. Avila, D. M. Ojcius, and O. Yilmaz, “The oral microbiota: living with a permanent guest.,” *DNA Cell Biol.*, vol. 28, no. 8, pp. 405–411, 2009.

[25] G. D. Tribble and R. J. Lamont, “Bacterial invasion of epithelial cells and spreading in periodontal tissue,” *Periodontol. 2000*, vol. 52, no. 1, pp. 68–83, 2010.

[26] W. J. Loesche, “Role of Streptococcus mutans in human dental decay.,” *Microbiol. Rev.*, vol. 50, no. 4, pp. 353–380, 1986.

[27] R. H. Selwitz, A. I. Ismail, and N. B. Pitts, “Dental caries,” *Lancet*, vol. 369, no. 9555, pp. 51–59, 2007.

[28] R. P. Allaker, “The Use of Nanoparticles to Control Oral Biofilm Formation,” *J. Dent. Res.*, vol. 89, no. 11, pp. 1175–1186, 2010.

[29] L. Li, L. Guo, R. Lux, R. Eckert, D. Yarbrough, J. He, M. Anderson, and W. Shi, “Targeted antimicrobial therapy against Streptococcus mutans establishes protective non-cariogenic oral biofilms and reduces subsequent infection,” *Int. J. Oral Sci.*, vol. 2, no. 2, pp. 66–73, 2010.

[30] “Dentists Develop New Treatment That Reverses Tooth Decay Naturally,” *Masculine*

Life, 2014. [Online]. Available: http://www.insiderlifestyle.com/wp-content/uploads/2014/06/new-tooth-decay-treatment.jpg.

[31] I. Freshney, "Application of Cell Cultures to Toxicology," in *Cell Culture Methods for In Vitro Toxicology*, G. Stacey, A. Doyle, and M. Ferro, Eds. Springer Science & Business Media, 2013.

[32] G. Stacey, P. Bar, and R. Granville, "Primary Cell Cultures and Immortal Cell Lines," *Encycl. Life Sci.*, pp. 1–6, 2009.

[33] X. S. Yue, M. Fujishiro, C. Nishioka, T. Arai, E. Takahashi, J. S. Gong, T. Akaike, and Y. Ito, "Feeder cells support the culture of induced pluripotent stem cells even after chemical fixation," *PLoS ONE*, vol. 7, no. 3. pp. 1–9, 2012.

[34] F. Joris, B. B. Manshian, K. Peynshaert, S. C. De Smedt, K. Braeckmans, and S. J. Soenen, "Assessing nanoparticle toxicity in cell-based assays: influence of cell culture parameters and optimized models for bridging the in vitro-in vivo gap.," *Chem. Soc. Rev.*, vol. 42, no. 21, pp. 8339–8359, Nov. 2013.

[35] M. A. Dickson, W. C. Hahn, Y. Ino, V. Ronfard, J. Y. Wu, R. A. Weinberg, D. N. Louis, F. P. Li, and J. G. Rheinwald, "Human keratinocytes that express hTERT and also bypass a p16(INK4a)-enforced mechanism that limits life span become immortal yet retain normal growth and differentiation characteristics.," *Mol. Cell. Biol.*, vol. 20, no. 4, pp. 1436–1447, 2000.

[36] S. Prime, S. Nixon, and I. Crane, "The behaviour of human oral squamous cell carcinoma in cell culture," *J. Pathol.*, vol. 160, no. 3, pp. 259–269, 1990.

[37] M. Zubair, A. Ekholm, H. Nybom, S. Renvert, C. Widen, and K. Rumpunen, "Effects of Plantago major L. leaf extracts on oral epithelial cells in a scratch assay," *J. Ethnopharmacol.*, vol. 141, no. 3, pp. 825–830, 2012.

[38] M. R. Milward, I. L. C. Chapple, H. J. Wright, J. L. Millard, J. B. Matthews, and P. R. Cooper, "Differential activation of NF-kappaB and gene expression in oral epithelial cells by periodontal pathogens.," *Clin. Exp. Immunol.*, vol. 148, no. 2, pp. 307–24, 2007.

[39] F. Milde, D. Franco, A. Ferrari, V. Kurtcuoglu, D. Poulikakos, and P. Koumoutsakos, "Cell Image Velocimetry (CIV): boosting the automated quantification of cell migration in wound healing assays.," *Integr. Biol. (Camb).*, vol. 4, no. 11, pp. 1437–47, 2012.

[40] J. Adds and E. Larkcom, *Tools, Techniques and Assessment in Biology: A Course Guide for Students and Teachers*. Nelson Thornes, 1999.

[41] T. Mosmann, "Rapid colorimetric assay for cellular growth and survival: application to proliferation and cytotoxicity assays.," *J. Immunol. Methods*, vol. 65, no. 1–2, pp. 55–63, 1983.

[42] Biomedica, "EZ4U (NONRADIOACTIVE CELL PROLIFERATION AND CYTOXICITY)." [Online]. Available: http://www.eaglebio.com/content/bi-5000_EZ4U_Nonradioactive_Cell_Proliferation_and_Cytoxicity_ELISA_Assay_Kit.pdf.

[Accessed: 28-Jul-2016].

[43] D. Dehlinger, L. Suer, M. Elsheikh, J. Peña, and P. Naraghi-Arani, “Dye free automated cell counting and analysis.,” *Biotechnol. Bioeng.*, vol. 110, no. 3, pp. 838–847, Mar. 2013.

[44] N. Jaccard, L. D. Griffin, A. Keser, R. J. Macown, A. Super, F. S. Veraitch, and N. Szita, “Automated method for the rapid and precise estimation of adherent cell culture characteristics from phase contrast microscopy images.,” *Biotechnol. Bioeng.*, vol. 111, no. 3, pp. 504–517, Sep. 2014.

[45] R. Biggs and R. L. Macmillan, “The error of the red cell count,” *J. Clin. Pathol.*, vol. 1, no. 5, pp. 288–291, Nov. 1948.

[46] N. S. Prathalingam, W. W. Holt, S. G. Revell, S. Jones, and P. F. Watson, “The precision and accuracy of six different methods to determine sperm concentration.,” *J. Androl.*, vol. 27, no. 2, pp. 257–262, 2006.

[47] E. K. Seaman, E. Goluboff, N. BarChama, and H. Fisch, “Accuracy of semen counting chambers as determined by the use of latex beads.,” *Fertil. Steril.*, vol. 66, no. 4, pp. 662–665, Oct. 1996.

[48] J. P. Brillard and G. R. Mcdaniel, “The Reliability and Efficiency of Various Methods for Estimating Spermatozoa Concentration,” *Poult. Sci.*, vol. 64, pp. 155–158, 1985.

[49] T. L. Riss, R. A. Moravec, A. L. Niles, H. A. Benink, T. J. Worzella, and L. Minor, “Cell viability assays,” in *Assay Guidance Manual*, Bethesda (MD): Eli Lilly & Company and the National Center for Advancing Translational Sciences, 2013, pp. 1–23.

[50] D. B. Murphy and M. W. Davidson, *Fundamentals of Light Microscopy and Electronic Imaging*. John Wiley & Sons, 2012.

[51] J. Lojk, U. Cibej, D. Karlas, L. Sajn, and M. Pavlin, “Comparison of two automatic cell-counting solutions for fluorescent microscopic images,” *J. Microsc.*, vol. 260, no. 1, pp. 107–116, 2015.

[52] U. Agero, L. G. Mesquita, B. R. a Neves, R. T. Gazzinelli, and O. N. Mesquita, “Defocusing microscopy.,” *Microsc. Res. Tech.*, vol. 65, no. 3, pp. 159–65, Oct. 2004.

[53] A. H. Fischer, K. A. Jacobson, J. Rose, and R. Zeller, “Hematoxylin and Eosin Staining of Tissue and Cell Sections,” in *Preparation of Cells and Tissues for Fluorescence Microscopy*, vol. 5, S. and Goldman, Ed. Cold Spring Harbor Laboratory Press, 2008, p. pdb.prot4986.

[54] F. Zernike, “Observation of Transparent Objects,” *Physica*, vol. 9, no. 10, pp. 974–986, 1942.

[55] N. T. Shaked, Z. Zalevsky, and L. L. Satterwhite, *Biomedical Optical Phase Microscopy and Nanoscopy*. Academic Press, 2012.

[56] D. B. Murphy, R. Oldfield, S. Schwartz, and M. W. Davidson, “Introduction to Phase Contrast Microscopy,” *Nikon*. [Online]. Available:

http://www.microscopyu.com/articles/phasecontrast/phasemicroscopy.html. [Accessed: 17-Jun-2016].

[57] I. Vartiainen, C. Holzner, I. Mohacsi, P. Karvinen, A. Diaz, G. Pigino, and C. David, “Artifact characterization and reduction in scanning X-ray Zernike phase contrast microscopy,” *Opt. Express*, vol. 23, no. 10, p. 13278, 2015.

[58] E. Horn and R. Zantl, “Phase-Contrast Light Microscopy of Living Cells Cultured in Small Volumes,” *Microscopy and Analysis*, vol. 20, no. 3, pp. 5–7, 2006.

[59] K. Spring, “Fluorescence Microscopy,” *Encycl. Opt. Eng.*, no. April 2013, pp. 37–41, 2011.

[60] B. Chazotte, “Labeling nuclear DNA using DAPI,” *Cold Spring Harb. Protoc.*, vol. 6, no. 1, pp. 80–83, 2011.

[61] J. R. Lakowicz, “Quenching of Fluorescence,” in *Principles of Fluorescence Spectroscopy*, 2006, pp. 227–330.

[62] F. Piccinini, A. Kiss, and P. Horvath, “CellTracker (not only) for dummies,” *Bioinformatics*, vol. 32, no. 6, pp. 955–957, 2016.

[63] K. L. Urish, B. M. Deasy, and J. Huard, “Automated classification and visualization of fluorescent live cell microscopy images,” *J. Microsc.*, vol. 249, no. 3, pp. 206–214, 2013.

[64] B. Chazotte, “Labeling nuclear DNA with Hoechst 33342,” *Cold Spring Harb. Protoc.*, vol. 6, no. 1, pp. 83–86, 2011.

[65] D. Karra and R. Dahm, “Transfection Techniques for Neuronal Cells,” *J. Neurosci.*, vol. 30, no. 18, pp. 6171–6177, 2010.

[66] R. Thavarajah, V. M. Kazhiyur, J. Elizabeth, U. K. Rao, and K. Ranganathan, “Chemical and physical basics of routine formaldehyde fixation,” *J. Oral Maxillofac. Pathol.*, vol. 16, no. 3, pp. 400–405, 2012.

[67] E. C. T. Yeung, C. Stasolla, M. J. Sumner, and B. Q. Huang, “Plant microtechniques and protocols,” *Plant Microtech. Protoc.*, pp. 23–43, 2015.

[68] J. Kovačević and G. K. Rohde, “Overview of Image Analysis Tools and Tasks for Microscopy,” in *Microscopic Image Analysis for Life Science Applications*, Artech Press, 2007, pp. 56–67.

[69] R. C. Gonzalez and R. E. Woods, *Digital Image Processing*. Prentice Hall, 2007.

[70] N. Otsu, “A Threshold Selection Method from Gray-Level Histograms,” *IEEE Trans. Sytstems, Man Cybern.*, vol. 20, no. 1, pp. 62–66, 1979.

[71] J. C. Russ, *Introduction to Image Processing and Analysis*. CRC Press, 2007.

[72] A. Rosenfeld, “Image Analysis,” in *Digital Image Processing Techniques*, M. P. Ekstrom, Ed. Academic press, 1984, pp. 257–286.

[73] I. Pitas, *Digital Image Processing Algorithms and Applications*. John Wiley & Sons, 2000.

[74] J. Serra, *Image analysis and mathematical morphology*. London: Academic Press, 1982.

[75] R. M. Haralick, S. R. Sternberg, and X. Zhuang, "Image Analysis Using Mathematical Morphology," *Pattern Anal. Mach. Intell. IEEE Trans.*, no. 4, pp. 532–550, 1987.

[76] D. A. Randell, Z. Cui, and A. G. Cohn, "A spatial logic based on regions and connection," in *Proc. 3rd Int. Conf. on Knowledge Representation and Reasoning*, 1992, vol. 1, pp. 165–176.

[77] D. A. Randell, G. Landini, and A. Galton, "Discrete Mereotopology for Spatial Reasoning in Automated Histological Image Analysis," *IEEE Trans. Pattern Anal. Mach. Intell.*, vol. 35, no. 3, pp. 568–581, 2013.

[78] H. Strange, Z. Chen, E. R. E. Denton, and R. Zwiggelaar, "Modelling mammographic microcalcification clusters using persistent mereotopology," *Pattern Recognit. Lett.*, vol. 47, pp. 157–163, 2014.

[79] G. Landini, D. A. Randell, and A. P. Galton, "Discrete Mereotopology in Histological Imaging," in *Proceedings of the 17th conference on Medical Image Understanding and Analysis*, 2013, pp. 101–106.

[80] Z. Pincus and J. Theriot, "Comparison of quantitative methods for cell-shape analysis.," *J. Microsc.*, vol. 227, no. Pt 2, pp. 140–156, 2007.

[81] C. C. Reyes-Aldasoro, "Retrospective shading correction algorithm based on signal envelope estimation," *Electron Lett*, vol. 45, no. 9, pp. 454–456, 2009.

[82] J. B. T. M. Roerdink and A. Meijster, "The Watershed Transform : Definitions , Algorithms and Parallelization Strategies," *Fundam. Informaticae*, vol. 41, pp. 187–228, 2001.

[83] S. Choi and C. Kim, "Automatic initialization active contour model for the segmentation of the chest wall on chest CT," *Healthc. Inform. Res.*, vol. 16, no. 1, pp. 36–45, 2010.

[84] J. Qi, "Dense nuclei segmentation based on graph cut and convexity-concavity analysis.," *J. Microsc.*, vol. 253, no. 1, pp. 42–53, 2014.

[85] T. F. Chan, B. Y. Sandberg, and L. a. Vese, "Active Contours without Edges for Vector-Valued Images," *J. Vis. Commun. Image Represent.*, vol. 11, no. 2, pp. 130–141, 2000.

[86] R. Ali, M. Gooding, T. Szilágyi, B. Vojnovic, M. Christlieb, and M. Brady, "Automatic segmentation of adherent biological cell boundaries and nuclei from brightfield microscopy images," *Mach. Vis. Appl.*, vol. 23, no. 4, pp. 607–621, 2011.

[87] K. Wu, D. Gauthier, and M. D. Levine, "Live cell image segmentation," *Biomed. Eng. IEEE Trans.*, vol. 42, no. 1, pp. 1–12, 1995.

[88] A. Korzynska, W. Strojny, A. Hoppe, D. Wertheim, and P. Hoser, “Segmentation of microscope images of living cells,” *Pattern Anal. Appl.*, vol. 10, no. 4, pp. 301–319, 2007.

[89] Z. Yin, T. Kanade, and M. Chen, “Understanding the phase contrast optics to restore artifact-free microscopy images for segmentation.,” *Med. Image Anal.*, vol. 16, no. 5, pp. 1047–62, 2012.

[90] J. Sarsby, E. Claridge, G. Nash, D. Thickett, H. Jeffery, and S. Zheng, “Restoration of phase contrast microscopy images for the analysis of lung epithelial scratch wound repair assays,” in *Medical imaging understanding and analysis, Swansea*, 2012, pp. 101–106.

[91] I. Seroussi, D. Veikherman, N. Ofer, S. Yehudai-Resheff, and K. Keren, “Segmentation and tracking of live cells in phase-contrast images using directional gradient vector flow for snakes.,” *J. Microsc.*, vol. 247, no. 2, pp. 137–46, 2012.

[92] C. F. Koyuncu, S. Arslan, I. Durmaz, R. Cetin-Atalay, and C. Gunduz-Demir, “Smart markers for watershed-based cell segmentation,” *PLoS One*, vol. 7, no. 11, p. e48664, 2012.

[93] R. Bensch and O. Ronneberger, “Cell Segmentation and Tracking in Phase Contrast Images using Graph Cut with Asymmetric Boundary Costs,” in *International symposium on Biomedical Imaging, Brooklyn*, 2015, pp. 1220–1223.

[94] G. Topman, O. Sharabani-yosef, and A. Gefen, “A Method for Quick , Low-Cost Automated Confluency Measurements,” *Microsc. Microanal.*, vol. 17, no. 6, pp. 915–922, 2011.

[95] A. Zaritsky, S. Natan, J. Horev, I. Hecht, L. Wolf, E. Ben-Jacob, and I. Tsarfaty, “Cell motility dynamics: a novel segmentation algorithm to quantify multi-cellular bright field microscopy images.,” *PLoS One*, vol. 6, no. 11, p. e27593, Jan. 2011.

[96] N. Jaccard, N. Szita, and L. D. Griffin, “Trainable segmentation of phase contrast microscopy images based on local Basic Image Features histograms Trainable segmentation General approach,” in *Medical imaging understanding and analysis, London*, 2014, no. April 2015, pp. 47–52.

[97] S. Horikoshi and N. Serpone, “Introduction to Nanoparticles,” in *Microwaves in Nanoparticle Synthesis: Fundamentals and Applications*, 2013, pp. 1–24.

[98] R. Toy, P. M. Peiris, K. B. Ghaghada, and E. Karathanasis, “Shaping cancer nanomedicine: The effect of particle shape on the in vivo journey of nanoparticles,” *Nanomedicine (Lond.)*, vol. 4, no. 164, pp. 121–134, 2011.

[99] A.-I. Moreno-Vega, T. Gómez-Quintero, R.-E. Nuñez-Anita, L.-S. Acosta-Torres, and V. Castaño, “Polymeric and Ceramic Nanoparticles in Biomedical Applications,” *J. Nanotechnol.*, vol. 2012, no. -, pp. 1–10, 2012.

[100] S. Arora, J. M. Rajwade, and K. M. Paknikar, “Nanotoxicology and in vitro studies: the need of the hour.,” *Toxicol. Appl. Pharmacol.*, vol. 258, no. 2, pp. 151–165, Jan. 2012.

[101] O. Salata, “Applications of nanoparticles in biology and medicine.,” *J. Nanobiotechnology*, vol. 2, no. 1, pp. 1–6, 2004.

[102] K. Mijnendonckx, N. Leys, J. Mahillon, S. Silver, and R. Van Houdt, “Antimicrobial silver: uses, toxicity and potential for resistance.,” *Biometals*, vol. 26, no. 4, pp. 609–621, Aug. 2013.

[103] S. Prabhu and E. K. Poulose, “Silver nanoparticles: mechanism of antimicrobial action, synthesis, medical applications, and toxicity effects,” *Int. Nano Lett.*, vol. 2, no. 1, pp. 32–42, 2012.

[104] M. Ahamed, M. S. Alsalhi, and M. K. J. Siddiqui, “Silver nanoparticle applications and human health.,” *Clin. Chim. Acta.*, vol. 411, no. 23–24, pp. 1841–1848, Dec. 2010.

[105] K. Chaloupka, Y. Malam, and A. M. Seifalian, “Nanosilver as a new generation of nanoproduct in biomedical applications.,” *Trends Biotechnol.*, vol. 28, no. 11, pp. 580–588, Nov. 2010.

[106] X. Chen and H. J. Schluesener, “Nanosilver: a nanoproduct in medical application.,” *Toxicol. Lett.*, vol. 176, no. 1, pp. 1–12, Jan. 2008.

[107] W.-R. Li, X.-B. Xie, Q.-S. Shi, H.-Y. Zeng, Y.-S. Ou-Yang, and Y.-B. Chen, “Antibacterial activity and mechanism of silver nanoparticles on Escherichia coli.,” *Appl. Microbiol. Biotechnol.*, vol. 85, no. 4, pp. 1115–22, Jan. 2010.

[108] S. Arora, J. Jain, J. M. Rajwade, and K. M. Paknikar, “Cellular responses induced by silver nanoparticles: In vitro studies.,” *Toxicol. Lett.*, vol. 179, no. 2, pp. 93–100, Jul. 2008.

[109] S. Ahmed, M. Ahmad, B. L. Swami, and S. Ikram, “A review on plants extract mediated synthesis of silver nanoparticles for antimicrobial applications: A green expertise,” *J. Adv. Res.*, vol. 7, no. 1, pp. 17–28, 2016.

[110] M. Tejamaya, I. Römer, R. C. Merrifield, and J. R. Lead, “Stability of Citrate, PVP, and PEG Coated Silver Nanoparticles in Ecotoxicology Media,” *Environ. Sci. Technol.*, vol. 46, no. 13, pp. 7011–7017, 2012.

[111] I. Sur, D. Cam, M. Kahraman, A. Baysal, and M. Culha, “Interaction of multi-functional silver nanoparticles with living cells.,” *Nanotechnology*, vol. 21, no. 17, p. 175104, Apr. 2010.

[112] M. Milić, G. Leitinger, I. Pavičić, M. Zebić Avdičević, S. Dobrović, W. Goessler, and I. Vinković Vrček, “Cellular uptake and toxicity effects of silver nanoparticles in mammalian kidney cells,” *J. Appl. Toxicol.*, vol. 35, no. 2014, pp. 581–592, 2014.

[113] O. Choi, K. K. Deng, N.-J. Kim, L. Ross, R. Y. Surampalli, and Z. Hu, “The inhibitory effects of silver nanoparticles, silver ions, and silver chloride colloids on microbial growth.,” *Water Res.*, vol. 42, no. 12, pp. 3066–74, 2008.

[114] A. Besinis, T. De Peralta, and R. D. Handy, “The antibacterial effects of silver, titanium dioxide and silica dioxide nanoparticles compared to the dental disinfectant

chlorhexidine on Streptococcus mutans using a suite of bioassays.," *Nanotoxicology*, vol. 8, no. 1, pp. 1–16, 2014.

[115] A. Dziedzic, R. Kubina, R. J. Bułdak, M. Skonieczna, and K. Cholewa, "Silver nanoparticles exhibit the dose-dependent anti-proliferative effect against human squamous carcinoma cells attenuated in the presence of berberine," *Molecules*, vol. 21, no. 3, pp. 365–382, 2016.

[116] S. Pal, Y. K. Tak, and J. M. Song, "Does the antibacterial activity of silver nanoparticles depend on the shape of the nanoparticle? A study of the Gram-negative bacterium Escherichia coli.," *Appl. Environ. Microbiol.*, vol. 73, no. 6, pp. 1712–1720, Mar. 2007.

[117] G. A. Sotiriou and S. E. Pratsinis, "Antibacterial activity of nanosilver ions and particles," *Environ. Sci. Technol.*, vol. 44, no. 14, pp. 5649–5654, 2010.

[118] K.-H. Cho, J.-E. Park, T. Osaka, and S.-G. Park, "The study of antimicrobial activity and preservative effects of nanosilver ingredient," *Electrochim. Acta*, vol. 51, no. 5, pp. 956–960, 2005.

[119] J. S. Kim, E. Kuk, K. N. Yu, J.-H. Kim, S. J. Park, H. J. Lee, S. H. Kim, Y. K. Park, Y. H. Park, C.-Y. Hwang, Y.-K. Kim, Y.-S. Lee, D. H. Jeong, and M.-H. Cho, "Antimicrobial effects of silver nanoparticles.," *Nanomedicine*, vol. 3, no. 1, pp. 95–101, 2007.

[120] P. Cronholm, H. L. Karlsson, J. Hedberg, T. A. Lowe, L. Winnberg, K. Elihn, I. O. Wallinder, and L. Möller, "Intracellular uptake and toxicity of Ag and CuO nanoparticles: A comparison between nanoparticles and their corresponding metal ions," *Small*, vol. 9, no. 7, pp. 970–982, 2013.

[121] A. E. Egger, C. Rappel, M. A. Jakupec, and C. G. Hartinger, "Europe PMC Funders Group Development of an experimental protocol for uptake studies of metal compounds in adherent tumor cells," vol. 24, no. 1, pp. 51–61, 2012.

[122] S. Kim, J. E. Choi, J. Choi, K. H. Chung, K. Park, J. Yi, and D. Y. Ryu, "Oxidative stress-dependent toxicity of silver nanoparticles in human hepatoma cells," *Toxicol. Vitr.*, vol. 23, no. 6, pp. 1076–1084, 2009.

[123] Z. Xiu, Q. Zhang, H. L. Puppala, V. L. Colvin, and P. J. J. Alvarez, "Negligible Particle-Specific Antibacterial Activity of Silver Nanoparticles," *Nano Lett.*, vol. 12, pp. 4271–4275, 2012.

[124] C. Lok, C. Ho, R. Chen, Q. He, W.-Y. Yu, H. Sun, P. Kwong-Hang Tam, J.-F. Chiu, and C. Che, "Proteomic analysis of the mode of antibacterial action of silver nanoparticles.," *J. Proteome Res.*, vol. 5, no. 4, pp. 916–924, 2006.

[125] E. J. Park, J. Yi, Y. Kim, K. Choi, and K. Park, "Silver nanoparticles induce cytotoxicity by a Trojan-horse type mechanism," *Toxicol. Vitr.*, vol. 24, no. 3, pp. 872–878, 2010.

[126] C. Marambio-Jones and E. Hoek, "A review of the antibacterial effects of silver nanomaterials and potential implications for human health and the environment," *J. Nanoparticle Res.*, vol. 12, p. 21, 2010.

[127] I. Sondi and B. Salopek-Sondi, “Silver nanoparticles as antimicrobial agent: a case study on E. coli as a model for Gram-negative bacteria.,” *J. Colloid Interface Sci.*, vol. 275, no. 1, pp. 177–182, Jul. 2004.

[128] G. a. Martínez-Castañón, N. Niño-Martínez, F. Martínez-Gutierrez, J. R. Martínez-Mendoza, and F. Ruiz, “Synthesis and antibacterial activity of silver nanoparticles with different sizes,” *J. Nanoparticle Res.*, vol. 10, no. 8, pp. 1343–1348, Jul. 2008.

[129] P. V Asharani, M. P. Hande, and S. Valiyaveettil, “Anti-proliferative activity of silver nanoparticles.,” *BMC Cell Biol.*, vol. 10, no. 65, pp. 1–14, Jan. 2009.

[130] P. V Asharani, G. Low, K. Mun, M. P. Hande, and S. Valiyaveettil, “Cytotoxicity and Genotoxicity of Silver,” *ACS Nano*, vol. 3, no. 2, pp. 279–290, 2009.

[131] F. Faedmaleki, F. H. Shirazi, A. Salarian, and H. Ashtianid, Hamidreza Ahmadi Rastegara, “Toxicity Effect of Silver Nanoparticles on Mice Liver Primary Cell Culture and HepG2 Cell Line,” *Iran. J. Pharm. Res.*, vol. 13, no. 1, pp. 235–242, 2014.

[132] M. V. D. Z. Park, A. M. Neigh, J. P. Vermeulen, L. J. J. de la Fonteyne, H. W. Verharen, J. J. Briedé, H. van Loveren, and W. H. de Jong, “The effect of particle size on the cytotoxicity, inflammation, developmental toxicity and genotoxicity of silver nanoparticles.,” *Biomaterials*, vol. 32, no. 36, pp. 9810–9817, Dec. 2011.

[133] D. Guo, L. Zhu, Z. Huang, H. Zhou, Y. Ge, W. Ma, J. Wu, X. Zhang, X. Zhou, Y. Zhang, Y. Zhao, and N. Gu, “Anti-leukemia activity of PVP-coated silver nanoparticles via generation of reactive oxygen species and release of silver ions.,” *Biomaterials*, vol. 34, no. 32, pp. 7884–7894, Oct. 2013.

[134] S. T. Stern and S. E. McNeil, “Nanotechnology safety concerns revisited,” *Toxicol. Sci.*, vol. 101, no. 1, pp. 4–21, 2008.

[135] M. E. Samberg, S. J. Oldenburg, and N. a Monteiro-Riviere, “Evaluation of silver nanoparticle toxicity in skin in vivo and keratinocytes in vitro.,” *Environ. Health Perspect.*, vol. 118, no. 3, pp. 407–413, Mar. 2010.

[136] X. Liu, P. Lee, C. Ho, V. C. H. Lui, Y. Chen, C. Che, P. K. Tam, and K. K. Wong, “Silver nanoparticles mediate differential responses in keratinocytes and fibroblasts during skin wound healing,” *ChemMedChem*, vol. 5, no. 3, pp. 468–475, 2010.

[137] K. H. L. Kwan, X. Liu, M. K. T. To, K. W. K. Yeung, C. Ho, and K. K. Y. Wong, “Modulation of collagen alignment by silver nanoparticles results in better mechanical properties in wound healing.,” *Nanomedicine*, vol. 7, no. 4, pp. 497–504, 2011.

[138] Z.-H. Jiao, M. Li, Y.-X. Feng, J.-C. Shi, J. Zhang, and B. Shao, “Hormesis effects of silver nanoparticles at non-cytotoxic doses to human hepatoma cells.,” *PLoS One*, vol. 9, no. 7, p. e102564, 2014.

[139] J. M. Corrêa, M. Mori, H. L. Sanches, A. D. Da Cruz, E. Poiate, and I. A. V. P. Poiate, “Silver nanoparticles in dental biomaterials,” *Int. J. Biomater.*, vol. 2015, no. Article ID 485275, pp. 1–9, 2015.

[140] L. F. Espinosa-Cristóbal, G. a Martínez-Castañón, E. J. Téllez-Déctor, N. Niño-Martínez, N. V Zavala-Alonso, and J. P. Loyola-Rodríguez, "Adherence inhibition of Streptococcus mutans on dental enamel surface using silver nanoparticles.," *Mater. Sci. Eng. C. Mater. Biol. Appl.*, vol. 33, no. 4, pp. 2197–2202, 2013.

[141] M. S. Holden, J. Black, A. Lewis, M. Boutrin, E. Walemba, T. S. Sabir, D. S. Boskovic, A. Wilson, H. M. Fletcher, and C. C. Perry, "Antibacterial Activity of Partially Oxidized Ag / Au Nanoparticles against the Oral Pathogen Porphyromonas gingivalis W83," *J. Nanomater.*, vol. 2016, no. Article ID 9605906, pp. 1–11, 2016.

[142] M. Samiei, A. Farjami, S. M. Dizaj, and F. Lotfipour, "Nanoparticles for antimicrobial purposes in Endodontics: A systematic review of in vitro studies," *Mater. Sci. Eng. C*, vol. 58, pp. 1269–1278, 2016.

[143] K.-Y. Y. Nam, "In vitro antimicrobial effect of the tissue conditioner containing silver nanoparticles," *J. Adv. Prosthodont.*, vol. 3, no. 1, pp. 20–24, 2011.

[144] S. Kasraei, L. Sami, S. Hendi, M.-Y. Alikhani, L. Rezaei-Soufi, and Z. Khamverdi, "Antibacterial properties of composite resins incorporating silver and zinc oxide nanoparticles on Streptococcus mutans and Lactobacillus.," *Restor. Dent. Endod.*, vol. 39, pp. 109–14, 2014.

[145] J. F. Hernández-Sierra, F. Ruiz, D. C. C. Pena, F. Martínez-Gutiérrez, A. E. Martínez, A. D. J. P. Guillén, H. Tapia-Pérez, and G. M. Castañón, "The antimicrobial sensitivity of Streptococcus mutans to nanoparticles of silver, zinc oxide, and gold.," *Nanomedicine*, vol. 4, no. 3, pp. 237–40, 2008.

[146] S. Gurunathan, "Rapid biological synthesis of silver nanoparticles and their enhanced antibacterial effects against Escherichia fergusonii and Streptococcus mutans," *Arab. J. Chem.*, vol. In Press, 2014.

[147] J. Ponten and E. Saksela, "Two established in vitro cell lines from human mesenchymal tumours," *Int. J. Cancer*, vol. 2, no. 5, pp. 434–447, 1967.

[148] S. Rehman, M. Ikram, R. J. Baker, M. Zubair, E. Azad, S. Min, K. Riaz, K. H. Mok, and S. Rehman, "Synthesis, characterization, in vitro antimicrobial, and U2OS tumoricidal activities of different coumarin derivatives.," *Chem. Cent. J.*, vol. 7(1), no. 68, pp. 1–12, 2013.

[149] G. Todaro and H. Green, "Quantitative studies of the growth of mouse embryo cells in culture and their development into established lines," *J. Cell Biol.*, vol. 17, no. 2, pp. 299–313, 1963.

[150] Logos Biosystems, "LUNA™ Automated Cell Counter," 2012. [Online]. Available: http://logosbio.com/cell_counters/luna/features.php.

[151] J. Kapuscinski, "DAPI: a DNA-Specific Fluorescent Probe," *Biotech. Histochem.*, vol. 70, no. 5, pp. 220–233, 1979.

[152] S. A. Latt and G. Stetten, "Spectral studies on 33258 Hoechst and related bisbenzimidazole dyes useful for fluorescent detection of deoxyribonucleic acid

synthesis," *J. Histochem. Cytochem.*, vol. 24, no. 1, pp. 24–33, 1976.

[153] W. S. Rasband, "ImageJ." U. S. National Institutes of Health, Bethesda, Maryland, USA.

[154] A. D. Edelstein, M. a Tsuchida, N. Amodaj, H. Pinkard, R. D. Vale, and N. Stuurman, "Advanced methods of microscope control using μManager software," *J. Biol. Methods*, vol. 1, no. 2, p. 10, 2014.

[155] A. R. Shahverdi, A. Fakhimi, H. R. Shahverdi, and S. Minaian, "Synthesis and effect of silver nanoparticles on the antibacterial activity of different antibiotics against Staphylococcus aureus and Escherichia coli.," *Nanomedicine*, vol. 3, no. 2, pp. 168–171, Jun. 2007.

[156] S. Alaluusua and O. Renkonen, "Streptococcus mutans establishment and dental caries experience in children from 2 to 4 years old," *Eur. J. Oral …*, vol. 91, no. 6, pp. 453–457, 1983.

[157] J. W. Bartholomew and T. Mittwer, "The Gram Stain," *Bact. Rev.*, vol. 16, no. 1, pp. 1–29, 1952.

[158] J. A. Creighton, C. G. Blatchford, and M. G. Albrecht, "Plasma resonance enhancement of Raman scattering by pyridine adsorbed on silver or gold sol particles of size comparable to the excitation wavelength," *J. Chem. Soc. Faraday Trans. 2 Mol. Chem. Phys.*, vol. 75, pp. 790–798, 1979.

[159] D. E. Koppel, "Analysis of Macromolecular Polydispersity in Intensity Correlation Spectroscopy: The Method of Cumulants," *J. Chem. Phys.*, vol. 57, p. 4814, 1972.

[160] M. Maeder and Y.-M. Neuhold, *Practical Data Analysis in Chemistry*. Elsevier, 2007.

[161] R. Pecora, Ed., *Dynamic Light Scattering*. Plenum Press New York, 1985.

[162] Malvern Instruments Ltd., "Dynamic Light Scattering (DLS)," *Malvern.com*. [Online]. Available: http://www.malvern.com/en/products/technology/dynamic-light-scattering/. [Accessed: 11-Apr-2017].

[163] Sigma-Aldrich, "Silver dispersion nanoparticles," 2015. [Online]. Available: http://www.sigmaaldrich.com/catalog/product/aldrich/730785?lang=en&region=GB. [Accessed: 01-Dec-2015].

[164] D. B. Williams and C. B. Carter, *Transmission Electron Microscopy*, 2nd ed. Springer US, 2009.

[165] S. Sternberg, "Biomedical Image Processing," *Computer (Long. Beach. Calif).*, vol. 16, no. 1, pp. 22–34, 1983.

[166] J. Bernsen, "Dynamic Thresholding of Grey-Level Images," in *Proc. of the 8th Int. Conf. on Pattern Recognition, Madrid*, 1986, pp. 1251–1255.

[167] G. Landini, "Advanced shape analysis with ImageJ," in *Proceedings of the Second ImageJ user and developer Conference*, 2008, pp. 116–121.

[168] J. W. Olesik, "Elemental Analysis Using ICP-OES and ICP/MS," *Anal. Chem.*, vol. 63, no.

1, p. 12A–21A, 1991.

[169] The MathWorks Inc., “Matlab.” Natick, MA.

[170] “GraphPad Prism.” GraphPad Software, La Jolla, California, USA, 2015.

[171] C. W. Dunnett, “A Multiple Comparison Procedure for Comparing Several Treatments with a Control,” *J. Am. Stat. Assoc.*, vol. 50, no. 272, pp. 1096–1121, 1955.

[172] J. W. Tukey, “Comparing Individual Means in the Analysis of Variance,” *Biometrics*, vol. 5, no. 2, pp. 99–114, 1949.

[173] N. Bindslev, “Hill in hell,” in *Drug-Acceptor Interactions*, 2008, pp. 257–282.

[174] H. Hotelling, “Analysis of a complex of statistical variables into principal components,” *J. Educ. Psychol.*, vol. 24, pp. 417–441, 498–520, 1936.

[175] M. D. Abramoff, Y. H. Kwon, D. Tso, H. Li, S. Berriga, P. Soliz, and R. Kardon, “A spatial truncation approach to the analysis of optical imaging of the retina in humans and cats,” *2004 2nd IEEE Int. Symp. Biomed. Imaging Macro to Nano, Washingt. DC*, vol. 2, no. 1, pp. 1115–1118, 2004.

[176] W. S. Rasband, “ImageJ.” U. S. National Institutes of Health, Bethesda, Maryland, USA, 2012.

[177] J. B. MacQueen, “Some Methods for Classification and Analysis of Multivariate Observations,” *5th Berkeley Symp. Math. Stat. Probab. 1967*, vol. 1, no. 233, pp. 281–297, 1967.

[178] J. Sacha, “ImageJ Plugins.” 2016.

[179] A. J. Izenman, *Modern Multivariate Statistical Techniques: Regression, Classification, and Manifold Learning*, vol. 65. Springer, 2009.

[180] C. Kingsford and S. L. Salzberg, “What are decision trees?,” *Nat Biotechnol*, vol. 26, no. 9, pp. 1011–1013, 2009.

[181] L. Jost, “Entropy and diversity,” *Oikos*, vol. 113, no. 2, pp. 363–375, 2006.

[182] D. M. W. Powers, “Evaluation: From precision, recall and f-measure to roc., informedness, markedness & correlation,” *J. Mach. Learn. Technol.*, vol. 2, no. 1, pp. 37 – 63, 2011.

[183] E. R. Davies, *Computer and Machine Vision: Theory, Algorithms, Practicalities*, 4th Editio. Academic Press, 2012.

[184] M. I. Naseer, H. Zubair, Ikramullah, and M. ok Kim, “Effect of Fetal Calf Serum on Cellular Proliferation of Mouse Y1,” *Pakistan J. Med. Sci.*, vol. 25, no. 3, pp. 500–504, 2009.

[185] L. S. Bambang, J. P. Mazzucotelli, M. Moczar, F. Beaujean, and D. Loisance, “Effects of cryopreservation on the proliferation and anticoagulant activity of human saphenous vein endothelial cells,” *J. Thorac. Cardiovasc. Surg.*, vol. 110, no. 4, pp. 998–1004,

1995.

[186] N. Oya, F. Zlzer, and C. S. Frank Werner, “Effects of Serum Starvation on Radiosensitivity, Proliferation and Apoptosis in Four Human Tumor Cell Lines with Different p53 Status,” *Strahlentherapie und Onkol.*, vol. 179, no. 2, pp. 99–106, 2003.

[187] G. Landini, “Auto Threshold,” *ImageJ.net*, 2016. [Online]. Available: http://imagej.net/Auto_Threshold.

[188] L. Huang and M.-J. J. Wang, “Image thresholding by minimizing the measures of fuzziness,” *Pattern Recognit.*, vol. 28, no. 1, pp. 41–51, 1995.

[189] J. M. Prewitt and M. L. Mendelsohn, “The analysis of cell images,” *Ann. N. Y. Acad. Sci.*, vol. 128, no. 3, pp. 1035–1053, 1966.

[190] S. Ridler, TW Calvard, “Picture Thresholding Using an Iterative Selection Method,” *Syst. Man Cybern. IEEE Trans.*, vol. 8, no. 8, pp. 630 – 632, 1978.

[191] C. Li and P. Tam, “An Iterative Algorithm for Minimum Cross Entropy Thresholding,” *Pattern Recognit. Lett.*, vol. 18, no. 8, pp. 146–165, 1998.

[192] J. Kapur, P. Sahoo, and A. Wong, “A New Method for Gray-Level Picture Thresholding Using the Entropy of the Histogram,” *Graph. Model. Image Process.*, vol. 29, no. 3, pp. 273–285, 1985.

[193] C. Glasbey, “An analysis of histogram-based thresholding algorithms,” *CVGIP Graph. Model. Image Process.*, vol. 55, no. 1, pp. 532–537, 1993.

[194] J. Kittler and J. Illingworth, “Minimum error thresholding,” *Pattern Recognit.*, vol. 19, no. 1, pp. 41–47, 1986.

[195] W.-H. Tsai, “Moment-preserving thresholding: a new approach,” in *Document image analysis*, IEEE Computer Society Press Los Alamitos, CA, USA, 1995, pp. 44–60.

[196] W. Doyle, “Operations Useful for Similarity-Invariant Pattern Recognition,” *J. ACM*, vol. 9, no. 2, pp. 259–267, 1962.

[197] A. G. Shanbhag, “Utilization of information measure as a means of image thresholding,” *Graph. Model. Image Process.*, vol. 56, no. 5, pp. 1049–9652, 1994.

[198] G. Zack, W. Rogers, and S. Latt, “Automatic measurement of sister chromatid exchange frequency,” *J. Histochem. Cytochem*, vol. 25, no. 7, pp. 741–753, 1977.

[199] J. Yen, F. Chang, and S. Chang, “A New Criterion for Automatic Multilevel Thresholding,” *IEEE Trans. Image Process.*, vol. 4, no. 3, pp. 370–378, 1995.

[200] Y. Boykov, O. Veksler, and R. Zabih, “Fast approximate energy minimization via graph cuts,” in *Proceedings of the Seventh IEEE International Conference on Computer Vision*, 1999, pp. 377–384.

[201] Y. Boykov and V. Kolmogorov, “An Experimental Comparison of Min-Cut/Max-Flow Algorithms for Energy Minimization in Computer Vision,” *IEEE Trans. Pattern Anal. Mach. Intell.*, vol. 26, no. 9, pp. 1124 – 1137, 2004.

[202] T. Dietenbeck, M. Alessandrini, D. Friboulet, and O. Bernard, “CREASEG: a free software for the evaluation of image segmentation algorithms based on level-set,” *Image Process. (ICIP), 2010 17th IEEE Int. Conf.*, pp. 665–668, 2010.

[203] S. Lankton, “Active Contours,” *Shawn Lankton Online*, 2007. [Online]. Available: http://www.shawnlankton.com/2007/05/active-contours/.

[204] J. M. S. Lemons, X.-J. Feng, B. D. Bennett, A. Legesse-Miller, E. L. Johnson, I. Raitman, E. A. Pollina, H. A. Rabit, J. D. Rabinowitz, and H. A. Coller, “Quiescent Fibroblasts Exhibit High Metabolic Activity,” *PLoS Biol.*, vol. 8, no. 10, pp. 1–16, 2010.

[205] M. Al-Musawi, J. Durham, J. M. Whitworth, S. J. Stone, D. R. Nixdorf, and R. A. Valentine, “Effect of topical neuromodulatory medications on oral and skin keratinocytes,” *J. Oral Pathol. Med.*, vol. 46, no. 2, pp. 134–141, 2016.

[206] R. van Horssen, N. Galjart, J. a P. Rens, A. M. M. Eggermont, and T. L. M. ten Hagen, “Differential effects of matrix and growth factors on endothelial and fibroblast motility: application of a modified cell migration assay.,” *J. Cell. Biochem.*, vol. 99, no. 6, pp. 1536–1552, 2006.

[207] M. N. M. Walter, K. T. Wright, H. R. Fuller, S. MacNeil, and W. E. B. Johnson, “Mesenchymal stem cell-conditioned medium accelerates skin wound healing: an in vitro study of fibroblast and keratinocyte scratch assays.,” *Exp. Cell Res.*, vol. 316, no. 7, pp. 1271–1281, 2010.

[208] B. Zhao, H. C. van der Mei, M. Rustema-Abbing, H. J. Busscher, and Y. Ren, “Osteoblast integration of dental implant materials after challenge by sub-gingival pathogens: a co-culture study in vitro,” *Int. J. Oral Sci.*, vol. 7, no. July, pp. 250–258, 2015.

[209] Sigma-Aldrich, “Silver nanopowder, <100 nm particle size, contains PVP as dispersant, 99.5% trace metals basis.” .

[210] P. R. Twentyman and M. Luscombe, “A study of some variables in a tetrazolium dye (MTT) based assay for cell growth and chemosensitivity.,” *Br. J. Cancer*, vol. 56, pp. 279–285, 1987.

[211] J. Choi, V. Reipa, V. M. Hitchins, P. L. Goering, and R. a Malinauskas, “Physicochemical characterization and in vitro hemolysis evaluation of silver nanoparticles.,” *Toxicol. Sci.*, vol. 123, no. 1, pp. 133–143, 2011.

[212] S. M. Hussain, K. L. Hess, J. M. Gearhart, K. T. Geiss, and J. J. Schlager, “In vitro toxicity of nanoparticles in BRL 3A rat liver cells.,” *Toxicol. In Vitro*, vol. 19, no. 7, pp. 975–983, 2005.

[213] L. F. Espinosa-Cristóbal, G. a. Martínez-Castañón, R. E. Martínez-Martínez, J. P. Loyola-Rodríguez, J. F. Reyes-Macías, and F. Ruiz, “Antibacterial effect of silver nanoparticles against Streptococcus mutans,” *Mater. Lett.*, vol. 63, no. 29, pp. 2603–2606, 2009.

[214] K. Loza, J. Diendorf, C. Sengstock, L. Ruiz-Gonzalez, J. M. Gonzalez-Calbet, M. Vallet-Regi, M. Köller, and M. Epple, “The dissolution and biological effects of silver nanoparticles in biological media,” *J. Mater. Chem. B*, vol. 2, no. 12, pp. 1634–1643,

2014.

[215] E. Khan, R. M. Shelton, P. R. Cooper, J. Hamburger, and G. Landini, “Architectural characterization of organotypic cultures of H400 and primary rat keratinocytes,” *J. Biomed. Mater. Res. Part A*, vol. 100A, no. 12, pp. 3227–3238, 2012.